Nanostructured Electrodes for Low Temperature Solid Oxide Fuel Cells

TECHNISCHE UNIVERSITÄT DARMSTADT

Erklärung zur Dissertation

Hiermit versichere ich, dass ich meine Dissertation selbstständig und nur mit den angegebenen Quellen und Hilfsmitteln angefertigt habe. Diese Arbeit hat in gleicher oder ähnlicher Form noch keiner Prüfungsbehörde vorgelegen.

Darmstadt, den 23.02.2016

(Cahit Benel)

Abstract

The reduction of the operating temperatures of solid oxide fuel cells (SOFCs) below 600 °C is one of the primary objectives to make them cost competitive with existing energy conversion technologies. However, the low ionic conductivity of the electrolytes and the sluggish electrochemical reaction rates at the electrodes are the major issues, which limit the performance of SOFCs at reduced operating temperatures. While the effect of limited ionic conductivity of the electrolytes at lower operating temperatures has been compensated by decreasing the electrolyte thicknesses, the utilization of nanostructured electrodes with enhanced electrochemical activities has been one of the most common approaches to overcome the electrode limitations associated with the reduced operating temperatures.

The aim of the thesis is to obtain high performance nanostructured electrodes for SOFCs in a cost-effective and easily scalable production method. The state-of-the-art electrode materials of $La_{0.6}Sr_{0.4}CoO_{3-\delta}$ (LSC) and $Ni-Ce_{0.8}Gd_{0.2}O_{2-\delta}$ (NiO-GDC20) with ultrafine microstructure and high phase purity are synthesized by salt-assisted spray pyrolysis method. Nanostructured electrode thin films fabricated by spin coating of the water-based dispersions of LSC and NiO-GDC20 nanoparticles exhibit a three-dimensional porous microstructure with a grain size of around 50 nm. The electrochemical performances of the resulting electrode layers with thicknesses below 1 μm are optimized in the symmetrical cell configuration for the purpose to integrate them into the micro-solid oxide fuel cell (micro-SOFC) devices, which typically employ costly physical vapor deposited Pt thin film electrodes. The proof of concept for the fabrication of porous micro-SOFC electrodes by spin coating of suspensions of electrode nanoparticles is reported for the first time, and the first set of electrochemical data (12 mW/cm^2 at 500 °C) demonstrates the feasibility of the developed thin film electrode fabrication method. Furthermore, the synthesized electrode materials are examined in ceria-based anode supported SOFC design. The promising initial electrochemical results (318 mW/cm^2 at 600 °C) set the ground for further optimization of the anode supported LSC|$Ce_{0.9}Gd_{0.1}O_{2-\delta}$ (GDC10)|Ni-GDC20 cells.

Acknowledgements

Many people have contributed to the success of this work and I would like to thank all of them.

Foremost, I would like to express my sincerest gratitude to Prof. Dr.-Ing. Horst Hahn for giving me the opportunity to work in his group and providing excellent research conditions. Throughout my PhD work, he always gave me freedom and support to conduct my own research ideas. I always appreciated his confidence in me as well as the possibilities that he provided to present my results in international conferences around the globe, which was always a great opportunity to meet other scientists, exchange valuable ideas, and start active collaborations.

Prof Dr. Wolfgang Ensinger is gratefully acknowledged for being the co-examiner of this thesis.

I am also thankful to Prof. Dr. Wolfgang Donner and Prof. Dr. Jürgen Janek for being on my examination committee.

Dr. Azad Darbandi is gratefully acknowledged for his supervision during the initial phase of this work and his continuous support even after he left the group. It would be impossible to finalize this work as it is without his valuable contribution and guidance.

I am thankful to Dr. Ruzica Djenadic for her kind support, guidance, and encouragement throughout my work. Her contributions in dynamic light scattering, zeta potential and low temperature surface area measurements are gratefully acknowledged. I am also grateful to her for countless productive discussions that we had and proof reading of this work.

I wish to express my gratitude to Dr. Oliver Clemens for his contribution in X-ray diffraction experiments. I appreciate his continuous efforts to keep the X-ray diffractometer in a working condition, his generous help in structure refinement, and his proof reading parts of the thesis.

A part of this work would not have been possible without active collaborations. Therefore, I am grateful to Dr. Michel Prestat and Dr. Anna Evans from the Institute of Inorganic Nonmetallic Materials at ETH Zurich (Switzerland) for introducing me the fascinating world of micro solid oxide fuel cells and our fruitful collaboration. Dr. Julia Martynczuk is acknowledged for the FIB-SEM investigations of the corresponding samples.

I would like to thank all my former and current colleagues in the group of Prof. Hahn as well as from other research groups for their support and the friendly working atmosphere in the Material Science Department at Technische Universität Darmstadt and in the Institute of Nanotechnology at Karlsruhe Institute of Technology. I also wish to express my gratitude to Renate Hernichel for managing the administrative work and for her kind support. Dr. Di Wang is acknowledged for excellent TEM imaging.

Special thanks go to Jochen Rank and his team in the mechanical workshop in the Material Science Department at Technische Universität Darmstadt for manufacturing the unique components required for the spray pyrolysis and the sample holders for the high temperature

Table of Content

1. Introduction

Ever since the Industrial Revolution in 18th century, combustion of the fossil fuels such as coal, oil, and natural gas has been the primary way of the energy generation. However, the continued availability of fossil fuels, their cost, and the environmental effects of the increasing emission of greenhouse gasses are the major concerns. Therefore, alternative energy conversion systems with lower or zero carbon emissions have to replace the conventional fossil fuel dependent technologies.

One of the alternative energy conversion systems is the fuel cell technology, in which the chemical energy within the fuel is converted directly into the electrical energy through a series of electrochemical reactions. Figure 1-1 illustrates the general concept of the fuel cells. The electrochemical reactions taking place at the electrodes lead to the formation of electrons and ions. The electrons and ions generated at one electrode have to be consumed in the other electrode to maintain charge balance within the fuel cell. Therefore, these species must be transported from the locations where they are generated to the locations where they are consumed. In terms of electrons, the transport is maintained as long as an electronically conductive path is present, which typically consists of the electronically conductive electrodes, the interconnects, and the external circuit. The transport of ionic species is accomplished by the electrolyte layer, which provides a pathway for the ions to flow. Flowing electrons along the external circuit provide power when a load is introduced in between and a fuel cell continues to generate electricity as long as fuel and oxidant are supplied continuously.

There are several types of fuel cells, which are usually named after their ionic conducting electrolyte membranes: polymer electrolyte membrane fuel cells (PEMFCs), alkaline fuel cells (AFCs), phosphoric acid fuel cells (PAFCs), molten carbonate fuel cells (MCFCs), and solid oxide
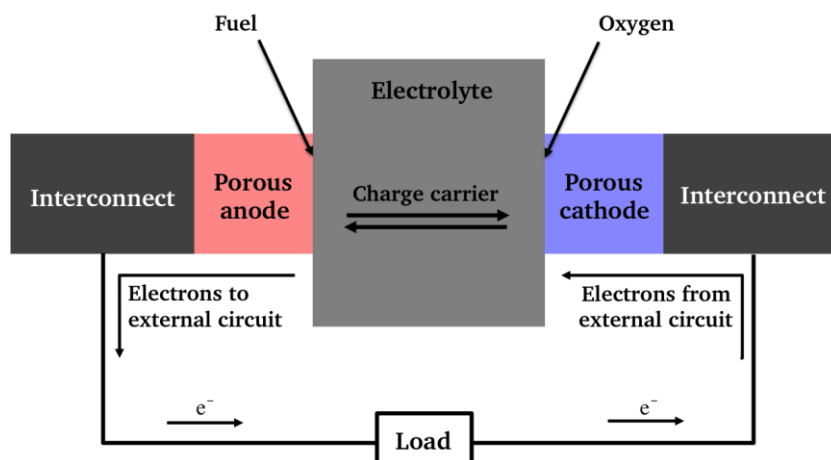
Figure 1-1: General concept of the fuel cells.

fuel cells (SOFCs), among which SOFCs have drawn a great interest because of their fuel flexibility, long-term stability, and high conversion efficiencies [1]–[7].

The main components of an SOFC, which are electrolyte, anode, cathode, and interconnects, have to fulfill specific requirements. The electrolyte has to be a gas-tight membrane exhibiting high ionic conductivity but negligible electronic conductivity. On the other hand, the electrodes must be porous to be able to transport gaseous reactants to the electrolyte/electrode interfaces. In addition to high electronic conductivity, electrode materials have to display high catalytic activity towards the desired electrochemical reactions. Moreover, the transport of oxygen ions by electrode material is not necessary but particularly advantageous in terms of increasing the number of active reactions sites for the electrochemical reactions. Finally, interconnects have to exhibit high electronic conductivity but negligible ionic conductivity. Since SOFCs exhibit layered configurations, the compatibilities between the elements such as well-matching thermal expansion behavior, good interfacial adhesion, and chemical compatibility are essential.

1.1. Objectives of SOFC Research

Despite the conceptual attractiveness of the SOFC technology, the major obstacle, in the way of its commercialization, had been the requirement of high operating temperatures (800–1000 °C), which results in high manufacturing and running costs, long start-up and shut-down times, and high degradation rates. Therefore, one of the main objectives of the SOFC community has been the development of SOFCs with high power densities operating at temperatures below 700 °C, which is nowadays the state-of-the-art operating temperature for SOFCs based on oxygen ion conducting yttria-stabilized zirconia (YSZ) electrolyte [8]. The reduction of the operating temperatures even below 600 °C would allow the use of less expensive sealant and metallic interconnect materials, and eliminate the degradation issues. However, the ionic transport processes and electrochemical reactions are thermally activated, and they become sluggish with decreasing temperatures. Thus, the efforts to reduce the operating temperatures of SOFCs have focused predominantly on decreasing the diffusion path length for the ions (*i.e.*, reducing the electrolyte thickness), the development of novel materials with enhanced transport and catalytic properties at low temperatures, and the optimization of their properties.

Considerable reduction in SOFC operating temperatures has been first realized by reducing the thickness of electrolytes, which minimizes the Ohmic losses within the cell by decreasing the length of the diffusion path for oxygen ions. This approach required the change of the cell geometry from the conventional *electrolyte-supported design* with an electrolyte thickness typically higher than 100 μm towards the *electrode-supported design*, in which thin electrolyte layers with thicknesses lower than 20 μm are deposited onto thermo-mechanically stable porous electrode supports. Recently, advances in the deposition of thin film electrolyte layers with thicknesses below 1 μm by physical vapor deposition techniques have resulted in the cells with peak power densities above 500 mW/cm^2 at 500 °C [9], which is a notable low-temperature performance for a YSZ-based anode supported SOFC. Additionally, innovations in thin-film deposition techniques and microfabrication processes have drawn considerable attention towards the miniaturization of SOFC devices (micro-SOFC) as battery replacement for portable applications such as mobile phones and laptops [10]–[17]. Potentially, micro-SOFCs offer higher energy per volume and weight compared to batteries, since their fuel flexibility allows utilization of high energy density hydrocarbons [18]–[20]. A parallel approach for cutting down the electrolyte-caused Ohmic losses has been to find alternative materials with improved ionic conductivities compared to the conventional YSZ electrolyte. Examples of such material systems are doped ceria, doped

lanthanum gallate, and doped bismuth oxide [21]–[26]. The proton-conducting electrolytes such as doped barium cerates and doped barium zirconates are also promising alternatives [27]–[32]. Even though Ohmic losses can be reduced by one to two orders of magnitude by substituting YSZ with alternative electrolyte materials, the uncertainties about their long-term stability, material compatibility with the adjoining cell components, and undesirable electronic conduction under operating conditions still make the YSZ one of the most desirable electrolyte material choices for SOFC applications [33].

Another important strategy to lower operating temperatures of SOFCs has focused on the reduction of losses associated with electrochemical processes taking place at electrodes, which can be achieved by developing novel electrodes with high activities towards oxygen reduction and fuel oxidation, and by engineering the microstructures of the electrode layers. At lower operating temperatures, the activation energies required by the electrochemical reactions become larger, which can only be overcome at the expense of the cell voltage resulting in high voltage losses at low temperatures. In terms of cathode, $La_{1-x}Sr_xMnO_{3-\delta}$ (LSM)-based perovskites have been one of the most popular choices for the conventional high temperature SOFCs due to their thermomechanical compatibility with the YSZ electrolyte as well as sufficient electrochemical performance [34]–[36]. However, the low ionic conductivity and the slow oxygen surface exchange kinetics of LSM restrict the electrochemical reactions to the triple phase boundaries (TPBs) [36], where the gas phase meets the electronically conducting cathode and the ionically conducting electrolyte phases. The localization of electrochemical reactions at or near the cathode/electrolyte interface significantly limits the number of active reactions sites and eventually the overall performance of the SOFCs. Typically, the oxygen ion transport within the cathode layer is favored, as it delocalizes the charge transfer reactions from the cathode/electrolyte interface to the entire cathode layer. Thus, mixed-ionic-electronic-conducting (MIEC) cathodes such as $La_{1-x}Sr_xCo_{1-y}Fe_yO_{3-\delta}$ (LSCF), $Ba_{1-x}Sr_xCo_{1-y}Fe_yO_{3-\delta}$ (BSCF), and $La_{1-x}Sr_xCoO_{3-\delta}$ (LSC) have been intensively studied, which have been reported to have enhanced catalytic activity in the lower temperature range of 450–600 °C [37]–[39]. Due to the mixed conductive nature, the oxygen ion exchange is extended effectively over the entire surface of the cathode. Even though these novel cathodes yield considerably lower polarization losses, there are issues in terms of their thermomechanical and chemical compatibility with the YSZ electrolyte and their long-term stability [40]–[42]. Similar to the cathode, the anodes have to combine electronic (or mixed ionic-electronic) conductivity, electrochemical activity for fuel oxidation, thermomechanical and chemical stability under operation, and compatibility with the other components of the cell. Considering such rigorous requirements, only a few candidates are available. Conventionally, metallic anodes such as platinum (Pt) and nickel (Ni) were used as anodes. Especially, Ni had been employed as anode material for several years due to its excellent catalytic activity towards fuel oxidation [43]. However, its significant thermal expansion coefficient mismatch with YSZ and the tendency of Ni grains to agglomerate at elevated temperatures lead to thermomechanical failure and reduction of active reaction sites at the anode/electrolyte interface, respectively. At that point, the development of ceramic-metal composite (*cermet*) Ni-YSZ anode has been a major breakthrough [44], as it meets most of the essential requirements for SOFC anodes. Since then, Ni-YSZ cermet has been the most commonly used SOFC anode material. The fully percolated Ni grains within the porous YSZ matrix provide the electronic conductivity along with the required catalytic activity, while the YSZ phase provides thermomechanical stability to the anode layer, hinders coarsening of Ni grains at elevated temperatures, and increases the number of active reaction sites for the fuel oxidation by extending the TPB length with its oxygen ion conductivity [43]. To reduce the anodic overpotentials, considerable work has been done to replace the ionically conductive zirconia matrix with ceramics having enhanced transport properties such as doped ceria [45]–[48]. Even

though cermet anodes have sufficient electrochemical performance in the anode-supported cell geometry, the use of Ni-based anodes lead to the problem of coke formation when operating on hydrocarbon fuels [43]. Furthermore, the large volume changes caused by redox cycles and intolerance to sulfur impurities are the major drawbacks of the Ni-based cermet anodes [6]. Therefore, alternative anode materials, which are more resistant to coke formation and sulfur poisoning such as lanthanum chromite, strontium titanate, and strontium molybdate have been under development [49]–[53].

In addition to the strategies focusing on the intrinsic properties, the electrochemical performance of the electrodes can be enhanced at lower operating temperatures by increasing the number of active reaction sites. For composite electrodes (*e.g.,* LSM-YSZ and cermets), the major research effort has focused on the optimization of the electrode microstructure to maximize TPB length, since the TPBs are required for electrochemical reactions. For MIEC electrodes, the oxygen exchange at perovskite/air or perovskite/fuel is believed to be one of the rate-determining steps for oxygen reduction or fuel oxidation, respectively. Thus, an enhancement of the electrochemical activity can be achieved by nanostructuring and/or increasing the electrode thickness creating a large number of electrochemically active sites [8], [21], [33], [36], [54].

1.2. Objectives of the Thesis and Outline

One of the main objectives of the thesis is the realization of nanostructured electrodes with high electrochemical performance at low operating temperatures for the SOFC applications, which requires cost effective synthesis and processing techniques compatible with the current SOFC fabrication standards. The thesis also targets to integrate porous thin-film electrodes onto freestanding micro-SOFC membranes using a cost-effective atmospheric-deposition method. Finally, the fabrication of an anode-supported SOFC using the developed techniques throughout this thesis and its electrochemical characterization are intended.

The outline of the thesis is as follows:

Chapter 2 gives an introduction to SOFCs, in which the working principle, the different sources of cell polarization, SOFC materials and components along with the manufacturing techniques, and the electrochemical methods used to determine the performance of fuel cells and components are elaborated.

Chapter 3 gives a detailed description of the methods used for synthesis, processing, and characterization of the materials and the cell components. A special emphasis is put on passing down the know-how gained in terms of the nanoparticle synthesis and cell fabrication methods. Therefore, the details of the synthesis and film deposition methods are given comprehensively.

Chapter 4 emphasizes the effects of the synthesis parameters on the morphology and structure of the state-of-the-art nanostructured electrode materials, $La_{0.6}Sr_{0.4}CoO_{3-\delta}$ (LSC) and $NiO-Ce_{0.8}Gd_{0.2}O_{2-\delta}$ (NiO-GDC20). Furthermore, the chemical composition and the specific surface areas of the nanoparticles are studied.

Chapter 5 deals with the fabrication of nanostructured thin film electrodes via spin coating, which is a cost-effective deposition technique and highly compatible with the current SOFC production technology. Additionally, the electrochemical performance of thin porous electrodes of LSC and Ni-GDC20 is studied using electrochemical impedance spectroscopy.

Chapter 6 describes the successful integration of the developed electrode processing technique in the micro-SOFC technology, which effectively can be used to replace currently used expensive and time consuming thin film deposition methods. Furthermore, anode-supported SOFCs with LSC cathodes and Ni-GDC20 anode supports are realized and the first set of electrochemical data is presented.

Chapter 7 gives some concluding remarks and outlook for a possible future work aiming to improve the electrochemical performance of the micro-SOFCs and the anode-supported SOFCs developed in this work.

2. Solid Oxide Fuel Cell Basics

Solid oxide fuel cells (SOFC) are electrochemical devices that convert the chemical energy within the fuel directly into the electrical energy. Figure 2-1 illustrates cross-sectional view of an SOFC consisting of three active layers: an air electrode (cathode), an electrolyte, and a fuel electrode (anode). SOFCs typically operate at temperatures above 600 °C. Higher operating temperatures (800–1000 °C) allow the use of hydrocarbons such as natural gas as fuels after being internally reformed to CO and H_2 gases [1]. If hydrocarbon fuels are to be utilized for low temperature cells, an external fuel reformer has to be used to convert the fuel gas into the mixture of H_2 and CO_2 [25], [55]. For the sake of simplicity, the principle of operation is discussed in terms of hydrogen as fuel and oxygen as oxidant.

The air flows through the porous cathode layer where the oxygen molecules are reduced to the oxygen ions by accepting electrons from the cathode following Equation 2.1.

$$1/2\,O_2(g) + 2e^-(\text{cathode}) \rightarrow O^{2\text{-}}(\text{electrolyte}) \qquad (2.1)$$
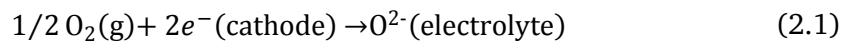
The oxygen ions are then transported through the gas-tight electrolyte layer, which is a predominantly oxygen-ion conductor, towards the anode. In the fuel-rich porous anode region, the oxygen ions react with the ambient fuel gas (H_2) following Equation 2.2 and release the electrons to the anode layer.
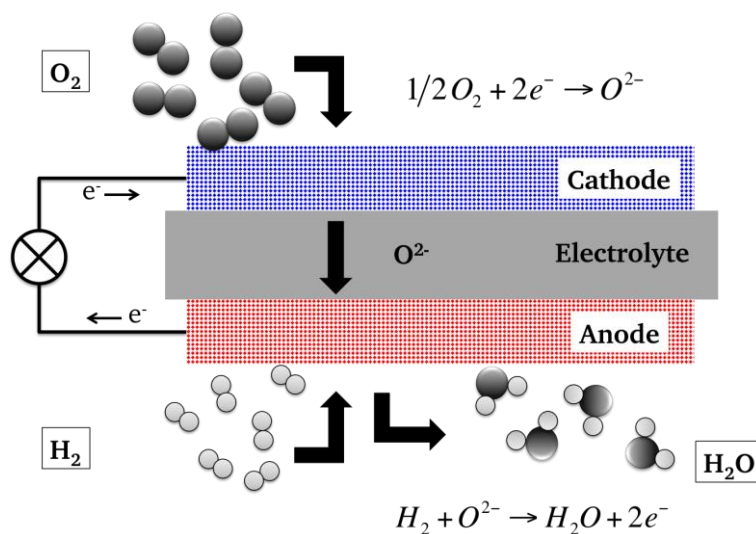
Figure 2-1: Cross-sectional schematic view of a solid oxide fuel cell.

$$H_2(g) + O^{2-}(\text{electrolyte}) \rightarrow H_2O(g) + 2e^- (\text{anode}) \qquad (2.2)$$
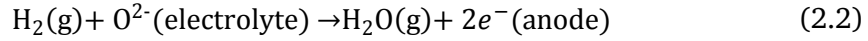
It can be easily seen that the sum of the Equations 2.1 and 2.2 corresponds to the oxidation reaction of hydrogen (Equation 2.3.).

$$H_2(g) + 1/2\, O_2(g) \rightarrow H_2O(g) \qquad (2.3)$$

The spatial separation of the redox reactions in Equations 2.1 and 2.2 forces electrons required for the electrochemical processes to flow through an external circuit, which in turn generates the electric current. The reversible voltage ($E°$) for an electrochemical reaction under standard-state conditions is given by

$$E° = - \frac{\Delta \hat{G}°}{n \cdot F} \qquad (2.4)$$

where $\Delta \hat{G}°$ is the standard molar free energy change for the fuel cell reaction, n is the number of moles of electrons transferred, and F is the Faraday's constant. Under open circuit conditions (*i.e.*, when no current is drawn from the cell), the voltage arising between the electrodes at an arbitrary temperature, T is predicted by the Nernst equation (Equation 2.5)

$$E_{Nernst} = E° - \frac{R \cdot T}{n \cdot F} \cdot \ln \frac{\prod a_{products}^{v_i}}{\prod a_{reactatns}^{v_i}} \qquad (2.5)$$

where E_{Nernst} is the Nernst voltage, R is the universal gas constant, T is the absolute temperature, $a_{products}$ and $a_{reactants}$ are the activities of product and reactant species, respectively; and v_i is the stoichiometric coefficient of species. When the Nernst equation is applied to the hydrogen-oxygen fuel cell reaction, it becomes:

$$E_{Nernst} = E° - \frac{R \cdot T}{2 \cdot F} \cdot \ln \frac{a_{H_2O}}{a_{H_2} \cdot a_{O_2}^{1/2}} \qquad (2.6)$$

The activity of the species a_i for an ideal gas is given as

$$a_i = \frac{P_i}{P°} \qquad (2.7)$$

where P_i and the $P°$ represent the partial pressure of the species (H_2O, H_2, and O_2) and the standard-state-pressure, respectively. Therefore, the activities of the reaction species can be changed by their unitless partial pressure values. This leads to the final form of Nernst equation for a hydrogen fuel cell:

$$E_{Nernst} = E° - \frac{R \cdot T}{2 \cdot F} \cdot \ln \frac{P_{H_2O}}{P_{H_2} \cdot P_{O_2}^{1/2}} \qquad (2.8)$$
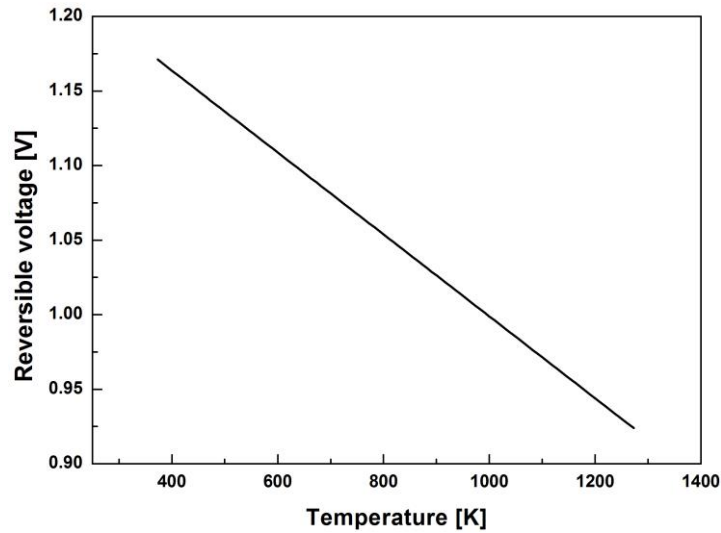
Figure 2-2: Reversible voltage versus temperature for electrochemical oxidation of hydrogen fuel gas.

where the partial pressures of the gaseous reactants and products are denoted as P_{H_2}, P_{O_2}, and P_{H_2O}.

At constant pressure, the reversible voltage (E_T) is also temperature dependent and can be calculated using the Equation 2.9.

$$E_T = E° + \frac{\Delta\hat{s}}{n \cdot \text{F}} \cdot (T - T_0) \qquad (2.9)$$

where the change in the entropy, $\Delta\hat{s}$ is assumed to be independent of temperature; $E°$ and T_0 are the standard-state reversible voltage and standard temperature, respectively. The linear dependence of the reversible voltage of an SOFC on the absolute temperature is shown in Figure 2-2. Even though the reversible voltage and eventually the Nernst voltage decrease with increasing operating temperature, the irreversible losses associated with the reaction and transport kinetics tend to increase with decreasing temperatures. As it will be covered in following section, the real fuel cell performance typically increases with increasing temperature.

2.1. Fuel Cell Kinetics

As it was presented in the previous section, the voltage difference appearing between the two SOFC electrodes under open circuit conditions is predicted by the Nernst equation (Equation 2.5). It is assumed that the activities of the species, namely partial pressures of reactants and products, are constant at the electrode zones. This assumption is valid only if the fuel and oxidant concentrations are sufficiently high at the electrode compartments. However, the Nernst equation does not apply at any given current density drawn from the fuel cell, because the electrochemical and transport processes are carried out irreversibly under the operation conditions. At a given current density, a portion of the open circuit voltage is sacrificed in order to overcome the impedances of such processes.

The difference between the actual cell voltage at a given current density and the reversible cell voltage for the fuel cell reaction is called polarization or overpotential, which itself is a function of current density. The polarizations observed in the fuel cells can be classified in terms of their origins as:
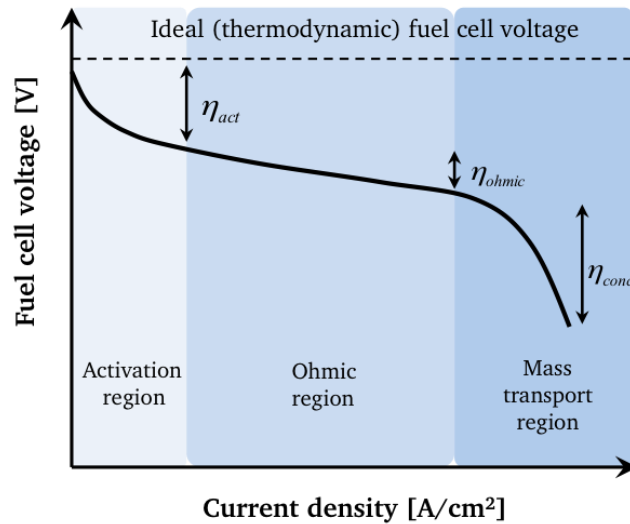
Figure 2-3: Schematic plot of voltage versus current density of an SOFC showing different type of polarizations (figure redrawn after [6]).

- Fuel crossover and internal currents;
- Activation polarization (η_{act});
- Ohmic polarization (η_{ohmic});
- Concentration polarization (η_{conc}).

 Figure 2-3 shows a typical current density–voltage (*j–V*) polarization curve of a fuel cell with voltage being a function of current density. The activation polarization usually dominates in the low current density region, whereas the voltage losses originating from the concentration polarization are dominant at high current densities when the overall rate of the reaction is determined by the slowest step of transport of the reactants to the electrode/electrolyte interfaces. Thus, the actual voltage output of an SOFC can be written as follows:

$$E = E_{Nernst} - \eta_{act} - \eta_{ohmic} - \eta_{conc} \qquad (2.10)$$

2.1.1. Fuel Crossover and Internal Currents

In principle, the electrolyte layer should only allow the transport of ions. However, a certain amount of fuel and electrons can cross over the electrolyte layer, which in turn causes a voltage loss of the cell. Usually, the effects of fuel crossover and electronic current across the electrolyte layer are negligible; therefore their influence on the voltage output of the cell is not included in the Equation 2.10.

2.1.2. Activation Polarization

The electrode reactions fundamentally require charge transfer processes, in which neutral reactants are transformed into ions and ions are converted into neutral species. Furthermore, the electrochemical reactions at the electrodes are multi-step processes, generally consisting of several parallel reaction pathways. Since the reaction mechanisms depend highly on the material properties and the microstructure of the electrodes, it is not straightforward to determine a single rate-determining reaction step. Plausible reaction steps for oxygen reduction and fuel oxidation

reactions are given for purely electronic conducting single-phase electrodes for the purposes of description [56].

Cathode:

The overall oxygen reduction reaction given in Equation 2.1 might occur by the following series of basic steps:

1) Surface adsorption of oxygen molecules on the cathode:

$$1/2\,O_2(g) \rightarrow 1/2\,O_{2_{ads}}(cathode) \tag{2.11}$$
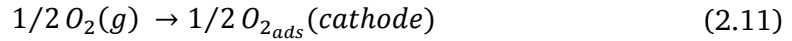
2) Dissociation of adsorbed oxygen molecules into adsorbed atoms:

$$1/2\,O_{2_{ads}}(cathode) \rightarrow O_{ads}(cathode) \tag{2.12}$$
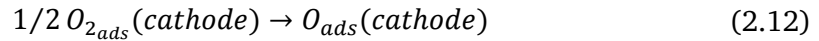
3) Surface diffusion of adsorbed oxygen atoms to the TPBs:

$$O_{ads}(cathode) \rightarrow O_{ads}(TPB) \tag{2.13}$$
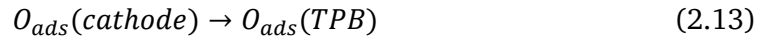
4) Formation of oxide ions by electron transfer and incorporation of these ions into the electrolyte:

$$O_{ads}(TPB) + 2e^-(cathode) + V_O^{\cdot\cdot}(electrolyte) \rightarrow O_O^x(electrolyte) \tag{2.14}$$
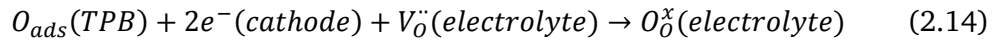
Anode:

The overall fuel oxidation reaction given in Equation 2.2 might occur by the following series of basic steps:

1) Surface adsorption hydrogen molecules on the anode:

$$H_2(fuel\ gass) \rightarrow H_{2_{ads}}(anode) \tag{2.15}$$
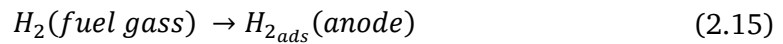
2) Dissociation of adsorbed hydrogen molecules into adsorbed atoms:

$$1/2\,H_{2_{ads}}(anode) \rightarrow H_{ads}(anode) \tag{2.16}$$
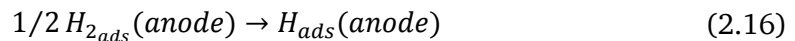
3) Surface diffusion of adsorbed hydrogen atoms to the TPBs:

$$H_{ads}(anode) \rightarrow H_{ads}(TPB) \tag{2.17}$$
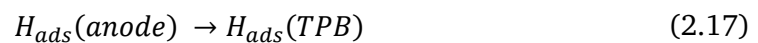
4) Formation of water vapor by anodic reaction:

$$O_O^x(electrolyte) + 2H_{ads}(TPB) \rightarrow H_2O(g) + 2e^-(anode) + V_O^{\cdot\cdot}(electrolyte) \tag{2.18}$$
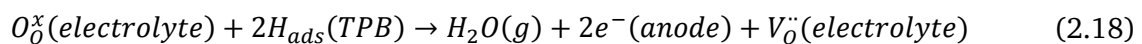
In both cathodic and anodic reactions, the overall reaction rate will be limited by the slowest step in the series, whereas the remaining reaction steps can be expected to be close to equilibrium. However, it is also possible that two or more steps exhibit similar kinetic barriers. In order the overall reaction to proceed, the activation energy barrier of the rate determining reaction step needs to be overcome. This energy barrier is generally associated with the activation polarization (η_{act}), which in turn affects the electrode reaction rate, or more precisely the current density drawn from the fuel cell, which is a function of several factors such as intrinsic catalytic properties of the electrode material, temperature, microstructure, and reactant concentrations. The relationship between the activation polarization (η_{act}) and current density (j) is given by the Butler-Volmer equation [56]:

$$j = j_0 \cdot \left[\exp\left(\alpha \cdot \frac{n \cdot \mathrm{F} \cdot \eta_{act}}{\mathrm{R} \cdot T} \right) - \exp\left(-(1 - \alpha) \cdot \frac{n \cdot \mathrm{F} \cdot \eta_{act}}{\mathrm{R} \cdot T} \right) \right] \qquad (2.19)$$

where j_0 is the exchange current density, n is the number of electrons transferred in the electrochemical reaction, and α is the charge transfer coefficient.

The charge transfer coefficient (α) is a dimensionless positive number, which is considered to be equal to 0.5 for fuel cells [57]. The exchange current density (j_0) is proportional to the anodic and cathodic electrode reaction rates at the equilibrium potential. Even though there is no net current under such conditions, the exchange current density concept is useful to represent the rates at equilibrium. From the fuel cell point of view, a high exchange current density means a high electrochemical rate and ultimately high fuel cell performance. As it can be seen in the Equation 2.19, the relationship between activation potential and current density is nonlinear and does not allow a straightforward determination of the activation polarization as a function of the current density. Nevertheless, the limiting cases of the Butler-Volmer equation lead to the expression of the activation polarization as a function of the current density.

In the case of low current density ($\left| \frac{\alpha \cdot n \cdot \mathrm{F} \cdot \eta_{act}}{\mathrm{R} \cdot T} \right| \ll 1$ and $\left| \frac{(1-\alpha) \cdot n \cdot \mathrm{F} \cdot \eta_{act}}{\mathrm{R} \cdot T} \right| \ll 1$), the Butler-Volmer equation can be simplified as

$$j = j_0 \cdot \frac{n \cdot \mathrm{F} \cdot \eta_{act}}{\mathrm{R} \cdot T} \qquad (2.20)$$

or

$$\eta_{act} = \frac{\mathrm{R} \cdot T}{n \cdot \mathrm{F} \cdot j_0} \cdot j \qquad (2.21)$$

The term $\frac{\mathrm{R} \cdot T}{n \cdot \mathrm{F} \cdot j_0}$ is defined as charge transfer resistance and has the units of area specific resistance, $\Omega \ \mathrm{cm}^2$. However, it should be noted that the linear relationship between the activation polarization and current density in low current density region is not Ohmic. Typically, the charge transfer process under these conditions can be described using a parallel resistor–capacitor circuit (RC circuit). Therefore, capacitive part of the charge transfer resistance cannot be obtained in DC measurements, since the response time of the processes are rather long. However, the values of resistance and capacitance can be estimated experimentally by frequency response measurements.

At large activation overpotentials (or more precisely in the high current density regime, where $\left| \frac{\alpha \cdot n \cdot \mathrm{F} \cdot \eta_{act}}{\mathrm{R} \cdot T} \right| \gg 1$), the second exponential component in the Equation 2.19 is much smaller than the first, therefore it may be neglected. This leads to

$$j = j_0 \cdot \exp\left(\frac{\alpha \cdot n \cdot \text{F} \cdot \eta_{act}}{\text{R} \cdot T}\right) \qquad (2.22)$$

or

$$\ln j = \ln j_0 + \frac{\alpha \cdot n \cdot \text{F} \cdot \eta_{act}}{\text{R} \cdot T} \qquad (2.23)$$

Solving this equation for η_{act} gives:

$$\eta_{act} = -\left(\frac{\text{R} \cdot T}{\alpha \cdot n \cdot \text{F}}\right) \cdot \ln j_0 + \left(\frac{\text{R} \cdot T}{\alpha \cdot n \cdot \text{F}}\right) \cdot \ln j \qquad (2.24)$$

which is the well-known Tafel equation and usually generalized in the form of

$$\eta_{act} = k + s \cdot \ln j \qquad (2.25)$$

where s is known as the Tafel slope. The plot of the logarithm of the current density against the overpotential is called the Tafel plot. The slope, s gives the value of transfer coefficient (α) and the intercept, k gives the exchange current density (j_0) [6], [56].

2.1.3. Ohmic Polarization

The total Ohmic resistance of a fuel cell is essentially a combination of resistances arising from different components of the device such as the electrical resistances ($R_{electronic}$) in the electrodes, current collector layers, and interconnects, and the ionic resistance in the electrolyte (R_{ionic}). Thus, the Ohmic loss of a fuel cell can be generalized as

$$\eta_{ohmic} = I \cdot R_{ohmic} = I \cdot (R_{electronic} + R_{ionic}) \qquad (2.26)$$

where I is the current. However, in most of SOFCs, the main contribution to the Ohmic loss can be attributed to the electrolyte, since its ionic resistivity is typically much greater than the electronic resistivity of the anode and cathode layers. Changing the current (I) in Equation 2.26 with current density (j) leads the Ohmic polarization of an SOFC to be defined as

$$\eta_{ohmic} = j \cdot ASR_{ohmic} \qquad (2.27)$$

where ASR_{ohmic} is the area-normalized resistance, also known as area-specific resistance (ASR) responsible for the Ohmic losses within the cell. The use of area specific resistance allows fuel cells of different sizes and geometries to be compared.

2.1.4. Concentration Losses

During fuel cell operation there will be a slight reduction in the concentrations of the oxygen and fuel gas in the cathode and anode regions, respectively. The degree of the concentration change of

the reactants depends highly on the current being taken from the fuel cell, as well as partial pressures of the reactants, microstructure of the electrodes, and reactant delivery efficiency of the fuel cell device. Especially at high current densities, the fuel and oxidant gasses are consumed at the electrode surfaces faster than they can be replenished. This phenomenon is observed as a voltage drop in the j–V curve of a fuel cell, which is called concentration loss, η_{conc} and estimated by:

$$\eta_{conc} = \frac{R \cdot T}{n \cdot F} \cdot \left(1 + \frac{1}{\alpha}\right) \cdot \ln\left(\frac{j_L}{j_L + j}\right) \tag{2.28}$$

where j_L is the limiting current density, which causes the reactant concentrations to fall to zero. A fuel cell cannot maintain above the limiting current density, which is given by the following equation:

$$j_L = n \cdot F \cdot D^{eff} \cdot \frac{C_R^*}{\tau} \tag{2.29}$$

where D^{eff} is effective reactant diffusivity within the electrode layer, τ is the electrode (diffusion layer) thickness, and C_R^* is the bulk (flow channel) reactant concentration. Therefore, the strategies to prevent the concentration losses focus on increasing the limiting current densities of the electrode layers [56].

2.2. Cell Components

The main components of a single SOFC (electrolyte, anode, and cathode) are illustrated in Figure 2-1. When single cells are stacked together to design SOFC systems with higher power output, two more cell components, interconnect and sealant, are required.

2.2.1. Electrolyte

The electrolyte is a crucial component of an SOFC, through which ions diffuse from one electrode to another, thus leading to a potential difference between anode and cathode. Some notable examples of electrolyte materials are ZrO_2-, CeO_2-, Bi_2O_3-based oxides with fluorite structure and $LaGaO_3$-based perovskites. The oxygen ion transport is typically mediated by oxygen vacancies, and takes place by the thermally activated hopping of an oxygen ion from one site to the nearest oxygen vacancy site. This results in an ion flux and an oxygen vacancy flux with opposite directions [58].

The following properties are required for an efficient electrolyte [33]:

- Ionic conductivity has to be sufficiently high at operating temperatures ($\sim$0.1 S/cm);
- High electronic resistivity (*i.e.*, negligible electronic conductivity);
- Thermodynamic and chemical stability under the fuel cell operating conditions;
- Chemical inertness towards electrode materials during fabrication and operation;
- Compatibility of thermal expansion behavior with adjoining cell components;
- Resistivity to thermal cycling and thermal shock;
- Sufficient mechanical strength in the form of thin and strong films without any gas leaks;
- Low costs for materials and processing.

Electrolytes with fluorite structure

YSZ is certainly the most widely used electrolyte material for SOFCs, which is produced by doping ZrO_2 with Y_2O_3. Undoped ZrO_2 has fluorite crystal structure that exhibits polymorphism with monoclinic, tetragonal, and cubic phases. The monoclinic phase of undoped ZrO_2 is thermodynamically stable at temperatures below 1170 °C, and undergoes a phase transformation from monoclinic over tetragonal (at 1170 °C) to cubic (at 2370 °C) as shown below. The fluorite crystal structure of cubic ZrO_2 shown in Figure 2-4, in which zirconia ions form an *fcc* lattice, while the oxygen ions are placed in a simple cubic arrangement in the tetrahedral holes.

$$\text{Monoclinic} \xleftrightarrow{1170\,°C} \text{Tetragonal} \xleftrightarrow{2370\,°C} \text{Cubic} \xleftrightarrow{2715\,°C} \text{Melt}$$

The large volume change accompanying the phase transition from the tetragonal to the monoclinic hinders the production of stable dense ZrO_2 products, since the typical sintering temperatures are above monoclinic-tetragonal phase transition temperature. The doping of ZrO_2 with cubic oxides such as MgO, CaO, Y_2O_3 and Sc_2O_3 stabilizes the tetragonal and cubic polymorphs over a wide temperature range, resulting in the realization of partially or fully stabilized ZrO_2 ceramic parts. Furthermore, the aliovalent doping of ZrO_2 leads to oxygen vacancy defects. As the doping content increases, the number of vacant oxygen sites increases leading to a significant oxygen ion conductivity of the material. However, there is an upper limit for the level of doping, beyond which the ionic conductivity starts to decrease. With increasing dopant concentration the distances between the dopants and oxygen vacancies become smaller, which leads to stronger electrostatic interactions between the dopants and oxygen vacancies. Such interactions form associations within the crystal structure, which impede the mobility of oxygen ions and vacancies. This phenomenon does not only happen in ZrO_2-based materials, but also in other oxides such as CeO_2 and Bi_2O_3 [33]. Considering the oxygen vacancy concentration for improved ionic conductivity and the simultaneous formation of associations hindering the ionic conductivity, the optimum dopant concentration of Y_2O_3 is 6–8 mol.% [6].

Doped-CeO_2 is another common oxygen-ion-conducting ceramic material, which has been considered as an alternative to realize low temperature SOFCs due to its high ionic conductivity compared to the conventional YSZ-based electrolytes. CeO_2 possesses the same fluorite crystal structure as ZrO_2 and exhibits low ionic conductivity due to the insufficient amount of oxygen vacancies. The mobile oxygen vacancies are introduced by the substitution of Ce^{4+} ions by trivalent cations such as Sm^{3+}, Y^{3+}, and Gd^{3+}. The ionic conductivity of the doped-CeO_2 highly depends on
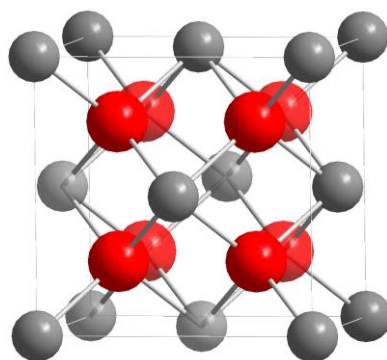
Figure 2-4: Schematic representation of the cubic fluorite crystal structure exhibited by zirconia. The oxygen anions (red) occupy the tetrahedral holes in the fcc lattice of zirconuim cations (gray).

the type of dopant and its concentration. The highest values of ionic conductivities for CeO_2 electrolytes are obtained by doping with Sm^{3+} and Gd^{3+}, and the dopant concentrations are typically in the range of 10–20 mol.% [6]. Despite the high ionic conductivity, the ceria-based materials have several drawbacks in terms of SOFC electrolyte application. At temperatures higher than 600 °C and lower oxygen partial pressures (*i.e.*, on the anode side of the SOFC), the Ce^{4+} ions are partially reduced to Ce^{3+}. This leads to electronic conductivity of the electrolyte layer extending from the anode side towards the cathode and eventually voltage losses. The lattice expansion of CeO_2 under reducing atmospheres is another disadvantage causing the thermomechanical instability of the cell. Nevertheless, the advantages of CeO_2-based electrolytes over YSZ can be exploited at lower operating temperatures, at which higher ionic conductivities of CeO_2-based electrolytes are prominent, and their drawback associated with the electronic conductivity is suppressed. In case high temperature operation is required, a thin YSZ coating on the anode side can prevent the electronic conduction across the electrolyte.

The high temperature cubic polymorph of Bi_2O_3 also exhibits fluorite structure and its intrinsically high oxygen ion conductivity stems from the high oxygen vacancy concentration, which is about 25% of the oxygen sublattice sites [59]. In fact, cubic-Bi_2O_3-based electrolytes exhibit highest ionic conductivity values among all the oxygen ion conductors. To stabilize the high temperature cubic-Bi_2O_3 at lower temperatures, some of the Bi cations are substituted with rare-earth dopants (Y^{3+}, Dy^{3+}, or Er^{3+}), and/or with cations having higher valances such as W^{5+} or Nb^{4+}. Even though cubic-Bi_2O_3-based electrolytes show considerably high ionic conductivities, they are metastable when cooling below 600 °C and undergo a phase transition from cubic to a poor ionic conducting monoclinic phase [59]. Furthermore, high electronic conductivity, volatilization of Bi_2O_3 at moderate temperatures, high corrosion activity, and low thermomechanical strength are the other disadvantages of Bi_2O_3-based electrolytes [6].

Electrolytes with perovskite structure

Perovskite oxides are promising materials for both oxygen ion and proton conducting SOFC electrolytes [6], [60]. An ideal perovskite oxide has the general stoichiometry of ABO_3 (or more generally ABX_3) and consists of a three-dimensional network of corner-sharing BO_6 octahedra. As illustrated in Figure 2-5, the B cations are located in the center of an octahedron formed by oxygen ions and each octahedron shares each of its corner oxygen ions with a neighboring BO_6 octahedron. The A-cations are surrounded by 12 oxygen ions in the cavity formed by eight corner-sharing octahedra.

Goldschmidt who conducted much of the early work about perovskites also established the principle of tolerance factor for the structure, t_G [61]:

$$t_G = \frac{r_A + r_X}{\sqrt{2}(r_B + r_X)}$$

(2.30)

where r_A, r_B, and r_X are the radii of the A-site, B-site, and X-site ions, respectively. The value of t_G lies between approximately 0.80 and 1.10. The ideal cubic perovskite arrangement (space group $Pm\bar{3}m$) is typically obtained for the compounds with t_G values between 0.89 and 1. As the value of t_G decreases, the structure of the unit cell is shifted from cubic to triclinic as a result of the increased distortions [62].
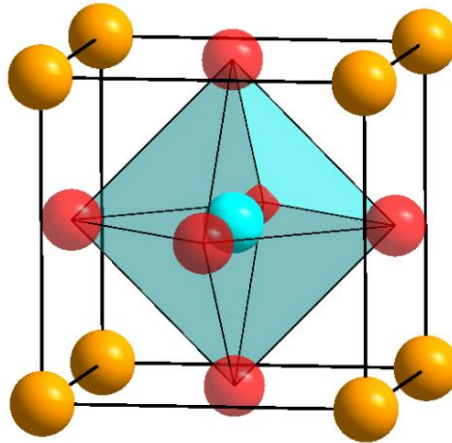
Figure 2-5: Schematic representation of the lattice structure of perovskite, ABO$_3$. The cations of A (yellow) are located at the corners, cation of B (blue) is located in the center, and oxygen anions (red) are at the face centers.

The group of LaGaO$_3$-based materials is one of the most studied perovskites for oxygen-ion conducting SOFC electrolytes [23], [63], [64]. High ionic conductivity of LaGaO$_3$ is obtained by increasing the oxygen ion vacancy concentration and also by keeping the lattice distortion at minimum, which is achieved by substituting A-site La^{3+} ions with alkaline earth elements (Sr^{2+}, Ba^{2+}, and Ca^{2+}) and B-site Ga^{3+} with divalent metal cations such as Mg^{2+}. The resulting complex perovskite, La$_{1-x}$Sr$_x$Ga$_{1-y}$Mg$_y$O$_{3-\delta}$ is known as the LSGM-type electrolyte material. The conductivity of LSGM is purely ionic and typically higher than those of YSZ and Gd-doped CeO$_2$ (GDC), and somewhat lower than that of Bi$_2$O$_3$-based electrolytes over a wide temperature range. However, at lower temperatures (T<700 °C), CeO$_2$-based electrolytes have higher ionic conductivities. The thermal expansion behavior of LSGM matches well with YSZ. Therefore, LSGM electrolytes are potentially strong candidates for intermediate temperature range (700–1000 °C) SOFCs, but they also have some disadvantages such as [6]:

- Volatilization of gallium oxide;
- Formation of undesirable secondary phases during processing;
- High cost of gallium;
- Reactivity with common electrode materials.

Among proton conducting perovskites, Y-doped BaCeO$_3$ and BaZrO$_3$ are promising candidates for SOFC electrolyte applications because of the high ionic conductivity for protons at low temperatures [28], [31], [32]. However, the chemical instability of such proton conducting ceramics in CO$_2$ atmospheres limits practical applications [6].

2.2.2. Anode

The purpose of an anode in an SOFC is to offer active reaction sites for the fuel gas to react with the oxygen ions delivered by the electrolyte layer. Considering the operational environment of the anode (high temperature and reducing atmospheres) along with functional requirements, material selection is a key factor in terms of SOFC performance. In particular, the following properties are required for the anode materials [33]:

- High catalytic activity to minimize activation polarizations associated with the electrochemical processes;
- High electronic conductivity;

- Microstructural features facilitating a high number of reaction sites for the electrochemical processes;
- Thermodynamic and chemical stability under the fuel cell operating conditions;
- Chemical inertness towards electrolyte and interconnect materials during fabrication and operation;
- Compatibility of thermal expansion behavior with adjoining cell components;
- Resistivity to thermal cycling and thermal shock;
- Sufficient mechanical strength in the form of thin films with porous microstructure;
- Low material and processing costs.

Formerly, metallic single-phase anodes such as Pt, Fe, Cu, Co, and Ni had been used as anodes. Especially, Pt and Ni had been the primary choice of anode materials because of their high catalytic activity. Even though single-phase metallic anodes meet certain requirements listed above, they suffer mostly from thermomechanical and chemical instabilities under SOFC operating conditions. Typically, metallic anodes are unable to maintain their porous microstructure as well high number of active reaction sites at elevated temperatures due to the coalescence and subsequent grain growth. Furthermore, the complications associated with their thermal expansion coefficient mismatch with that of YSZ have ruled out the use of single-phase metallic anodes in SOFCs. To overcome the disadvantages of metallic anodes, the ceramic-metal composite (cermet) anodes have been introduced as an alternative to single-phase metallic anodes. In cermet anodes, the primary roles of the metallic phase are the catalytic oxidation of fuel gas and the conduction of resulting electrons from the reaction sites to the interconnects. An ion conducting ceramic phase is added to support the metallic phase structurally. In particular, the ceramic phase inhibits the coarsening of the metallic particles and provides a well-matching thermal expansion coefficient to that of electrolyte material. The ion conducting ceramic phase also plays an important role in the fuel oxidation by providing additional pathways for oxygen ion transport. Another important phase is the fuel gas, which has to diffuse to the electrochemical reaction zones, namely triple phase boundaries (TPBs). The performances of cermet anodes, therefore, do not only depend on the material properties of its individual components but also on their combined microstructural features. Despite the recent advances in pure ceramic oxide anodes, cermets are still state-of-the-art anodes in SOFCs because of their sufficient electrochemical performance [43].

Ceramic-metal composite (cermet) anodes

Ni-YSZ cermets are the most commonly used anodes in SOFCs, since they meet most of the previously listed requirements. They are typically fabricated by sintering NiO and YSZ powders after a thorough blending process to ensure a well-percolated composite. The resulting NiO-YSZ structure is reduced to Ni-YSZ functional anodes upon exposure to a fuel gas. The volume change associated with the reduction of NiO to Ni leads to the formation of porous anode microstructure. If necessary, the porosity of the anodes can also be modified by the use of an organic pore former, which is burnt off during the initial sintering stage of NiO-YSZ.

In Ni-YSZ anodes, the Ni phase is responsible for the electronic conductivity and catalytic activity, while the YSZ phase acts as a structural framework inhibiting coarsening of Ni grains at elevated temperatures and adjusting the thermal expansion coefficient of the anode layer ($TEC_{\text{Ni-YSZ}}=12.5\cdot10^{-6}$ 1/K [65]) to that of adjoining YSZ electrolyte ($TEC_{\text{YSZ}}=10.5\cdot10^{-6}$ 1/K [65]). Furthermore, the YSZ phase offers conduction path for the oxygen ions within the anode layer, which effectively extends the active reaction sites for the anode reactions.

The electrical conductivity of cermets is strongly influenced by the content of the metallic phase. The minimum Ni loading for an active Ni-YSZ cermet anode fabricated by a conventional tape casting method has been reported to be around 30 vol.%, which was determined by

measuring the electrode conductivity of the cermet as a function of the Ni loading (above 30 vol.% Ni, the electronic conductivity of the anode exceeds 10^3 S/cm at 1000 ℃ [66]). However, the optimum metal phase loading to minimize activation polarization under typical fuel cell operation depends on several factors such as fabrication method, microstructure, and morphology, and typically lies in the range of 40–50 vol. % [48], [67], [68].

Even though Ni-based cermet anodes, especially Ni-YSZ, meet most of the criteria for being an adequate anode material choice, there are several drawbacks [33]: coke formation under the operation with hydrocarbon fuels, degradation after prolonged operation, and large volume changes upon redox cycling. Nickel is an excellent catalyst for carbon-carbon bond formation [6] and the use of hydrocarbon fuels leads to the deposition of carbon species on the Ni particles. The blocking of active reaction sites with carbon deposits eventually leads to the deterioration of the fuel cell performance. Furthermore, the number of active reaction sites for fuel oxidation is reduced after prolonged operation due to the coarsening of Ni grains and agglomeration. Such cermet anodes also experiences large volume changes upon redox cycling, which leads to the mechanical instability of the anode layer.

Fuel oxidation in cermet anodes

The Figure 2-6 shows the overall electrochemical oxidation mechanism of hydrogen fuel along with the transport and diffusion pathways of the species in a cermet anode. The electrochemical oxidation of hydrogen given in Equation 2.2 is assumed to take place at or near TPB of anode, electrolyte, and gas (fuel) phases. This assumption is based on the localization of respective electronic, ionic, and molecular transport characteristics of the distinct anode components. The metallic phase is a purely electronic conductor and the electrolyte conducts predominantly oxygen ions. Moreover, the fuel gas transport is only associated with the gas diffusion within the porous anode structure. The assumption is confirmed by the experimental work done on geometrically model anode structures with well-defined, two-phase and three-phase boundaries [69]–[71]. While the overall fuel oxidation process is agreed upon, there is a discrepancy in the literature concerning the elementary reaction steps which are rate determining. Nevertheless, the kinetics of each elementary step strongly depends on the material properties, microstructure, processing, and the experimental conditions under which the anode is tested.

Since the electrochemically active reactions sites for fuel oxidation are localized near TPBs, one of the most common strategies to minimize the activation polarization associated with anode layers has been to increase the density of TPBs within the anode layer. The fabrication of porous and highly percolated cermet anodes with high specific surface areas leads to the realization of
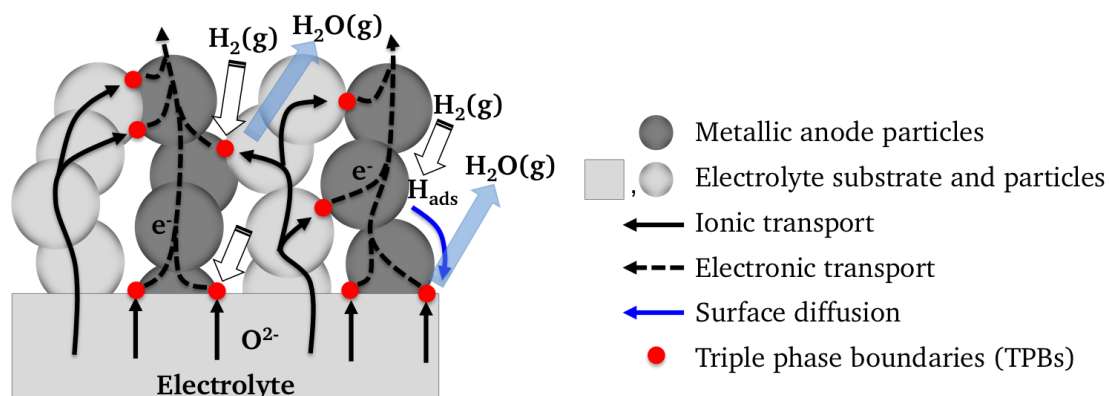

Figure 2-6: Structure of a cermet anode and overall fuel oxidation mechanism for a H_2-O_2 SOFC.

high performance anodes. Furthermore, the metallic and ceramic components of the cermet anodes can be replaced individually with alternative materials having enhanced catalytic activity and ionic conductivity.

Alternative anode materials

There has been a growing interest in alternative single-phase oxide materials to overcome the disadvantages associated with cermet anodes. However, the research is still at a stage of finding suitable candidates to substitute standard cermet anodes. The materials of interest are doped CeO_2 and perovskite-type transition metal oxides with mixed ionic-electronic conductivity in reducing atmospheres [72].

The rare earth doped CeO_2 compounds exhibit ionic conductivity due to the high number of oxygen vacancies. In reducing atmospheres, the electronic conductivity is induced by the partial reduction of Ce^{4+} ions to Ce^{3+}. $Ce_{0.6}Gd_{0.4}O_{3-\delta}$ has been investigated as a single-phase anode material and a good performance has been obtained with hydrogen fuel. Despite of the absence of carbon precipitation, the catalytic activity towards methane oxidation has been found to be insufficient [73].

Perovskites have also been extensively investigated as potential SOFC anode materials, among which lanthanum chromites, strontium titanates, and strontium molybdates are most promising candidates [50]–[53], [74].

2.2.3. Cathode

The cathode is the part of SOFC where the oxygen reduction reaction takes place and the material requirements are analogous to the ones of anode. Along with the compatibility, chemical stability, thermomechanical strength, and cost, the catalytic activity towards oxygen reduction and electronic conductivity are the most crucial requirements [33]. In the earliest phases of SOFC development, Pt has been considered as a cathode material because of its sufficient catalytic activity towards oxygen reduction. Although, Pt is expensive and thermomechanically unstable under oxidizing atmospheres at elevated temperatures, it is one of the most employed cathode components in polymer electrolyte membrane fuel cells (PEMFC) and in micro-SOFCs [10], [75]. Yet, the SOFC technology requires low cost materials to be commercialized and less expensive perovskite oxides have drawn considerable attention as cathode materials for SOFC applications. Typical perovskite cathode materials include $La_{1-x}Sr_xMnO_{3-\delta}$ (LSM), $La_{1-x}Sr_xCo_{1-y}Fe_yO_{3-\delta}$ (LSCF), and $La_{1-x}Sr_xCoO_{3-\delta}$ (LSC), which show good oxidation resistance and high catalytic activity under SOFC operating conditions.

Perovskite cathodes

The flexibility to accommodate variety of elements and the tolerance against extensive modifications make perovskite ceramics important for industrial applications, as their electrical, magnetic, and catalytic properties can be tailored by selective doping. This has resulted in the production of numerous perovskites, some of which have been considered as potential SOFC cathode materials. According to Adler [36], the perovskite cathodes can be classified into two categories: electronic conducting and mixed ionic-electronic conducting cathodes.

Among the electronic conducting cathodes, the perovskite $La_{1-x}Sr_xMnO_{3-\delta}$ ($0.1 \leq x \leq 0.25$) has been one of the most comprehensively studied cathode material systems. In the perovskite lattice, the A-sites are occupied by La- and Sr-cations, while B-sites are filled by Mn-cations. The substitution of Sr^{2+} for La^{3+} results in a charge imbalance in the lattice, which is compensated

either by the formation of oxygen vacancies or by the change of the oxidation state of Mn ions from 3+ to 4+. The corresponding compensation mechanism is governed by partial pressure of O_2 and temperature. At low O_2 partial pressures ($\sim 10^{-9}$ mbar) the formation of oxygen vacancies is dominant, whereas under SOFC operating conditions the charge neutrality is balanced by the formation of electronic defects in the perovskite lattice [76]. At high temperatures, the performance of LSM as a cathode material is satisfactory due to its high electronic conductivity ($\sigma_{el} \approx 10^2$ S/cm at 800 °C in air [35]). LSM-based cathodes have distinguishable advantages over high performance mixed ionic-electronic conducting cathodes. First of all, with the appropriate amount of Sr^{2+} doping, the thermal expansion coefficients of LSM and YSZ can be well matched. This results in the reduction of thermal stresses between electrode and electrolyte layers generated by thermal cycling of the cell. Another advantage of LSM is that it is thermodynamically more stable compared to the Co- and Fe-based perovskite cathodes [33]. Nevertheless, the chemical compatibility of LSM and YSZ is poor at interfaces, as electronically insulating secondary phases are formed under operating conditions of SOFC [77]. Moreover, moderate oxygen ion conductivity of LSM ($\sigma_{ion} \approx 10^{-8}$ S/cm at 800°C in air [78]) limits the overall cathode performance at low operating temperatures. Therefore, the research focus has been shifted towards alternative cathode materials with mixed ionic-electronic conductivities.

Mixed ionic-electronic conducting perovskite oxides such as $La_{1-x}Sr_xCoO_{3-\delta}$ (LSC), $La_{1-x}Sr_xCo_{1-y}Fe_yO_{3-\delta}$ (LSCF), and $Ba_{1-x}Sr_xCo_{1-y}Fe_yO_{3-\delta}$ (BSCF) have been popularly used as SOFC cathode materials. Particularly, LSC exhibits an extraordinarily high electronic conductivity and large oxygen vacancy concentration resulting in a significant ionic conductivity and catalytic activity towards oxygen reduction [36], [39], [79], [80]. The oxidation states of La- and Sr-ions are fixed to 3+ and 2+, respectively, while Co-ions have valance states between 3+ and 4+. Upon Sr^{2+} substitution for La^{3+} ions, the charge neutrality in the lattice can be maintained either by the formation of oxygen vacancies or by the change of the oxidation state of Co ions. Both ionic and electronic compensation processes for the charge neutrality take place simultaneously and compete with each other depending on the level of doping, partial pressure of O_2, and temperature [81]. The relationship between mean oxidation state of Co (η), oxygen nonstoichiometry (δ), and content of Sr-dopant (x) for $La_{1-x}Sr_xCoO_{3-\delta}$ is given by [82]:

$$\eta = 3 + x - 2\delta \qquad (2.31)$$

where δ is the oxygen deficiency of the material. Using the experimental data, Mizusaki et al. [82] have observed the following tendency of the defect chemistry for LSC over a wide temperature range. For $x \leq 0.2$, the charge neutrality is compensated by increase of the mean Co oxidation state, η. For $0.2 < x < 0.5$, the increase of Sr dopant content mainly contributes to an increase in oxygen nonstoichiometry, δ. For $x > 0.5$, an increase of Sr doping level leads to a further increase of the mean Co oxidation state, η. For $La_{1-x}Sr_xCoO_{3-\delta}$, highest electronic conductivity values ($\sigma_{el} \approx$ 2000–2300 S/cm at T=600 °C in air [83]–[85]) have been reported for x=0.4. For the same Sr content, an approximate oxygen ion conductivity of 10^{-2} S/cm at 600 °C in air has been reported [81]. Therefore, LSC is of particular interest to reduce SOFC operation temperatures below 650 °C. However, the major drawbacks of LSC-based cathodes are the thermal expansion coefficient mismatch between LSC and YSZ, poor chemical compatibility between LSC and YSZ, and its chemical instability under SOFC operating conditions. The volume change of LSC perovskite lattice upon heating is not only a result of thermal expansion but also of chemical expansion, which is associated with the formation of oxygen vacancies [86]–[88]. The thermal expansion coefficient for LSC has been reported in the range of $18 \cdot 10^{-6}$–$26 \cdot 10^{-6}$ 1/K [81], [84], [88], [89], which does

not match with the thermal expansion coefficients of YSZ (TEC_{YSZ}=10.5·10^{-6} 1/K [65]) and GDC (TEC_{GDC}=12·10^{-6} 1/K [90]). This distinct mismatch leads to thermomechanical stresses upon thermal cycling of the cell and eventually to the mechanical failure of the cell components. Similar to LSM, the formation of the secondary phases ($SrZrO_3$ and La_2ZrO_7) have been reported for LSC-YSZ interfaces by many groups [91]–[93], which has two important effects on overall SOFC performance. First, the insulating zirconates forming at cathode/electrolyte interface hinder charge transfer processes and ultimately cause increased polarization losses. Secondly, they lead to the deviations from the desired cathode stoichiometry and thus to differences in material properties such as electronic and ionic conductivity, catalytic properties, and phase stability. In terms of chemical stability, LSC-based cathodes suffer from the degradation phenomena involving segregation of cation species (especially Sr) at cathode surfaces [94]–[97]. Despite the major drawbacks, LSC-based mixed ionic–electronic conducting perovskites continue to be the state of-the-art materials for the SOFC cathode applications due to their superior electrochemical performance.

Oxygen reduction

Figure 2-7 illustrates three different types of porous cathode structures, in which the transport pathways for the various species are shown. For the conventional porous electronic conducting cathode materials (Figure 2-7a) such as Pt or LSM, O_2 reduction reaction (ORR) and subsequent incorporation of O^{2-} ions into the electrolyte are typically considered to be localized at the TPB zones at which O_2, cathode, and electrolyte phases are physically in contact. Oxygen molecules are generally considered to adsorb on cathode surfaces, where they undergo electrocatalytic reduction step(s) yielding partially reduced species. These electrochemically active species must transport along surfaces, interfaces, or through the bulk of the cathode material towards the electrolyte to be fully incorporated [36]. In case of mixed ionic-electronic conducting cathode materials such as LSC and LSCF (Figure 2-7b), the bulk pathway becomes available for ORRs in addition to the surface path. Therefore, the O_2 reduction is not only restricted to the TPB zones but also can take place
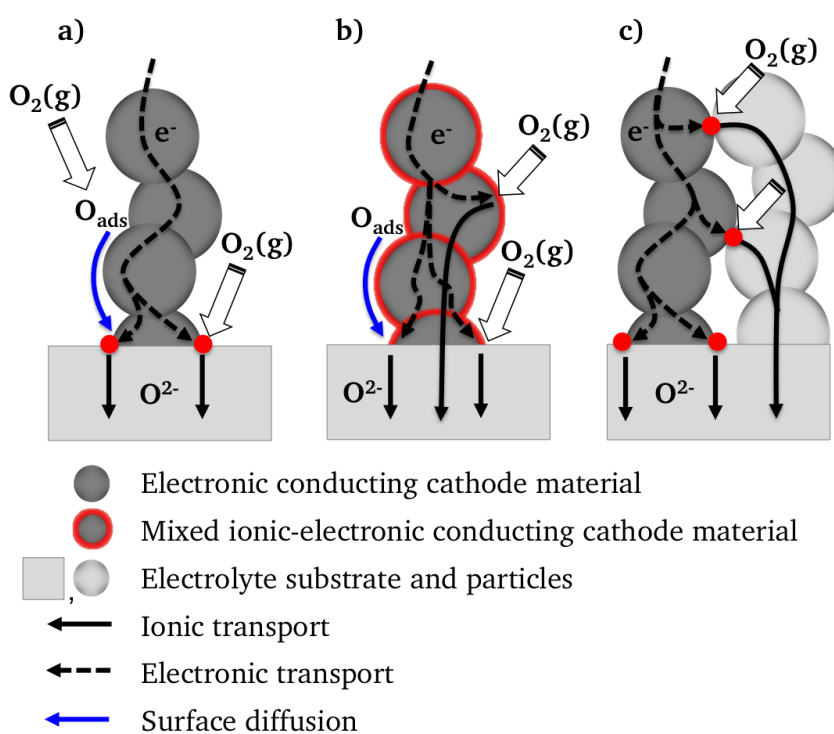
Figure 2-7: Oxygen reduction at a) a pure electronic, b) mixed conducting, and c) composite cathodes.

over a significant portion of the cathode surface. The mixed ionic-electronic conduction can also be obtained by percolating an electronic conductor (*e.g.,* LSM) and an ionic conductor (*e.g.*, YSZ, GDC) to yield a composite microstructure as illustrated in Figure 2-7c. Contrary to intrinsically mixed ionic-electronic conductors, the mixed conduction properties are realized at the microscopic, not at the atomistic level [56].

Despite the simplicity of the overall ORR, the process consists of a number of complex steps on atomic and molecular scales such as adsorption, dissociation, surface and bulk diffusion, charge transfer, and incorporation of oxygen into bulk. For mixed ionic-electronic conducting cathodes, potential elementary reaction steps of ORR are listed in Table 2-1 [98], where the parallel surface pathway for the ORR is neglected.

Table 2-1: Elementary steps of ORR in mixed ionic-electronic conducting cathodes.

#	Reaction Step
1	Diffusion of O_2 molecules to the cathode
2	Adsorption of O_2 on the cathode surface
3	Dissociation of O_2 molecules into atomic oxygen species
4	Charge transfer from the cathode to oxygen species before/after dissociation
5	Incorporation of O^{2-} ions into crystal defect sites in the bulk of cathode
6	Bulk diffusion of O^{2-} ions through the cathode towards the cathode/electrolyte interface
7	Incorporation of O^{2-} ions into crystal defect sites in the bulk of electrolyte

In such multistep electrochemical reactions, the slowest step is considered to be the rate-determining step (RDS) and the rest of the parallel processes are assumed to be in equilibrium. It is also noteworthy to mention that an electrochemical process does not necessarily consist of a single RDS but two or more reaction steps exhibiting similar kinetics. Furthermore, the kinetics of each step strongly depends on the cathode material, microstructure, processing of the electrode, and the experimental conditions under which the cathode is tested.

2.3. Cell Designs

Under typical operating conditions, a single SOFC delivers a voltage output less than 1 V. Therefore, several cells are combined together using interconnects to obtain high power outputs. The cells can be simply connected in series to gain higher voltage or in parallel to yield higher current. This assembly is known as *fuel cell stack,* or just a *stack*. Most of the SOFC stack development has focused on the tubular and planar designs, which are illustrated in Figure 2-8.

Figure 2-8: Schematic diagrams of a) tubular and b) planar SOFC designs.

The tubular SOFCs (Figure 2-8a) are typically fabricated by depositing thin film components on a cylindrical porous tube acting as structural support and electrode (either anode or cathode), which is produced by extrusion followed by high temperature sintering. Subsequently, the electrolyte, anode/cathode, a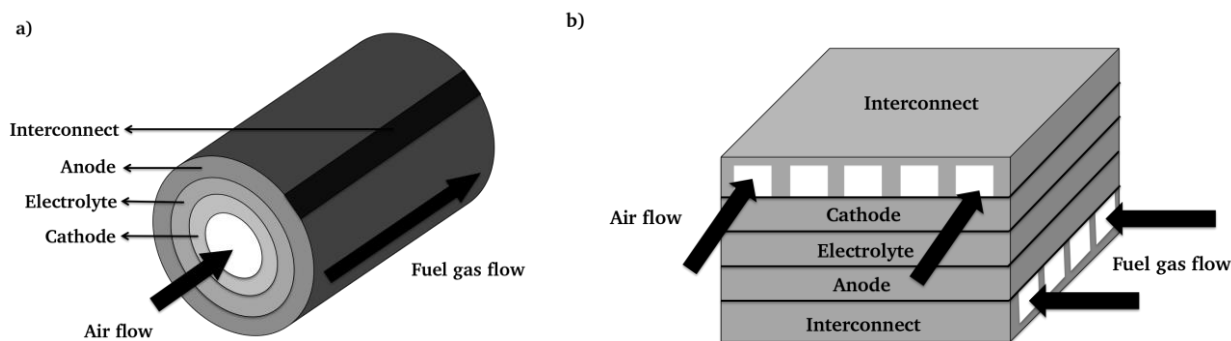nd interconnect components are deposited onto the porous support tube. The main advantage of the tubular design is that there is no need for sealing. Westinghouse Electric Corporation (USA) pioneered the tubular design and their 100 kW system was successfully operated for over two years on desulfurized natural gas without any significant performance degradation [2]. However, low power densities, the long start-up times, and expensive fabrication processes are the major drawbacks [99].

Despite the progress in the tubular design, low manufacturing costs and high areal/volumetric power densities make the planar SOFC design more favorable, which consists of thin and flat cell components as illustrated in Figure 2-8b. The cells are usually fabricated by cost-effective conventional ceramic processing techniques such as tape casting and screen printing, which are stacked using interconnection components with gas flow channels. The interconnection components are also responsible for gas separation and current collection. These requirements and the additional constraints such as cost and simplicity of manufacturing have narrowed the choice of materials for interconnects. High temperature SOFCs employ perovskite-type lanthanum- and yttrium-based chromites as interconnect materials. However, the material and processing costs are problematic. Eventually, the reduction of operating temperatures facilitates the use of metallic materials for interconnects, which are less expensive and easy to fabricate [6], [99].

The planar SOFCs can be classified into two broad categories based on the support type: self-supporting and externally supported cells. In the self-supporting configuration, often the thickest component acts as a structural support. Thus, SOFCs can be designed in electrolyte-, cathode-, and anode-supported configurations. On the other hand, the mechanical stability of the externally supported SOFCs is provided by porous and electrochemically inactive metal substrates. The various cell configurations of planar SOFCs are illustrated in Figure 2-9.
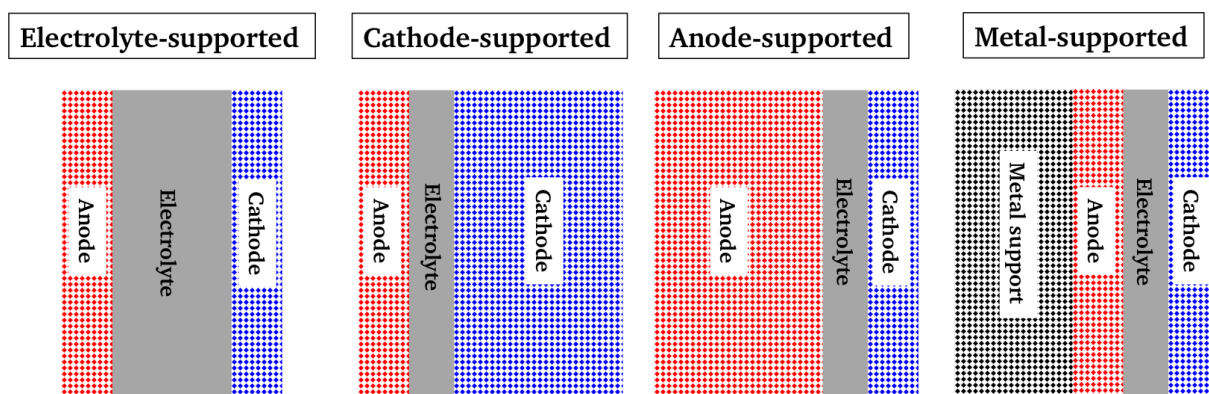
Figure 2-9: Electrolyte-electrode assembly approaches for SOFCs: Electrolyte-supported (the electrolyte forms the structural support for the cell), cathode-supported (the cathode forms the structural support for the cell), anode-supported (the anode forms the structural support for the cell), and metal-supported (electrochemically inactive metal substrate forms the structural support for the cell) SOFCs.

Electrolyte-supported SOFCs

In the electrolyte-supported design, the electrolyte is the thickest part of the SOFC and acts as a structural support for the whole cell structure. The electrolyte materials are typically processes by conventional ceramic processing techniques and sintered at high temperatures to obtain dense, gas tight, and thermomechanically robust electrolyte supports with thicknesses in the range of 200–500 μm [34]. The thin porous electrode layers with thicknesses of 100–200 μm are deposited on

both sides of the electrolyte by various deposition methods [99] and subsequently heat treated to attain adhesion between the components [6]. Despite the good thermomechanical properties, electrolyte-supported cells suffer from high Ohmic polarization due to large electrolyte thicknesses. Therefore, high operating temperatures (800–1000 °C) are required.

Cathode-supported SOFCs

In the cathode-supported fuel cell assembly, the cathode is the thickest (1–2 mm) component of the cell. The increased thickness of the cathode layer gives the structural stability to the whole cell, while the porosity of the cathode structure allows sufficient gas permeation. The typical processing techniques involve die pressing, extruding, or tape casting of cathode powders with binders and pore formers followed by high temperature sintering step [99]. Between the resulting porous cathode support and dense electrolyte, usually a thin (10–30 μm) active cathode layer with finer particle size is applied to facilitate the O_2 reduction reaction by providing a high number of active reaction sites. After a thin electrolyte layer (5–20 μm) is deposited, the cathode-electrolyte structure is annealed to obtain porous cathode support coupled with a gas tight electrolyte. Finally, an anode layer (100–200 μm) is deposited onto the electrolyte [6].

The advantage of the cathode supported SOFCs is the dramatic reduction of the Ohmic losses due to the reduced thickness of the electrolyte layer. However, the thermomechanical properties of the cathode-supported cells are not as good as the electrolyte-supported cells. Therefore, delamination and cracking can cause failure of the cell. Furthermore, the thick cathode layer leads to a substantial increase of the concentration polarization of the cell [6].

Anode-supported SOFCs

In the anode-supported fuel cell assembly, the anode supports the entire SOFC mechanically and is the thickest (1–2 mm) component of the cell. The increased thickness of the anode layer gives the structural stability to the cell, while the porosity of the anode structure allows sufficient gas circulation. The manufacturing methods are analogous to of the cathode-supported cell design. The assembly consists of a porous anode support, a thin (10–30 μm) active anode layer with finer particle size, a thin electrolyte (5–20 μm), and a cathode layer (100–200 μm) [6].

Similar to the cathode-supported design, the thermomechanical properties of the anode-supported SOFCs are not as satisfying as electrolyte-supported cells. Although considerably thick anode-support layers also result in higher concentration polarization, the overall performances of anode-supported SOFCs surpass those of the cathode-supported SOFCs due to the following reasons [6]:

- The reactant concentration at the anode side is typically 5 times larger than the O_2 concentration at the cathode side (21 vol.% O_2).
- The increased anode thickness improves the conversion efficiency of the cell in case a hydrocarbon fuel is utilized, by increasing the residence time of the fuel within the anode structure.

Metal-supported SOFCs

Contrary to the previously described self-supporting SOFCs, the metal-supported SOFCs consist of electrochemically active components only as thick as necessary and porous metallic substrates for mechanical stability and current collection. The potential advantages of metal-supported SOFCs over the self-supporting SOFCs are thermomechanical robustness, redox tolerance, rapid thermal cycling, and significant cost reduction. The requirements for the metallic support materials are

similar to those of cathode- and anode-support materials, such as gas permeability, oxidation or reduction resistance, electrical conductivity, thermal and chemical compatibility, mechanical strength, and low cost. The main disadvantage of metal-supported cells stems from the high sintering temperatures required by the conventional electrolyte deposition techniques such as tape casting and screen-printing. Subsequent to the co-sintering of metal-supported electrode-electrolyte bi-layers, it is typically challenging to retain the crucial properties of the metallic supports such as gas permeability and oxidation resistance [100], [101].

Micro-SOFC

State-of-the-art SOFC systems are mainly designed for stationary applications such as household units and small power plants with power output in the kilowatt to megawatt range [34], [102]. Due to the high specific energy and high energy density of hydrocarbons, the idea of miniaturization of SOFC technology (so-called micro-SOFC devices) as a battery replacement for mobile electronic devices with power requirements in the range of several watts has been proposed by a number of research groups [11], [14]–[16], [103]–[105]. The term "micro" should be highlighted, since it has dual meaning in terms of size and fabrication methods. On the one hand, micro stands for the fuel cell systems with chip-sized electrochemically active components compared to conventional SOFCs. On the other hand, it refers to the MEMS (micro-electro-mechanical systems) manufacturing processes used for their fabrication [10], [106]. In terms of design, the electrochemically active micro-SOFC membrane classically consists of two porous electrodes (cathode and anode), which are separated by a dense oxygen-ion-conducting electrolyte. This membrane with the trilayer structure can be either deposited sequentially on a porous substrate or supported by a micromachineable substrate material in the form of free-standing structure as shown in Figure 2-10. The typical porous substrates that have been used to support micro-SOFC membranes are porous Ni [105] and anodic Al_2O_3 templates [14], [107]. Dense micromachineable Foturan® substrates [19] and silicon wafers [16], [17], [108] have been also used to fabricate free-standing micro-SOFC membranes. Foturan® is a glass-ceramic substrate which can be structured by the UV-light exposure and subsequent wet etching. It is an electrical insulator, thus it can be used as a support material for free-standing micro-SOFC membranes without an insulating coating [10], [109]. Despite the semi-conducting properties and the complexity of the photolithographic processes, silicon wafers have been also used as substrates for micro-SOFC membranes. To use silicon as a substrate, an electrical insulating interlayer such as Si_3Ni_4 or SiO_2 is required to prevent short-circuiting. Furthermore, the thermal expansion coefficient of silicon (2.6×10^{-6} 1/K [110]) does not match with the micro-SOFC membranes (10–20×10^{-6} 1/K [10]). Nevertheless, silicon is one of the most commonly used support material in
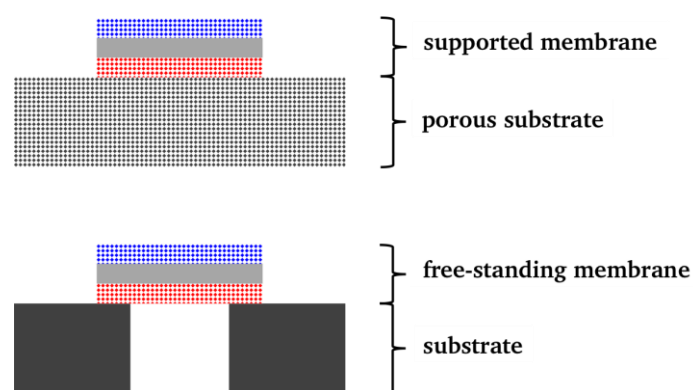

Figure 2-10: Schematic illustration of a supported micro-SOFC membrane on a porous substrate (top) and a free-standing micro-SOFC membrane (bottom).

$$1/2\,O_2 + 2e^- \rightarrow O^{2-}$$

$$H_2 + O^{2-} \rightarrow H_2O + 2e^-$$
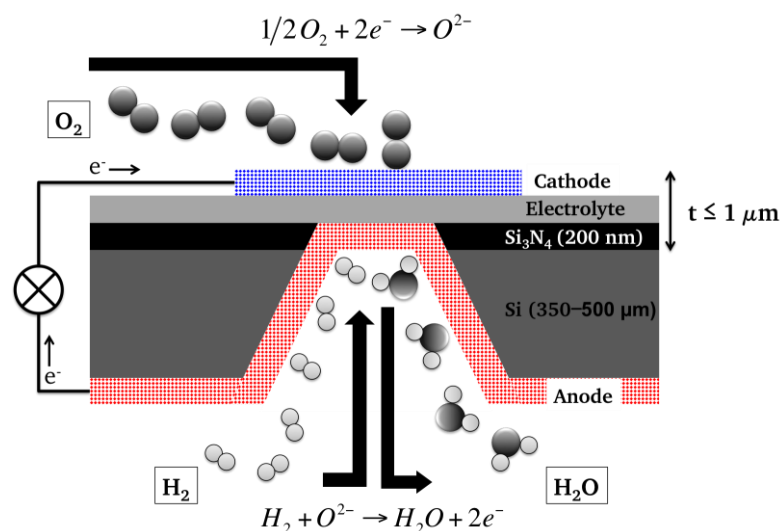
Figure 2-11: Cross-sectional schematic view and working principle of a silicon supported free-standing micro-SOFC membrane consisting of an electrolyte sandwiched between two porous electode layers. The total thickness of the active layers is less than 1 μm.

micro-SOFC community due to the standardized microfabrication processes in the semi-conductor industry. Regardless of the membrane design, it is essential to ensure the thermomechanical stability of the micro-SOFC membranes during the fabrication and service. Therefore, thermal stresses arising from different thermal expansion coefficients have to be taken into account carefully [10], [111], [112].

Apart from the thermo-mechanical stress engineering issues, the reduction of the operating temperatures below 450 °C is also crucial in terms of commercialization of micro-SOFCs. The reduction of the electrolyte thickness below 1 μm has been the main approach similar to the efforts made in conventional SOFC community to decrease the diffusion path length of charge carriers. YSZ and GDC are the state-of-the-art electrolyte materials used in micro-SOFCs, which are usually deposited by physical deposition methods such as sputtering and pulsed laser deposition (PLD). Reasonable area specific resistance values have been achieved for thin film YSZ electrolytes at low temperatures (ASR≈0.15 Ω cm^2, T<450 °C for 3YSZ electrolytes with thickness of 300 nm [112], [113]). On the other hand, the current Pt-based electrode technology is far from the optimum. Even though high performances have been reported by employing highly porous Pt electrodes at nanoscale, cost of the material and fabrication methods, and the long-term stability of the electrode layers at elevated temperatures are major concerns.

Figure 2-11 illustrates the typical Si-based freestanding micro-SOFC design and its working principle, which is similar to of the traditional SOFC illustrated in Figure 2-1. The detailed description of the fabrication process is given in the Section of 3.3.

2.4. Manufacturing Techniques of SOFC Components

Manufacturing techniques are crucial in terms of performance of SOFCs and their cost. Reproducibility, quality, cost-effectiveness, and ability to scale up have to be carefully considered when choosing and designing a specific fabrication process. The fabrication techniques also differ significantly for the particular cell components of different SOFC designs (planar or tubular).

In the case of planar SOFC design, the conventional fabrication techniques such as tape casting, screen-printing, and painting are the most preferred and well-established techniques. A typical electrolyte supported SOFC is fabricated by tape casting of the electrolyte support and screen-printing of anode and cathode layers on electrolyte. As the anode-supported SOFC design

has gained importance in terms of obtaining high performance SOFC systems at lower operating temperatures, numerous thin film deposition techniques have been considered for the SOFC fabrication. The introduction of thin film components into the SOFC technology has also enabled the realization of micro-SOFCs, which are potential energy sources for portable devices such as laptops and cell phones. The purpose of this section is to present the commonly used manufacturing techniques to fabricate SOFC components.

2.4.1. Conventional Ceramic Processing Techniques

Tape casting

Tape casting is a processing technique, which has been developed to obtain large-area, thin, flat ceramic layers and multilayers. The characteristics of the method such as up-scalability and cost-effectiveness make the tape casting process one of the most used fabrication techniques in SOFC manufacturing. The tape casting process involves a suspension of a ceramic powder dispersed in a liquid media, which consists of a combination of solvent, dispersant, binder, and plasticizer. The suspension is spread on a flat surface using the knife-edge of a doctor blade with a controlled thickness and the solvents are allowed to dry prior to the sintering process. The tape thickness is controlled by the spacing between the edge of the knife and surface of the casting. The thickness of the casted tapes ranges typically between >10 μm [114]. Multilayer tapes can be casted by sequentially one layer on top of another. The resulting tapes can be delaminated from the casting surface and cut into the desired size prior to sintering [1], [114], [115]. Tape casting is typically used to fabricate interconnects, dense electrolytes, porous anode supports, and co-sintered electrode-electrolyte bilayers [99].

Screen printing

Following tape casting, screen-printing is the second most common technique to fabricate SOFC components. Similar to tape casting method, screen-printing is also cost-effective and easy to scale up. The screen-printing process involves a suspension of a ceramic powder dispersed in a liquid media, which consists of a combination of solvent, dispersant, and binder. The suspension has usually higher viscosity compared to the tape casting method, therefore it is known as "ink" [116]. A blade is moved along the patterned mesh to push the ink through the apertures on the mesh and to wet the substrate below, which leads to a film with thickness typically >5 μm after firing [114]. Layers with larger thicknesses can be deposited by sequential printing [48]. Screen-printing is mainly used to fabricate porous electrode layers and dense electrolyte layers on anode supports [114], [116].

Die pressing

Die pressing is commonly used to fabricate simple SOFC components such as electrolyte and electrode supports. The method involves the compaction of ceramic powders under high pressures within a die with the shape of the desired component and a subsequent sintering step. Depending on the powder formulation and sintering conditions, the microstructure of the resulting product can be controlled. It is also possible to fabricate SOFC components with multiple layers such as anode-electrolyte bilayers by co-pressing and co-sintering approaches [33], [117].

2.4.2. Thin Film Deposition Techniques

In the last decades, thinner SOFC elements, particularly electrolytes with thicknesses below 1 μm, have been extensively investigated to compensate for the performance losses associated with the limiting ionic transport of the electrolyte materials. The advances in thin film deposition techniques have also lead to the emergence of a new platform known as micro-SOFCs.

Sputtering

Sputtering is a physical vapor deposition technique, in which material is eroded from a solid cathode target by bombardment with positively charged ions and deposited onto a surface. A noble gas (generally Ar) fed between the target and substrate is exposed to an electric field to induce ionization and eventually to generate plasma of electrons and positive ions. The positively charged ions accelerate towards negatively charged target. The momentum transfer leads the individual atoms or molecules to break free from the target material and sputtering of the thin films occurs. The potential at the metallic targets can be generated by DC power sources, but a radio frequency (RF) power source is needed to sputter dielectric materials [118]. In terms of the costs of equipment, sputtering is an expensive method and has a deposition rate of a few nanometers per minute. The sputtered films are polycrystalline with columnar microstructure. Varying the deposition conditions can control the film microstructure such as grain size and porosity [119].

Sputtering of thin film electrolytes especially YSZ [120]–[122] and GDC [123]–[125] have been primarily investigated in the SOFC field. On the other hand, porous NiO-YSZ [126], [127] anode layers have been successfully realized as thin-film anodes. Sputtering of LSC [128] and LSCF [129] thin-film cathodes on YSZ and GDC have been also reported.

Pulsed laser deposition

Pulsed layer deposition (PLD), similar to sputtering is also a physical vapor deposition technique, in which a high power laser pulses are employed to ablate material from a target composed of the desired thin film material. The ablation of the target material leads to the deposition of the target material onto a proximately positioned substrate. PLD has drawn increasing attention over the last two decades, since multi-component stoichiometric films can be fabricated from a single target [118].

Dense SOFC thin-film electrolytes such as YSZ [130], [131], GDC [132], [133], and LSGM [134], [135] have been realized by PLD. Porous and dense electrodes such as LSM, BSCF, LSCF, LSC, NiO-GDC [136]–[140] have been also deposited using PLD. Recently, a thin YSZ-GDC bi-layer electrolyte and a nanostructured LSC cathode layer have been sequentially deposited by PLD on a porous NiO-YSZ anode support and an extraordinary low temperature performance for the YSZ-based anode supported SOFC has been reported (500 mW cm^{-2} at 500 °C) [9]. Nevertheless, the difficulty of scaling up the process and the high cost of physical vapor deposition techniques are the most significant obstacles for the application of such techniques in the industrial production of SOFCs.

Chemical vapor deposition

Chemical vapor deposition (CVD) involves transport of a precursor gas or gasses onto heated substrates to be coated. The chemical reactions, which result in the deposition of desired product, happen near or on the hot surfaces. In thermally activated CVD, the deposition is initiated and continued by heat. There are variety of CVD processes utilized to fabricate SOFC components such as atomic layer deposition (ALD), metal-organic chemical vapor deposition (MOCVD), and aerosol-

assisted chemical vapor deposition (AACVD) [141]–[145]. The CVD processes have been mainly used to fabricate dense and gas-tight electrolyte layers on dense and porous substrates [146].

Spray deposition

Spray deposition is a processing technique to fabricate dense and porous oxide films and ceramic coatings. Typical spray deposition equipment consists of an atomizer, precursor solution, substrate heater, and temperature controller. The deposition method has varieties in terms of the atomization technique such as pressurized gas spray deposition, ultrasonic spray deposition, and electrostatic spray deposition. All methods involve the generation of an aerosol of a liquid precursor solution, which is directed onto the heated substrate. The precursor solution in the aerosol phase undergoes the stages of evaporation and decomposition near or on the surface of the substrate, which leads to the deposition of the desired film on the substrate [119], [147].

Spray deposition techniques have been extensively used to produce thin film components of SOFCs, since the process is cost-effective, versatile, and up scalable. Both dense electrolyte layers (YSZ [148], GDC [149]) and porous electrodes (LSCF [150], NiO-GDC [139]) have been fabricated by spray deposition methods.

Spin- and dip-coating

The spin- and dip coating processes are atmospheric, liquid-based methods and extensively used to fabricate thin ceramic coatings. In spin coating, the coating material within a suspension is applied to the center of the substrate and spread by centrifugal force. During the rotation, the excess coating material spins off the edges of the substrate and the remaining material on the substrate forms the desired film. The thickness of the film depends on several factors such as speed of spinning, viscosity and concentration of the suspension. In dip-coating process, a substrate is immersed into a reservoir of liquid precursor and withdrawn in a controlled way. As the substrate is withdrawn from the liquid media, a layer is deposited on the substrate. The deposition is influenced by several factors such as immersion time, withdrawal speed, number of dipping cycles, and concentration of the solution. In case of ceramic coatings, an annealing step is required to achieve crystallization and proper adhesion between the substrate and deposited film for both spin- and dip-coating processes [99].

Porous thin-film electrodes (LSM [151], [152], LSCF [153], [154], NiO-SGC [155]) and dense thin electrolytes (YSZ [156], [157] and GDC [158], [159]) on porous anode-supports have been successfully fabricated by spin- and dip-coating processes for the SOFC application.

Metal organic deposition

Metal organic deposition technique is an atmospheric, liquid-based, spin- or dip-on based method to fabricate thin films. In this technique, the precursor solution consisting of metal organic salts of the desired final product is applied onto a substrate in the form of uniform coating. Subsequent pyrolysis step leads the soft metal organic film to form the desired ceramic coating [91].

The depositions of YSZ electrolyte [160], GDC buffer layer [161], porous LSM-YSZ composite cathode [162], and thin porous LSC cathodes [79] have been successfully demonstrated by metal organic deposition method.

2.5. Current-Voltage Measurement

As previously presented (Figure 2-3), the overall performance of a fuel cell is best described by its current density–voltage (j–V) response, which displays the voltage output for a given load of

current density. The *j–V* curve of a fuel cell is typically measured with a potentiostat/galvanostat setup, which draws a fixed current from the cell and simultaneously measures the corresponding output voltage. The complete *j–V* response of a fuel cell can be obtained by sweeping over the entire current range to a predetermined value. Typically, the current and the power outputs of the cells are normalized to the active surface areas leading to current and power densities for the ease of performance comparison among different types of fuel cells. To perform a reliable *j–V* analysis, a steady state system is required and the test conditions should be noted.

The voltage drop of a fuel cell associated with a current load is not instantaneous and requires a period of time to reach its steady state conditions. This delay is caused by various factors such as unstable cell temperature and reactant concentrations. Thus, the measurements recorded under non-steady state conditions will be ambiguous. Typically, larger fuel cells need more time to reach steady state compared to small ones. Therefore, different approaches are used depending on the size of the fuel cell systems. For the large systems, the voltage response is monitored at a given current load until no significant change is observed in time. The *j–V* curve is plotted integrating a number of data points (10–20) to overcome the time constraints of the experiment. On the other hand, *j–V* curve measurements can be done in slow-scan mode for small fuel cells, as they reach the steady state conditions rather rapidly. The current load is gradually increased and the corresponding voltage response is recorded to generate the pseudo-steady state *j–V* curve. The most important requirement of pseudo-steady state measurements is to keep the sweep rate of the current load sufficiently slow.

The fuel cell performance is dependent of the testing conditions and they should be documented in detail to make proper comparisons among distinct fuel cell systems. The most crucial test conditions to be noted are temperature, pressure, and flow rates of the fuel and oxidant.

In general, *j–V* measurements are useful to illustrate the overall quantitative performance of a fuel cell system. However, it is also possible to extract the individual contributions to the voltage loss using the Tafel equation (Equation 2.24). The Ohmic and concentration contributions can be neglected at low current densities. As predicted by the Tafel equation, the *j–V* curves at low current densities show a linear behavior when plotted in logarithmic scale. The linear data fitting at low current density region and its extension through the *j–V* curve leads to an approximate estimation of activation losses and the sum of Ohmic and concentration losses separately at each current density [6].

2.6. Electrochemical Impedance Spectroscopy

While the *j–V* measurements provide an overall quantification of the performance of a fuel cell; the major sources of polarizations associated with Ohmic, activation, and concentration losses can be accurately distinguished only by electrochemical impedance spectroscopy (EIS). This section of the thesis focuses only on specific features, which are particularly crucial for understanding of the EIS experiments and analyses presented later in Chapters 5 and 6.

Analogous to the Ohmic resistance, the impedance is a measure of the opposition of a circuit to the flow of electrical current when a voltage is applied. Unlike resistance, impedance is a frequency-dependent phenomenon. Thus, impedance *Z* of a circuit is given by the ratio between the frequency dependent voltage, $V(\omega)$ and the current, $I(\omega)$ responses [6]:

$$Z(\omega) = \frac{V(\omega)}{I(\omega)} \qquad (2.32)$$

where ω is the angular frequency.

In an impedance spectroscopy experiment, the specimen is perturbed with a small alternating voltage, $\Delta V(\omega)$ and resulting current response, $\Delta I(\omega)$ is recorded.

$$\Delta V(\omega, t) = V_0 \cdot e^{-i \cdot \omega \cdot t} \tag{2.33}$$
$$\Delta I(\omega, t) = I_0 \cdot e^{-i \cdot (\omega \cdot t + \phi)} \tag{2.34}$$

where t is the time, V_0 and I_0 are the voltage and current amplitudes, respectively, and ϕ is the phase difference between voltage and current. Then, the impedance Z is given by:

$$Z(\omega) = \frac{V(\omega)}{I(\omega)} = \frac{V_0}{I_0} \cdot e^{i \cdot \phi} \tag{2.35}$$

The Euler relation ($e^{i \cdot \phi} = \cos\phi + i \cdot \sin\phi$) leads to:

$$Z(\omega) = Z'(\omega) + i \cdot Z''(\omega) \tag{2.36}$$

where $Z'(\omega)$ and $Z''(\omega)$ are the real and imaginary parts, respectively.

$$Z'(\omega) = Z_{real} = |Z| \cdot \cos\phi \tag{2.37}$$

$$Z''(\omega) = Z_{imag} = |Z| \cdot \sin\phi \tag{2.38}$$

$$|Z| = \frac{V_0}{I_0} = \sqrt{Z'^2 + Z''^2} \tag{2.39}$$

The experimental impedance data are typically displayed in the forms of Cole-Cole (Nyquist) and Bode-Bode plots. In the former, the negative imaginary part of the impedance ($-Z_{imag}$) is plotted versus the real part of the impedance (Z_{real}). The major shortcoming of this type of representation is the implicitness of the frequency data. In the Bode-Bode plots, the absolute impedance, $|Z|$ and phase angle, ϕ are complementarily plotted versus frequency ω or $f = \omega/2\pi$. Like typical spectroscopic representations, the frequency data are displayed explicitly in Bode-Bode plots. Figure 2-12 illustrates the impedance data of two different circuits in the forms of Nyquist and Bode-Bode plots. Depending on the complexity of the impedance data, the interpretation can be straightforward or very complicated. The most popular approach is the use of the equivalent model circuits, which approximates the measured impedance over the wide range of frequencies using various circuit elements such as resistors, inductors, capacitors, and their combinations. In a simplest case, the impedance behavior of an electrochemical interface reaction can be described by a parallel combination of a resistor (R) and a capacitor (C). The resistor models the kinetics of the electrochemical reaction, while the capacitor reflects the capacitive nature of the interface [6]. The impedance of this RC circuit is given by

$$Z_{RC}(\omega) = \frac{R}{1 + i \cdot \omega \cdot R \cdot C} \tag{2.40}$$
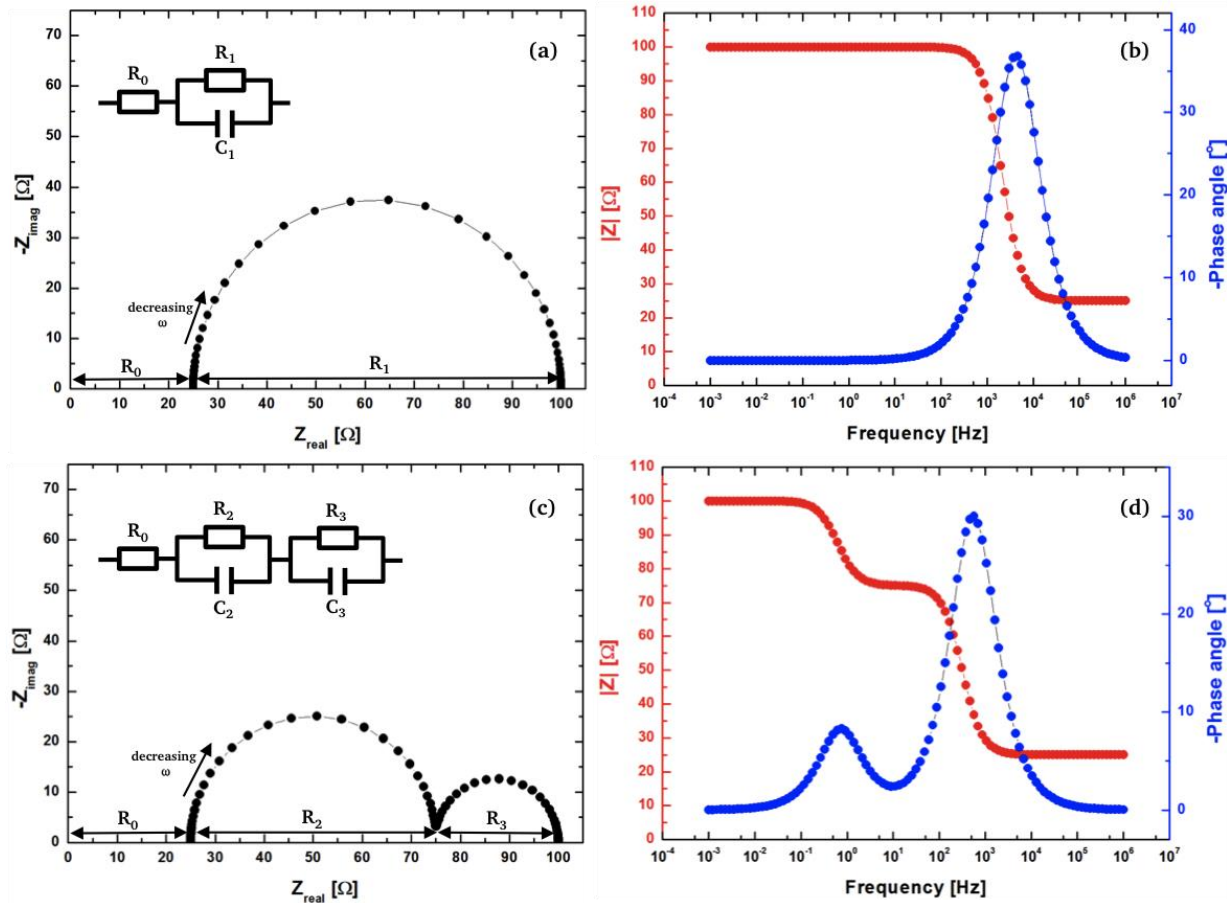
Figure 2-12: Simulated impedance spectra of a) one RC element ($R_0=25\ \Omega$, $R_1=75\ \Omega$, and $C_1=10^{-6}$ F) and b) two RC elements connected in series with considerably distinctive relaxation times ($R_0=25\ \Omega$, $R_2=50\ \Omega$, $C_2=10^{-5}$ F, $R_3=25\ \Omega$, $C_3=10^{-2}$ F). The Bode-Bode plots of the curcuits with one (b) and two (d) R-C elements are displayed next to the corresponding Nyquist plots.

In the complex impedance plane, such an element illustrated in Figure 2-12a leads to a semicircle with a diameter of R_1, which provides information about the polarization of an electrochemical process. At high frequency region, the impedance of the system approaches zero because the capacitors act as short circuits. On the other hand, capacitors act as open circuits at low frequencies. Therefore, the impedance response of the resistor itself defines the impedance of the system. In the intermediate frequency regime, impedance response of the system is both capacitive and resistive. The frequency at the apex of the semicircle, ω_R (i.e., relaxation frequency) is given by the time constant of the interface (τ_{RC}) [6]:

$$\omega_R = \frac{1}{\tau_{RC}} = \frac{1}{R \cdot C} \tag{2.41}$$

Two RC elements joined in series lead to well-separated semicircles (Figure 2-12c) in case they have sufficiently different relaxation frequencies. For a real system, the impedance responses of different processes with similar resistances can be easily distinguished if their capacitances differ greatly. The characteristic capacitance values in solid-state ionics depend strongly on the physical origin of the particular process (Table 2-2). Therefore, impedance spectroscopy is one of the most attractive characterization tools in electrochemistry.

Table 2-2: Typical capacitance values for different physical processes for thin film mixed ionic electronic conducting cathodes [98].

Capacitance	Origin	Typical value [F/cm^2]
C_{bulk}	Dielectric relaxation in bulk material	$\sim 10^{-12}$
C_{gb}	Grain boundary polarization in a polycrystalline material	$\sim 10^{-8}$
C_{dl}	Electrical double layer polarization at solid/solid interface	$\sim 10^{-5}$
C_{chem}	Oxygen stoichiometry polarization in the bulk of a mixed conducting thin film electrode	$\sim 10^{-2}$

In case of non-ideal (real) systems, a so-called constant phase element Q is typically used instead of the capacitor of an RC element. The deviation of the impedance response from the ideal RC behavior usually stems from the three-dimensional nature of the interfaces and local inhomogeneity in the material [163], [164]. The impedance of a constant phase element is given by

$$Z_Q(\omega) = \frac{1}{Q \cdot (i \cdot \omega)^n} \tag{2.42}$$

And the impedance of an RQ element, $Z_{RQ}(\omega)$ becomes

$$Z_{RQ}(\omega) = \frac{R}{1 + R \cdot Q \cdot (i \cdot \omega)^n} = \frac{R}{1 + (i \cdot \omega \cdot \tau_{RQ})^n} \tag{2.43}$$

with a time constant, τ_{RQ}:

$$\tau_{RQ} = \sqrt[n]{R \cdot Q} \tag{2.44}$$

where n is a measure of the degree of deviation from the ideal system. For $n=1$, the constant phase element is nothing but a capacitance. As the value of n gets smaller than unity, the impedance response starts to deviate from the ideal RC behavior and appear as depressed semicircles as illustrated in Figure 2-13. From the fitting parameters of Q and n, the true capacitance of the corresponding electrochemical process, C^* and corresponding relaxation frequency, f^* can be calculated according to

$$C^* = \sqrt[n]{(R^{1-n} \cdot Q)} \tag{2.45}$$

and

$$f^* = \frac{1}{2\pi} (R \cdot Q)^{-\frac{1}{n}} \tag{2.46}$$

, respectively.

However, such depressed semicircles can also emerge from two or more serial RC processes with comparable relaxation frequencies. Therefore, a great attention must be paid in the process of fitting the experimental data using equivalent circuits. Typically, the relaxation frequencies depend strongly on experimental conditions such as temperature and partial pressures of reactant species. By changing them in a systematic manner, separate impedance responses for different processes
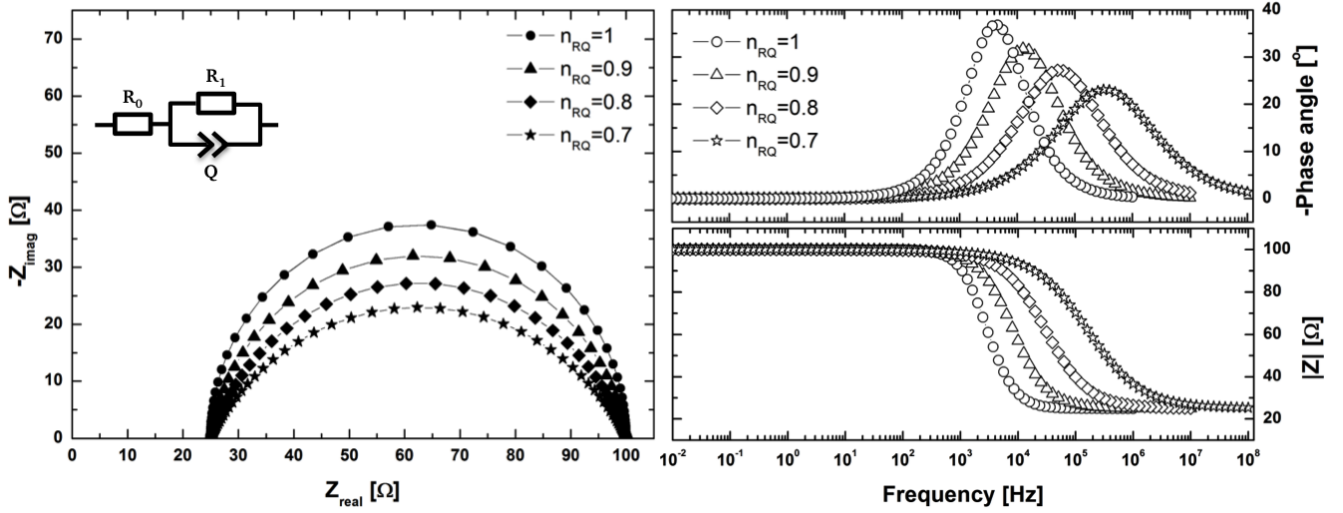
Figure 2-13: Simulated impedance spectra of one RQ element (R_0=25 Ω, R_1=75 Ω, and $C = 10^{-6}$ F) for different n values in Nyquist and Bode-Bode plots. For n=1, the impedance response of the RQ element is idential to of the RC element shown in Figure 2-12a. As the value of n gets smaller than 1, depressed semicircles are obtained.

can be distinguished. In this work, the experimental impedance data are also interpreted using the equivalent circuit models commonly proposed in the literature. When the model is thought to be unreliable, the polarization values are estimated simply by projecting the impedance data on the real axis of the complex impedance plane.

The obtained polarization data from the EIS experiments are commonly normalized to the geometry of the specimen, since fuel cells are generally compared on a unit-area basis. The area-normalized resistance, also known as area-specific resistance (ASR), is a measure of polarization losses with the unit of Ω cm^2 and given by

$$ASR_{pol} = Area_{fuel\ cell} \cdot R_{pol} \qquad (2.47)$$

2.7. Performance Evaluation

In the literature, the area-specific resistance and power density values are regularly used to define and compare the performance of individual SOFC components and complete cells. The electrodes are compared in terms of activation and mass transport polarizations, while the electrolytes are rated according to their contribution to the Ohmic polarization of the SOFC. In general, the maximum power density obtained from a SOFC is highly dependent on the different sources of polarizations of each cell element.

A few examples of activation polarizations arising from the (B)LSC(F)-based cathodes and the Ni-based cermet anodes are given in Table 2-3 and Table 2-4, respectively. Different performances of the comparable electrode material systems are deliberately exemplified within each table to illustrate the broad range of performance reported in literature. The deviations within the ASR values by one or two orders of magnitude is particularly caused by the variety of the fabrication techniques and resulting microstructural features. Similarly, the power outputs of anode-supported SOFCs fabricated using the electrode materials mentioned above are listed in Table 2-5. Approximately one order of magnitude performance deviation of the SOFCs operating at the same temperature and under similar conditions does not stem only from distinctive performances of electrodes but also from the Ohmic polarization management of the electrolyte layers.

Table 2-6 compares the open-circuit voltage and electrochemical performance of different micro-SOFCs. Even though a direct comparison in terms of cell performance is difficult to make due to the non-uniformity of the test conditions (*i.e.*, temperature and fuel composition), it is possible to state that the membranes, which are not gas tight, lead to low open circuit voltages and eventually poor electrochemical performance of micro-SOFCs. Therefore, a great effort has been invested to fabricate thermomechanically stable thin-film electrolyte membranes. Further advances have shown that an increase of the active membrane area through three-dimensional nanopatterning (*i.e.* corrugating) is one of the most efficient approaches to obtain high performance micro-SOFCs. An *et. al.* have reported a sensational high power output of 1.3 W/cm^2 at 450 °C [17]. Nevertheless, the cost and the solid-state dewetting of Pt thin-film electrodes demand for the integration of oxide- and cermet-based electrodes into the micro-SOFC technology.

Table 2-3: Comparison of the electrochemical performance of (B)LSC(F)-based cathodes.

Cathode	Deposition method	Electrolyte	ASR_{pol} (Ω cm^2) at 600 °C, air	Cathode thickness (μm)	Grain size (nm)	E_a (eV)	Ref.
$La_{0.6}Sr_{0.4}CoO_{3-\delta}$	Flame spray dep.	GDC20	0.96	0.2	38	1.52	[165]
$La_{0.6}Sr_{0.4}CoO_{3-\delta}$	Screen-printing	GDC10	0.96	-	43	-	[166]
$La_{0.6}Sr_{0.4}CoO_{3-\delta}$	Slurry spray dep.	GDC10	0.17 (700 °C)	~15	~250	-	[167]
$La_{0.6}Sr_{0.4}CoO_{3-\delta}$	PLD	9.5YSZ	0.1	0.2	35	1.4	[39]
$La_{0.6}Sr_{0.4}CoO_{3-\delta}$	MOD	GDC10	0.023	0.2	17	1.42	[79]
$La_{0.6}Sr_{0.4}CoO_{3-\delta}$	PLD	GDC10	0.13	1	25–35	1.34	[168]
$La_{0.5}Sr_{0.5}CoO_{3-\delta}$	PLD	GDC10	0.089	0.72	8	-	[169]
$La_{0.5}Sr_{0.5}CoO_{3-\delta}$	MOD	GDC20 on 3.5YSZ	0.13	0.3	54	1.07	[170]
$La_{0.5}Sr_{0.5}CoO_{3-\delta}$	MOD	8YSZ	0.146	0.3	54	1.07	[170]
$La_{0.6}Sr_{0.4}CoO_{3-\delta}$ + GDC20	Slurry spray dep.	GDC20	0.24	20	50–200	-	[171]
$La_{0.6}Sr_{0.4}CoO_{3-\delta}$ + GDC20	Screen-printing	GDC10	0.052	15	~250	-	[172]
$La_{0.6}Sr_{0.4}Co_{0.2}Fe_{0.8}O_{3-\delta}$	Spin-coating	GDC20 on 8YSZ	0.74	<1	<68	1.47	[153]
$La_{0.6}Sr_{0.4}Co_{0.2}Fe_{0.8}O_{3-\delta}$	Spray dep.	GDC20	2.05	~0.4	65	1.55	[150]
$La_{0.6}Sr_{0.4}Co_{0.2}Fe_{0.8}O_{3-\delta}$	PLD	GDC20	9.3	~0.4	65	1.49	[150]
$La_{0.6}Sr_{0.4}Co_{0.2}Fe_{0.8}O_{3-\delta}$	PLD + Spray dep.	GDC20	1.03	~0.4	65	1.18	[150]
$La_{0.6}Sr_{0.4}Co_{0.8}Fe_{0.2}O_{3-\delta}$	Spin-coating	GDC10	0.048	10	130	-	[173]
$La_{0.6}Sr_{0.4}Co_{0.2}Fe_{0.8}O_{3-\delta}$ + GDC20	Spin-coating	GDC20 on 8YSZ	0.371	<1	<68	1.13	[153]
$Ba_{0.25}La_{0.25}Sr_{0.5}Co_{0.8}Fe_{0.2}O_{3-\delta}$	Spray dep.	GDC20	0.76	~0.4	35	1.28	[150]
$Ba_{0.25}La_{0.25}Sr_{0.5}Co_{0.2}Fe_{0.8}O_{3-\delta}$	Spin-coating	GDC20 on 8YSZ	0.038	<1	<68	1.33	[153]

Table 2-4: Comparison of the electrochemical performance of Ni-based cermet anodes.

Anode	Deposition method	Electrolyte	ASR_{pol} (Ω cm^2) at 600 °C	Anode thickness (μm)	Grain size (nm)	E_a (eV)	Test conditions	Ref.
Ni-GDC20 (60/40 vol.%)	Spray dep.	GDC20	0.34	0.5±0.1	16	1.45	N$_2$:H$_2$ 4:1 (3 vol.% H$_2$O)	[139]
Ni-GDC20 (60/40 vol.%)	Spray dep.	GDC20	1.73	0.8±0.1	53	1.45	N$_2$:H$_2$ 4:1 (3 vol.% H$_2$O)	[139]
Ni-GDC20 (50/50 vol.%)	PLD	GDC20	0.68	0.8±0.1	-	1.46	N$_2$:H$_2$ 4:1 (3 vol.% H$_2$O)	[139]
Ni-GDC20 (60/40 vol.%)	Spray dep.	8YSZ	7.2	0.5–0.8	53	0.77	N$_2$:H$_2$ 4:1 (3 vol.% H$_2$O)	[139]
NiO-GDC10 (50/50 wt.%)	Screen-printing	GDC10	1.22 (650 °C)	~30	<1000	1.58–1.93	N$_2$:H$_2$ 9:1 (3 vol.% H$_2$O)	[174]
Ni-ScSZ10 (40/60 vol.%)	Screen-printing	8YSZ	2.5	-	~1000	-	Pure H$_2$ (3 vol.% H$_2$O)	[175]
Ni-ScSZ10 (40/60 vol.%)	Screen-printing	8YSZ	3.6	-	~1000	-	N$_2$:H$_2$ 1:1 (3 vol.% H$_2$O)	[175]
Ni-GDC10 (60/40 mol.%)	Spray dep.	8YSZ	0.61 (650 °C) 0.095 (700 °C)	~20	1500	0.86	Pure H$_2$ (humidified)	[176]
Ni-GDC20 (60/40 vol.%)	Screen-printing	GDC10		~20	~1000	0.55	Pure H$_2$ (3 vol.% H$_2$O)	[177]
Ni-GDC10 (78/22 mol.%)	Screen-printing	GDC10	0.14	-	~100	-	Pure H$_2$ (3 vol.% H$_2$O)	[178]
NiO-GDC20 (65/35 wt.%)	Impregnation	GDC10	1.3	~15	~250	1.41	N$_2$:H$_2$ 19:1 (3 vol.% H$_2$O)	[179]
Ni-GDC20 (60/40 vol.%)	Screen-printing	8YSZ	1.05	~15	<500	0.90	N$_2$:H$_2$ 4:1 (3 vol.% H$_2$O)	[180]
Ni-SDC15 (60/40 wt.%)	Screen-printing	LSGM	1.8	~35	-	1.01	Pure H$_2$	[181]

Table 2-5: Comparison of the open-circuit voltage and electrochemical performance of different anode-supported SOFCs.

SOFC materials (anode|electrolyte|cathode)	Electrolyte thickness (μm)	OCV (V)	Power density (mW/cm²)	T (°C)	Test conditions	Ref.
Ni-YSZ|8YSZ/GDC|LSC	1.2	1.05	1480	600	Cathode: air; Anode: pure H_2, 3 vol.% H_2O	[9]
Ni-YSZ|8YSZ/GDC|LSC	~10	1.1	270	600	Cathode: air; Anode: pure H_2	[171]
Ni-YSZ|8YSZ/GDC|LSC	1	1.1	1400	600	Cathode: air; Anode: pure H_2, 3 vol.% H_2O	[182]
Ni-YSZ|8YSZ|LSC	~1.5	1.147	611	600	Cathode: air; Anode: pure H_2	[183]
Ni-GDC|GDC|LSC	15	~0.9	1580	600	Cathode: air; Anode: pure H_2, 3 vol.% H_2O	[172]
Ni-YSZ|8YSZ/GDC|LSC	-	~1.05	~190	600	Cathode: 20 vol.% O_2; Anode: pure H_2, 3 vol.% H_2O	[184]
Ni-GDC|GDC|LSCF-GDC	30	0.882	1021	600	Cathode: air; Anode: pure H_2	[185]
Ni-GDC|GDC|LSCF-GDC	~25	0.93	850	650	Cathode: air; Anode: pure H_2, 3 vol.% H_2O	[186]
Ni-GDC|GDC|LSCF-GDC	~49	0.963	422	600	Cathode: air; Anode: pure H_2, 3 vol.% H_2O	[187]
Ni-GDC|GDC|LSCF	16	0.92	650	600	Cathode: pure O_2; Anode: pure H_2, 3 vol.% H_2O	[188]
Ni-SDC|SDC|BSCF	20	~0.85	1010	600	Cathode: air; Anode: pure H_2, 3 vol.% H_2O	[37]

Table 2-6: Comparison of the open-circuit voltage and electrochemical performance of different micro-SOFCs.

micro-SOFC materials (anode|electrolyte|cathode)	Electrolyte thickness (μm)	OCV (V)	Power density (mW/cm²)	T (°C)	Test conditions	Ref.
Ni|8YSZ|Pt	0.2	0.87 (550 °C)	7	450	Cathode: air; Anode: N_2:H_2 97:1	[189]
Pt|8YSZ|Pt	0.07	1.09	677	400	Cathode: air; Anode: pure H_2	[15]
Pt|8YSZ|Pt	0.22	1.10	270	350	Cathode: air; Anode: pure H_2	[103]
Pt|8YSZ-8YSZ|Pt	0.75	1.05	152	550	Cathode: air; Anode: N_2:H_2 4:1, 3 vol.% H_2O	[104]
Pt|8YSZ|BSCF	0.1	0.63	35	520	Cathode: air; Anode: pure H_2, 3 vol.% H_2O	[190]
Pt|3YSZ|Pt	3	0.98	12	500	Cathode: air; Anode: N_2:H_2 4:1 and 3 vol.% H_2O	[191]
Pt|8YSZ|Pt	0.9	1.02	350	500	Cathode: air; Anode: N_2:H_2 24:1	[14]
Pt|8YSZ|Pt	0.108	0.968	1037	500	Cathode: air; Anode: N_2:H_2 19:1, 3 vol.% H_2O	[192]
Ru-GDC|8YSZ|Pt	0.1	0.97	275	485	Cathode: air; Anode: humidified CH_4	[193]
Pt|YDC|Pt	0.06	1.08	1300	450	Cathode: air; Anode: pure H_2	[17]
Pt|3YSZ|LSC	0.3	1.06	262	450	Cathode: air; Anode: N_2:H_2 4:1, 3 vol.% H_2O	[112]

3. Experimental Methods

3.1. Nanoparticle Synthesis

The cathode and anode nanoparticles are synthesized by ultrasonic spray pyrolysis (USP) and salt-assisted spray pyrolysis (SASP) techniques, where in the latter the precursor solution is modified by the addition of NaCl. Figure 3-1 shows the schematic view of the synthesis setup, which consists of four major parts: a precursor delivery unit (atomization chamber and a gas supplying unit), a hot-wall reactor for the pyrolysis, a filter-based powder collection unit, and a vacuum pump.

A pressure gradient is achieved using a vacuum pump located at the end of the synthesis line. The pressure is maintained at 900 mbar using a Baratron pressure gauge (MKS Instrument 628A) positioned between the pyrolysis zone and the powder collection unit, a butterfly valve (MKS Instruments 253B), and a pressure controller (MKS Instrument 651C).

In the atomization chamber, the precursor solution is nebulized by a transducer (TDK, NB series, Japan) operating at resonant frequency in the range of 1.6–1.75 MHz. The atomized precursor droplets are carried into the pyrolysis zone continuously by a constant O_2 gas flow (5 SLM, N48) regulated by a mass flow controller (MKS Instruments 1179A) and a gas controller (MKS Instrument 647B). The pyrolysis zone consists of a 450 mm long horizontal tube furnace (CTF 1200, Carbolite, UK) and an aluminum oxide tube (Degussit AL23, Friatec, Germany) with an inner diameter of 20 mm. The pyrolyzed nanoparticles are collected on a glass fiber filter (Sartorius, Germany) located in the powder collection unit, which is kept above 120 °C using a heating tape (HBS 450, Horst, Germany) to avoid the water vapor condensation. At the end of the synthesis, the powder is scraped off from the filter.
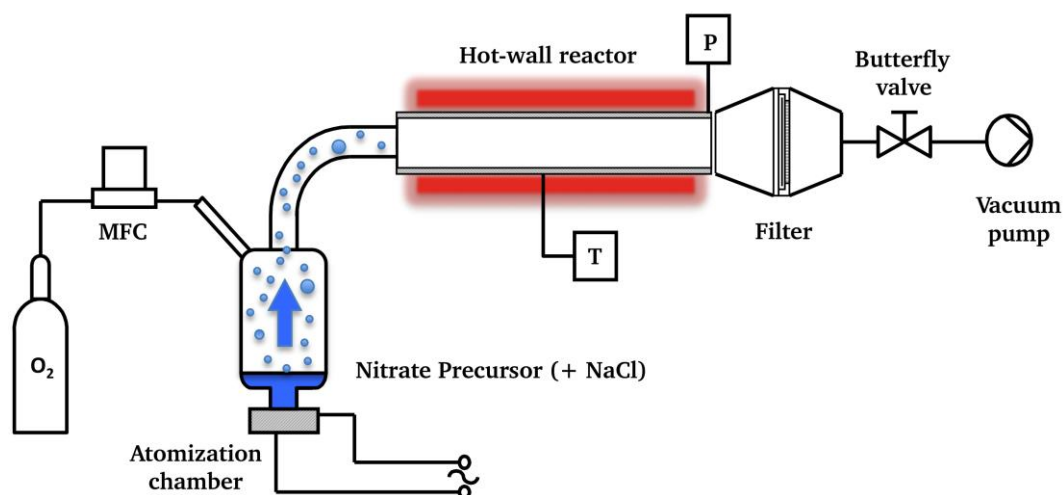

Figure 3-1: Schematic view of the ultrasonic spray pyrolysis setup.

The water-based precursor solutions to synthesize the nanoparticles of $La_{0.6}Sr_{0.4}CoO_{3-\delta}$ (LSC), $La_{0.5}Sr_{0.5}Mn_{0.5}Co_{0.5}O_{3-\delta}$ (LSMCo), $La_{0.9}Sr_{0.1}Mn_{0.5}Cr_{0.5}O_{3-\delta}$ (LSMCr), and $NiO-Ce_{0.8}Gd_{0.2}O_{2-\delta}$ (NiO-GDC20, 60-40 wt.%) are prepared by dissolving the corresponding metal nitrates stoichiometrically in deionized water. For each synthesis, the concentration of the total metal ions in the precursor solutions is fixed to 0.05 M, while the concentration of NaCl is varied within the range of 0–1 M. The precursors used to synthesize the LSC, LSMCo, LSMCr, and NiO-GDC20 powders are listed in Table 3-1.

Table 3-1: The chemicals used for the precursor solutions.

Precursor	Provider	Purity (%)
$La(NO_3)_3 \cdot 6H_2O$	Sigma-Aldrich, Germany	99.99
$Sr(NO_3)_2$	Sigma-Aldrich, Germany	>99
$Co(NO_3)_3 \cdot 6H_2O$	Sigma-Aldrich, Germany	>98
$Mn(NO_3)_3 \cdot 4H_2O$	Merck, Germany	99.5
$Cr(NO_3)_3 \cdot 9H_2O$	Alfa Aesar, Germany	99.99
$Ni(NO_3)_3 \cdot 6H_2O$	Sigma-Aldrich, Germany	99.999
$Ce(NO_3)_3 \cdot 6H_2O$	Alfa Aesar, Germany	99.99
$Gd(NO_3)_3 \cdot 6H_2O$	Sigma-Aldrich, Germany	99.99
NaCl	Sigma-Aldrich, Germany	>99.5

3.2. Fabrication of Fuel Cell Components

3.2.1. Spin Coating

The thin film electrodes and $Ce_{0.8}Gd_{0.2}O_{2-\delta}$ (GDC20) interlayers are fabricated by spin coating of stabilized suspensions of LSC, LSMCo, LSMCr, NiO-GDC20, and commercial GDC20 ($Ce_{0.8}Gd_{0.2}O_{2-\delta}$; particle size <100 nm, specific surface area >100 m^2/g, Sigma-Aldrich, Germany) nanoparticles. The GDC20 interlayers are only used when LSC, LSC-GDC20, LSMCo, and LSMCr electrodes are deposited on YSZ substrates (8 mol.% Y_2O_3, thickness: 200 μm, Itochu, Japan) to prevent undesired interfacial reactions leading to the formations of $SrZrO_3$ and La_2ZrO_7 phases taking place at elevated temperatures. A three-step spin coating procedure is developed to fabricate all thin film components (Table 3-2). For the spin-up step, a relatively high acceleration is chosen to obtain a full coverage of the substrate surface with the suspensions. A solvent evaporation step of three minutes is used to ensure the substantial removal of solvent from the spin-coated layers. Lastly, the residual suspensions typically accumulated at the edges of the substrates are removed owing to the high acceleration of the final spin-off step.
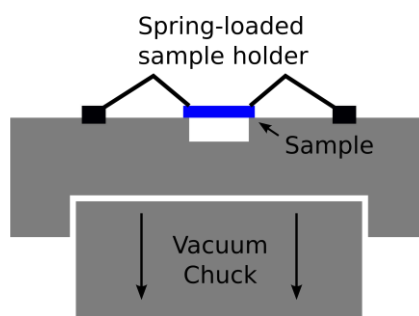

Figure 3-2: The schematic view of the sample holder designed to prepare symmetrical samples by spin coating.

Table 3-2: The three-step spin coating procedure for the thin film fabrication.

Steps	Acceleration (rpm/s)	Speed (rpm)	Duration (s)
Spin-up	100	2000	20
Solvent evaporation	0	2000	180
Spin-off	200	3000	5

Subsequent to the spin coating, the samples are annealed to achieve a proper adhesion to the underlying substrates. The GDC20 interlayers are annealed at 950 °C for 4 h in air, while the electrode layers are annealed in the temperature range of 550–1000 °C for 2 h in air. A heating and cooling rate of 3 °C/min is used for all samples.

The original sample holder (the vacuum chuck) of the spin coater is not appropriate for the symmetrical sample preparation, as it is not possible to fabricate thin films on both sides of the substrates without damaging the already deposited layers. Therefore, a spring-loaded sample holder (Figure 3-2) is designed to enable symmetrical electrode deposition.

3.2.2. Screen Printing

Screen printing is used to fabricate the current collector layers for cathodes, the electrolyte layers on the anode supports, and thick LSC cathodes.

The LSM ink ($(La_{0.8}Sr_{0.2})_{0.95}MnO_{3-\delta}$; d50: 0.39 μm, specific surface area: 4.66 m^2/g, solid loading: 62–72 wt.%, Fuel Cell Materials, USA) for the cathode current collector layers is commercially available, while the YSZ and GDC electrolyte inks are prepared by ball milling the commercially available YSZ ($(Y_2O_3)_{0.08}(ZrO_2)_{0.92}$; d50: 0.5–0.7 μm, specific surface area: 6–9 m^2/g, tape casting grade, Fuel Cell Materials, USA) and $Ce_{0.90}Gd_{0.10}O_{2-\delta}$ (GDC10; d50; 0.1–0.4 μm, specific surface area: 5–8 m^2/g, tape casting grade, Fuel Cell Materials, USA) powders with a terpineol based ink vehicle (Fuel Cell Materials, USA) at a vibrational frequency of 25 Hz for 20 minutes. The solid loadings of the 8YSZ and GDC10 inks are adjusted to 75 wt.%. The inks for the deposition of the thick LSC cathode layers are prepared also by ball milling (at a vibrational frequency of 25 Hz for 20 minutes) the synthesized LSC nanoparticles with the terpineol based ink vehicle. The solid loading of the LSC ink is adjusted to 40 wt.%.

After the screen printing using a 325-mesh screen (*i.e.*, 325 wires/inch), the samples are dried at 100 °C for 2 h. The LSM current collector layers are annealed in-situ during the high temperature electrochemical testing (at 550–750 °C for 1 h in air) to burn off the organic component of the ink and achieve a proper adhesion to the underlying cathode layers. High annealing temperatures are not preferred to sustain the nanostructured features of the cathode layers underneath. On the other hand, to achieve dense and gas-tight 8YSZ and GDC10 electrolyte layers, high sintering temperatures and long durations are required, *i.e.*, 1350–1450 °C for 3 h in air.

3.2.3. Powder Consolidation

To fabricate electrolyte substrates and anode supports, corresponding powders are consolidated by uniaxial pressing (497 MPa, diameter of 8 mm) and subsequently heat-treated.

To form the electrolyte substrates, $Ce_{0.9}Gd_{0.1}O_{2-\delta}$ powders (GDC10; d50: 0.1–0.4 μm, specific surface area: 5–8 m^2/g, tape casting grade, Fuel Cell Materials, USA) are compacted and consequently sintered at 1400 °C for 3 h in air with a heating and cooling rate of 2 °C/min. While

NiO-GDC20 powders obtained from salt-assisted spray pyrolysis are compacted to form the anode supports and then sintered at 900 °C for 2 h in air with a heating and cooling rate of 1 °C/min.

3.3. Fabrication of Micro-SOFCs

This part of the work is done as a collaboration project between the Joint Research Laboratory Nanomaterials (TU Darmstadt, Germany) and the Nonmetallic Inorganic Materials (ETH Zürich, Switzerland) groups. The Si-based micro-SOFCs with freestanding electrolytes are fabricated at ETH Zürich, while thin LSC cathodes are integrated into micro-SOFCs at TU Darmstadt. Ultimately, the fuel cell tests are conducted at ETH Zürich.

The microfabrication flowchart illustrated in Figure 3-3 shows two different fabrication approaches to obtain the identical end product. The distinct approaches are followed to create different platforms for the deposition of LSC cathodes: (*i*) pre-etched ($3YSZ|Si_3N_4|Si$) (Figure 3-3c left) and (*ii*) freestanding ($3YSZ|Si_3N_4$) (Figure 3-3c right) membranes.

i) To fabricate pre-etched ($3YSZ|Si_3N_4|Si$) membranes for the LSC deposition, the double side Si_3N_4 coated (200 nm) silicon chips (2×2 cm^2, 380 μm thick) are used as substrates. The surface of the bottom Si_3N_4 is partially structured using photolithography and reactive ions etching (Figure 3-3, step a). The wet pre-etching of Si chip is performed at 90 °C in a custom-made bath filled with 20 mol.% aqueous KOH solution (Figure 3-3, step b). The YSZ (3 mol.% Y_2O_3, 3YSZ) films with a thickness of 300 nm are fabricated by PLD (Surface PLD workstation, Hückelhoven, Germany) with a 248 nm excimer laser (fluence of 2.1 J/cm^2). The target–substrate distance and the substrate temperature are adjusted to 5.5 cm and 400 °C, respectively. The oxygen pressure is set to $2.67 \cdot 10^{-6}$ mbar (2 mTorr) (Figure 3-3, step c). The LSC films with a thickness of 250 nm are deposited on the 3YSZ electrolytes by a single-step spin coating (spin speed: 1200 rpm, acceleration: 200 rpm/s, spin duration: 150 s) of stabilized suspensions of LSC with solid loading of 10 wt.%, followed by annealing at 550 °C for 1 h in air with a heating and cooling rate of 3 °C min^{-1} (Figure 3-3, step d). A protective coating (FSC-H, Rohm and Haas, Coventry, UK) is brushed on the LSC thin film side of the Si chips to protect the films against KOH attack during the complete wet etching of the Si (Figure 3-3, step e). The remaining Si is then removed by the second wet etching step in KOH until the top layers are visible as freestanding membranes and the protective coating is removed by acetone (Figure 3-3, step f). The underlying Si_3N_4 layer is removed by reactive ion etching (RIE80 Oxford Instruments UK, 50 sccm CHF$_3$ and 5 sccm O$_2$ at 100 W for 200 s) to yield Si chips with 30 free-standing LSC|3YSZ membranes (Figure 3-3, step g).

ii) To fabricate freestanding ($3YSZ|Si_3N_4$) membranes for the LSC deposition, the silicon chips (2×2 cm^2, 380 μm thick) with 30 integrated free-standing Si_3N_4 membranes (390×390 μm^2, 200 nm thickness) are purchased from Embedded Microsystems Bremen, Germany (Figure 3-3, right). The YSZ (3 mol. % Y_2O_3, 3YSZ) films with a thickness of 300 nm are fabricated by PLD (Surface PLD workstation, Hückelhoven, Germany) with a 248 nm excimer laser (fluence of 2.1 J/cm^2). The target–substrate distance and the substrate temperature are adjusted to 5.5 cm and 700 °C, respectively. The oxygen pressure is set to $2.67 \cdot 10^{-6}$ mbar (2 mTorr) (Figure 3-3, step c). The LSC films with a thickness of 250 nm are deposited on the 3YSZ electrolytes by a single-step spin coating (spin speed: 1200 rpm, acceleration: 200 rpm/s, spin duration: 150 s) of stabilized suspensions of LSC with solid loading of 10 wt.%, followed by annealing at 550 °C for 1 h in air with a heating and cooling rate of 3 °C/min (Figure 3-3, step d). The underlying Si_3N_4 layer is removed by reactive ion etching (RIE80 Oxford Instruments UK, 50 sccm CHF$_3$ and 5 sccm O$_2$ at 100 W for 200 s) to yield Si chips with 30 free-standing LSC|3YSZ membranes (Figure 3-3, step g).

Si wafer, double-side coated with Si$_3$N$_4$

Si wafer integrated with free-standing Si$_3$N$_4$ membranes

390 µm

a)

b)

c)

d)

e)

f)

g)

h)

i)

390 µm

Si (380 µm)   3YSZ (300 nm)
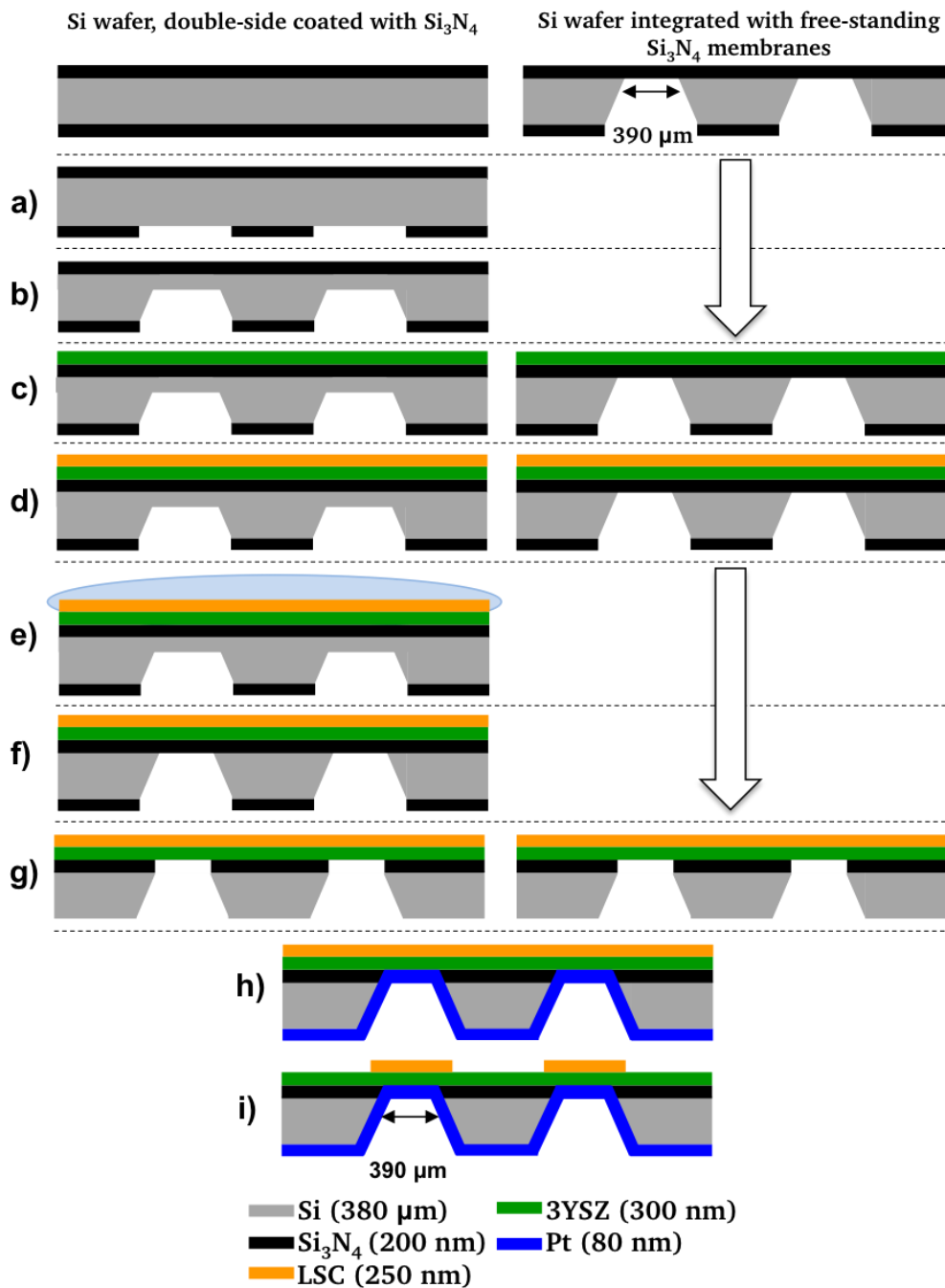Si$_3$N$_4$ (200 nm)   Pt (80 nm)
LSC (250 nm)

Figure 3-3: Microfabrication process of the free-standing LSC|3YSZ|Pt micro- SOFC membranes.

For both types of the samples, an 80 nm thin Pt anode is deposited at 25 °C by d.c. magnetron sputtering (PVD products, Wilmington, MA, USA) in 0.999·10^{-4} mbar (75 mTorr) of Ar and 100 W plasma power during 246 s onto the entire rear side of the Si wafer piece (Figure 3-3, step h). Either the complete micro-SOFC array consisting of 30 freestanding membranes is electrochemically characterized or the micro-SOFCs are separated from each other carefully by scratching off the LSC layers around the membranes (Figure 3-3, step i). The freestanding membranes are examined by light microscopy (Polyvar MET, Reichert-Jung, Depew NY, USA) after each deposition step and after fuel cell testing.

3.4. Fabrication of Anode-supported SOFCs

Figure 3-4 shows the major steps of the fabrication process of the anode-supported SOFCs consisting of the methods introduced in the Section 3.2. NiO-GDC20 nanopowders (salt-assisted spray pyrolyzed, 60:40 by weight) are consolidated by uniaxial pressing (497 MPa, diameter of 8 mm, thickness of 0.8–1 mm) and partially sintered at 900 °C for 2h (Figure 3-4, step a). The GDC10 electrolyte layer is deposited on pre-sintered anode supports by screen printing and dried at 100 °C for 2 h. The anode-electrolyte bilayers are fully sintered at 1400 °C for 3h in air to achieve a gas tight electrolyte layer (Figure 3-4, step b). LSC cathodes are deposited either by spin coating or by screen printing to obtain cathode layers with low (below 1 μm) and high (10–15 μm) thicknesses, respectively. After the deposition of cathode layers, the samples are annealed at 900°C for 2 h in air (Figure 3-4, step c). Finally, the commercially available LSM ink is screen-printed on the spin-coated LSC cathodes as current collector layers and dried at 100 °C for 2 h (Figure 3-4, step d), while the cells with screen-printed LSC cathodes are characterized without a current collector layer.
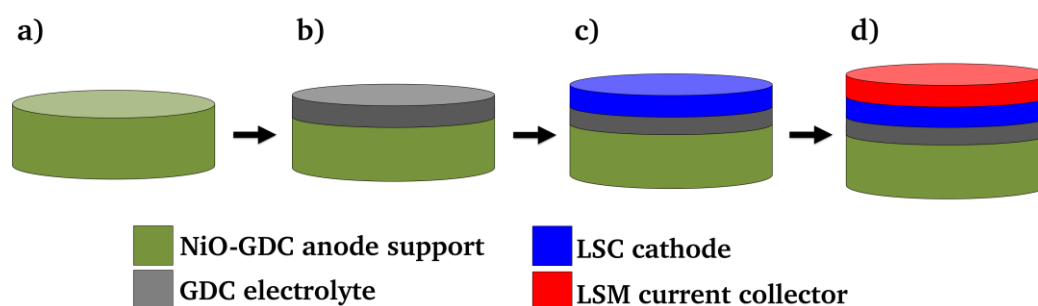

Figure 3-4: Fabrication process of the anode-supported SOFCs.

3.5. Characterization Methods

3.5.1. Scanning Electron Microscopy

The scanning electron microscopy (SEM) analyses are performed to characterize the microstructure of the synthesized nanoparticles and the fabricated fuel cell components using either a LEO GEMINI 1530 (Zeiss, Germany) or a Philips XL30 FEG. For the micro-SOFC samples, the thicknesses of the electrodes and electrolyte are determined from focused ion beam (FIB; Helios Nanolab 600i, FEI, The Netherlands) cross-sectional images. The samples are first protected by a carbon deposition and the trenches are milled down using an ion current of 7.7 pA under an acceleration voltage of 30 kV.

Energy dispersive X-ray spectroscopy (EDS) analyses within the Philips XL30 FEG SEM are performed to confirm the elemental compositions of the synthesized nanoparticles.

Thin conductive films of either Au-Pd or Au are sputtered onto the SEM specimens using Quorum Q300T D or Balzers SCD 050 sputter coaters to prevent the electrical charging, while the EDS specimens are coated by carbon using the Balzers SCD 050 sputter coater in carbon filament evaporation mode.

3.5.2. Transmission Electron Microscopy

The scanning transmission electron microscopy (STEM) and energy dispersive X-ray spectroscopy (EDS) analyses are carried out for representative powder samples in a FEI Titan 80-300 transmission electron microscope. The powders are first dispersed in ethanol and then dropped onto the TEM Cu grids.

3.5.3. Low Temperature Nitrogen Adsorption

The specific surface areas of the synthesized nanoparticles are evaluated using a low-temperature nitrogen adsorption instrument (Autosorb-3b, Quantachrome, USA). Prior to the measurement, the samples are degassed at 150 °C for approximately 15 h under vacuum to remove the moisture and any adsorbed gasses. The specific surface area is extracted from the linear part of adsorption curve according to the Brunauer–Emmett–Teller (BET) method [194].

3.5.4. X-ray Diffraction

X-ray diffraction (XRD) patterns are recorded in the Bragg-Brentano (θ-2θ) geometry for every synthesized sample using a D8 Advance X-ray diffractometer (Bruker AXS, Germany) with Ni-filtered Cu Cu K_α radiation (λ=0.15406 nm) generated at 30 kV and 40 mA. A position sensitive detector (VÅNTEC-1) with a fixed divergence slit of 0.3° is used to collect the XRD data. For most of the samples a 2θ scan range of 15-85°, a step width of $\Delta(2\theta)$=0.015° and an acquisition time of 1.0 second per step are used.

The structure refinements and quantitative phase analyses of the as-recorded patterns are carried out by the Rietveld method using the software TOPAS 4.2 (Bruker AXS, Germany). The instrumental broadening for the XRD data is determined using the scans of the reference LaB_6 (NIST 660a) powder.

3.5.5. Dynamic Light Scattering & Zeta Potential Measurements

The particle size distribution and zeta potential measurements are carried out using a ZetaSizer Nano ZS (Malvern Instrument, UK). The as synthesized nanoparticles are dispersed in either acidic or basic solvents depending on the stability of the material using a compact ultrasonic finger (Hielscher UP400H, Germany) subsequent to the removal of NaCl by water rinsing. The measurements of size and zeta potential are performed simultaneously over the pH range of 2–12.

3.5.6. High Temperature Impedance Spectroscopy

The electrochemical characterization of the symmetrical cells is conducted by impedance spectroscopy using a Solartron 1260 impedance/gain-phase analyzer. To perform high temperature impedance measurements (in the temperature range of 350–650 °C), two different sample holders are used. The impedance measurements of symmetrical cathode samples are performed using the in-house built setup [195]. The samples are positioned between two alumina pieces, which are slotted to allow a homogeneous gas distribution over the surfaces of the samples. Platinum meshes (mesh 100) are used as metallic electrodes on both sides of the sample. Two platinum wires are spot-welded to each mesh to serve as current and voltage probes. The proper
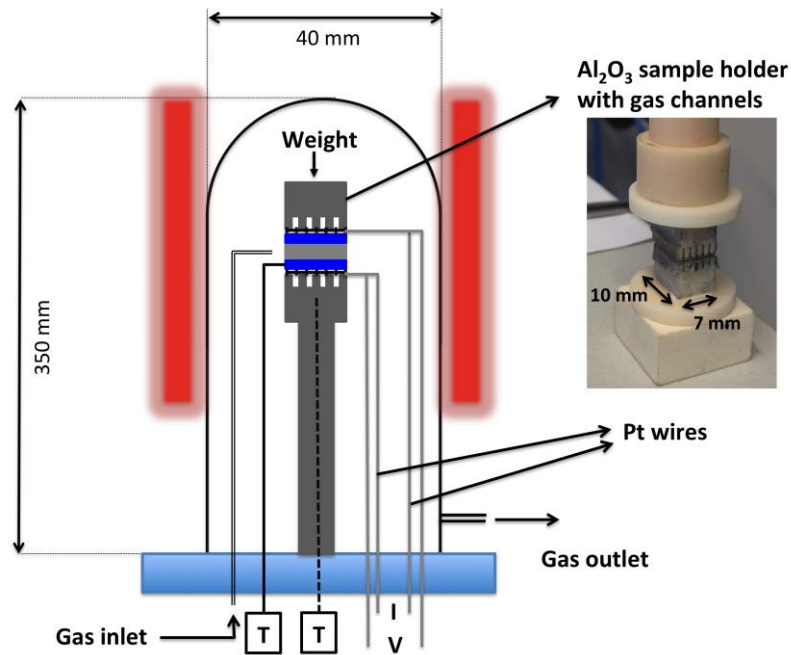
Figure 3-5: The schematic view of the sample holder for high temperature impedance measurements of symmetrical anode samples (not to the scale).

contacts between the sample and Pt meshes are achieved using an alumina piece with an approximate weight of 100 g.

Since low partial pressure of oxygen is crucial for the anode impedance measurements, a gas tight sample holder is built using the same principle of sample fixing. The schematic view of the sample holder is given in Figure 3-5, which consists of an alumina tube (OD=40 mm, length=350 mm, with one closed end, Friatec Degussit AL23), an alumina sample holder with Pt gauze probes, a tube furnace, and a KF flange with the electrical, gas and thermocouple feeds. The platinum wires and electrical feeds within the KF flange are shielded carefully. The gas inlet line is fed through the flange and located close to the sample to ensure homogeneous gas distribution around the sample. In addition to the thermocouple of the tube furnace, two thermocouples are positioned very close to the sample to ensure precise measurement of the sample temperature. The partial pressures of oxygen and hydrogen gasses within the sample holders are adjusted by diluting the oxygen and ARCAL 15 (5 $\pm$ 0.5 vol.% H_2 in Ar) gasses with nitrogen and argon, respectively, using mass flow controllers. A water bubbler is used to humidify the gas mixtures at room temperature for the anode measurements.

The sample measurement geometry is schematically represented in Figure 3-6. The typical thickness is below 1 μm for the thin electrodes, while the thickness of the current collector layer
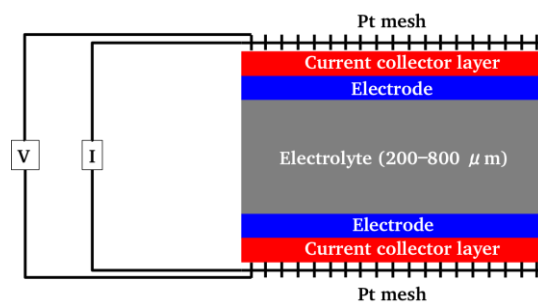

Figure 3-6: Schematic view of the symmetrical electrode samples (not to the scale).

varies depending on the electrode. A screen-printed LSM current collector layer with the thickness of 10–15 μm is used to measure the cathodes symmetrically, whereas an 80 nm thick platinum layer is sputtered symmetrically onto the anodes for the impedance measurements. The corresponding thickness values are confirmed by SEM images.

3.5.7. Fuel Cell Testing

Micro-SOFC testing

The micro-SOFC tests are conducted at ETH Zürich. The schematic view and the photograph of the measurement setup are given in Figure 3-7a and c, which consists of two parallel quartz glass tube assemblies for the gas delivery. The Si chips with micro-SOFC arrays are positioned between the openings of the quartz tubes and sealed using a ceramic fiber paper (Fiberfrax, Unifrax, UK). For the fuel cell testing, the freestanding micro-SOFC membranes are contacted using flat-pressed Pt wires (80 μm diameter), with the bent wire tip being covered with Pt paste. The Pt-electrode contacts are confirmed by the optical microscopy images. The micro-SOFC membranes are electrochemically tested with a Zahner IM6 workstation between 300 °C and 550 °C with air (1 bar, 268 sccm) as the oxidant and 3 vol. % humidified H_2 (1 bar, 54 sccm) diluted in N_2 (1 bar, 214 sccm) as fuel. Figure 3-7d shows a micro-SOFC array in the test-rig and the corresponding temperature-time profile of the fuel cell measurement. All samples are heated at 3 °C/min and
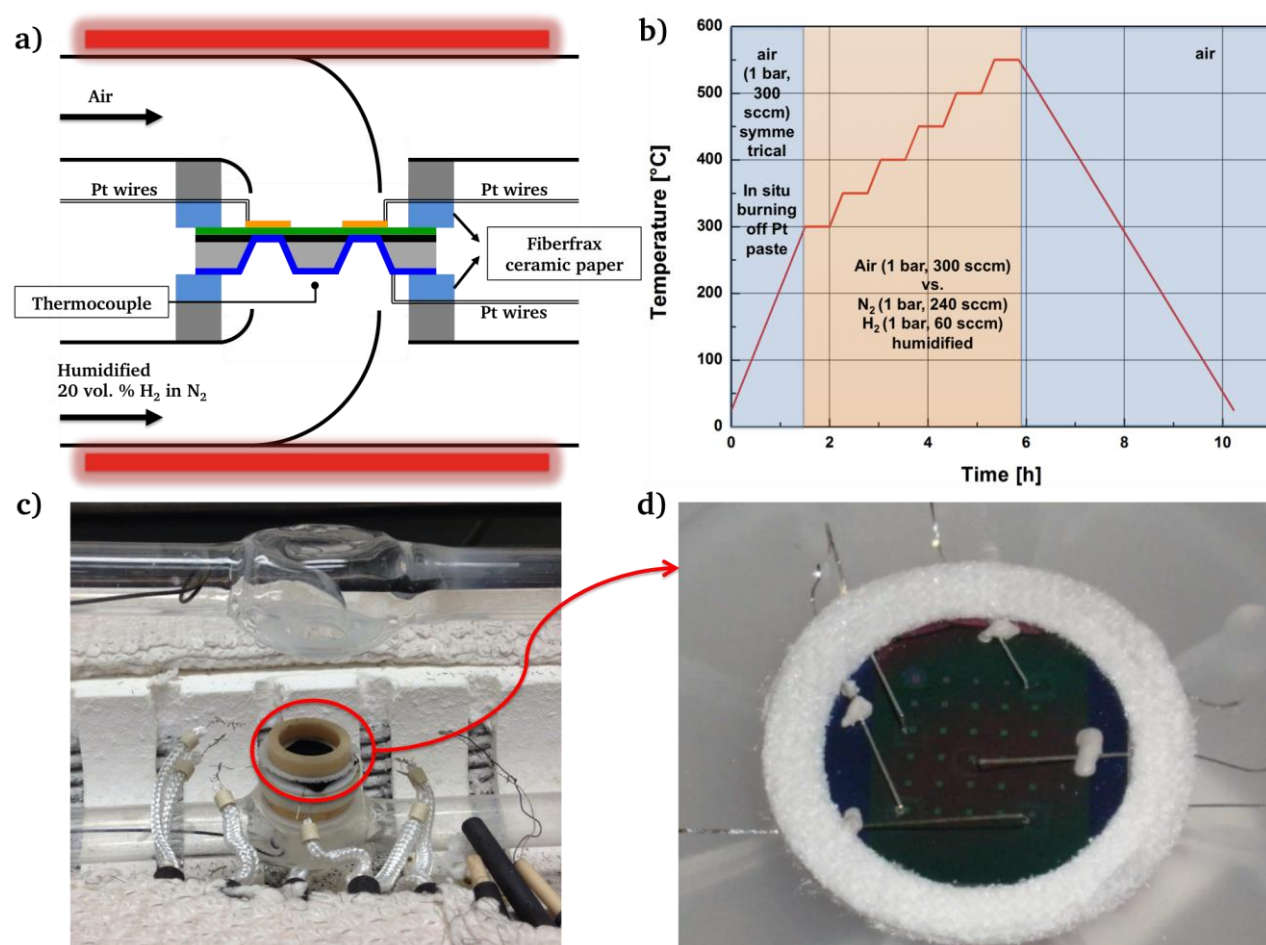

Figure 3-7: Schematic view (left) and photograpgh (right) of the setup used for fuel cell testing of micro-SOFC samples (not to the scale). A contacted micro-SOFC in the test-rig (left) and the temperature-time profile of the fuel cell testing (right).
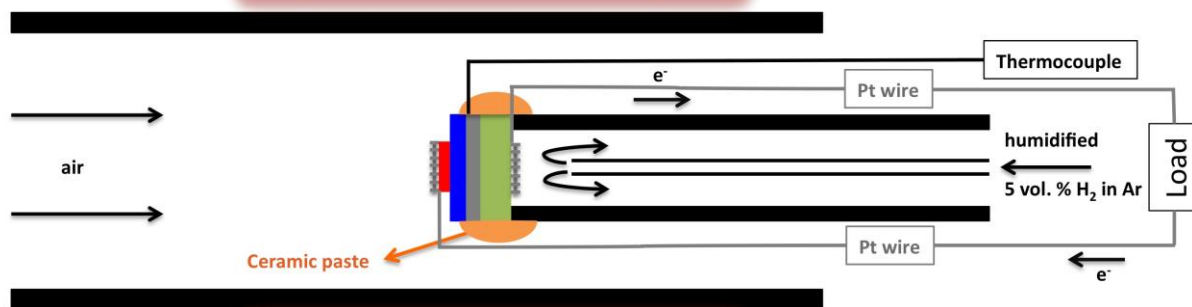
Figure 3-8: Schematic view of the setup used for fuel cell testing of anode-supported SOFC samples (not to the scale).

cooled at 2 °C/min.

Anode-supported SOFC testing

The schematic view of the measurement setup is given in Figure 3-8. Pt mesh (mesh 100)-Pt wire (100 μm diameter) assemblies are contacted to the anode and cathode layer using an Au paste (85–90 wt.% Au, ChemPur, Germany). The anode supported SOFCs are fixed to the one open end of an alumina tube (OD=10 mm, ID=8 mm, Friatec Degussit AL23) using a high temperature ceramic paste (Cerambond 522, Aremco Products Inc., USA). The ceramic paste and a gas tight Swagelok connection with a gas inlet and a gas outlet located on the other side of the alumina tube accomplish the sealing of the anode side. A thermocouple is positioned adjacent to the sample to record the sample temperature. The test-rig is placed horizontally into a tube furnace and air is supplied towards the cathode side of the sample using an alumina tube with a larger diameter. The necessary temperature profile to cure the ceramic paste (93 °C for 2 h + 260 °C for 2 h) is performed in-situ within the fuel cell testing during the heating-up step up to 700 °C supplying air flow of 250 sccm for both sides of the sample. After a dwell time of 1 hour at 700 °C under air (the organic component of the Au paste is burnt off and proper electrical contacts between electrode layers and Pt meshes are achieved), the anode side is exposed to a reducing atmosphere (5 vol.% H_2 in Ar) for 1 hour to realize the complete reduction of NiO to Ni. All samples are heated at 2 °C/min and cooled at 3 °C/min. Electrochemical characterization is conducted using a Solartron
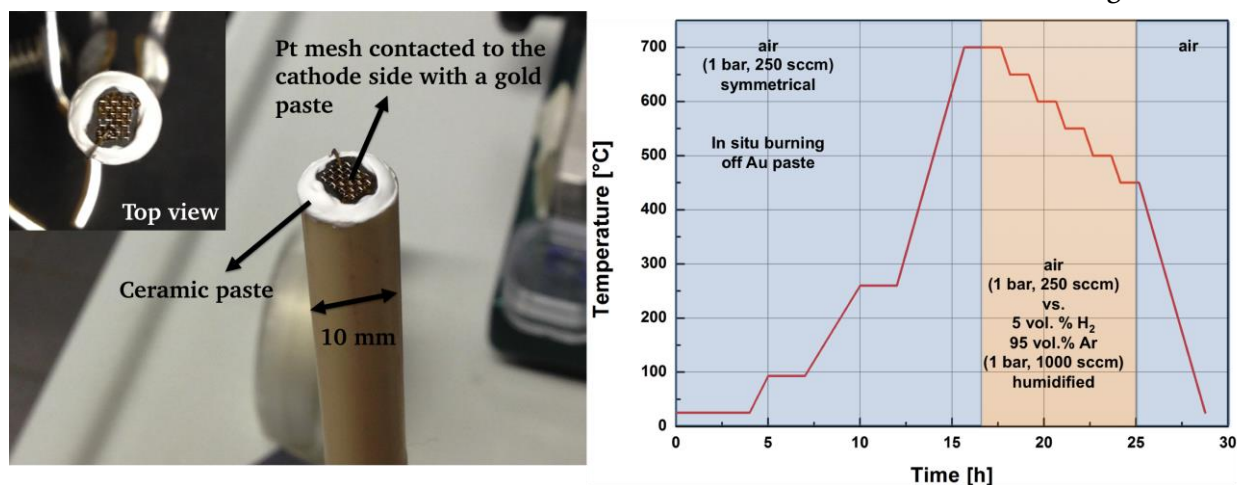
Figure 3-9: A contacted anode-supported SOFC sample fixed to an alumina tube using a high temperature ceramic paste and the time-temperature program of the fuel cell testing with in-situ curing of the ceramic paste.

1260 Impedance gain/phase analyzer coupled to a Solartron 1287 electrochemical interface between 650 °C and 450 °C with air (1 bar, 250 sccm) as the oxidant and humidified 5 vol.% H_2 in Ar (1 bar, 1000 sccm) as fuel. Figure 3-9 shows an anode-supported SOFC sample fixed to the sample holder (before the measurement) and the corresponding temperature-time profile of the fuel cell measurement.

4. Nanostructured Electrode Materials

The electrochemical performance of SOFCs strongly depends on the characteristics of their electrode layers such as microstructural features and material choice. To improve the performance of SOFCs, nanostructured electrodes have been considered, as their high surface area to volume ratio creates a large number of active sites for the electrochemical processes. Furthermore, the performance can be improved by engineering novel electrode materials with enhanced catalytic activities, which is typically accomplished by tailoring the properties of potential electrode materials. The desired material properties of electrode materials such as conductivity, phase stability, and thermal expansion behavior are obtained by precise elemental doping. Therefore, novel processes are needed for the synthesis of nanostructured electrode materials with the control of morphology, particle size, chemical composition, and phase purity and distribution.

Nanostructured electrode materials for SOFCs can be obtained by a large variety of bottom-up methods based on liquid-, aerosol- or vapor-phase processes [33], [54], [196]. Wet chemical routes such as precipitation and sol-gel synthesis methods have been extensively used to obtain various metal oxide nanoparticles. Even though powders with small grain sizes can be produced, the formation of hard agglomerates is mostly unavoidable [197], which leads to a substantial reduction of the active surface area. Nevertheless, it is possible to obtain nanoparticles with low degree of agglomeration by using steric stabilization agents [198] but the additional annealing steps required to burn off the organic surfactants and to promote the crystallization might lead to grain growth and alter the morphology of the particles. Among the vapor-phase synthesis processes, flame spray pyrolysis and chemical vapor synthesis are the most widely used ones to manufacture commercial quantities of nanoparticles. However, it is not trivial to control the morphology and size of the particles in the case of flame spray pyrolysis [199]. Powders synthesized by chemical vapor synthesis consist of typically non-agglomerated nanoparticles with narrow size distributions [200], yet it is challenging to control the stoichiometry of multi-component metal oxide nanoparticles due to the individual evaporation behavior of the metal-organic precursors. In comparison to the previously mentioned synthesis techniques, aerosol-based synthesis methods such as spray pyrolysis can be a more versatile and economically alternative to synthesize nanostructured materials [201]. The control of particle size and morphology can be accomplished by adjusting the process parameters such as atomization technique, time-temperature history, and precursor chemistry. Furthermore, the stoichiometric retention on the droplet scale is particularly advantageous for the synthesis of multi-component metal oxide nanoparticles in terms of homogeneous chemical composition and phase distribution.

Within this chapter, the state of art electrode materials $La_{0.6}Sr_{0.4}CoO_{3-\delta}$ (LSC) and NiO-$Ce_{0.8}Gd_{0.2}O_{2-\delta}$ (NiO-GDC20) are synthesized by ultrasonic spray pyrolysis (USP) and salt-assisted spray pyrolysis (SASP) methods and are characterized in terms of morphology, chemical composition and crystal structure. The results of the prospective anode material systems of
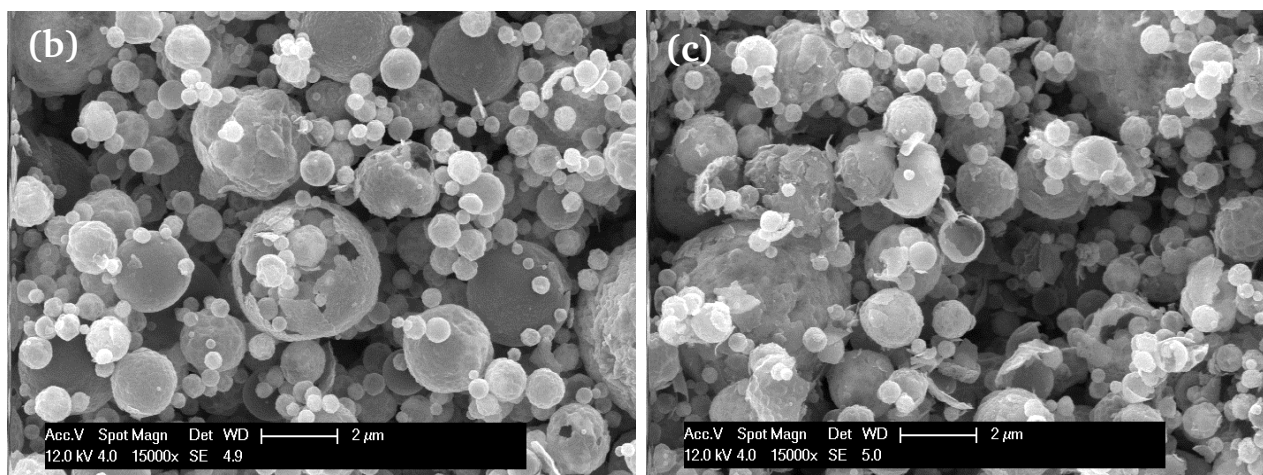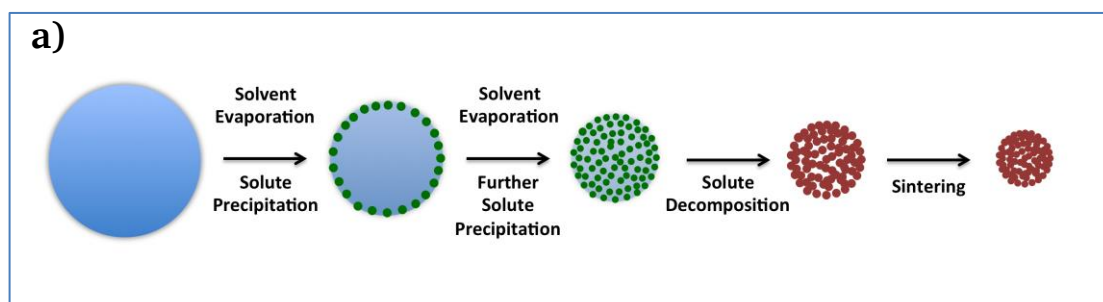
Figure 4-1: a) Illustration of the particle formation in an ultrasonic spray pyrolysis process. SEM images of b) LSC and c) NiO-GDC20 powders synthesized at 775 °C.

$La_{0.5}Sr_{0.5}Mn_{0.5}Co_{0.5}O_{3-\delta}$ (LSMCo) and $La_{0.9}Sr_{0.1}Mn_{0.5}Cr_{0.5}O_{3-\delta}$ (LSMCr) are not reported due to their poor electrochemical performance.

4.1. Morphology

In USP method, a precursor solution is atomized into droplets by a piezoelectric transducer and continuously carried into a hot reaction zone. The precursor droplets undergo a series of stages within the pyrolysis zone, *i.e.*, solvent evaporation, solute precipitation, decomposition, and sintering (Figure 4-1a). The final particle size of the product essentially depends on the generated precursor droplet size, since the concept of the synthesis method relies on the fact that one droplet forms one product particle [201]. The SEM images of the as-synthesized powders of LSC and NiO-GDC20 show the typical hollow sphere morphology of ultrasonic spray pyrolysis (Figure 4-1b–c). Such shell-like particle morphology is observed when the precursor concentrations are relatively low. The evaporation of the solvent from the droplet surface occurs at a rate faster than the diffusion of the solute, which leads to an increase of the solute concentration near the surface of the droplets. Above the critical super-saturation concentration, the solute starts to precipitate and decompose on the surface of the droplets, thereby resulting in a shell-like particle formation [202]. The SEM images in Figure 4-1b and c indicate that most of the particles retain their hollow sphere morphology and only a small fraction of the particles have broken shells. The conservation of the shell-like particle morphology can be explained by the high solvent permeability of the precipitate shells. If the precipitate shells are sufficiently permeable, they can be preserved as hollow spheres during the evaporation of the solvent from the droplet [201]. In addition, it is observed that the particle sizes are broadly distributed over a range of 0.1–3.0 μm. The broad particle size distribution of spray pyrolyzed powders is often associated with the high density of droplets in the
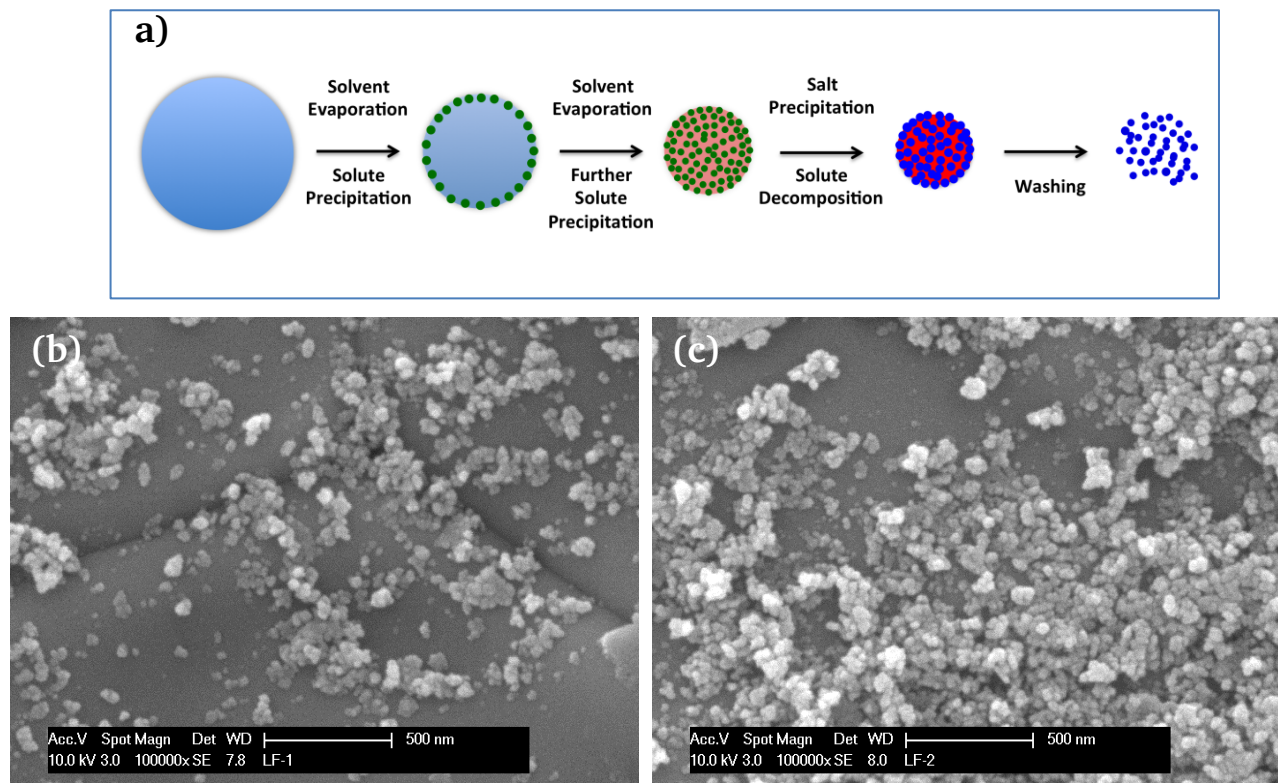
Figure 4-2: a) Illustration of particle formation in a salt-assisted spray pyrolysis process. SEM images of b) LSC and c) NiO-GDC20 powders synthesized at 775 °C (after water rinsing).

aerosol phase as the droplet collisions and subsequent coalescence lead to the formation of larger secondary droplets within the pyrolysis zone. It is also noteworthy to mention that the hollow spheres are essentially nanoporous due to the porosity between precipitated solute nanocrystallites. However, they are virtually inseparable in most cases as they form strongly agglomerated and/or sintered three-dimensional networks [203].

It has been recently reported that the incorporation of non-volatile, bystander inorganic salts with the precursor solutions and subsequent water rinsing of ultrasonic spray pyrolyzed product lead to the fragmentation of the polycrystalline microspheres into much smaller nanoparticles [204]. This modified synthesis route is known as salt-assisted spray pyrolysis (SASP). Figure 4-2a illustrates the particle formation process of SASP. This novel technique depends on the distribution of salt on the surfaces of crystallites during the pyrolysis stage of the synthesis, which effectively inhibits the agglomeration and sintering of the primary particles emerged from the solute decomposition. The SEM images of salt-assisted spray pyrolyzed LSC and NiO-GDC20 powders (Figure 4-2b–c) show substantial difference in terms of morphology, particle size and distribution compared to the powders produced by conventional spray pyrolysis method (Figure 4-1b–c), while all the other synthesis parameters are kept unchanged. Instead of the hollow sphere morphology, both LSC and NiO-GDC20 powders consist of well-dispersed nanoparticles with a low degree of agglomeration and the particle sizes are distributed over a narrow range of 25–75 nm. For both material systems, the modification of precursor by NaCl leads to particle size reduction by a factor of 20–40. It is also observed that the powders have significantly sharpened particle size distributions compared to the USP derived powders. In contrast to the USP method, the size distribution of particles obtained by SASP is apparently independent of the size distribution of the precursor droplets, which can be explained by the effective separation of precipitated solute nanocrystallites within the droplets by the NaCl phase. Various morphological characteristics of

nanoparticles can be obtained by changing the process parameters within the SASP. Therefore, the effects of the salt concentration and the synthesis temperature on the morphology are studied using LSC nanoparticles as a model system.

4.1.1. Effect of NaCl Concentration on Morphology

The SEM images in the Figure 4-3 illustrate the morphological evolution of LSC powders synthesized at 775 °C as the concentration of NaCl is changed from 0 to 1 M. The synthesis pressure and the total cation concentration of La, Sr, and Co are kept constant at 900 mbar and 0.05 M, respectively, for each synthesis. SEM images of the powders obtained by SASP are taken subsequent to the water rinsing. The SEM image Figure 4-3a shows that the LSC powder synthesized without NaCl consists of spherical hollow particles with diameters in the range of 0.1–3 μm. On the other hand, when the precursor solution contains NaCl, it is observed that the particle sizes of LSC powders are reduced predominantly down to the nanometer scale. At relatively low concentrations of NaCl (0.25 M), the primary LSC nanoparticles with approximate particle size of 50 nm form agglomerated secondary particles in micrometer scale. This is most probably due to the insufficient amount of inert salt phase, which cannot hinder the agglomeration and sintering of the primary LSC nanoparticles, as it is evident from Figure 4-3b. The degree of agglomeration is reduced substantially, as the concentration of NaCl increases to 0.5 M. Nevertheless, flake-like agglomerates with sizes around 250 nm are observed in SEM images
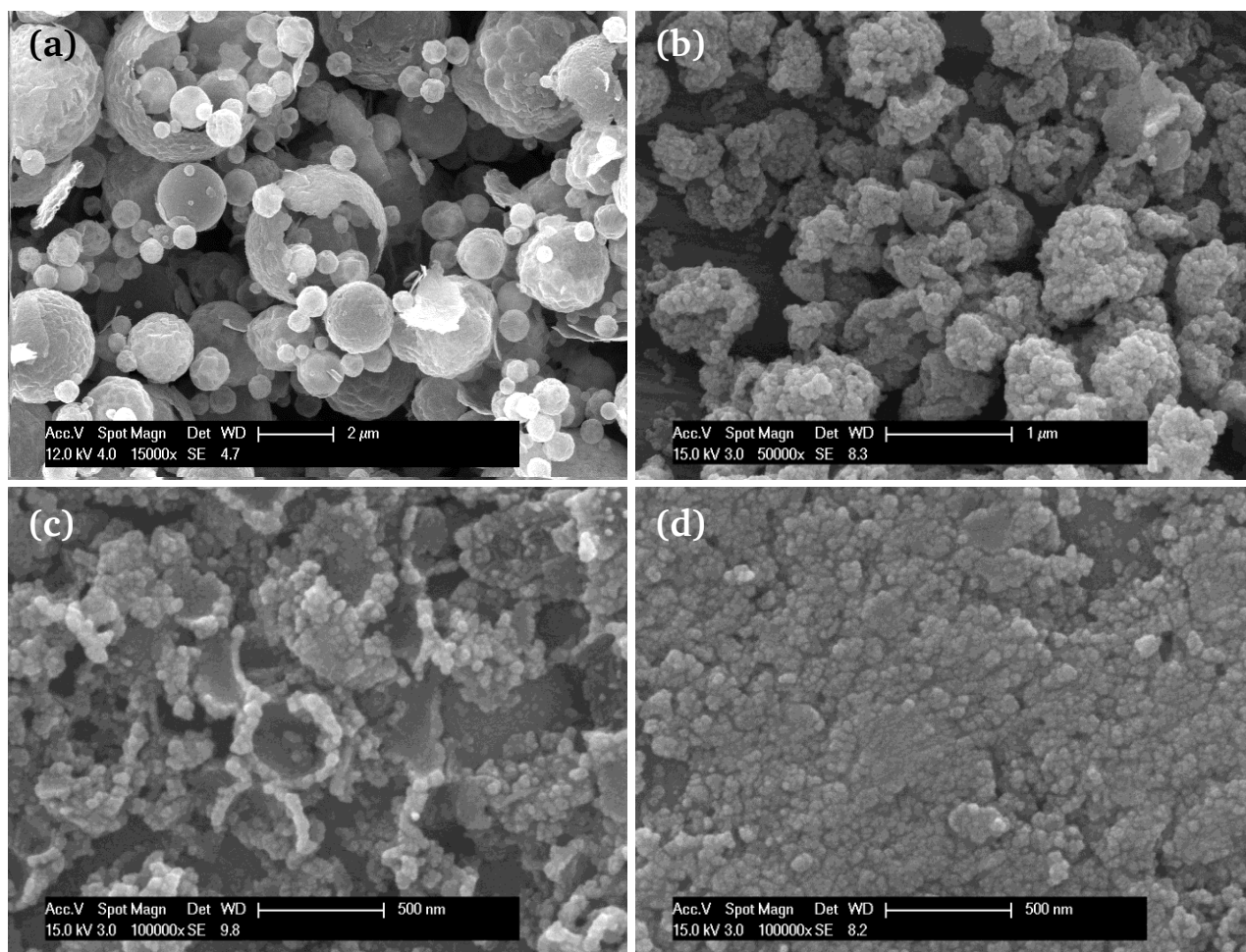

Figure 4-3: SEM images of LSC particles synthesized at 775 °C with various NaCl concentration of a) 0 M, b) 0.25 M, c) 0.5 M, d) 1.0 M. The SEM images of the particles in b, c, and d are taken after water rinsing.

(Figure 4-3c). At the salt concentration of 1.0 M, a complete fragmentation of the LSC powder is accomplished (Figure 4-3d) subsequent to the water rinsing of the as-synthesized product.

4.1.2. Effect of Synthesis Temperature on Morphology

To investigate the influence of the pyrolysis temperature on the morphology of the product, LSC nanoparticles are synthesized at different temperatures. The synthesis pressure and the total cation concentration of La, Sr, and Co are kept constant at 900 mbar and 0.05 M, respectively, for each synthesis. Figure 4-4 shows the SEM images of the powders synthesized at 700 °C, 775 °C, 900 °C, and 1000 °C with the NaCl concentration fixed to 1.0 M. As it is evident from the SEM images in Figure 4-4a and b, LSC nanoparticles with a low degree of agglomeration and an approximate primary particle size of 50 nm can be obtained at synthesis temperatures below 800 °C. However, a considerable amount of agglomerates in the size range of 0.2–1 µm are observed in the LSC powders synthesized at 900 °C (Figure 4-4c). As the synthesis temperature reaches to 1000 °C, the degree of agglomeration continues to increase. Moreover, it is observed that the primary particles of LSC sinter to form dense particles in the size range of 0.5–1 µm (Figure 4-4d), since crystal growth and molecular diffusion processes are fast at increased synthesis temperatures. Even though the primary LSC nanoparticles are surrounded by sufficient amount of NaCl, when the salt phase is melted (m.p. = 801 °C), it behaves as a molten solvent and eventually facilitates the sintering and densification processes of the primary particles. In this case, the LSC agglomerates
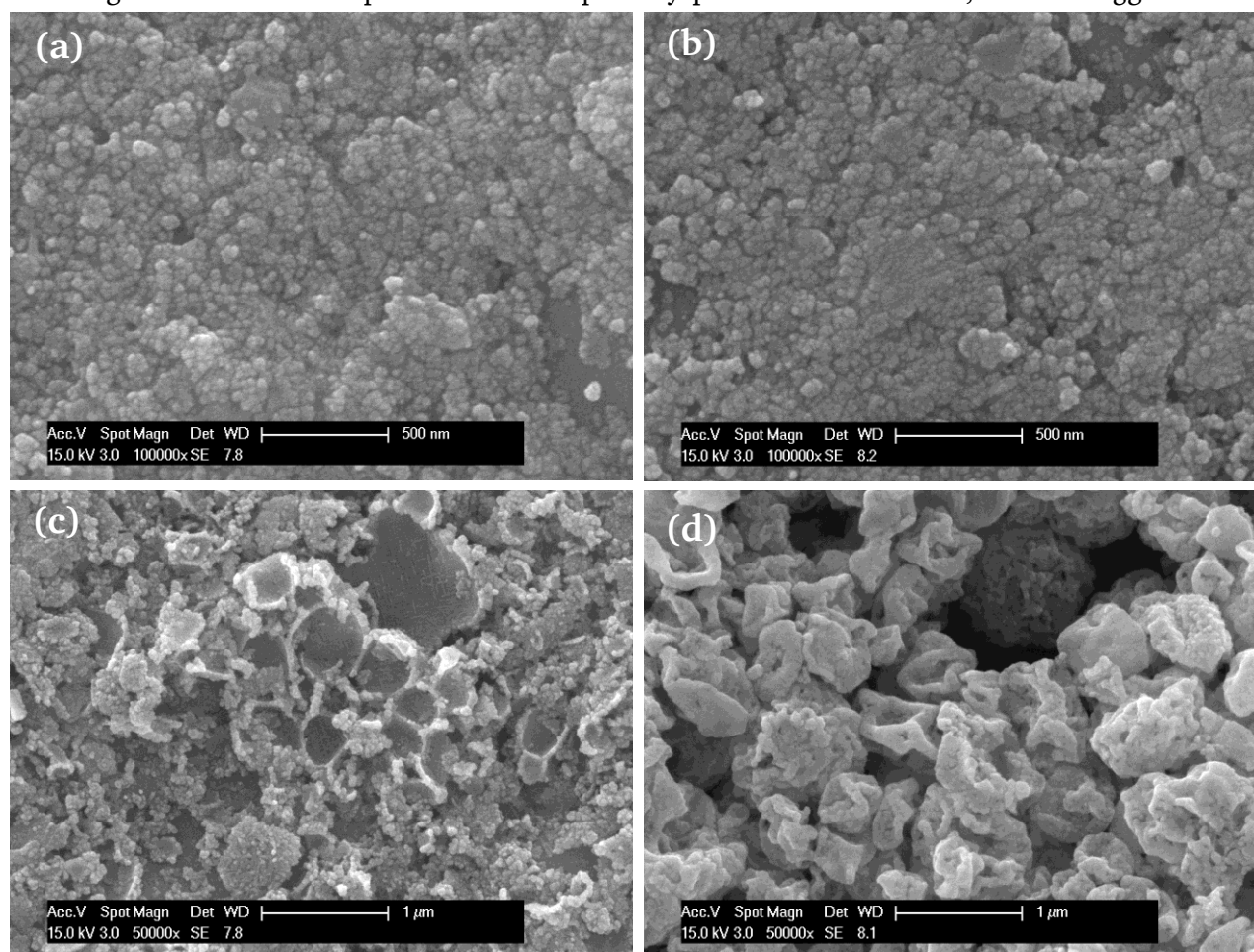

Figure 4-4: SEM images of LSC particles at different synthesis temperatures: a) 700 °C b) 775 °C, c) 900 °C, d) 1000 °C. The SEM images of the particles are taken after washing with water.

can be self-sintered without any obstacle. On the other hand, at synthesis temperatures below melting point of the NaCl the sintering of the LSC nanoparticles can be prevented because of the effective covering of the nanoparticle surfaces with the non-molten salt phase.

4.2. Specific Surface Area

The electrochemical reactions in electrodes take place at particular sites. For cermet anodes, *e.g.*, $Ni-Ce_{0.8}Gd_{0.2}O_{2-\delta}$ (Ni-GDC20), the oxidation of the fuel gas is localized near the triple-phase boundaries (TPBs), where metallic electron conductor catalyst (Ni), oxygen ion conductor electrolyte (GDC20) and fuel gas meet. Analogously, the oxygen reduction kinetics is governed by the oxygen exchange at the cathode/air interface for mixed-ionic electronic cathodes, *e.g.*, $La_{0.6}Sr_{0.4}CoO_{3-\delta}$. Therefore, a high surface area of the starting electrode materials would increase the number of active sites for the electrochemical reactions.

Table 4-1: Specific surface area measured by nitrogen adsorption method for LSC and NiO-GDC20 powders synthesized by ultrasonic spray pyrolysis and salt-assisted spray pyrolysis at 775 °C

Synthesis Method	Electrode	Specific Surface Area (m^2/g)
USP	LSC	39
SASP	LSC	60
USP	NiO-GDC20	39
SASP	NiO-GDC20	66

Table 4-1 presents the Brunauer-Emmett-Teller (BET) specific surface areas of USP- and SASP-derived LSC and NiO-GDC20 powders extracted from linear part of adsorption. It is observed that the salt-assisted synthesis of electrode materials leads to a substantial surface area enhancement of 50%.

4.3. Chemical Composition

In addition to the morphological properties; the purity, chemical composition and, homogeneity of the synthesized powders are crucial since small deviations in composition might lead to the
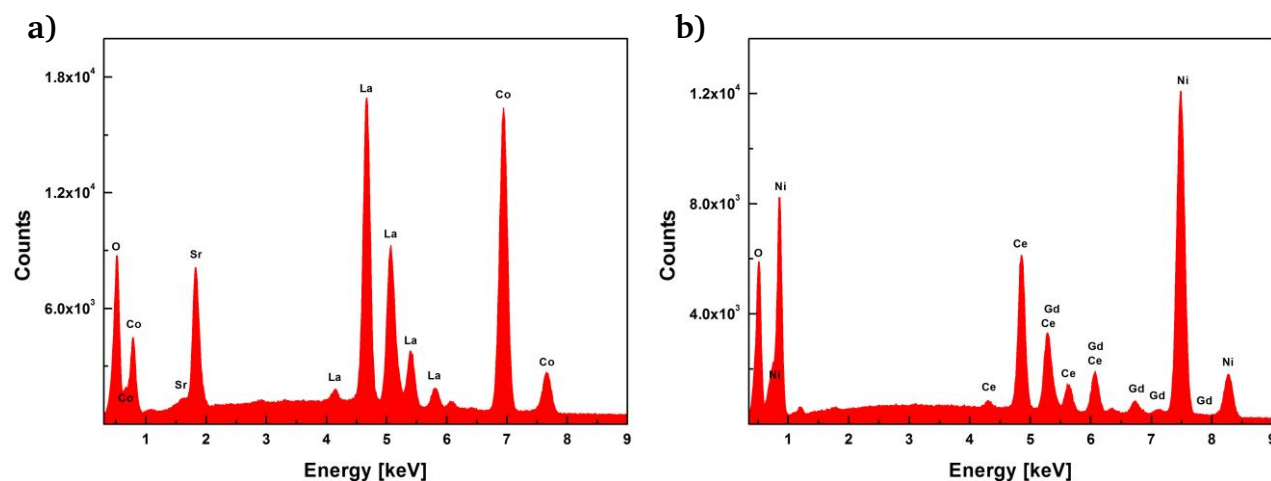

Figure 4-5: Energy dispersive X-ray spectra of (a) LSC and (b) NiO-GDC20 powders synthesized at 775 °C by SASP.

variation of material properties such as electronic and ionic conductivities, and catalytic activities. Therefore, the purity and chemical composition of the SASP-derived LSC and NiO-GDC20 powders are investigated using scanning electron microscopy coupled with energy dispersive X-ray spectrometer (SEM-EDS) subsequent to the NaCl removal by water rinsing. The corresponding representative EDS analyses are given in Figure 4-5. In both cases, neither a sodium peak nor a chloride peak is detected, which confirms the complete removal of the salt phase by water rinsing. Table 4-2 and 4-3 show that the calculated and the measured elemental compositions of LSC and NiO-GDC20 powders are in good agreement.

Table 4-2: Calculated and measured composition of LSC powder (after water rinsing) by EDS.

Calculated (mol.%)			Measured (mol.%)		
La	Sr	Co	La	Sr	Co
30.0	20.0	50.0	30.4	19.2	50.4

Table 4-3: Calculated and measured composition of NiO-GDC20 (60:40 wt.%) powder (after water rinsing) by EDS.

Calculated (mol.%)			Measured (mol.%)		
Ni	Ce	Gd	Ni	Ce	Gd
77.46	18.03	4.51	76.7	18.3	5.0

Figure 4-6 shows an STEM-EDS analysis conducted to identify the composition of the LSC nanoparticles on a submicrometer scale. The EDX spectrum (Figure 4-6b) acquired from the area indicated by the red box in Figure 4-6a reveals that the sample consists of the elements of La, Sr, Co, and O. The atomic ratio of La, Sr and Co calculated from this spectrum is consistent with the SEM-EDS measurements. The copper (Cu) signal observed in EDX spectrum in Figure 4-6b arises from the TEM grid. Furthermore, the elemental distribution of the LSC sample is characterized at nanometer scale by EDS displaying the integrated intensity of elemental signals as a function of beam position in the STEM mode. The STEM dark field image in Figure 4-7a and the corresponding elemental distributions of La, Sr, Co, and O (Figure 4-7b–e) show that the four elements are distributed homogeneously within the LSC nanograins.
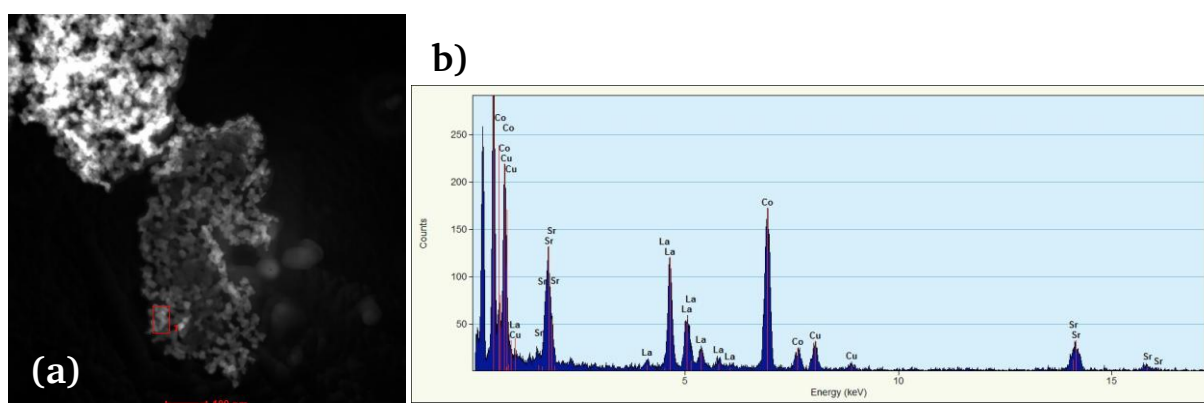

Figure 4-6: a) Dark field STEM image of LSC nanoparticles. b) EDX spectrum obtained from the area within the red frame indicated on the STEM image.
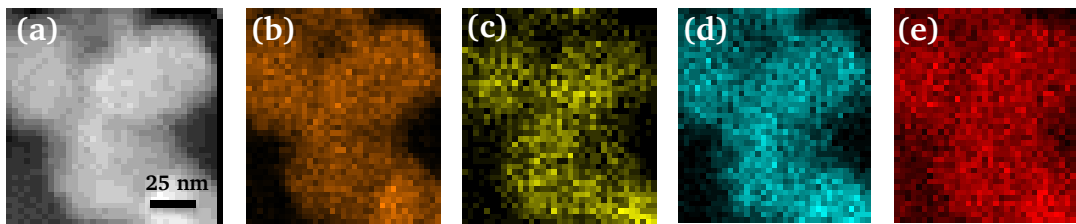
Figure 4-7: STEM image of the LSC sample (a) and high-resolution STEM-EDS elemental maps showing the distribution of (b) La, (c) Sr, (d) Co, and (e) O in nanoscale range.

4.4. Structure

4.4.1. Effect of Synthesis Temperature on the Crystal Structure of Nanoparticles

To investigate the influence of the synthesis temperature on the crystal structure of the nanoparticles, LSC and NiO-GDC20 powders are synthesized by SASP method at various temperatures, while the synthesis pressure, the total concentration of cations, and the NaCl concentration are kept constant at 900 mbar, 0.05 M, and 1.0 M, respectively. The X-ray diffraction (XRD) patterns of LSC powders synthesized at temperatures between 700 and 1000 °C are shown in Figure 4-8. At room temperature the samples exhibit rhombohedrally distorted perovskite structure with the space group $R\bar{3}c$ (no. 167). The lattice parameters obtained from the Rietveld refinement of the sample synthesized at 775 °C, $a = 5.4095(8)$Å and $\alpha_{int} = 60.31(4)°$, are in good agreement with literature data obtained for powders of the same elemental composition ($a = 5.4048$ Å and $\alpha_{int} = 60.33°$ [205]). According to Petrov *et. al.* [83], the change from cubic to rhombohedral structure at room temperature is caused by the La/Sr ratio being less smaller 1. The absence of NaCl reflections in XRD patterns confirms the complete removal of salt phase by the water rinsing procedure. Yet, a minor secondary phase of strontium carbonate ($SrCO_3$, ICSD #62) is observed in powders synthesized at 700 °C. The formation of $SrCO_3$ has been also reported for
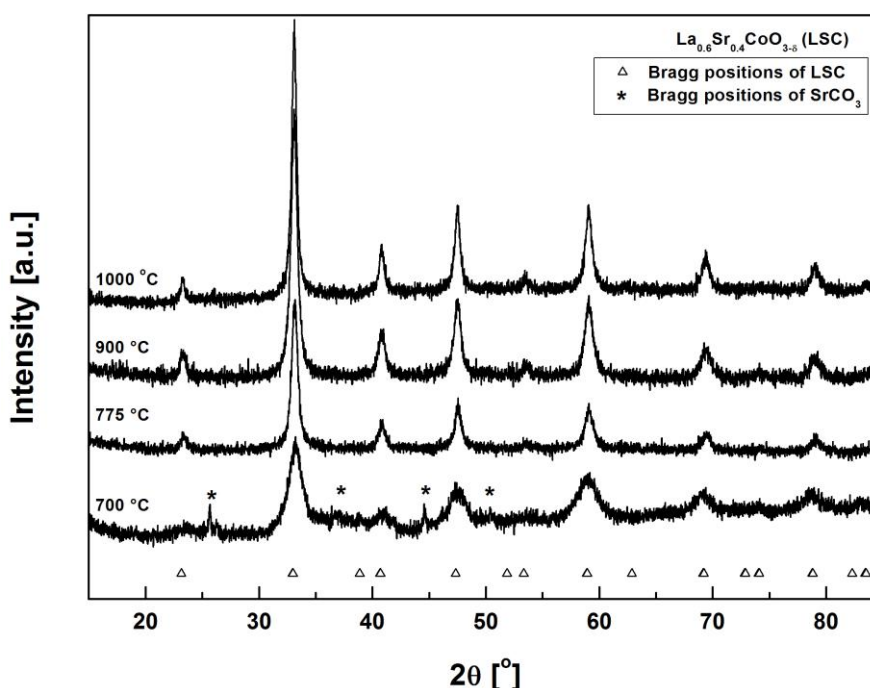

Figure 4-8: X-ray diffraction patterns of LSC samples synthesized at various pyrolysis temperatures between 700 °C and 1000 °C (after water rinsing).
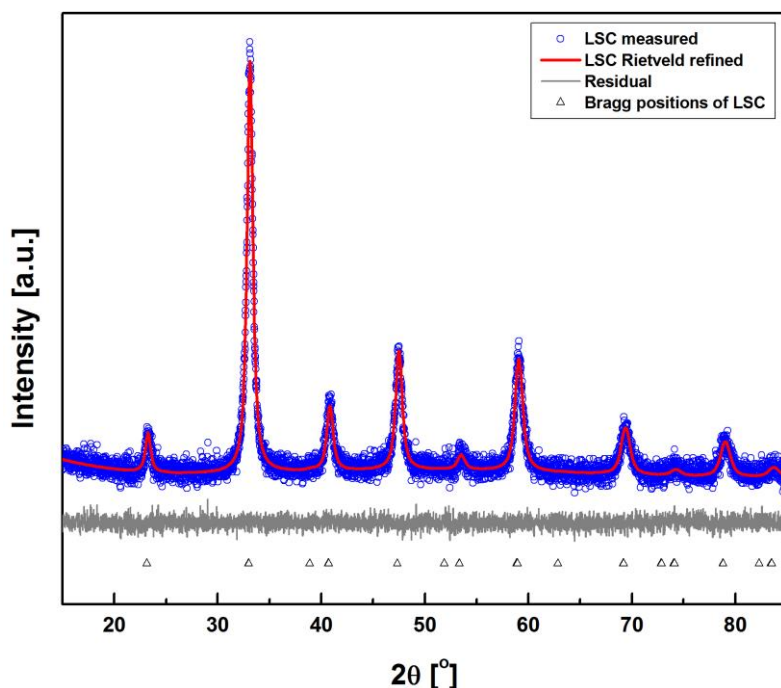
Figure 4-9: Rietveld refinement of LSC sample synthesized at 775 °C

the $La_{0.6}Sr_{0.4}Co_{0.2}Fe_{0.8}O_{3-\delta}$ cathodes obtained by USP method, where the precursor chemistry is modified by an organic complexing agent to obtain nanoparticles with high surface areas. Even though the precursor solution and reaction gas are carbon free in SASP method, the formation of $SrCO_3$ can be explained by the dissolution of CO_2 within the precursor solution or the intrusion of CO_2 into the reaction zone through a gas leak during the synthesis. As the synthesis temperature is increased to 775 °C and above, the formation of the secondary $SrCO_3$ phase is avoided and single-phase LSC powder is obtained at all synthesis temperatures. The increase of the synthesis temperature also leads to narrowing of the XRD reflections indicating the formation of larger crystallites, which is confirmed by Rietveld analysis. Figure 4-9 shows the XRD pattern of the LSC powder synthesized at 775 °C and its representative Rietveld analysis. The calculated lattice parameters and crystallite sizes are summarized in Table 4-4. The results reveal an increasing growth pattern of crystallite size of LSC nanoparticles as the synthesis temperature increases, which is most likely caused by the faster grain growth processes at high synthesis temperatures. On the other hand, the lattice parameters are independent of the synthesis temperature.

Table 4-4: Crystallite size and lattice parameter of LSC powders synthesized at 700 °C, 775 °C, 900 °C, and 1000 °C calculated by Rietveld refinement.

Synthesis temperature (°C)	775	900	1000
Crystallite size (nm)	11(1)	12.0(9)	13.9(6)
Lattice parameter, a (Å)	5.4095(8)	5.4091(6)	5.410(4)
Interaxial angle, α_{int} (°)	60.31(4)	60.29(3)	60.30(3)
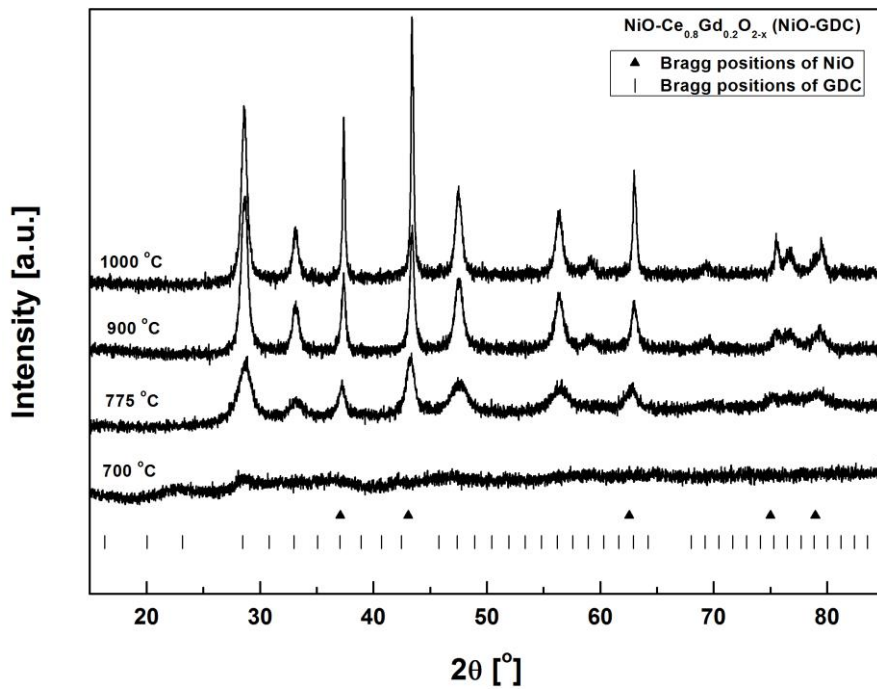
Figure 4-10: X-ray diffraction patterns of NiO-GDC20 samples synthesized at various pyrolysis temperatures between 700 °C and 1000 °C (after washing).

Figure 4-10 shows the XRD patterns of NiO-GDC20 (60:40 wt.%) composite powders synthesized at temperatures between 700 °C and 1000 °C. The synthesis at 700 °C results in a completely amorphous powder, since no reflections are detected in the XRD pattern. As the synthesis temperature is increased to 775 °C, the broad reflections belonging to NiO and GDC phases start to appear. Further increase of the synthesis temperature leads to narrowing of the XRD reflections indicating the formation of larger crystallites at higher synthesis temperatures. The crystalline
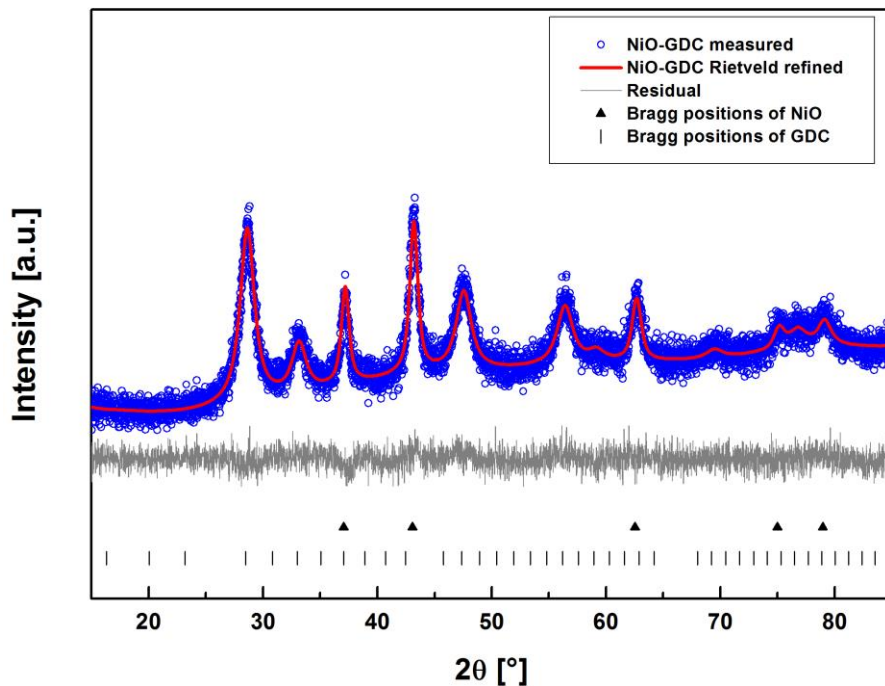
Figure 4-11: Rietveld refinement of NiO-GDC20 sample synthesized at 775 °C

powders consist of NiO and GDC phases with cubic rock salt and fluorite type structures (space groups of Fm$\bar{3}$m (no. 225)), respectively. The lattice parameters of NiO and GDC phases obtained from the Rietveld analyses are 0.4176(7) nm and 0.5423(8) nm, respectively, which are in good agreement with reported values (a_{GDC}=0.5426 nm [206] and a_{NiO}=0.41763 nm [207]). The absence of Gd$_2$O$_3$ reflections in XRD patterns and a relatively larger lattice parameter of GDC (a_{GDC}=0.5421(4) nm) compared to the undoped ceria (a_{CeO_2}=0.5413 nm [208]) confirms the complete dissolution of Gd in the ceria host lattice. Any impurity phase evidencing a reaction between NiO and GDC phases is not detected by XRD experiments at all synthesis temperatures. The effects of the synthesis temperature on the crystallite size, lattice parameter, and the phase composition of the samples are studied by the Rietveld analyses. Figure 4-11 shows measured XRD pattern of NiO-GDC20 composite powder synthesized at 775 °C and its representative Rietveld analysis. The obtained crystallite sizes, lattice parameters and phase compositions are summarized in Table 4-5. At all synthesis temperatures, the desired weight fraction between NiO and GDC20 phases (60:40 wt.%) is achieved. Similar to the synthesis of LSC nanoparticles, the formation of larger crystallites is observed in NiO-GDC20 composite powder, as the synthesis temperature is increased. The lattice parameters are found to be independent of the synthesis temperature.

Table 4-5: Crystallite sizes and lattice parameters of NiO and GDC phases, and their weight fraction within the NiO-GDC20 composite powders synthesized at 775 °C, 900 °C, and 1000 °C.

Synthesis temperature (°C)	775		900		1000	
Phase	NiO	GDC	NiO	GDC	NiO	GDC
Crystallite size (nm)	8(1)	4(1)	19(1)	7(1)	36.0(5)	10.2(4)
Lattice parameter, a (Å)	4.179(4)	5.423(5)	4.179(2)	5.421(2)	4.176(1)	5.423(2)
Weight (%)	58	42	61	39	59	41

4.4.2. Effect of NaCl on the Crystal Structure of Nanoparticles

To investigate the effect of NaCl on the crystal structure of the nanoparticles, LSC and NiO-GDC powders obtained from USP and SASP methods are compared. The pyrolysis temperature and pressure, and the total concentrations of the cations leading to the desired powders are set to 775 °C, 900 mbar, and 0.05 M, respectively, for each synthesis. The precursor solutions used in the USP method do not contain NaCl, while 1 M of NaCl concentration is chosen for the precursor solutions for SASP method.

The XRD patterns of NiO-GDC20 and LSC powders synthesized by USP and SASP methods (Figure 4-12) indicate that the desired phases are acquired independent of the synthesis method with high phase purities. NiO-GDC20 powders exhibit nanocrystalline nature consisting of NiO and GDC20 phases with cubic rock salt and fluorite type structures, respectively. In case of LSC, both synthesis methods result in the formation of single-phase nanocrystalline perovskite phase. The crystallite sizes, lattice parameters, and phase compositions (only for NiO-GDC20) of the NiO-GDC20 and LSC powders are calculated by the Rietveld analyses and summarized in Table 4-6 and Table 4-7, respectively.
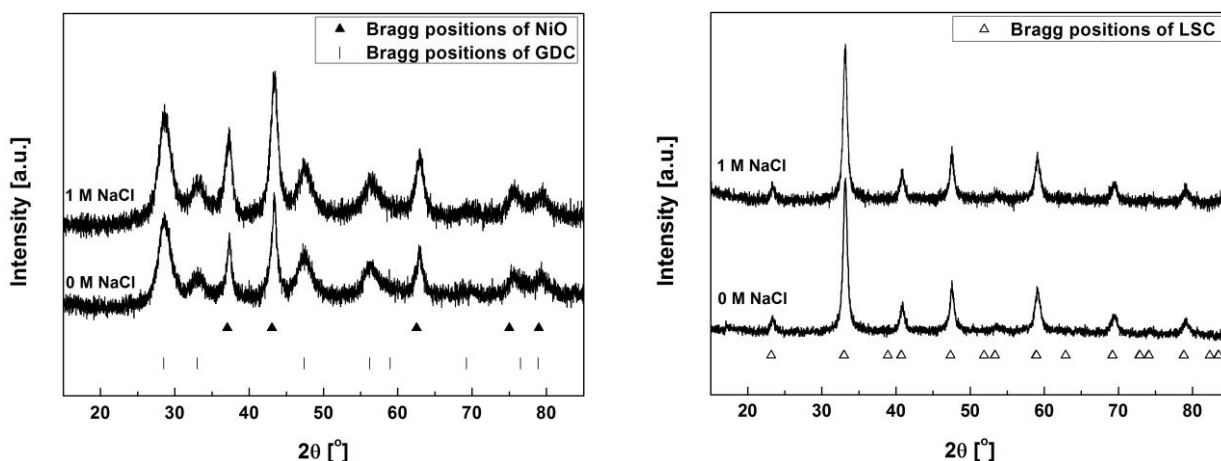
Figure 4-12: X-ray diffraction patterns of NiO-GDC20 and LSC samples synthesized at NaCl concentrations of 0 M and 1 M at 775 °C (after washing).

Table 4-6: Crystallite sizes and lattice parameters of NiO and GDC phases and their weight fraction within the composite powders synthesized at 775 °C using various NaCl concentrations calculated by Rietveld refinement.

NaCl concentration (M)	0		1	
Phase	NiO	GDC	NiO	GDC
Crystallite size (nm)	9(1)	5(1)	8(1)	4(1)
Lattice parameter, a (Å)	4.179(5)	5.420(5)	4.179(4)	5.423(5)
Weight (%)	59	41	58	42

Table 4-7: Crystallite sizes and lattice parameters of LSC powders synthesized at 775 °C using various NaCl concentrations calculated by Rietveld refinement.

NaCl Concentration (M)	0	1
Crystallite size (nm)	10(1)	11(1)
Lattice parameter, a (Å)	5.4089(7)	5.4095(8)
Interaxial angle, α_{int} (°)	60.29(5)	60.31(4)

Under the specified synthesis conditions, no distinct difference is observed in the crystallite sizes and lattice parameters of the powders derived by USP and SASP methods. However, in literature there are discrepancies about the effect of salt phase on the product crystallinity. The common observation states that the SASP method facilitates the crystallization process and eventually leads to powders with larger crystallite sizes than powders obtained from USP method. The different findings can be ascribed to the variation of the salt phase that is employed during the synthesis. Typically, the use of single or eutectic mixtures Na, K, and Li nitrates as an inert salt phase in SASP method leads to powders with larger crystallite sizes compared to USP derived powders. The reason lies in the fact that, such salts and their eutectic mixtures form a liquid-state media during the pyrolysis as their melting points are typically below 250 °C. This molten salt

phase can facilitate mass transport and ultimately lead to bigger crystallites. However, the use of inert salts such as NaCl with substantially higher melting temperatures and adjusting the pyrolysis temperatures below their melting points would not be expected to result in any enhancement of the crystallization processes.

4.5. Summary & Conclusions

The salt-assisted spray pyrolysis method allows for the synthesis of phase pure nanostructured electrode materials of $La_{0.6}Sr_{0.4}CoO_{3-\delta}$ and $NiO-Ce_{0.8}Gd_{0.2}O_{2-\delta}$. The morphology of the powders can be tailored in terms of particle size from the micro scale down the 50 nm by adjusting the synthesis parameters, *i.e.*, pyrolysis temperature and NaCl concentration of the precursor solution.

The modification of the ultrasonic spray pyrolysis method by the utilization of NaCl does not only result in nanoparticles with smaller particle sizes and narrower particle size distributions but also leads to a substantial increase in specific surface area by 50%, which is particularly crucial since high surface area of nanoparticulate electrodes would significantly increase the length of triple phase boundaries of cermet anodes and the number of active reaction sites of mixed ionic-electronic conductive cathodes.

The EDS analyses confirm the chemical composition and purity of the electrode materials both at micro (SEM) and nanoscale (STEM). It is verified that NaCl utilization does not lead to any contamination of the products, as neither Na nor Cl signal is detected in EDX spectroscopy analyses. In addition, STEM–EDX elemental mapping experiments indicate that a homogeneous elemental distribution at nanoscale is obtained.

The XRD analyses confirm the phase purity of the products and also the complete removal of NaCl phase from the synthesized material system by a water rinsing procedure.

Considering the morphological and structural characterizations, both LSC and NiO-GDC20 nanoparticles produced by SASP at 775 °C using 1 M of NaCl are chosen to fabricate the fuel cell components of LSC and NiO-GDC20 thin film electrodes, and NiO-GDC20 anode supports, as they possess higher specific surface areas and smaller particle sizes with lower degree of agglomeration compared to the powders obtained from USP method.

5. Thin Film Electrodes

Selected parts of this chapter have also been published in [209] *within the framework of this thesis. Corresponding sections – with minor conformations included – are indicated with a vertical gray bar at the inner page margin[1].*

Micro-solid oxide fuel cells (micro-SOFC) have drawn increasing attention as promising power sources for portable electronic devices with low power requirements (1–20 W) such as laptops, tablets, and smartphones [210]. To realize the utilization of micro-SOFCs in such electronic devices, the operating temperature has to be reduced to the range of 350–550 °C, at which thermal management of such small devices is possible [210], [211]. One of the major strategies to lower the operating temperature has been the use of thin film solid electrolytes with submicron thicknesses. Thus, Ohmic losses are minimized within the cell by reducing the length of the diffusion paths for oxygen ions. Micro-SOFC power densities as high as 1.3 W/cm^2 at 450 °C have been successfully demonstrated by utilization of an ultrathin (60 nm) electrolyte membrane [17]. So far, most of micro-SOFC membranes use platinum (Pt) thin film electrodes fabricated by physical vapor deposition methods, which have been shown to degrade both in air and in fuel atmospheres under fuel cell operating conditions. The degradation takes place by the coarsening of Pt grains within the porous electrode microstructure during operation leading to the formation of isolated metallic islands [212]–[214]. This results in the substantial reduction of number of triple-phase boundaries (TPBs) and in-plane conductivity of the electrode layers, and eventually poor cell performance. Therefore, it is of great interest to develop novel ceramic-based electrodes with high electrochemical activities at low temperatures and to integrate them into micro-SOFCs. As alternative for Pt electrodes, nanostructured $La_{0.6}Sr_{0.4}CoO_{3-\delta}$ (LSC) and $Ni-Ce_{0.8}Gd_{0.2}O_{2-\delta}$ (Ni-GDC20) thin film electrodes have been considered as cathode and anode, respectively, since they exhibit good thermal stability in the temperature range of 450–650 °C as well as high catalytic activity and electronic conductivity [79], [139].

Within this chapter, the stability of LSC and NiO-GDC20 nanoparticles obtained by salt-assisted spray pyrolysis (SASP), used for the thin film deposition by spin coating is investigated. Nanostructured electrodes of LSC and Ni-GDC20 with thicknesses in the range of 200–800 nm are realized on electrolyte substrates by spin coating of the stabilized dispersions of the SASP-nanoparticles. The electrochemical performance of the thin film electrodes is evaluated by electrochemical impedance spectroscopy (EIS) on symmetrical cells in the temperature range of 450–650 °C in order to demonstrate the applicability of the proposed electrode fabrication technique for the fabrication micro-SOFC devices.

5.1. Characterization of Dispersions

Zeta potential measurements are performed to evaluate the stabilities of the SASP-derived LSC and NiO-GDC20 nanoparticles, and the commercially available GDC20 nanoparticles. The LSC and NiO-GDC20 nanoparticles are used to fabricate thin film cathodes, while the commercially available GDC20 nanoparticles are employed to fabricate thin interlayers to prevent the potential chemical reactions between the LSC nanoparticles and the 8YSZ electrolyte substrates at elevated temperatures and also to fabricate LSC-GDC20 nanocomposite cathodes.

Figure 5-1 shows the zeta potential of the aqueous LSC and GDC20 dispersions as a function of pH. The zeta potential curves for both materials indicate that the nanoparticles have the highest degree of dispersion stability at pH values below 2 and above 10, but at low pH the nanoparticles are dissolving. Therefore, the dispersions of LSC and LSC-GDC20 nanoparticles are stabilized in aqueous NH_3 solutions at pH = 10. Particle size distribution measured at pH = 10 (Figure 5-1, inset) by dynamic light scattering shows the median particle diameter of 52±1 and 40±1 nm for LSC and GDC20 nanoparticles, respectively.

The zeta potential measurement of the SASP-derived NiO-GDC20 nanoparticles is presented in Figure 5-2. It is observed that zeta potential is positive over entire pH range. Positive zeta potential over entire pH range is already reported for some other materials such as diamond [215] and Al_2O_3 [216] nanoparticles. The highest surface charge for NiO-GDC20 nanoparticles is measured as 52 mV at pH=2.3. Therefore, the dispersions of NiO-GDC20 nanoparticles are stabilized in aqueous HNO_3 solutions at pH = 3. Lower pH values than 3 are avoided to prevent the nanoparticles from dissolving. The nanoparticle dispersions are stable below pH level of 5 over a long period (more than 24 hours). Above pH values of 5, particle agglomeration and sedimentation are observed (Figure 5-2, inset). Particle size distribution of the NiO-GDC20 nanoparticles measured at pH=2.3 (Figure 5-2, inset) by dynamic light scattering shows the medium particle diameter of 69±1 nm.
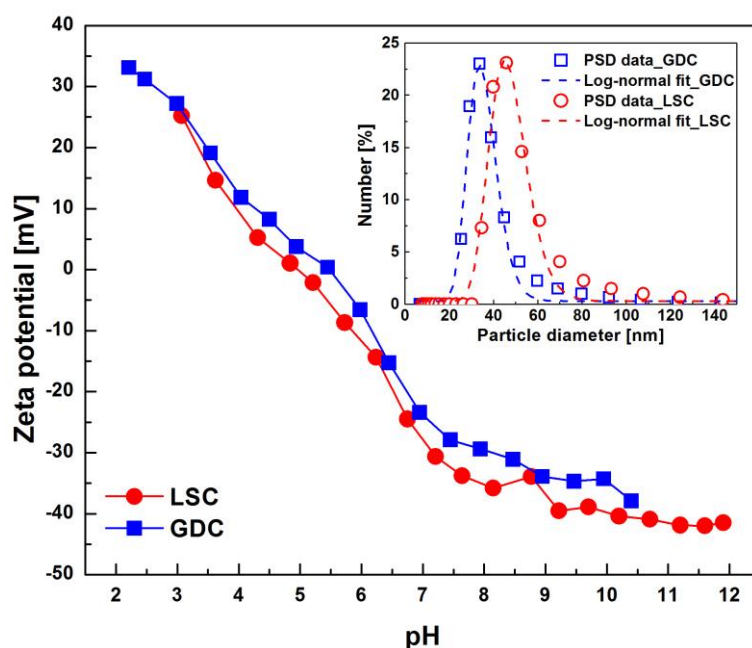

Figure 5-1: Zeta potential and particle size distribution (inset) of the SASP-derived LSC and the commercially available GDC20 nanoparticles.
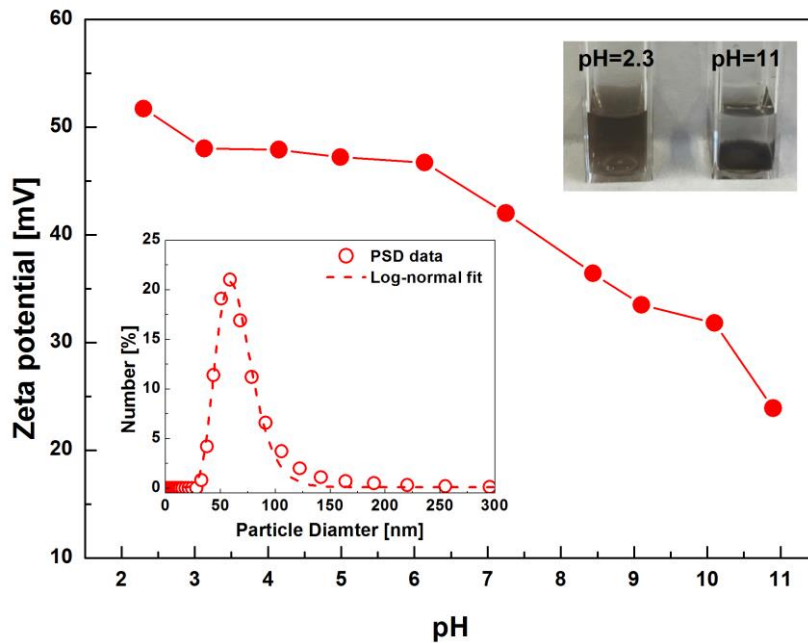
Figure 5-2: Zeta potential and particle size distribution (inset) of the SASP-derived NiO-GDC20 nanoparticles.

5.2. Fabrication of Thin Film Electrodes by Spin Coating

The SEM images in Figure 5-3a–e show the cross-sections of the spin-coated LSC (a–c) and Ni-GDC20 (d–e) electrode layers with thicknesses between 250 and 750 nm after 1 hour of annealing at 650 °C. The LSC cathodes are annealed under air, while NiO-GDC20 anodes are annealed under a reducing atmosphere (5 vol.% H_2 in Ar) to reduce NiO to Ni. The complete reduction of NiO within the anode layers is confirmed by XRD analyses (Figure 5-4). To avoid chemical reactions between LSC and 8YSZ, the LSC thin films are deposited either on 8YSZ substrates with thin GDC20 interlayers or directly on the GDC10 substrates, while the 8YSZ substrates are used for the deposition of Ni-GDC20 anodes due to the considerable electronic conductivity of CeO_2-based electrolytes under reducing atmospheres. This might have an effect on the EIS measurements conducted on the symmetrical anode samples under reducing atmospheres. The SEM images in Figure 5-3 reveal that the spin-coated LSC and Ni-GDC20 films are crack-free with a nanoparticulate microstructure. The electrode films are porous and a good contact between nanoparticles is established even after a short post-deposition annealing step at 650 °C. In addition, the films are homogeneous in thickness, continuous, and adhere well to the substrates.

The thickness of the electrode layers is controlled within the range of 200-800 nm by adjusting the solid loading of the dispersions, while the spin-coating parameters remain unchanged (for details, see Section 3.2.1). In Table 5-1, the effect of solid loading of the dispersion on the resulting film thickness is summarized.

Table 5-1: Solid loading of the nanoparticle suspensions and the resulting film thicknesses of spin-coated functional layers.

Solid loading (wt. %)	Film thickness (nm)
10	200–300
15	450–550
20	750–850
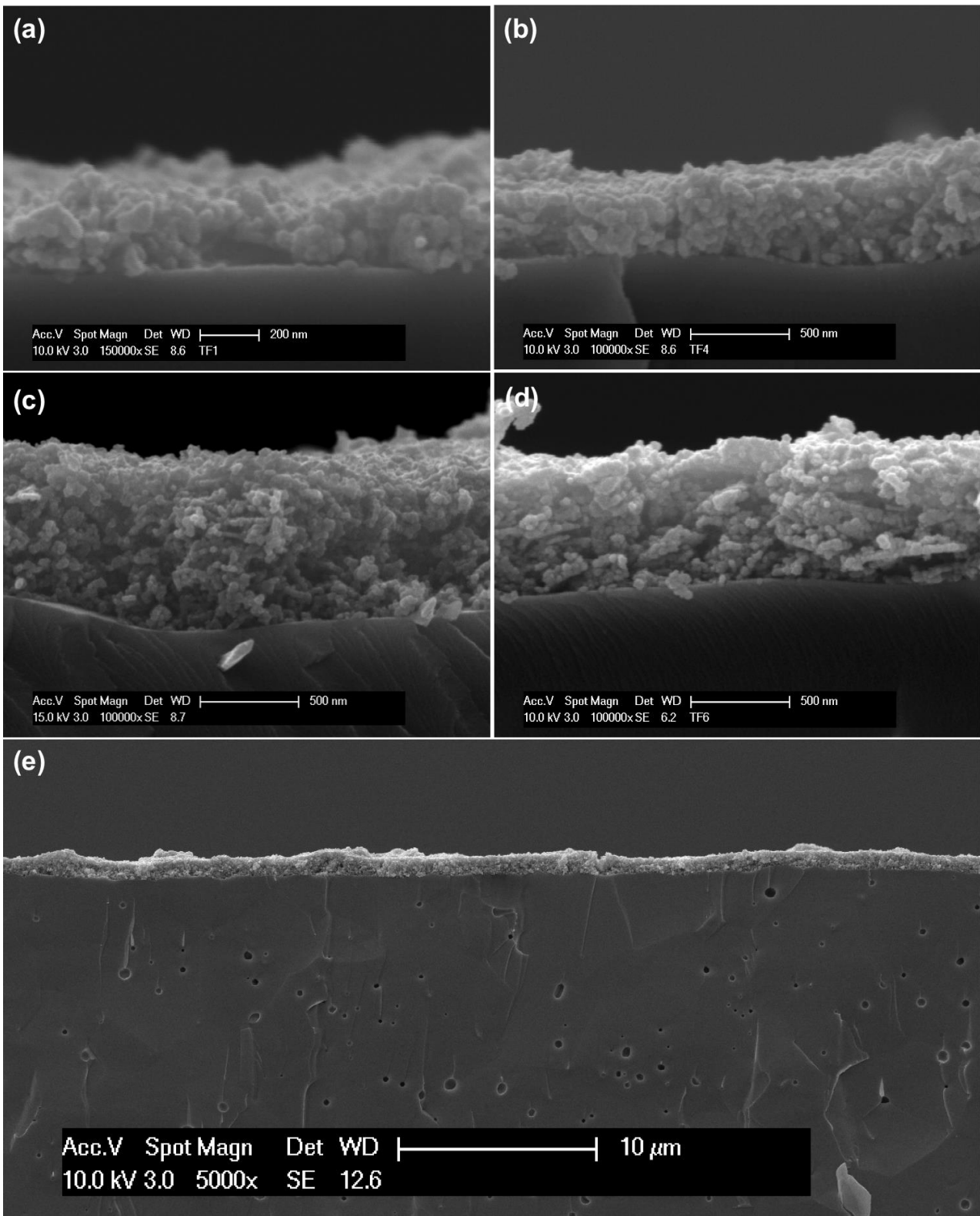
Figure 5-3: Cross-sectional SEM images of (a, b, c) LSC cathode functional layers on GDC10 substrates with approximate thicknesses of 250, 500, and 750 nm, respectively, and (d) Ni-GDC20 anode functional layer on 8YSZ substrate with an approximate thickness of 500 nm deposited on 8YSZ substrate, and (e) low magnification image of 500 nm thick Ni-GDC anode layer representing the continuity and homogeneity of the spin-coated thin film electrodes even after a reduction step at 650 °C for 1h.
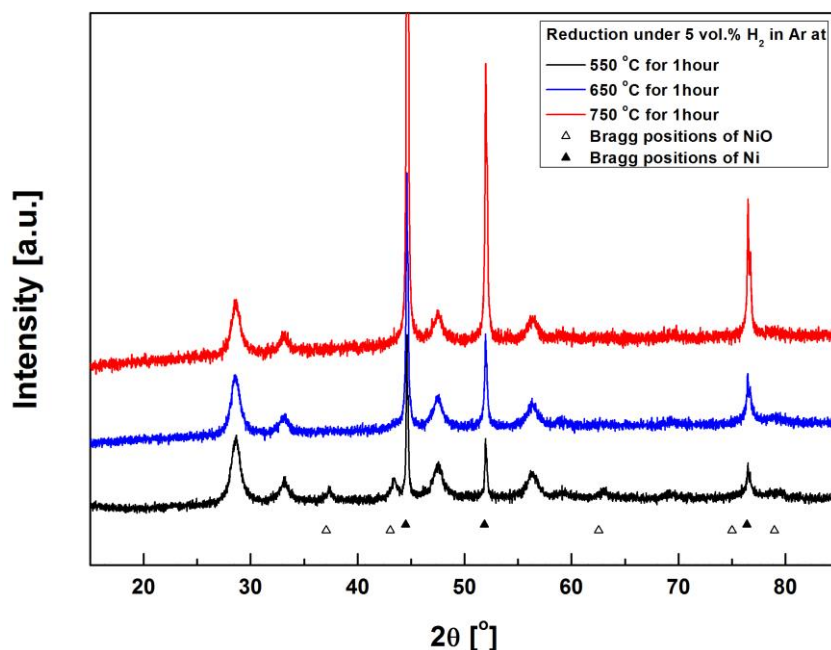
Figure 5-4: X-ray diffraction patterns of NiO-GDC20 nanoparticles after annealing at 550, 650, and 750 °C for 1 h.

5.3. Electrochemical Characterization of Thin Film Electrodes

In the SOFC community, the electrochemical performance of an electrode is typically expressed by its polarization resistance, which can be obtained by high temperature electrochemical impedance spectroscopy (EIS) experiments.

In this work, symmetrical cells are fabricated by spin coating stabilized dispersions of electrode nanoparticles and subsequently characterized by high temperature EIS. The area-specific electrode polarization resistance (ASR$_{pol}$) values extracted from the recorded impedance data represent the polarizations associated with the electrodes, *i.e.* the combination of the activation and the gas diffusion (mass transport) losses. The former is associated with the impedance against the electrochemical processes, while the latter is caused by the gas diffusion limitations of the electrode layers and the measurement setup.

5.3.1. LSC and LSC-GDC Cathodes

LSC Cathodes

The SEM images in Figure 5-5a and b show the cross-sections of the LSC cathodes with approximate thicknesses of 250 nm and 500 nm subsequent to annealing at 650 °C for 1 h. The LSC cathode layers are fabricated by spin coating of LSC dispersions on the GDC20|8YSZ|GDC20 electrolyte substrates symmetrically. It is evident that both functional LSC cathode layers and GDC20 interlayers are continuous and homogeneous in thickness, and that a proper contact at cathode/electrolyte interface is achieved even with a post-annealing temperature as low as 650 °C. The thickness of the GDC20 interlayers is found to be approximately in the range of 200–300 nm among different samples.

After spin coating of the thin LSC cathodes, the commercially available $(La_{0.8}Sr_{0.2})_{0.95}MnO_{3-\delta}$ (LSM) ink is screen printed symmetrically onto the samples to improve the current collection from the thin cathodes. The resulting layered structures of LSM|LSC|GDC20|8YSZ|GDC20|LSC|LSM are annealed in-situ during the high temperature EIS measurements at 650 °C for 1 h, after which
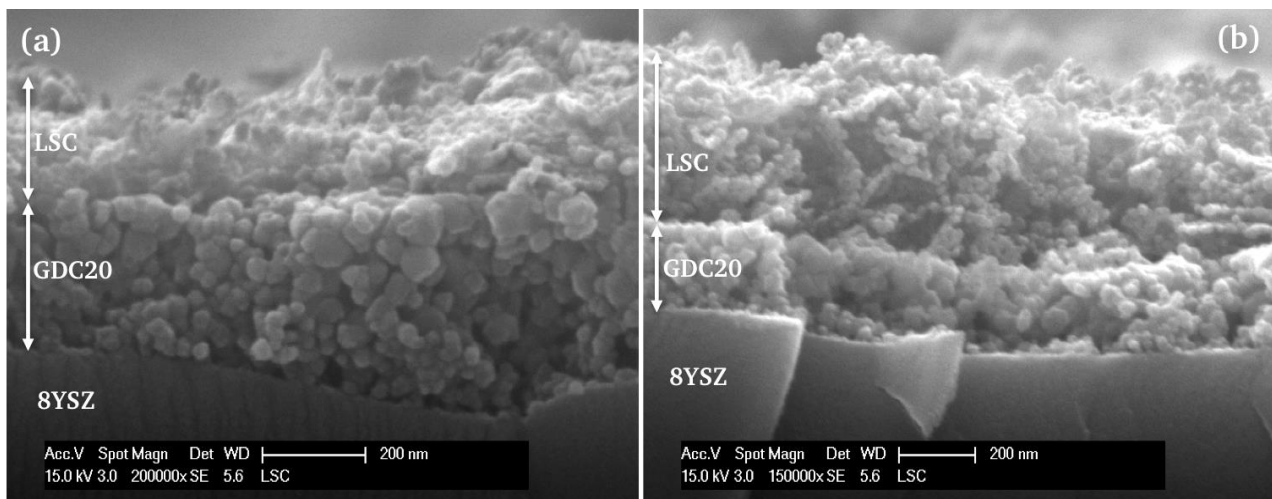
Figure 5-5: Cross-sectional SEM images of LSC cathode layers annealed at 650 °C for 1h with thicknesses of (a) 250 nm and (b) 500 nm deposited symmetrically on GDC|8YSZ|GDC electrolyte substrates.

the impedance spectra are recorded in the cooling cycle. The Figure 5-6a depicts the temperature profile used for the EIS analyses, in which each EIS measurement is indicated by an arrow. Figure 5-6b–d show the representative impedance spectra in the form of Nyquist plot obtained from the 250 nm thick LSC cathode at 650, 600, and 550 °C under a constant gas flow consisting of 21 vol.% O_2 and 79 vol.% N_2. The impedance spectra are normalized according to the surface areas of samples. It is observed that the impedance spectra consist of depressed semi-circles which are typical for the oxygen reduction at porous MIEC cathodes [36]. The high frequency impedance data do not intersect the real axes and the spectra cannot be resolved at frequencies higher than 1 MHz. Therefore, the impedance spectra are extrapolated towards the real axes to estimate the intersection point. The estimated high frequency intercept of the spectra, denoted as R_o, is typically caused by a series of resistance accounting for the Ohmic losses of the electrolyte and current collector layers, and the contact resistance of the experimental setup [91]. The estimated R_o values are found to be in the range of 6–7 Ω cm^2 at 600 °C for all symmetrical cells, which are mainly attributed to the Ohmic losses associated with the 200 μm thick 8YSZ electrolyte substrates. Based on this assumption, the calculated conductivities of 8YSZ electrolyte substrates are in the range of 0.29–0.33 S/m, which is in a good accordance with the reported conductivity value (0.316 S/m [33]) of bulk 8YSZ at 600 °C. Furthermore, the Ohmic polarization loss (ASR_{Ohmic}) of the 8YSZ substrates is measured under identical experimental conditions using a symmetrical cell consisting of 200 μm thick 8YSZ electrolyte and two Pt electrodes sputtered symmetrically on the 8YSZ electrolyte substrate, and comparable results are obtained in the same temperature range.

The total area specific polarization resistance (ASR_{pol}) of the cathode layers is obtained from the difference between the estimated high frequency and the observed low frequency intersections on the real axes of the Nyquist plots. The extracted polarization resistance values are divided by a factor of two accounting for the electrode layers on both sides of the electrolytes.

Figure 5-7 shows the temperature dependence of the ASR_{pol} of LSC cathodes with thicknesses of 250 and 500 nm. A good linearity between the ASR_{pol} of the cathode and the reciprocal temperature is obtained in the temperature range of 450–650 °C. The 250 nm thick LSC cathode shows an ASR_{pol} of 5.56 Ω cm^2 at 600 °C, while at the same temperature the 500 nm thick LSC cathode has an ASR_{pol} of 3.71 Ω cm^2. The activation energies of 1.42 $\pm$ 0.02 and 1.46 $\pm$ 0.05 eV are calculated for the LSC cathode layers with thicknesses of 250 and 500 nm, respectively, which are in a good agreement with the reported activation energies of LSC cathodes with the same chemical composition and comparable thicknesses. Hayd *et. al.* [79] have reported an activation energy of 1.41 eV for the 200 nm thick LSC cathodes obtained by metal organic deposition (MOD).
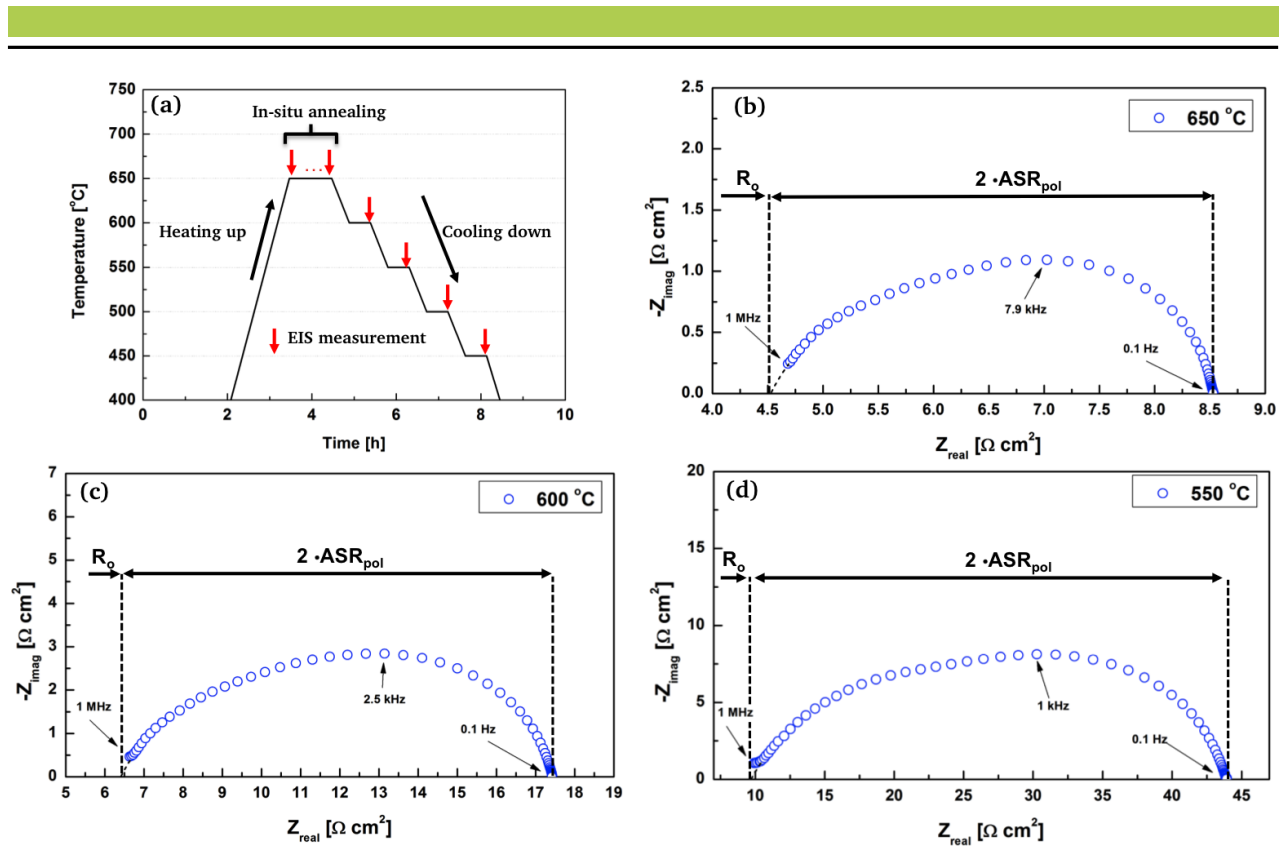
Figure 5-6: a) The temperature profile used for in-situ annealing of the as-deposited cathodes and for the EIS analyses, where each EIS measurement is indicated by an arrow. The impedance spectra are obtained from the LSM|LSC|GDC20|8YSZ|GDC20|LSC|LSM symmetrical cell with a 250 nm thick LSC cathode layer measured at (b) 650, (c) 600, and (d) 550 °C under a constant gas flow consisting of 21 vol.% O_2 and 79 vol.% N_2. The estimated Ohmic resistance of the cell is indicated by R_0, while ASR_{pol} stands for the estimated polarization resistance of the 250 nm thick LSC cathodes. The dashed lines in high frequency region of the spectra show the extrapolated part of the impedance spectra to estimate the high frequency intercepts.

An activation energy of 1.40 eV has been reported for the 200 nm thick pulsed layer deposited (PLD) LSC cathodes by Januschewsky *et. al.* [39].

The decrease of ASR_{pol} upon increasing the cathode thickness indicates that the oxygen exchange at the cathode/air interface is indeed one of the rate-determining steps of the oxygen reduction reaction [168]. This trend can be justified by the mixed ionic electronic conductivity of the LSC cathode, in which both surface and bulk pathways are active for oxygen reduction [36], [78]. The increase of the thickness of the nanostructured LSC cathode also leads to an increase of the number of the active reaction sites for the oxygen reduction and in turn an improvement of the cathode performance [217]. Noh *et. al.* have investigated the influence of the thickness of the pulsed layer deposited La$_{0.6}$Sr$_{0.4}$CoO$_{3-\delta}$ cathodes layers on their electrochemical performance and reported that the LSC cathodes with thicknesses in the range of 2–3 μm have optimum cell performance, while no further improvement has been observed above a thickness of 5 μm [217]. In conventional anode-supported SOFC design, the cathode thicknesses are typically in the range of 10–20 μm, while the total cell thickness has to be kept below 1 μm in order to maintain the thermomechanical stability of the freestanding micro-SOFC membranes [218]. Therefore, in this work the efforts to optimize the electrochemical performance of the spin-coated LSC cathodes do not focus on the increase of the cathode thicknesses above 500 nm.

The commercially available LSM paste is itself an electrocatalyst for oxygen reduction in addition to its current collection ability [153]. When used as a current collector on thin LSC cathodes, the LSM/LSC interface rather than the thin LSC cathodes might be electrochemically active. Therefore, an LSM|GDC20|8YSZ|GDC20|LSM cell without the spin-coated thin film LSC
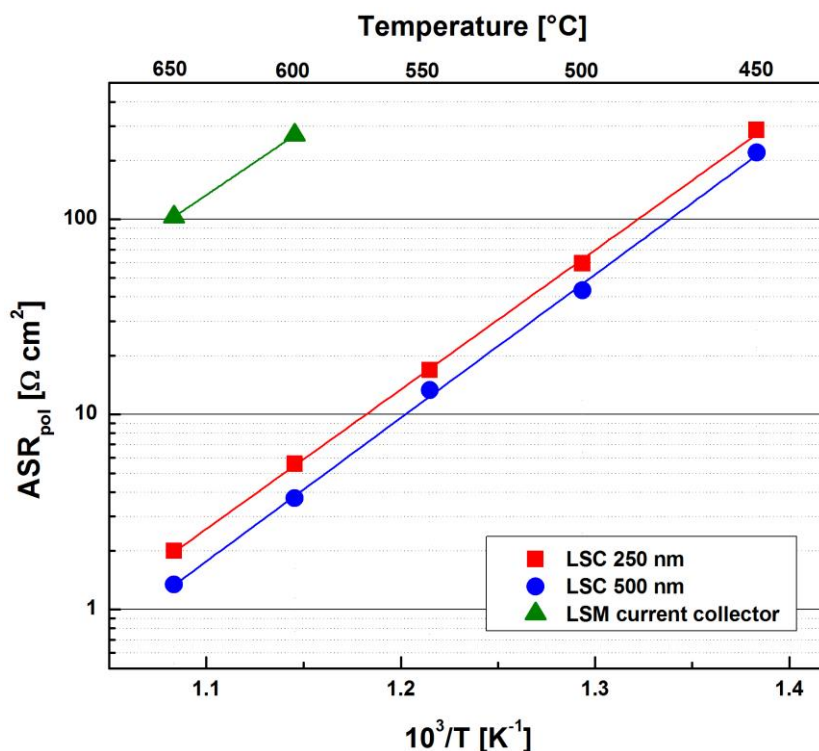
Figure 5-7: Area-specific polarization resistance (ASR$_{pol}$) of the thin film LSC cathodes with thicknesses 250 and 500 nm, and of screen-printed commercially available LSM current collector as a function of the reciprocal of the measurement temperature.

electrodes is prepared to compare the polarization resistance of the screen-printed LSM current collector layer to that of spin-coated thin LSC cathodes. The cell consisting of only LSM current collector as an active layer is measured at 650 °C and 600 °C (also included to the plot in Figure 5-7), and the polarization resistance of LSM/electrolyte interface is found to be approximately 270 Ω cm^2 at 600 °C, which verifies the correctness of the obtained polarization resistance values of the thin LSC cathodes.

LSC-GDC Composite Cathodes

One of the methods that has been commonly used to enhance the performance of the purely electronic conducting cathodes (*e.g.* Pt, LSM) is the percolation of an additional ionic conducting electrolyte phase within the cathode microstructure [34], [36], [153], [219]. The ionic conducting phase leads to the extension of the cathode/electrolyte interface over the entire cathode microstructure and eventually an increase of the number of active reaction sites (TPBs) for the oxygen reduction. Even though the oxygen reduction is not confined to the TPBs and the density of the active reactions sites are intrinsically higher in the MIEC (B)LSC(F)-based cathodes compared to purely electronic conducting cathodes [36], several authors have reported improvement of the electrochemical performance of MIEC cathodes upon compositing them with CeO$_2$-based electrolyte powders [153], [171], [220]–[222].

The similar approach is used as an alternative to the increase of the electrode thickness in order to improve the electrochemical performance of spin-coated LSC cathodes. The same commercially available GDC20 nanoparticles, which are used to deposit GDC20 interlayers between 8YSZ substrates and thin LSC cathodes, are utilized as the additional ionic conducting phase for the LSC-GDC20 nanocomposite cathodes. The results of zeta potential measurements previously presented (Figure 5-1) indicate that both LSC and GDC20 nanoparticles have relatively high dispersion stability in the pH range of 9–10.5. Therefore, for further thin film deposition steps
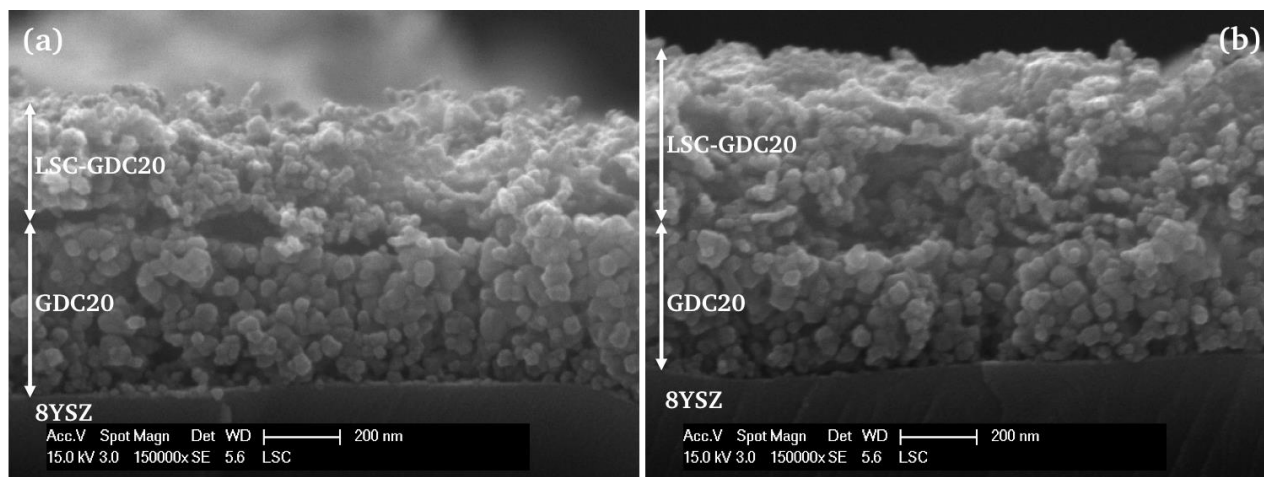
Figure 5-8: Cross-sectional SEM images of LSC-GDC20 (70:30 wt.%) cathode layers annealed at 650 °C for 1h with thicknesses of (a) 250 nm and (b) 500 nm deposited symmetrically on GDC20|8YSZ|GDC20 electrolyte substrates.

using spin coating, LSC-GDC20 nanocomposite dispersions are co-stabilized in aqueous NH_3 solutions at pH = 10. Furthermore, the particle size distributions of the GDC20 and LSC nanoparticles match well with each other, indicating that they are potentially compatible to percolate homogeneously within the thin LSC-GDC20 cathode layers.

The LSC-GDC20 composite cathodes with thicknesses of 250 nm and 500 nm are symmetrically deposited on the GDC20|8YSZ|GDC20 electrolyte substrates to be characterized electrochemically. The concentration of GDC20 within the cathodes is altered systematically in the range of 10–40 wt.% in order to find the optimum composition exhibiting lowest polarization resistance.

Figure 5-8 shows the representative SEM images of the cross-sections of the LSC-GDC20 (70:30 wt. %) cathodes with approximate thicknesses of 250 and 500 nm subsequent to annealing at 650 °C for 1 h. It is evident that both nanocomposite cathode layers and GDC interlayers are continuous and homogeneous in thickness, and that a good contact between the layers is achieved at a post-annealing temperature as low as 650 °C. The thickness of the GDC20 interlayers is found to be approximately in the range of 200–300 nm for different samples.

After spin coating of the thin LSC-GDC20 cathodes, the commercially available LSM ink is screen printed symmetrically onto the samples to serve as a current collector layer. The resulting layered structure of LSM|LSC-GDC20|GDC20|8YSZ|GDC20|LSC-GDC20|LSM is annealed in-situ during the high temperature EIS measurement at 650 °C for 1 h, after which the impedance spectra are recorded in the cooling cycle. Figure 5-9a depicts the temperature profile used for the EIS analyses, where each EIS measurement is indicated by an arrow. The representative impedance spectra of 250 nm thick LSC-GDC20 (70:30 wt.%) cathodes measured at 650, 600, and 550 °C under a constant gas flow consisting of 21 vol.% O_2 and 79 vol.% N_2 are shown in Figure 5-9b–d. The impedance spectra are normalized according to the surface areas of samples. The area-normalized polarization resistance (ASR_{pol}) of the cathode layers is obtained from the difference between the estimated high frequency and the observed low frequency intersections on the real axes of the Nyquist plots. The extracted polarization losses are divided by a factor of two accounting for the electrode layers on both sides of the electrolytes.

Figure 5-10a and b show the temperature dependence of the ASR_{pol} for the LSC-GDC20 composite cathodes with thicknesses of 250 nm and 500 nm, respectively. For the purpose of comparison, the ASR values obtained from pure LSC cathodes are also included into the plots. A good linearity between the ASR_{pol} of the nanocomposite LSC-GDC20 cathodes and the reciprocal temperature is obtained in the temperature range of 450–650 °C for all of the GDC20 compositions
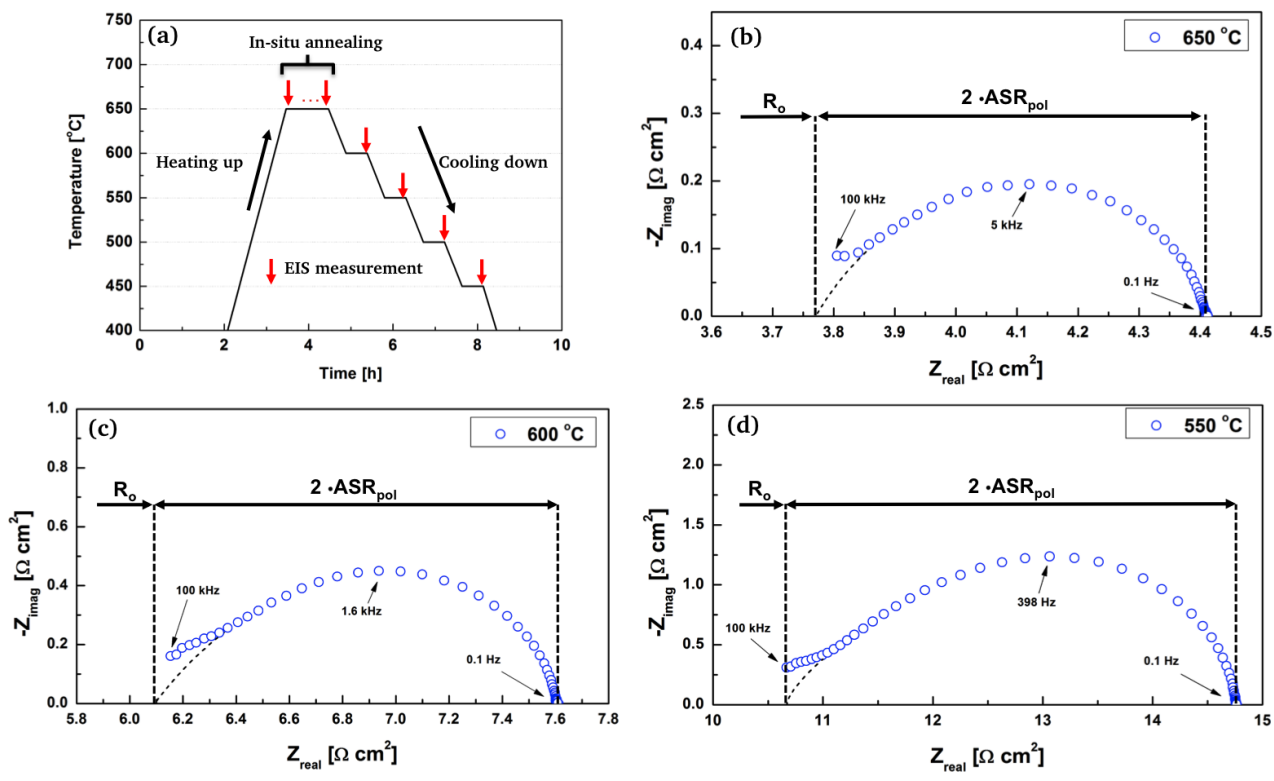
Figure 5-9: a) The temperature profile used for in-situ annealing of the as-deposited samples and for the EIS measurements, where each EIS measurement is indicated by an arrow. The impedance spectra of the LSM|LSC-GDC20|GDC20|8YSZ|GDC20|LSC-GDC20|LSM symmetrical cell with a 250 nm thick LSC-GDC20 (70:30 wt.%) cathode layer measured at (b) 650, (c) 600, and (d) 550 °C. The estimated Ohmic resistance of the cell is indicated by R_0, while ASR_{pol} stands for the estimated polarization resistance of the 250 nm thick LSC-GDC20 (70:30 wt.%) cathodes. The dashed lines at high frequency region of the spectra show the extrapolated part of the impedance spectra used to estimate the high frequency intercepts. The leveling off the impedance spectra at high frequencies is attributed to the response from the 8YSZ electrolyte substrate.

varying in the range of 10–40 wt.%. It is observed that the addition of the ionic conducting phase GDC20 into the LSC cathodes reduces the cathode polarization resistance significantly. Figure 5-11a and b show the dependence of the ASR_{pol} on the GDC composition within the LSC-GDC20 composite cathodes with thicknesses of 250 nm and 500 nm, respectively. For the 250 nm thick composite cathodes, the optimum GDC20 loading is found to be between 20–30 wt.%, as the LSC-GDC20 cathodes with those compositions show lowest ASR values in the temperature range of 450–650 °C. An ASR_{pol} values as low as 0.77 Ω cm^2 is obtained at 600 °C from the 250 nm thick LSC-GDC20 (70:30 wt.%) cathodes, while at the same temperature the single phase LSC cathodes with comparable thicknesses have an ASR_{pol} of 5.56 Ω cm^2. This considerable improvement of the cathode performance by a factor of seven at 600 °C might be attributed to the enhancement of the total ionic conductivity of the cathode layers upon addition of highly ionic conducting GDC20 nanoparticles, which in turn leads to an increase of the active reaction sites for the oxygen reduction in cathode microstructure. The similar trend is also observed for the 500 nm thick LSC-GDC20 composite cathodes. It is apparent from Figure 5-11b that the optimum GDC20 loading yielding the lowest ASR_{pol} values is 30 wt.%. An ASR_{pol} value as low as 0.24 Ω cm^2 is obtained at 600 °C from 500 nm thick LSC-GDC20 (70:30 wt.%) cathodes, while at the same temperature the single phase LSC cathodes with comparable thicknesses have an ASR_{pol} of 3.71 Ω cm^2. For the 500 nm thick LSC-GDC20 composite cathodes, an improvement of the ASR_{pol} by a factor of more than fifteen is observed.

Table 5-2 lists the activation energies calculated for the 250 nm and 500 nm thick LSC-GDC20 cathodes with various compositions. It is observed that the activation energies decrease upon
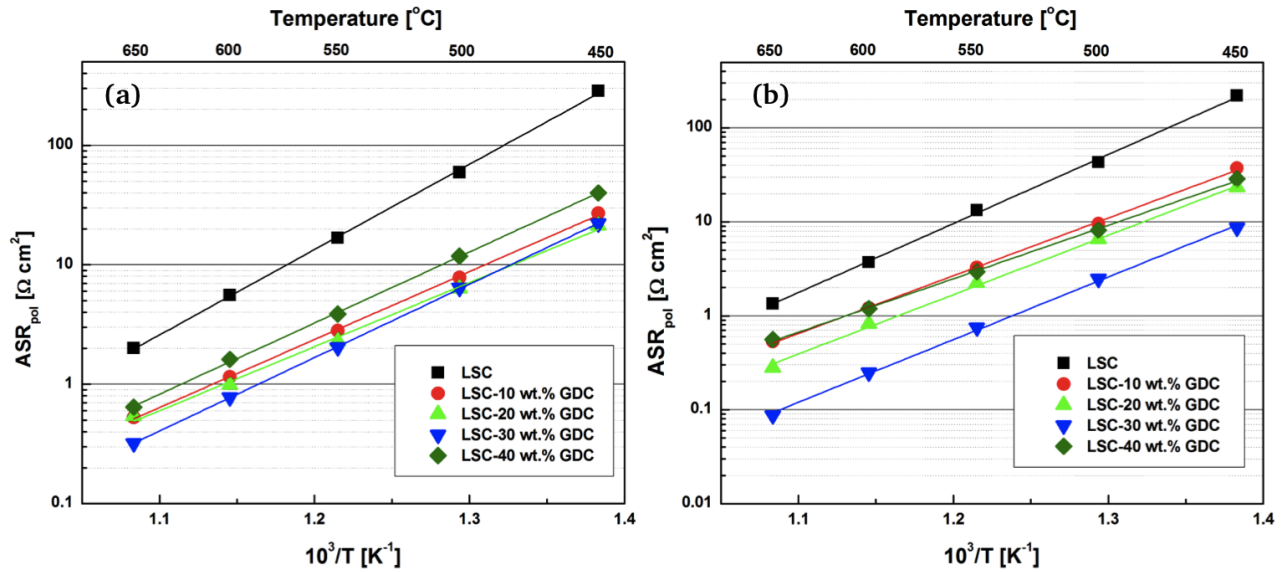
Figure 5-10: The area-specific polarization resistance (ASR_{pol}) of (a) 250 and (b) 500 nm thick LSC-GDC20 cathode layers as a function of the reciprocal of the measurement temperature.

addition of the ionic conducting GDC20 phase. Both trends of decreasing ASR and activation energies with increasing GDC20 content are in a good agreement with the literature data obtained from powder-processed composite MIEC cathodes. Tao *et. al* [171] have reported that 20 μm thick $La_{0.6}Sr_{0.4}CoO_{3-\delta}$-$Ce_xGd_{1-x}O_{2-\delta}$ (70:30 wt.%) composite cathodes have the lowest polarization resistance of 0.24 Ω cm^2 at 600 °C. According to Darbandi *et. al.* [153], the percolation of $Ce_{0.8}Gd_{0.2}O_{2-\delta}$ nanoparticles within the $La_{0.6}Sr_{0.4}Co_{0.2}Fe_{0.8}O_{3-\delta}$ (LSCF) cathode layers leads to the decrease both in the cathodic polarization resistance and in the corresponding activation energies. The spin-coated 1 μm thick LSCF-GDC (85:15 wt.%) composite cathodes are reported to have ASR values of 0.371 Ω cm^2 at 600 °C.
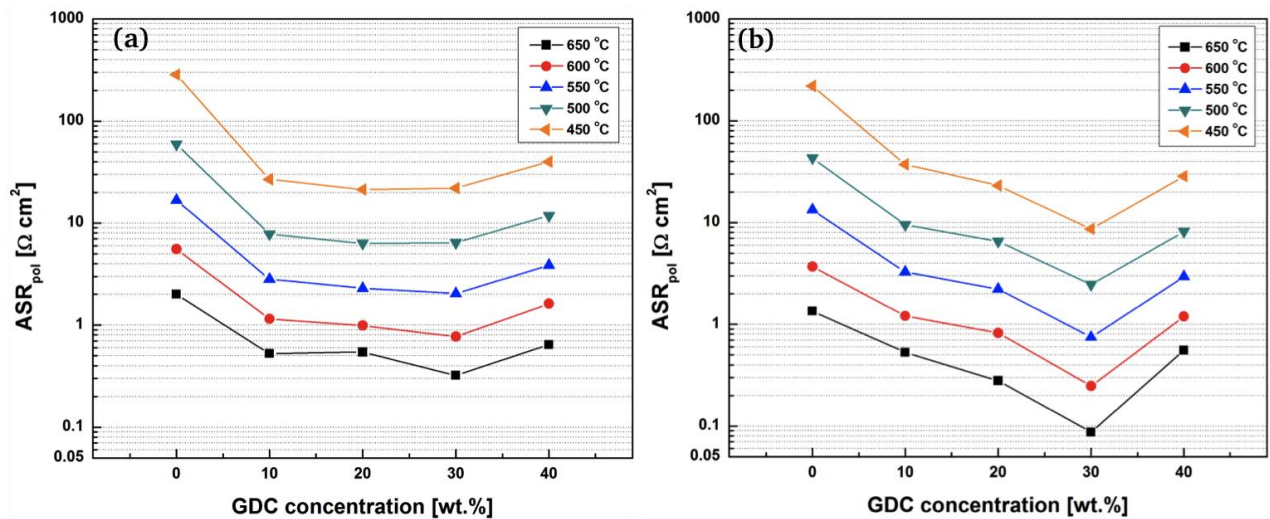

Figure 5-11: The dependence of the area-specific polarization resistance (ASR_{pol}) on the concentration of GDC for (a) 250 and (b) 500 nm thick LSC-GDC20 cathodes at different measurement temperatures.

Table 5-2: The activation energies calculated for the LSC and LSC-GDC20 cathodes with different cathode thicknesses and compositions.

GDC concentration (wt.%)	Activation energy (eV)	
	Cathode thickness=250 nm	Cathode thickness=500 nm
0	1.42 ± 0.02	1.46 ± 0.05
10	1.13 ± 0.01	1.22 ± 0.02
20	1.07 ± 0.03	1.25 ± 0.03
30	1.22 ± 0.01	1.32 ± 0.02
40	1.18 ± 0.02	1.13 ± 0.02

The conventional approach to obtain a good inter- and intra-layer contacts requires sintering of the multilayered SOFC structures at elevated temperatures [1], [99]. However, the sintering steps at high temperatures lead to substantial reduction of the active surface areas of the nanostructured electrodes due to the faster grain growth rates of the nanoparticles compared to microcrystalline powders. Furthermore, the thermomechanical stability of a micro-SOFC platform consisting of YSZ-based 300 nm thick free standing membranes (390 μm × 390 μm) is demonstrated only up to 600 °C [223]. Therefore, little is known about the stability of such micro-SOFC membranes at temperatures higher than 600 °C. Nevertheless, the 500 nm thick LSC cathodes are further annealed in the temperature range of 700–1000 °C to observe the effect of the annealing temperature on the cathode performance.

Effect of annealing temperature

Figure 5-12 shows the cross-sectional SEM images of spin-coated LSC cathodes subsequent to annealing at different temperatures. The SEM investigation shows that the post-deposition heat treatment has an influence on the microstructural features such as grain size, surface area, and porosity of the spin-coated cathode layers. Therefore, to investigate the effect of the annealing temperature on the electrochemical properties of the cathodes, LSC thin films are spin coated symmetrically on GDC10 substrates and annealed at different temperatures (800–1000 °C) for 2 h with a heating and cooling rate of 2 °C /min prior to the EIS measurements. The thicknesses of the cathode layers are comparable and approximately 500 nm. In order to avoid potential contact issues impeding the oxygen ion conductivity between the 8YSZ electrolyte substrates and GDC20 thin interlayers, the LSC cathodes are directly spin coated on GDC10 substrates. The LSC cathodes post-annealed at 650 °C (Figure 5-3b) and at 800 °C (Figure 5-12a) do not differ significantly in terms of grain size and microstructure. The increase of the annealing temperature to 900 °C leads to a grain growth of the LSC nanoparticles and possibly improved contacts at the cathode/electrolyte interface and between the LSC nanoparticles within the cathode layers. Despite the grain growth, the 500 nm thick LSC cathodes sustain its porous nanostructured nature subsequent to the annealing step at 900 °C. However, further increase of the annealing temperature to 1000 °C results in LSC cathode layers with substantially larger grains, which might be attributed to fast grain growth rates at higher annealing temperatures. In addition to the larger grain sizes, it is also observed that the number of necking sites between the LSC grains is increased. Even though this would lead to improved electronic and ionic transport abilities of the LSC cathode layers, the substantial reduction of the active surface area due to the increased grain size and the nanoparticle necking might hamper the oxygen exchange at the cathode/air interface and the gas transport processes though the cathode microstructure. The grain growth trend upon high temperature annealing observed for the LSC nanostructured cathodes is in a good accordance with the thermal stability study conducted by Darbandi *et. al.* [195] on the spray-pyrolyzed (B)LSC(F)-based perovskite cathode nanoparticles.
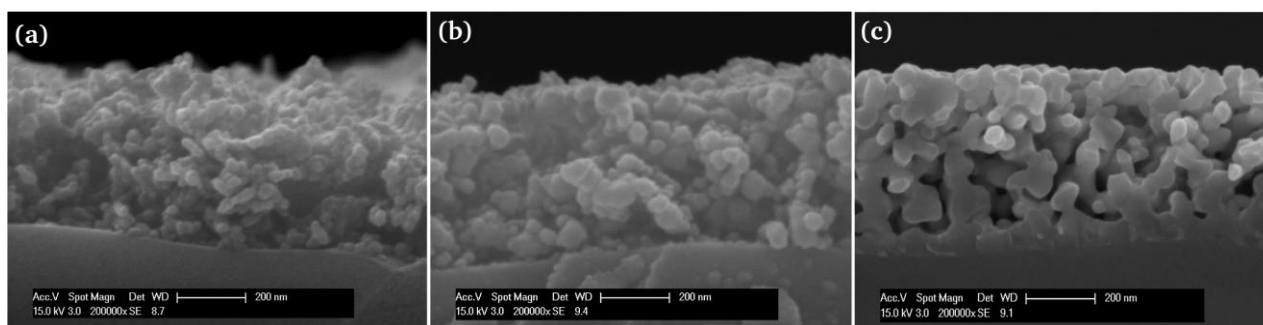
Figure 5-12: Cross-sectional SEM images of 500 nm thick LSC cathode layers on GDC10 electrolytes annealed at (a) 800, (b) 900, and (c) 1000 °C for 2h subsequent to the spin coating.

Figure 5-13a and b show two representative Nyquist plots of the impedance spectra obtained from a symmetrical cell LSM|LSC|GDC10|LSC|LSM consisting of 500 nm thick LSC cathodes annealed at 900 °C for 2h prior to the EIS measurement. The spectra are recorded isothermally at 650 °C and 600 °C under a constant gas flow consisting of 21 vol.% O_2 and 79 vol.% N_2. It is observed that the impedance spectra in the temperature range of 450–650 °C consist of one depressed semicircle and the experimental data are fitted with the equivalent circuit model shown in Figure 5-13a (inset), which is proposed by many authors for the MIEC powder-processed porous cathodes [114], [153], [165], [172], [224]. The inductance element L_1 accounts for the inductive effects of the Pt wires and measurement setup [165], [225], which is observed at high frequencies and typically at high temperatures. The resistance R_0 represents the combination of Ohmic losses caused by the GDC10 electrolyte, the electrodes, and the current collector layers [79]. At 600 °C for the symmetrical sample with 520 μm thick GDC10 electrolyte, the R_0 value is found to be 3.19 Ω cm^2 (Figure 5-13b). Since the electronic conductivities of LSC cathodes and LSM current collectors are expected to be high compared to the GDC10 electrolyte layer, it is assumed that R_0 might be mainly attributed to the Ohmic losses associated with the electrolyte layer. Based on this assumption, the conductivity of GDC10 electrolyte is calculated as 1.63 S/m at 600 °C, which is in a good accordance with the reported conductivity values of $Ce_{0.9}Gd_{0.1}O_{2-\delta}$ [24], [79].

The two parallel subcircuits R_1-CPE$_1$ and R_2-CPE$_2$ consisting of a resistance (R_1 or R_2) and a constant phase element (CPE$_1$ or CPE$_2$) describe the two rate limiting cathodic processes. Based on the literature [172], [226], [227], the high frequency behavior of the cathodic impedance (R$_1$-CPE$_1$) is attributed to the charge transfer processes, while the low frequency behavior (R$_2$-CPE$_2$) of the impedance is associated with non-charge transfer processes such as oxygen exchange at electrode/air interface and mass transport inside and outside of the cathode layer. The parameters used in the equivalent circuit models (*i.e.*, the admittance constant (Q) and the power of CPE (n)) along with the calculated true capacitance (C^*) and relaxation frequency (f^*) values are presented in Table 5-3. The capacitance values per unit area are around 10^{-3} F/cm^2, which is typical for the electrode-limited processes [33] and in accordance with the reported values for LSC thin film cathodes [39], [165], [228].
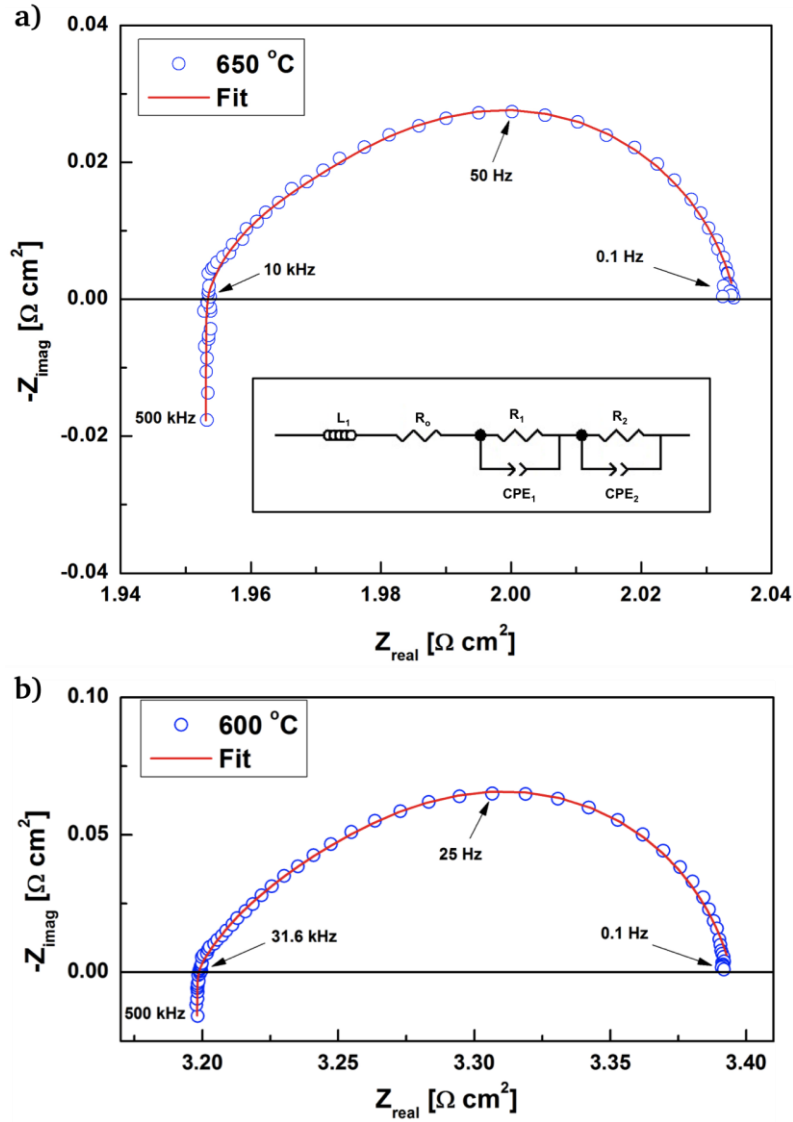
Figure 5-13: The impedance spectra of the LSM|LSC|GDC10|LSC|LSM symmetrical cell with a 500 nm thick LSC cathode layer measured at (a) 650 and (b) 600 °C. The whole symmetrical cell is annealed at 900 °C for 2 h with a heating and cooling rate of 2 °C/min prior to the EIS measurement. The spectra are fitted using the equivalent circuit (a, inset). The circles represent the experimental points, while the full lines represent fitting curves.

Table 5-3: The parameters used for the equivalent circuit model fitting of the impedance spectra at 650 and 600 °C obtained from the LSM|LSC|GDC10|LSC|LSM symmetrical cell with a 500 nm thick LSC cathode layer annealed prior to the EIS measurement at 900 °C for 2 h. The true capacitance (C^*) and the relaxation frequency (f^*) values calculated using the CPE parameters are also given for each process.

T	R_0	R_1	CPE$_1$		C_1^*	f_1^*	R_2	CPE$_2$		C_2^*	f_2^*
(°C)	($\Omega\,cm^2$)	($\Omega\,cm^2$)	Q_1	n_1	(F/cm^2)	(kHz)	($\Omega\,cm^2$)	Q_2	n_2	(F/cm^2)	(Hz)
650	1.953	0.0135	0.11	0.59	0.0014	8.2	0.0255	0.21	0.86	0.0079	73
600	3.190	0.0320	0.07	0.60	0.0011	4.15	0.0640	0.18	0.86	0.0087	28

The temperature dependence of the area normalized polarization resistance (ASR_{pol}) for 500 nm thick LSC cathodes annealed in the temperature range of 650–1000 °C is shown in Figure 5-14. A good linearity between the ASR_{pol} of the LSC cathodes and the reciprocal measurement temperature is obtained in the temperature range of 450–650 °C for all samples. It is observed that post-deposition annealing at high temperatures has a great impact on the cathode performance. An ASR_{pol} value as low as 0.096 Ω cm^2 at 600 °C is obtained for 500 nm thick LSC cathodes, which are

Figure 5-14: Area specific polarization resistance (ASR$_{pol}$) of the LSM|LSC|GDC20|8YSZ|GDC20|LSC|LSM symmetrical cell annealed at 650 °C for 1 h and LSM|LSC|GDC10|LSC|LSM symmetrical cells annealed at 800, 900, and 1000 °C for 2 h prior to the EIS measurements, as a function of measuring temperature.

annealed at 900 °C for 2 h prior to the EIS measurement. In comparison to the LSC cathodes annealed at 650 °C, the substantial improvement of the cathode performance almost by a factor of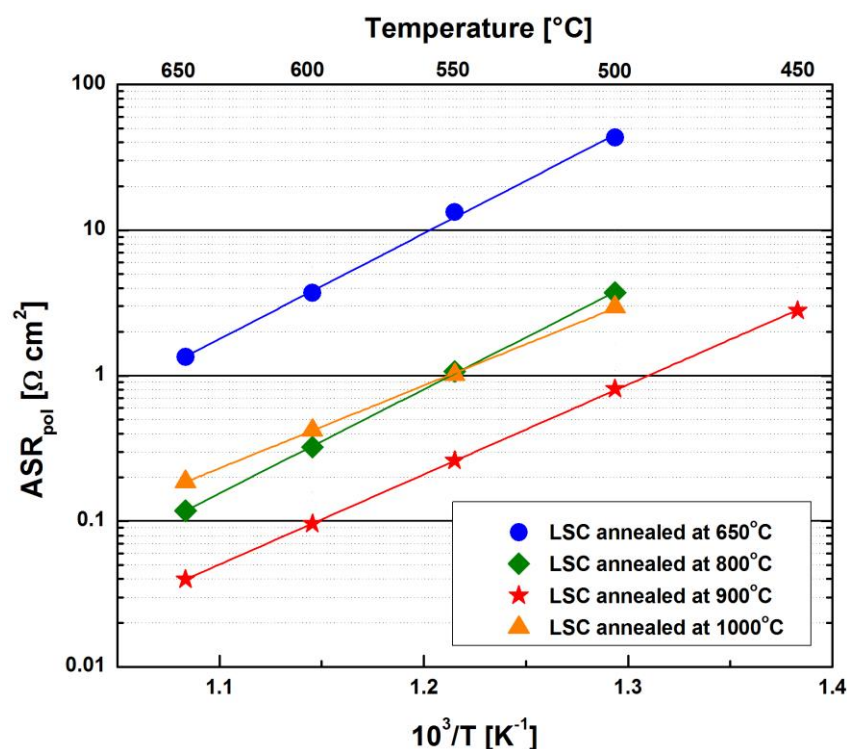 forty might be attributed to the reduction of contact resistances within the symmetrical cells. However, the increase of the annealing temperature further to 1000 °C leads to an increase of the polarization resistance. This can be explained by the reduction of the active surface area of the cathode layers due to faster grain growth observed at this post-deposition annealing temperature, which is confirmed by the SEM investigations (Figure 5-12c). Activation energies of 1.42 $\pm$ 0.02, 1.23 $\pm$ 0.01, and 1.13 $\pm$ 0.01 eV are calculated for the LSC cathodes annealed at 800, 900, and 1000 °C, respectively. It is observed that the activation energy of the LSC cathodes annealed at 800 °C is comparable to that of annealed at 650 °C (1.456 $\pm$ 0.046 eV). However, the activation energy of the cathodes seems to decrease as the annealing temperature increases. Based on the previous observations on the LSC-GDC20 composite cathodes and the SEM investigations conducted on the cathodes which are annealed at different temperatures this trend can be attributed to the improved oxygen ion conductivity of the cathode layers, which have potentially better particle connectivity due to the neck formation at higher annealing temperatures.

Figure 5-15 shows the comparison of the lowest ASR$_{pol}$ values obtained in this work with those of nanostructured (B)LSC(F)-based MIEC cathodes with submicron thicknesses reported in the literature. The plot is far from a complete literature review, and due to the variations in the cathode thicknesses and grain sizes (Table 5-4), it is not straightforward to draw a conclusion about the relationship between the oxygen reduction performance and the microstructural features of the LSC-based cathode films. Nevertheless, the spin coated LSC cathodes realized in this work are among the best cathodes reported, which makes them potential candidates for the nanoscaled SOFC applications aiming high performance at low operating temperatures. Detailed information on the cathodes (*i.e.*, deposition methods, cathode thicknesses, and grain sizes) revealed in Figure 5-15 are listed in Table 5-4.
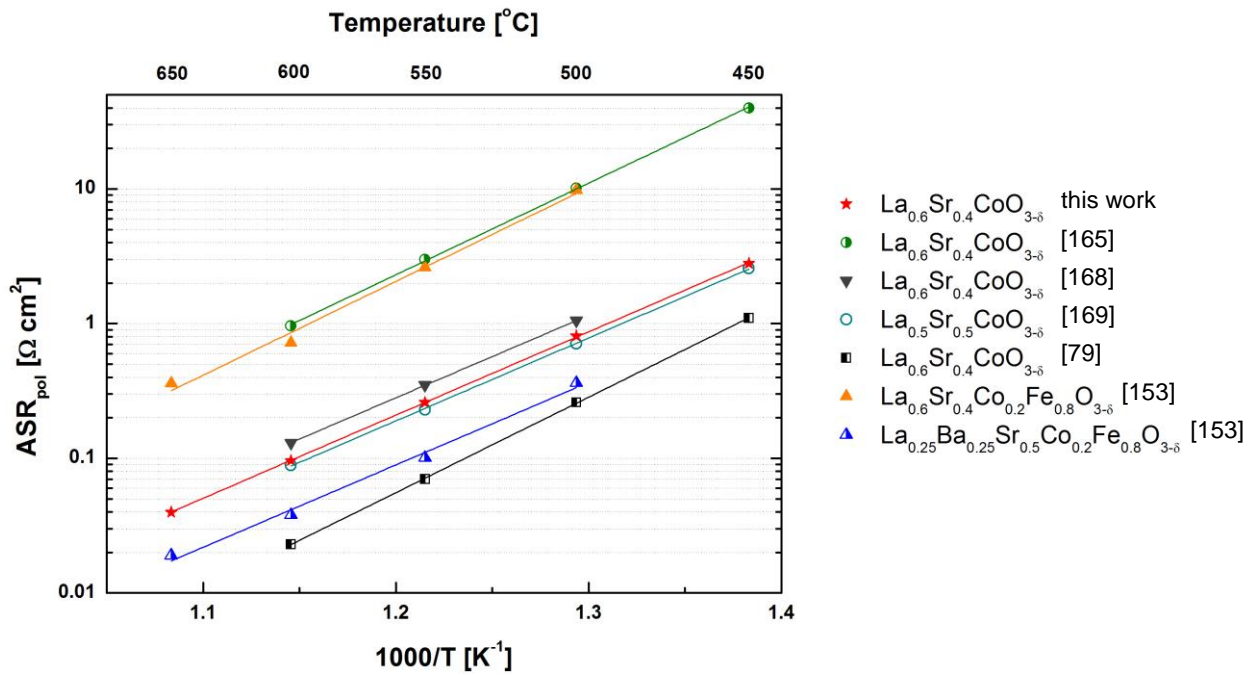
Figure 5-15: The comparison of the polarization resistance values of a few high-performance nanoscaled (B)LSC(F)-based cathodes with submicron thicknesses reported in the literature.

Table 5-4: Additional information on the (B)LSC(F)-based cathodes presented in Figure 5-15.

Cathode	ASR (Ω cm^2) at 600 °C	Deposition method	Cathode thickness (μm)	Grain size (nm)	Ref.
La$_{0.6}$Sr$_{0.4}$CoO$_{3-\delta}$	0.096	Spin coating	0.5	70	this work
La$_{0.6}$Sr$_{0.4}$CoO$_{3-\delta}$	0.023	MOD	0.2	17	[79]
La$_{0.5}$Sr$_{0.5}$CoO$_{3-\delta}$	0.09	PLD	0.72	8	[169]
La$_{0.6}$Sr$_{0.4}$CoO$_{3-\delta}$	0.13	PLD	1	50	[168]
La$_{0.6}$Sr$_{0.4}$CoO$_{3-\delta}$	0.96	Flame spray deposition	0.2	34	[165]
La$_{0.6}$Sr$_{0.4}$Co$_{0.2}$Fe$_{0.8}$O$_{3-\delta}$	0.72	Spin coating	<1	68	[153]
La$_{0.6}$Ba$_{0.25}$Sr0$_{.4}$Co$_{0.2}$Fe$_{0.8}$O$_{3-\delta}$	0.038	Spin coating	<1	68	[153]

5.3.2. Ni-Ce$_{0.8}$Gd$_{0.2}$O$_{2-\delta}$ Anodes

Thin film electrolytes and cathodes have been extensively investigated in the literature for the applications for anode-supported SOFCs and micro-SOFCs, respectively [119]. However, the information about thin film cermet anodes for micro-SOFC application is scarce. La O *et. al.* [127] have reported the applicability of the sputtered Ni-YSZ cermets to miniaturized SOFCs, but no data is given about the electrochemical performance. Muecke *et. al.* [139], [229] have reported on the electrochemical performance and the microstructural stability of the nanostructured Ni-GDC20 cermet anodes with thicknesses in the range of 500–800 nm fabricated by spray deposition. According to those studies, the lowest ASR$_{pol}$ of the thin film Ni-GDC20 anodes deposited on GDC10 and 8YSZ substrates are measured under humidified 20 vol.% H$_2$ in N$_2$ at 600 °C as 1.73 and 7.2 Ω cm^2, respectively. It has also been observed that a decrease of the grain size of the spray

deposited Ni-GDC20 anode layers down from 53 nm to 16 nm leads to a reduction in the ASR_{pol} from 1.73 to 0.34 Ω cm^2, which is mainly attributed to an increase of the active reaction sites for fuel oxidation. However, it has also been reported that the Ni-GDC20 anodes with smaller grains sizes are more susceptible to the degradation due to the faster Ni coarsening at operating temperatures. Recently, Takagi *et. al.* [193] have demonstrated the applicability of co-sputtered ruthenium (Ru)-GDC10 cermet anode thin films on the freestanding micro-SOFC consisting of 8YSZ membrane as thin electrolyte and sputtered Pt as cathode layers. Micro-SOFCs tested under humidified methane as fuel and air as oxidant exhibits an open circuit voltage of 0.97 V and a peak power density of 275 mW/cm^2 at 485 °C. Still, little is known whether the electrochemical performance of the thin film cermets is sufficient for the micro-SOFC applications. Therefore, in this work nanostructured Ni-GDC20 thin anodes with thicknesses approximately 500 nm are fabricated by spin coating of stabilized dispersions of the NiO-GDC20 (60:40 wt.%) nanoparticles obtained from salt-assisted spray pyrolysis, and the effect of the post-annealing temperature on the electrochemical performance is investigated.

Figure 5-16 shows the cross-sectional SEM images of Ni-GDC20 anodes, which are obtained by spin coating of stabilized dispersions of the NiO-GDC20 nanoparticles on 8YSZ substrates and subsequent annealing steps at different temperatures under a reducing atmosphere (5 vol.% H$_2$ in Ar). The SEM investigation of the Ni-GDC20 anodes shows that the post-deposition heat treatment has an influence on the microstructural features such as grain size, surface area, and porosity. The thicknesses of the anode layers are comparable and approximately 500 nm. The anodes post-annealed at 650 (Figure 5-3d) and at 800 °C (Figure 5-16a) do not differ significantly in terms of the grain size and microstructure. The increase of the annealing temperature to 900–1000 °C leads to a grain growth and possibly improved contacts at the anode/electrolyte interface and between the nanoparticles within the anode layers. Despite the observed grain growth, the 500 nm thick NiO-GDC20 anodes sustain its porous nanostructured microstructure subsequent to the annealing steps at 900 and 1000 °C (Figure 5-16b and c).

After the annealing steps, Pt films with thicknesses of 80 nm are sputtered symmetrically on the samples to serve as current collector layers. The resulting layered structure of Pt|Ni-GDC20|8YSZ|Ni-GDC20|Pt is characterized electrochemically in an atmospherically sealed furnace. The aforementioned temperature profile (Figure 5-6a) is used to record impedance spectra of the thin film anodes as well. During the EIS measurements, the samples are kept under reducing atmospheres with a constant gas flow (5 vol.% H$_2$ in Ar) while heating up to 650 °C to avoid the oxidation of Ni nanoparticles to NiO.

Figure 5-17a and b show two representative impedance spectra in the form of Nyquist plot obtained from a symmetrical cell consisting of 500 nm thick Ni-GDC20 anode layers annealed at 900 °C for 2h prior to the EIS measurement. The spectra are recorded isothermally at 650 °C and
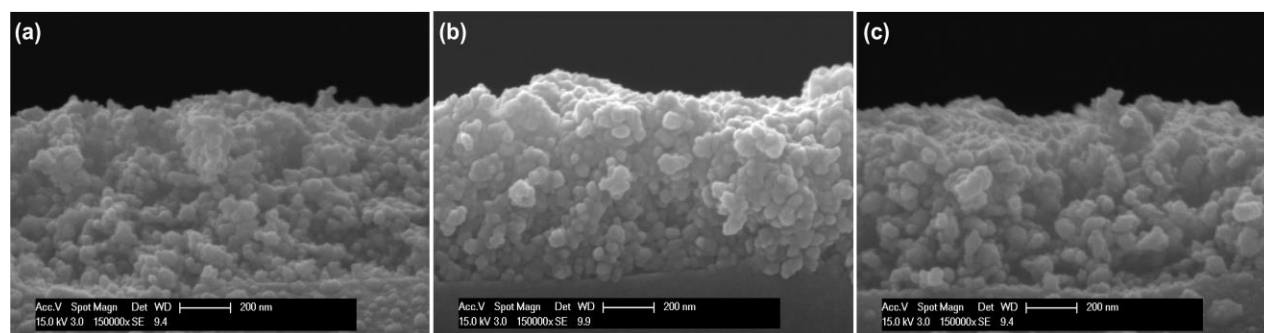
Figure 5-16: Cross-sectional SEM images of 500 nm thick Ni-GDC20 cathode layers annealed at (a) 800, (b) 900, and (c) 1000 °C for 2h subsequent to the spin coating of the stabilized dispersions of NiO-GDC20 (60:40 wt.%) nanoparticles. The samples are annealed under a gas flow consisting of 5 vol.% H$_2$ in Ar.

600 °C under a constant gas flow of humidified 5 vol.% H_2 in Ar. It is observed that the impedance spectra in the temperature range of 450–650 °C consist of at least three depressed semicircles. Therefore, the equivalent circuit model given in Figure 5-17a (inset) is used to fit the experimental data [230], [231], where the inductance element L_1 accounts for the inductive effects of the Pt wires and measurement setup [165], [225], which is observed at high frequencies and typically at high temperatures. The resistance R_0 represents the combination of Ohmic losses caused by the 8YSZ electrolyte, the Ni-GDC20 electrodes, and the current collector layers [79]. Each of the three parallel subcircuits R_1-CPE_1, R_2-CPE_2, and R_3-CPE_3 consisting of a resistance (R_i) and a constant phase element (CPE_i) describe the rate limiting anodic processes. The parameters used in the equivalent circuit models (*i.e.*, the admittance constant (Q) and the power of CPE (n)) along with the calculated true capacitance (C^*) and relaxation frequency (f^*) values are presented in Table 5-5.
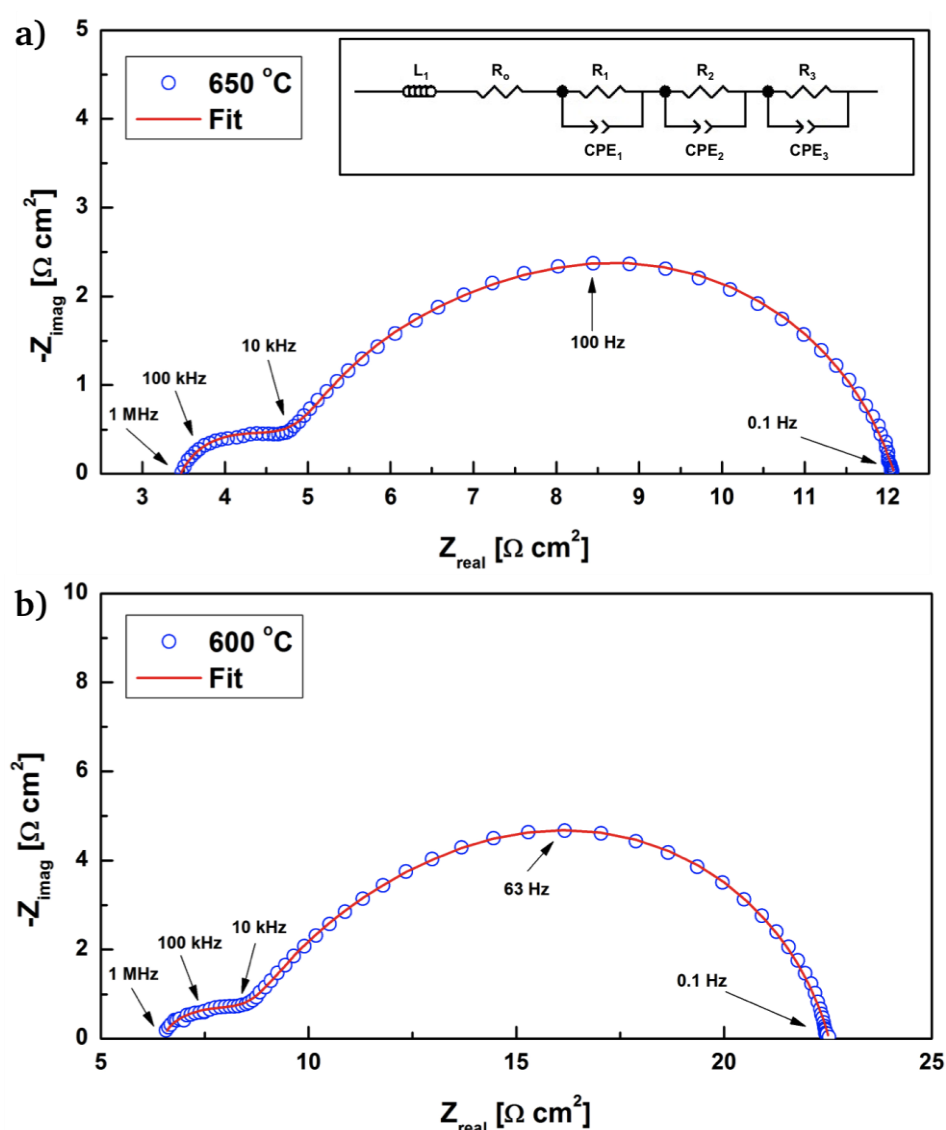
Figure 5-17: The impedance spectra of the Pt|Ni-GDC20|8YSZ|Ni-GDC20|Pt symmetrical cell with a 500 nm thick Ni-GDC20 anode layer measured at (a) 650 and (b) 600 °C. The symmetrical cell Ni-GDC20|8YSZ|Ni-GDC20 is annealed at 900 °C for 2 h with a heating and cooling rate of 2 °C/min prior to the EIS measurement. Pt current collector layers are sputtered symmetrically before the EIS measurement to achieve proper current collection from the thin anode layers. The spectra are fitted using the equivalent circuit (a, inset). The circles represent the experimental points, while the full lines represent fitting curves.

The capacitance of the process taking place at high frequencies is in the same order as a typical double layer capacitance, 10^{-5} F/cm^2 [70], [232]. Therefore, the high frequency behavior of the anodic impedance (R_1-CPE_1) is attributed to the charge transfer processes, which are taking place at the anode/electrolyte interfaces (at/near TPBs). The capacitance values for the semicircles at lower frequencies (R_2-CPE_2 and R_3-CPE_3) are calculated in the order of 10^{-4} F/cm^2 and they are attributed to the two rate limiting electrode processes such as adsorption and dissociation of H_2 on the electrode surfaces [232]. Contrary to the common observation in cermet anodes [230], [233], a low frequency process with high capacitance values (~ 1 F/cm^2) is not observed, which is typically attributed to bulk diffusion processes such as gas transport within the electrode microstructure [234].

Table 5-5: The parameters used for the equivalent circuit model fitting of the impedance spectra at 650 and 600 °C obtained from the Pt|Ni-GDC20|8YSZ|Ni-GDC20|Pt symmetrical cell with a 500 nm thick Ni-GDC20 anode layer annealed prior to the EIS measurement at 900 °C for 2 h. The true capacitance (C^*) and the relaxation frequency (f^*) values calculated using the CPE parameters are also given for each process.

T (°C)	R_0 ($\Omega\,cm^2$)	R_1 ($\Omega\,cm^2$)	CPE$_1$		C_1^* (F/cm^2)	f_1^* (kHz)	R_2 ($\Omega\,cm^2$)	CPE$_2$		C_2^* (F/cm^2)	f_2^* (kHz)
			Q_1	n_1				Q_2	n_2		
650	3.03	2.09	7.10^{-4}	0.51	1.10^{-6}	57	1.89	7.10^{-4}	0.86	$2.3.10^{-4}$	1.5
600	6.09	3.012	6.10^{-4}	0.50	1.10^{-6}	48	2.04	5.10^{-4}	0.85	$1.5.10^{-4}$	0.5

T (°C)	R_3 ($\Omega\,cm^2$)	CPE$_3$		C_3^* (F/cm^2)	f_3^* (Hz)
		Q_3	n_3		
650	5.11	$1.5.10^{-3}$	0.82	$5.1.10^{-4}$	75
600	11.39	7.10^{-4}	0.81	$2.3.10^{-4}$	58

The temperature dependence of the area normalized polarization resistance (ASR$_{pol}$) on the measurement temperature for the 500 nm thick Ni-GDC20 anodes annealed in the temperature range of 650–1000 °C and for the 80 nm thick sputtered Pt current collector is shown in Figure 5-18. A good linearity between the ASR$_{pol}$ of the anodes and the reciprocal temperature is obtained in the temperature range of 450–650 °C for all samples. It is observed that post-deposition annealing at high temperatures has an impact on the anode performance. The minimum ASR_{pol} value of 8.2 Ω cm^2 at 600 °C is obtained for the 500 nm thick Ni-GDC anode, which is annealed at 900 °C for 2 h prior to the EIS measurement. At the same measurement temperature, the anodes annealed at 650 and 800 °C give lowest ASR$_{pol}$ values of 31 and 16.6 Ω cm^2, respectively. The increase of the annealing temperature further to 1000 °C leads to an increase of the polarization resistance (9.28 Ω cm^2 at 600 °C). Activation energies of 0.82 $\pm$ 0.04, 0.82 $\pm$ 0.04, 0.91 $\pm$ 0.02, and 0.93 $\pm$ 0.03 eV are calculated for the Ni-GDC20 anodes annealed at 650, 800, 900, and 1000 °C, respectively, which are in a good agreement with the reported activation energies of 0.74 [235] and 0.77 eV [139] of the Ni-GDC20 cermet anodes. The electrochemical performance in the form of ASR$_{pol}$ agrees well with the spray deposited 500–800 nm thick NiO-GDC20 anodes on 8YSZ electrolytes having an ASR_{pol} of 7.2 Ω cm^2 at 600 °C [139].

It is well known that Pt itself is an excellent electrocatalyst for the oxidation of H_2 [17]. Therefore, a Pt|8YSZ|Pt symmetrical cell consisting of 200 μm thick electrolyte substrate and 80 nm thick symmetrically sputtered Pt layers is fabricated to compare the polarization resistance of the Pt current collector layers with those of Ni-GDC20 anodes. The cell with only sputtered Pt electrodes is prepared identically as the symmetrical cells with spin-coated anode layers with the exception that the spin-coated Ni-GDC20 anode is left out. The EIS measurement is conducted in the temperature range of 500–600 °C under identical conditions mentioned before. The polarization resistance of the Pt|8YSZ interface is found to be at least half order of magnitude larger than that of Ni-GDC20 anodes at the same measurement temperature. The activation energy
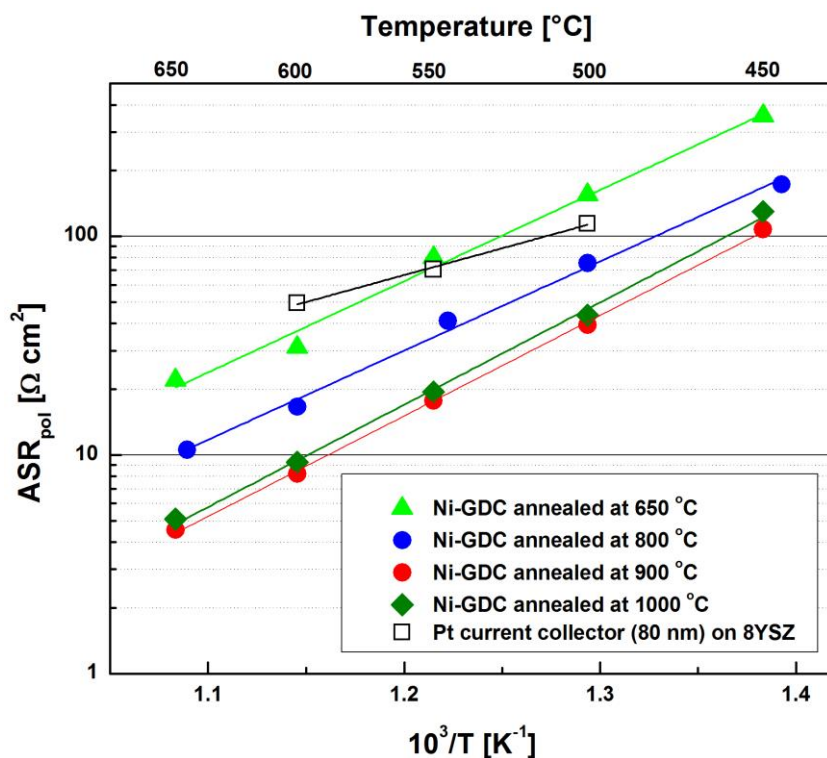
Figure 5-18: Area specific polarization resistances (ASR$_{pol}$) of the Pt|Ni-GDC20|8YSZ|Ni-GDC20|Pt and Pt|8YSZ|Pt symmetrical cells annealed at 650 °C for 1 h in-situ during, and of the Pt|Ni-GDC20|8YSZ|Ni-GDC20|Pt symmetrical cells annealed at 800, 900, and 1000 °C for 2 h prior to the EIS measurements, as a function of measuring temperature.

of the Pt|8YSZ interface is calculated as 0.486 ± 0.023 eV. Therefore, any possible catalytic contribution of the Pt current collector to the fuel oxidation performance of the Ni-GDC20 anodes can be neglected.

5.4. Summary & Conclusion

The nanostructured LSC cathodes and Ni-GDC20 anodes with thicknesses in the range of 200–800 nm are successfully fabricated on the electrolyte substrates. The fabrication of the thin film electrodes is realized by spin coating of the stabilized dispersions of the corresponding nanoparticles synthesized via salt-assisted spray pyrolysis method. The stability and particle size distribution of the dispersions are crucial to achieve continuous and homogeneous films with desired thicknesses. Therefore, zeta potential measurements are performed to evaluate the stabilities of synthesized LSC and NiO-GDC20 nanoparticles. The dynamic light scattering experiments reveal that the as-synthesized nanoparticles of LSC and NiO-GDC20 (60:40 wt.%) have medium particle diameters of 52±1 and 69±1 nm, respectively, in the water-based dispersions.

The electrochemical impedance spectroscopy measurements conducted on symmetrical cells reveal that a post-deposition annealing step at temperatures as low as 650 °C for 1 h is sufficient to obtain polarization resistance values of 3.71 and 30.3 Ω cm^2 at 600 °C for 500 nm thick LSC and Ni-GDC20 electrodes, respectively. The efforts to improve the performance of LSC cathodes include the fabrication of the LSC-GDC20 nanocomposite cathodes and the polarization resistance values of the 500 nm thick LSC cathodes are successfully reduced from 3.71 down to 0.24 Ω cm^2 by percolating highly ionic conductive GDC20 nanoparticles within the cathode microstructure. This performance improvement by a factor of more than fifteen is promising, since no high temperature annealing step is employed. Therefore, the proposed electrode fabrication method can

be integrated to the fabrication of the micro-SOFC devices as an alternative to the costly and time-consuming physical vapor deposition methods. Further investigations reveal that post-deposition annealing steps have a great impact on the electrochemical performance of the LSC cathodes. The 500 nm thick LSC cathodes annealed at 900 °C for 2 h lead to the minimum polarization resistance value of 0.096 Ω cm^2, which is among the best (B)LSC(F)-based cathodes with submicron thicknesses. Similar to the LSC cathodes, the post-deposition annealing step at 900 °C for 2 h lead to the minimum polarization resistance value of 8.2 Ω cm^2 for the 500 nm thick Ni-GDC20 anodes, which is also comparable to the reported polarization resistance values of the anodes with similar thicknesses, microstructural features, and composition.

The novel thin film processing method offers an inexpensive and easily scalable thin film electrode processing method compared to the vacuum based thin film fabrication techniques, such as PLD, CVD, and sputtering. The versatilty of proposed method and the high electrochemical parformance of the resulting electrodes makes this electrode fabrication technique an important candidate for nanoscaled electrode technology for low temperature SOFCs operating at 600 °C and below.

6. Fabrication of SOFC Devices

Selected parts of this chapter have also been published in [108] *within the framework of this thesis. Corresponding sections – with minor conformations included – are indicated with a vertical gray bar at the inner page margin[2].*

Low-temperature SOFCs have drawn significant attention due to their lower material and operation costs, greater reliability, and broader applicability to a wide range of applications from small scale portable electronics to large scale power generation systems compared to the conventional high- and intermediate-temperature SOFC systems [8]. To verify the applicability of the nanostructured electrodes presented in the previous chapter to the low-temperature SOFCs, the platforms of micro-SOFC and anode-supported SOFC are chosen. In the first part of this chapter, the integration of spin-coated LSC cathodes in freestanding micro-SOFC membranes is demonstrated as a low cost alternative to Pt electrodes. Furthermore, the proposed electrode fabrication technique is a promising alternative to the expensive and time-consuming physical vapor deposition methods, which are typically employed to fabricate the thin film electrode components of micro-SOFCs. In the second part of this chapter, the synthesized electrode materials within the framework of the thesis are tested in the state-of-the-art anode-supported SOFC design. The anode supports and thin electrolytes are fabricated by conventional ceramic processing techniques, *i.e.*, die pressing and screen printing, respectively. Gd-doped CeO_2-based SOFC is chosen due to the high ionic conductivity of CeO_2-based electrolytes compared to conventional ZrO_2-based electrolyte materials. The fabrication and electrochemical performance of anode-supported (LSC|GDC10|Ni-GDC20) SOFCs are reported.

6.1. Integration of Spin-Coated LSC Cathodes into Micro-Solid Oxide Fuel Cell Devices

One of the approaches to eliminate the degradation issues is to integrate oxide-based electrodes with better long-term microstructural stabilities in micro-SOFC devices than that of metal-based electrodes. To date, the fabrication of mixed ionic-electronic conducting (MIEC) (B)LSC(F) cathodes on micro-SOFC platforms has been only realized by physical vapor deposition techniques such as sputtering [12], [236], [237] and PLD [112], [238], among which the reported peak power densities of 200–262 mW/cm^2 in the temperature range of 400–450 °C by Evans *et. al*. [112] stand out. The same platform of LSC|3YSZ|Pt is used in this work to demonstrate the applicability of the cost effective fabrication of nanostructured MIEC electrodes by spin coating of a dispersion of nanoparticles on freestanding micro-SOFC membranes for the first time.

---

[2] Reprinted with persmission from [108]. ©2013, WILEY-VCH.

6.1.1. Preliminary Deposition Experiments

To confirm the applicability of the spin coating parameters optimized for the fabrication of nanoscaled electrodes in previous chapter, preliminary deposition experiments of LSC cathodes are conducted on the 3YSZ thin films fabricated by PLD on Si_3N_4|Si substrates (Figure 6-1), which are the typical platforms to obtain freestanding Si-based micro-SOFC membranes through several microfabrication steps. The test substrates do not contain any freestanding membranes, since the focus is set on the realization of the spin coating stabilized dispersions of LSC nanoparticles successfully on the pulsed layer deposited 3YSZ thin electrolytes. The initial experiments aiming to realize 250 nm thick LSC layers yield unsatisfactory electrode layers with non-uniform thicknesses and poor surface coverage. This behavior is attributed to the distinct surface properties of the electrolyte substrates (8YSZ and GDC10) used in previous chapter and pulsed layer deposited

■ 3YSZ (300 nm)　■ Si_3N_4 (200 nm)　■ Si (380 µm)
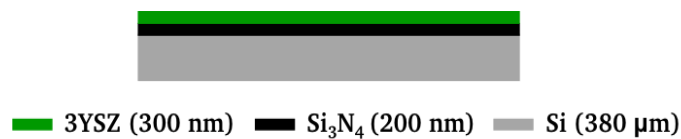
Figure 6-1: Schematic view of the 3YSZ|Si_3N_4|Si substrate, which are used in the preliminary spin coating experiments of stabilized dispersions of LSC nanoparticles on the 3YSZ thin films fabricated by PLD. The representation is not drawn to scale.
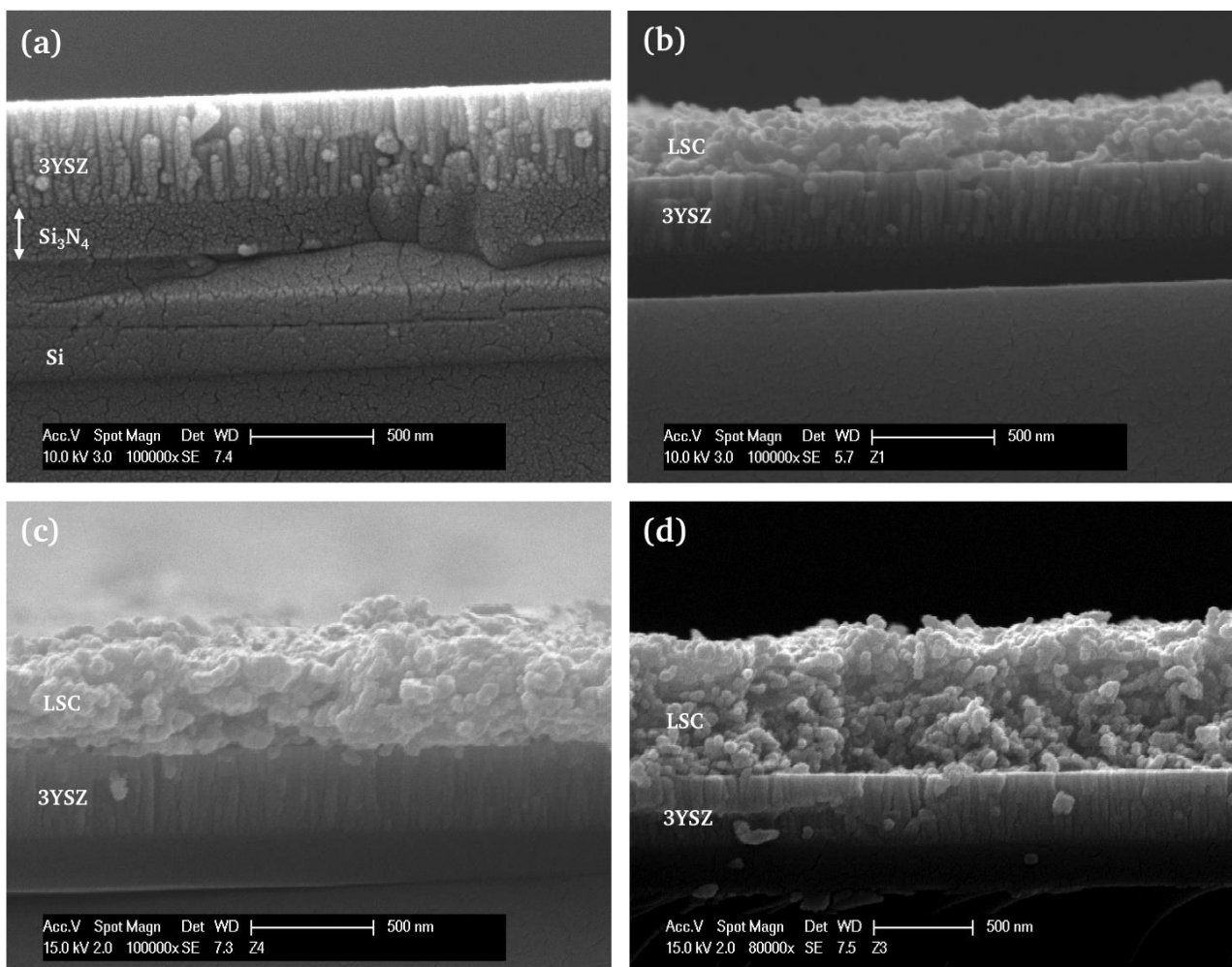
Figure 6-2: Cross-sectional SEM images of a) the 3YSZ|Si_3N_4|Si substrate and spin-coated LSC cathodes with thicknesses of b) 250 nm, c) 500 nm, and d) 750 nm on the 3YSZ|Si_3N_4|Si substrates after annealing at 550 °C for 1 h.

3YSZ thin films. Therefore, a single-step spin coating procedure (spin speed: 1200 rpm, acceleration: 200 rpm/s, spin duration: 150 s) is developed to fabricate nanostructured LSC cathodes on 3YSZ (PLD) thin films. Subsequent to the spin coating of the LSC dispersion, the samples are annealed at 550 °C for 1 h in air with a heating and cooling rate of 3 °C/min. Figure 6-2 shows the cross-sectional SEM images of the 3YSZ|Si$_3$N$_4$|Si substrate and LSC cathode layers with different thicknesses spin-coated on 3YSZ|Si$_3$N$_4$|Si substrates after the heat treatment at 550 °C for 1 h. The columnar microstructure of 3YSZ electrolyte layers is advantageous in terms of enhanced oxygen ion conductivity, as there are no blocking effects associated with the grain boundaries [112]. Varying the solid loading of the dispersions, while the spin coating parameters are kept unchanged, controls the thickness of the LSC thin films. The cathode layers with thicknesses of 250, 500, and 750 nm are realized using dispersions consisting of LSC nanoparticles with the solid loadings of 10, 15, and 20 wt.%, respectively. All spin-coated LSC cathodes exhibit a nanoparticulate microstructure with high porosity and good adhesion to the underlying 3YSZ layer. The nanoporous nature of spin-coated LSC cathodes is favorable to obtain a large active surface area for the oxygen incorporation. Furthermore, it is expected that this type of porous microstructure might reduce the thermal stresses originating from different thermal expansion coefficients of LSC (18–26×10^{-6} 1/K [81], [84], [88], [89]) and 3YSZ (10–11×10^{-6} 1/K [239]) compared to dense electrode/electrolyte bilayers, which are typically prone to spalling and delamination because of the interfacial shear stresses.

6.1.2. Electrode Fabrication and Electrochemical Characterization

The mechanical and thermo-mechanical stabilities are critical issues for the development of micro-SOFCs, which relies on the structural integrity of the thin film cell components during the fabrication and the operation. Especially, a vibration-generating deposition method like spin coating is considerably challenging, which might lead to the mechanical failure of the membranes even in the fabrication step. In order to keep the mechanical stability of the membranes during the cathode fabrication, two different approaches are followed to spin coat the dispersions consisting of LSC nanoparticles on Si-supported micro-SOFC membranes. The first approach relies on the mechanical support of the remaining Si substrate deliberately kept under the 3YSZ|Si$_3$N$_4$ bilayer after the initial wet chemical etching step as depicted in Figure 6-3a, in which 3YSZ is deposited at room temperature and exhibit a slight compressive stress of −270 ± 80 MPa [223]. In the second approach, thin LSC cathodes are directly spin-coated on freestanding 3YSZ|Si$_3$N$_4$ membranes exhibiting relatively higher compressive stress of −1100 ± 150 MPa [223] (Figure 6-3b) induced by higher deposition temperature of 3YSZ by PLD. Figure 6-3c–d show the top-view light
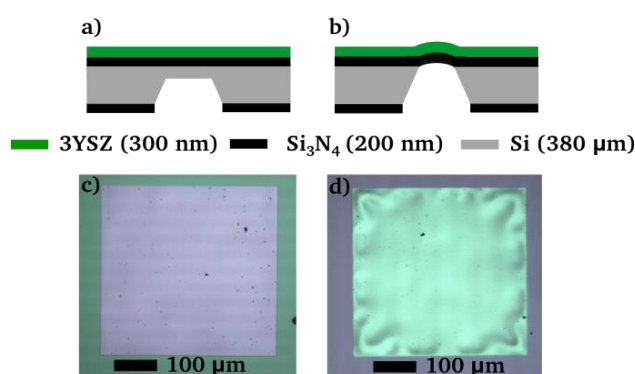

Figure 6-3: Schematic illustrations of (a) 3YSZ|Si$_3$N$_4$|Si and (b) freestanding 3YSZ|Si$_3$N$_4$ membranes employed for the integration of LSC cathodes by spin coating. Representative top-view light microscopy images of (c) 3YSZ|Si$_3$N$_4$|Si membranes (after complete wet chemical etching of Si) and (d) freestanding 3YSZ membranes.
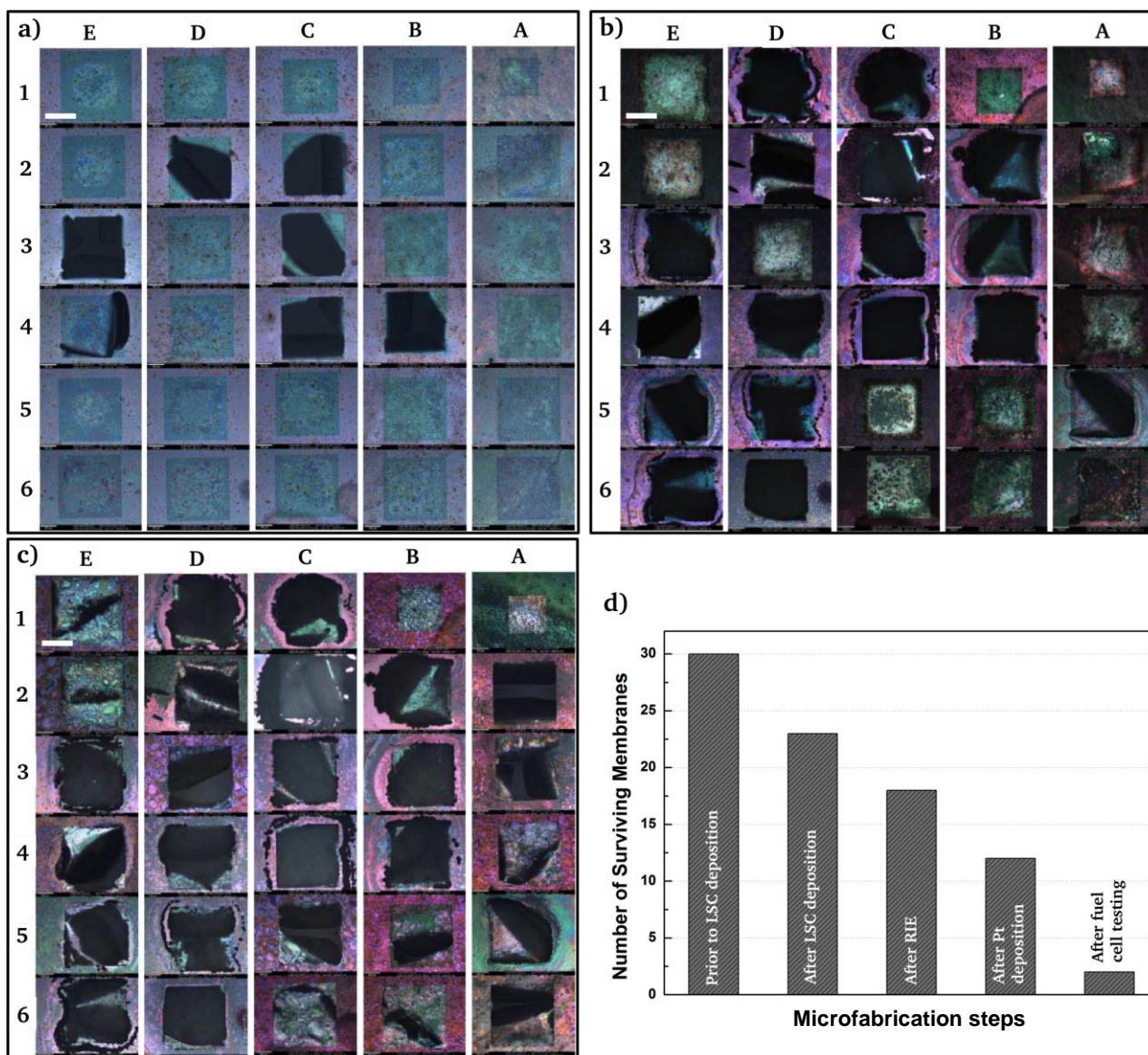
Figure 6-4: Optical microscopy (top-view) images of the LSC cathodes deposited on the 3YSZ|Si$_3$N$_4$|Si membranes after (a) spin coating followed by a heat treatment at 550 °C and wet chemical etching of silicon, (b) RIE of Si$_3$N$_4$ and Pt anode deposition, and (c) after fuel cell testing, (d) the number of surviving membranes after each fabrication step. The images are taken with incident light. A crack in the membrane A3 in Figure 6-4b is confirmed by imaging with transmitted light.

microscopy images of freestanding 3YSZ|Si$_3$N$_4$ membranes with slight and relatively higher compressive stresses, respectively. The membranes with relatively low compressive stresses look flat under the light microscope, while the 3YSZ membranes deposited at elevated temperatures have the characteristic buckling patterns associated with the compressive stresses within the films. Further information about the buckling patterns of pulsed layer deposited YSZ films can be found elsewhere [223], [240].

It is crucial to ensure high survival rates of micro-SOFC membranes after each of microfabrication and processing steps. Therefore, the mechanical integrity of the membranes is checked under a light microscope after each step. Figure 6-4a–c show the optical microscopy images of micro-SOFC membrane arrays at different fabrication steps, which are obtained by spin coating of 250 nm thick LSC cathode on a pre-etched 3YSZ|Si$_3$N$_4$|Si membrane. After the LSC deposition and subsequent wet chemical etching of the Si support layer (Figure 6-4a), the survival rate of the membranes is above 75%. However, after the subsequent steps of reactive ion etching of Si$_3$N$_4$ layer and Pt anode deposition, the number of surviving micro-SOFC membranes reduces

Figure 6-5: Cell voltage and power density curves obtained from 12 micro-SOFC membranes with 250 nm thick LSC cathodes deposited on 3YSZ membranes with slight compressive stress. The inset s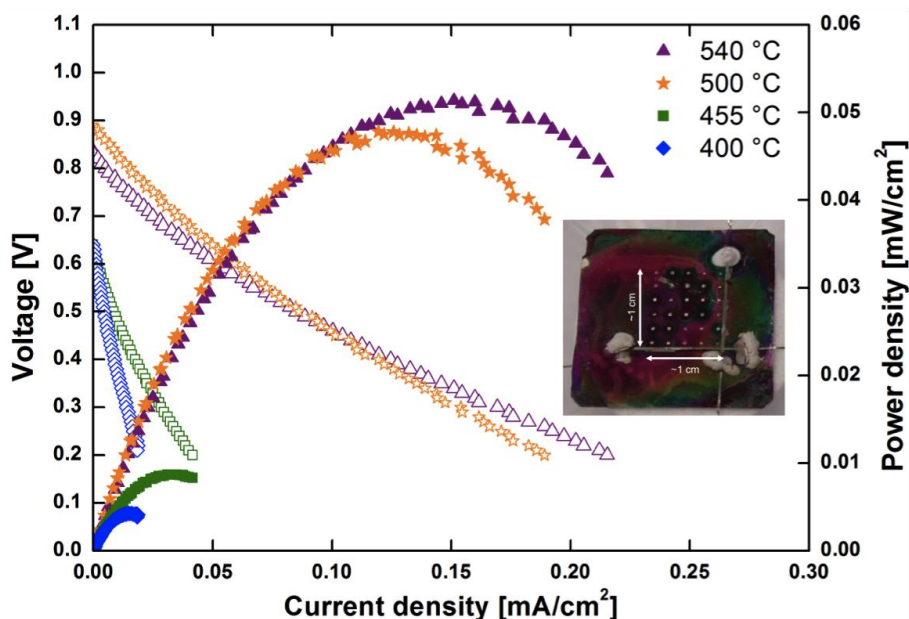hows the photograph of the Si chip with micro-SOFC array before the fuel cell testing and the Pt wires used for current collection. The damaged membranes are sealed from the anode side using a ceramic paste to prevent fuel cross-over.

from 23 to 12 prior to the fuel cell testing (Figure 6-4b). According to the Figure 6-4c, only 2 out of 30 micro-SOFC membranes survive after the fuel cell testing.

Figure 6-5 shows the current-voltage and power density characteristics of micro-SOFC array consisting of 12 membranes. The current and power density values are obtained by normalizing the experimental data with the total active surface area of 12 membranes. The open-circuit voltage (OCV) is 0.9 V and a maximum power density of 0.045 mW/cm^2 is obtained at 500 °C using air as oxidant and humidified 20 vol.% H_2 in N_2 as fuel. The lower than expected OCV (~1.1 V) of these micro-SOFCs can be attributed to micro-cracks in electrolytes. However, further drop of OCV with longer operation time down to 0.65 V suggests a high degree of fuel crossover across the micro-SOFC membranes, which agrees well with the post-analysis by optical microscopy of micro-SOFC membranes (Figure 6-4c). The maximum power density of 0.045 mW/cm^2 obtained at 500 °C is also gradually reduced after an operation time of 60 minutes down to 0.02 mW/cm^2. The failure mechanism of the 3YSZ membranes can be attributed to its thermomechanical instability and/or the thermal stress arising from the thermal expansion coefficient mismatch between the LSC cathode and 3YSZ electrolyte.

The initial poor electrochemical performance might also be attributed to the microstructural features of electrode layers of micro-SOFC membranes such as poor surface coverage, delamination, and Pt anode degradation. Therefore, a detailed SEM post-analysis of LSC cathode and Pt anode layers is conducted. Figure 6-6a–d show the top-view SEM images of LSC cathode and Pt anode layers, respectively. The high magnification images obtained from the areas marked by red rectangular indicate that both LSC and Pt electrodes have a good surface coverage on the freestanding 3YSZ membranes. The satisfactory surface coverage of freestanding membranes by spin-coated LSC cathode is also confirmed by optical microscopy images. The LSC cathode exhibits a nanoparticulate microstructure with high porosity and adheres well to the underlying 3YSZ layer, which is favorable for high surface exchange rate of the cathodic oxygen reduction reactions. Furthermore, the sputtered Pt anode layer seems to keep its dense microstructure after the fuel cell testing, as the formation of holes and a break in the symmetry of the original Pt film are not present.
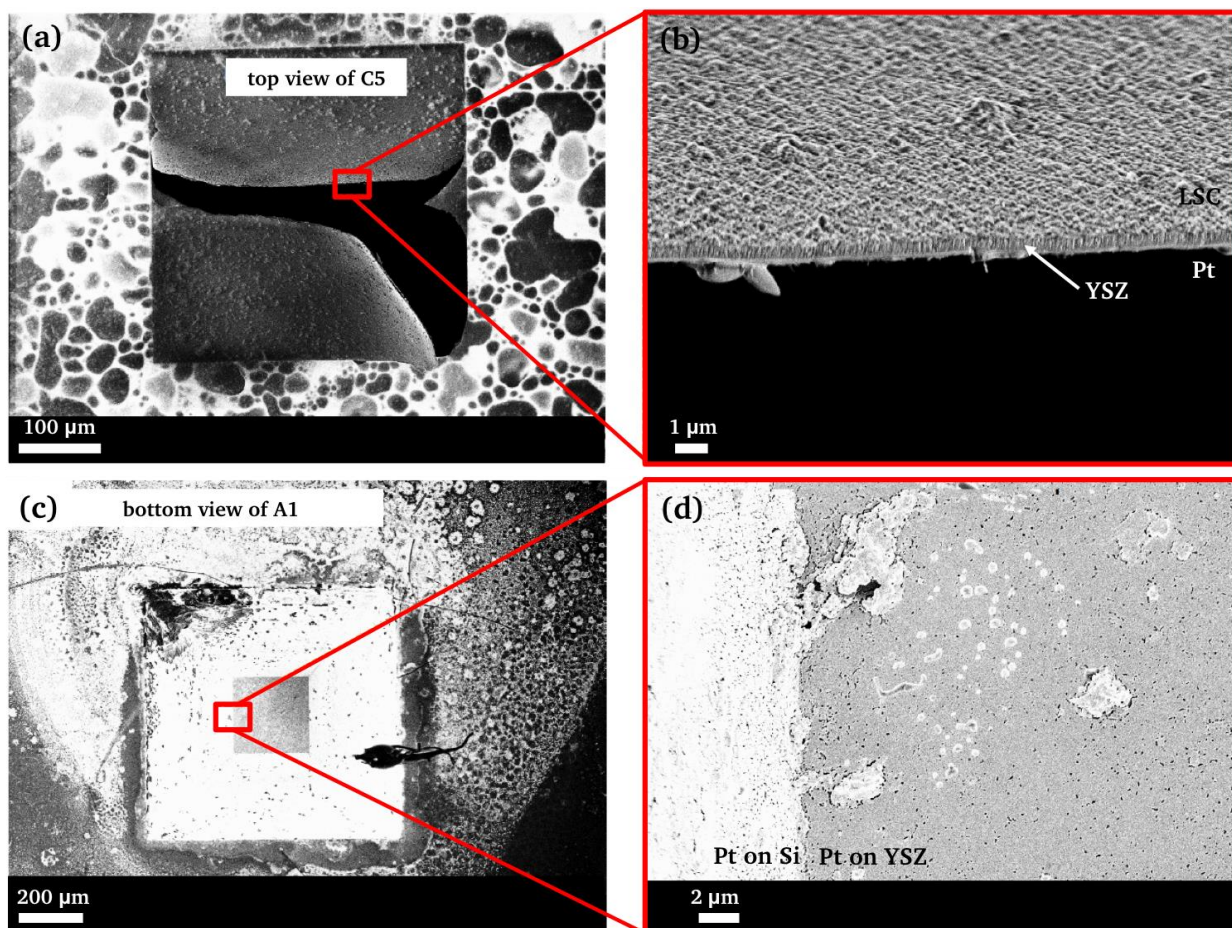
Figure 6-6: SEM analysis of LSC|3YSZ|Pt micro-SOFC membranes after the fuel cell testing. a) Top-view image of a micro-SOFC membrane (C5 in Figure 6-4c) c) covered by LSC cathode ruptured during the fuel cell testing and (b) high magnification image showing the cathode microstructure and cross-section of the membrane. c) Bottom-view image of a micro-SOFC membrane (A1 in Figure 6-4c) covered by Pt anode layer survived after the fuel cell testing and (d) high magnification image showing the anode microstructure.

The low electrochemical performance might also stem from the second wet chemical etching step of the microfabrication process, as the spin-coated LSC cathode is required to be covered by a protective layer, which is then removed by acetone washing. It is suspected that the use of such protective layer might disrupt the integrity of the LSC cathode layer. It might be also possible that any residue remained after the removal of the protective layer blocks the electrochemically active sites and reduces the in-plane electronic conductivity of thin LSC cathode and eventually leading to a poor electrochemical performance and current collection.

The promising results obtained from spin coating experiments of LSC cathodes on micro-SOFC membranes (survival rate ~75%), the stress engineering study of pulsed layer deposited freestanding YSZ membranes by Evans *et. al.* [223], and the mechanical stability investigation for such micro-SOFC membranes by Tölke *et. al.* [111] are encouraging results to use a modified approach for further attempts to integrate spin-coated LSC cathodes in micro-SOFCs, in which the thin LSC cathodes are directly spin-coated on freestanding membranes exhibiting relatively higher compressive stress. Figure 6-7a–c show the optical microscopy images of micro-SOFC membrane arrays obtained by spin coating of 250 nm thick LSC cathode on freestanding $3YSZ|Si_3N_4$ membranes at different fabrication steps. As presented in Figure 6-7d, it is possible to deposit the LSC cathodes on such 3YSZ membranes with high survival rates (>95%). The following fabrication steps (RIE of Si_3N_4 layer and Pt anode deposition) do not reduce the survival rate of the freestanding membranes significantly as depicted in Figure 6-7b and d. According to the Figure
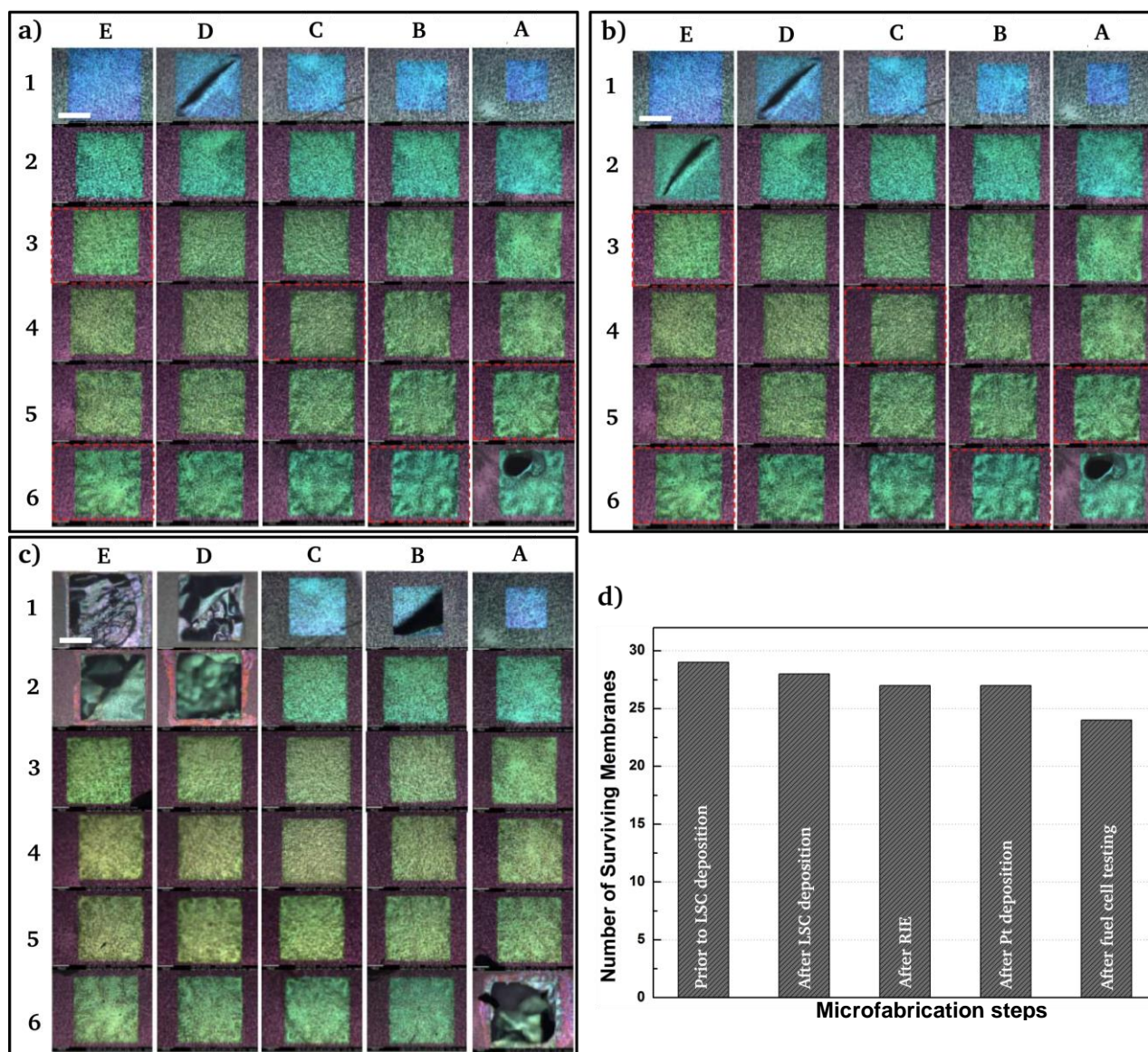
Figure 6-7: Optical microscopy (top-view) images of the LSC cathodes deposited on the 3YSZ|Si$_3$N$_4$ freestanding membranes after (a) spin coating followed by a heat treatment at 550 °C, (b) RIE of Si$_3$N$_4$ and Pt anode deposition, and (c) after fuel cell testing, (d) the number of surviving membranes after each fabrication step. The images are taken with incident light.

6-7c, 24 out of 30 micro-SOFC membranes survive after the fuel cell testing. This substantial improvement of the survival rates of micro-SOFC membranes is attributed to the high thermomechanical stability of 3YSZ films due to their high residual compressive stresses [223]. Furthermore, potential stresses arising from the thermal expansion coefficient mismatch between LSC and 3YSZ is compensated well by the residual compressive stress within the 3YSZ membranes.

The photograph of the Si chip consisting of a micro-SOFC array (LSC|3YSZ|Pt) is shown in Figure 6-8a. Several single micro-SOFCs are separated from each other by scratching off the spin-coated LSC cathode layers as shown in the optical microscopy image in Figure 6-8b. Pt wires with bent tips covered with Pt paste are used for current collection from individual cells (Figure 6-8c). The cell voltage and power density curves of the micro-SOFCs with buckled 3YSZ membranes with 250 nm thick cathodes are shown in Figure 6-8d and e. The cells exhibit a theoretical open-circuit voltage of 1.05 V using air as the oxidant and diluted hydrogen (20 vol.%) as the fuel in a temperature range of 355–550 °C. This indicates that the surviving membranes are gas-tight during the fuel cell testing and there is no fuel crossover. The micro-SOFC membrane in the

middle of the Si chip delivers a maximum power density of 12 mW/cm^2 at 500 °C (Figure 6-8d), whereas a maximum power density of 3 mW/cm^2 at 500 °C (Figure 6-8c) is obtained from the membrane towards the edge of the Si chip. The thickness distribution of the LSC cathodes is checked on different free-standing membranes on the same chip and it is observed that the thickness of LSC electrodes on the membranes close to the middle of the chip is higher about 50 nm than that close to the edge of the chip, which is typical for spin coating deposition process. Therefore, the higher electrochemical performance of the membrane in the center of the Si chip might be attributed to this non-uniform thickness distribution of the spin-coated LSC films, which yields relatively thicker LSC films in the center of the substrates and eventually more active sites for the oxygen incorporation.

Figure 6-9a–f show the top-view SEM and cross-sectional focused ion beam (FIB) microscopy images of LSC cathode and Pt anode layers after the fuel cell testing. Both LSC and Pt electrodes have a good surface coverage on freestanding 3YSZ membranes. Only the small dark areas are not covered by LSC cathodes as shown in Figure 6-9a and b. The microstructure of LSC cathode layer does not alter upon fuel cell testing, as the high magnification top-view image of the cathode layer in Figure 6-9b(inset) exhibits the typical nanoparticulate microstructure of the spin-coated LSC cathode layers. This type of nanoporous microstructure facilitates large surface exchange areas for oxygen reduction and induces lower shear stresses on the underlying 3YSZ electrolyte layer during the fuel cell operation compared to denser thin film oxide alternatives. Figure 6-9c and d indicate that sputtered Pt anodes are slightly degraded after the fuel cell testing, as the coarsening and the formation of holes within the thin film starts to emerge. It is also observed that the coarsening of the Pt anode layer is more pronounced on the sidewalls of Si chip (Figure 6-9c), since the formation of metallic islands is present. The degradation of Pt anode layers leads to poor
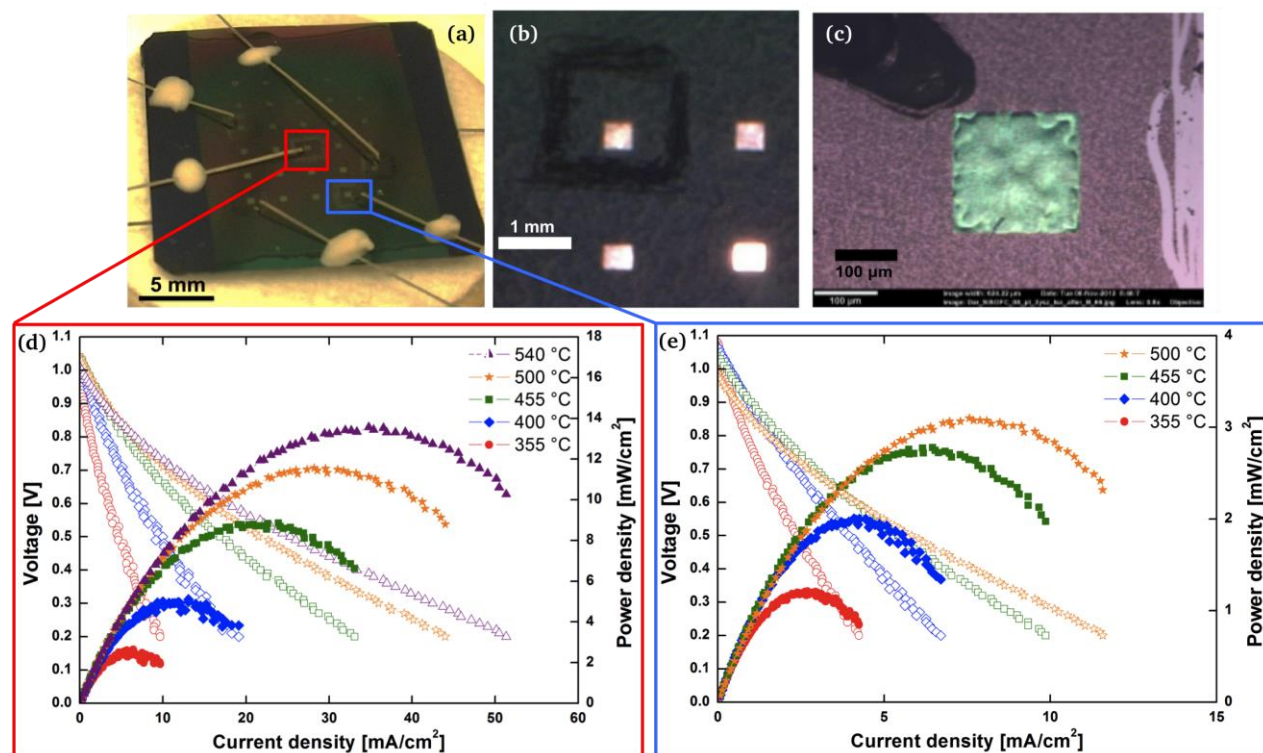
Figure 6-8: a) The photograph of the Si chip with micro-SOFC array (LSC|3YSZ|Pt). Pt wires (the tips being covered by Pt paste) used for current collection from individual micro-SOFC membranes. The micro-SOFC membranes are separated from each other on Si-chip by scratching off the spin-coated LSC cathode layer. b, c) Optical microscopy images, taken with transmitted and incident light, respectively, showing the separation of micro-SOFCs and the position of the current collecting Pt wire tip. Cell voltage and power density curves obtained from micro-SOFC membranes (d) in the middle and (c) towards the edge of the Si chip.

electrochemical performance with prolonged operation times because of the decrease of number of active reaction sites and poor current collection from the Pt anode layers.

The precise determination of the cathode thickness is important in terms of two aspects. First, the maximum electrode thickness which is limited by the thermal stresses within the electode-electrolyte bilayers gives a valuable information necessary to achieve thermomechanically stable micro-SOFC membranes. Secondly, the thickness of MIEC electrode layers has a direct effect on the electrochemical properties. Therefore, the microstructures of the LSC and Pt electrodes are investigated by cross-sectional FIB polished cuts, which are also used for the precise determination of the thickness of the electrode layers. Figure 6-9e and f show nanoparticulate LSC microstructure and that there is good adhesion to the underlying 3YSZ electrolyte layer. The 250 nm thick LSC cathodes have a grain size of 40–50 nm and exhibit a microstructure with homogeneously
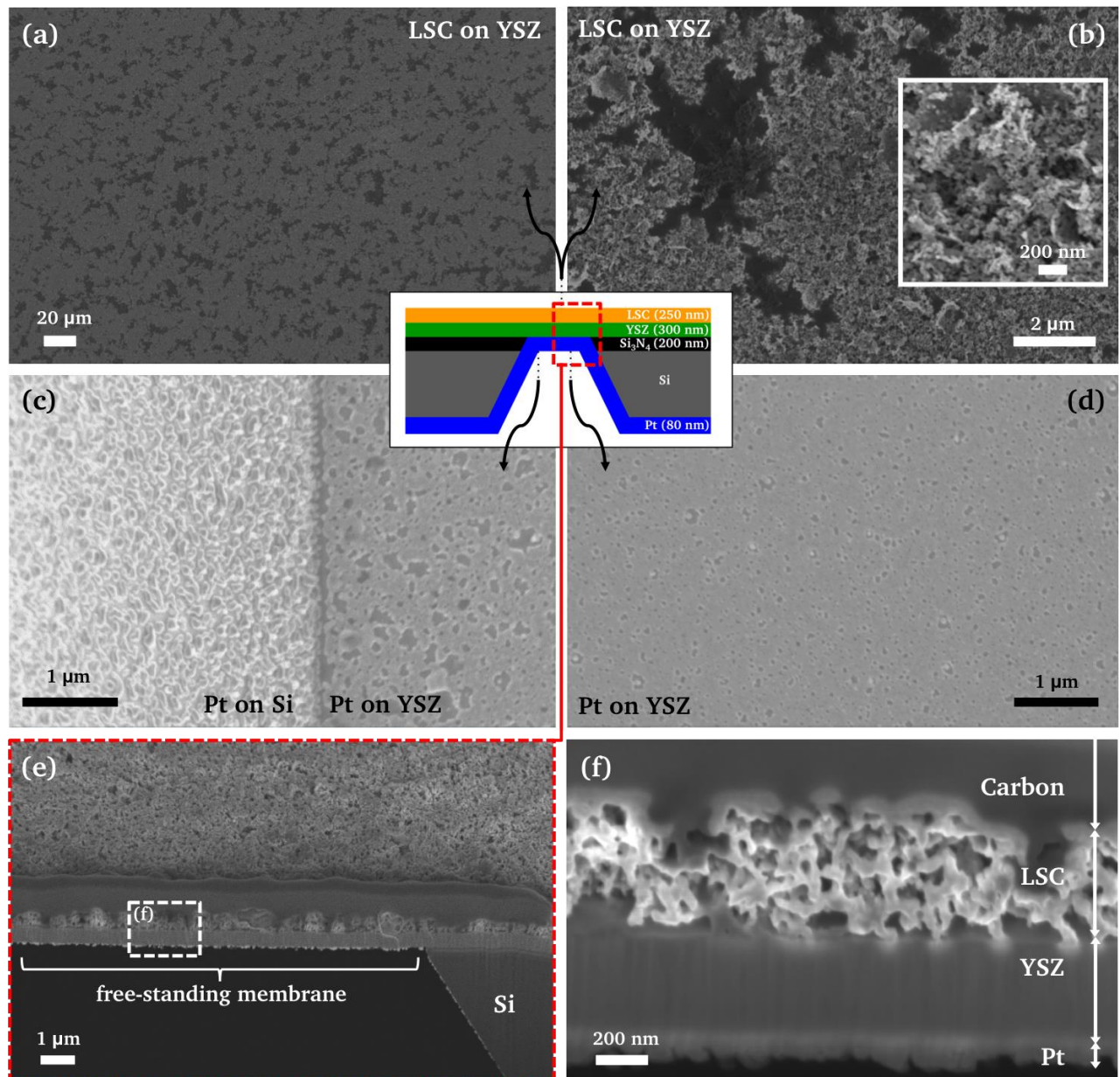
Figure 6-9: SEM (top-view) and FIB (cross-sectional) analyses of LSC|3YSZ|Pt micro-SOFCs with buckled 3YSZ membranes after the fuel cell testing. a) Top-view image of a micro-SOFC membrane covered by LSC cathode and (b) higher magnification images showing the cathode microstructure. c, d) Bottom-view image of a micro-SOFC membrane covered by Pt anode layer. e) FIB cross-sectional image of a freestanding buckled micro-SOFC membrane. f) High magnification image of the micro-SOFC membrane evidencing the 3D-architecture of the 250 nm thick cathode, the 300 nm thick dense 3YSZ electrolyte, and the 80 nm thick Pt anode layers in the membrane after testing at 500 °C for 1 h.
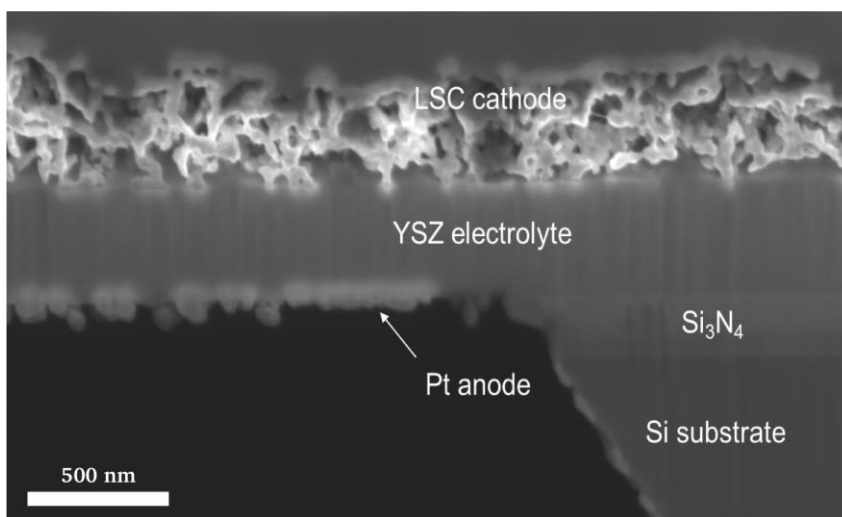
Figure 6-10: FIB cross-sectional image of a freestanding buckled micro-SOFC membrane after fuel cell testing at 550 °C for 1 h.

distributed pores, which is favorable for gas circulation and oxygen exchange. The 80 nm thick sputtered Pt anode layers seem to adhere well to the electrolyte layer. The degradation of anode layer asociated with the coarsening of Pt grains is more pronounced in Figure 6-10. Another important aspect, which can be observed in this sample is the broken continuity of the Pt anode layer especially at the trenches of the etched Si side-wall and the bottom of the freestanding membranes.

This first set of electrochemical data clearly demonstrates that it is possible to integrate porous electrodes using atmospheric deposition techniques in silicon-supported micro-SOFC membranes. Furthermore, the thickness of spin-coated LSC cathodes integrated in micro-SOFC membranes in this work is significantly higher than the (B)LSC(F)-based micro-SOFC cathodes reported in literature, which are typically fabricated by physical vapor deposition methods [104], [112], [190], [236], [237], [241]. This is a promising result for the future enhancement of the electrocatalytic activity of the MIEC cathode layers in micro-SOFC devices. However, the maximum power density obtained from the micro-SOFC membranes with spin-coated LSC cathodes is lower than the 200 mW/cm^2 of the micro-SOFC chips with pulsed layer deposited LSC cathodes measured at 400 °C [112]. Figure 6-11 presents the maximum power densities obtained in this work along with the literature data for micro-SOFCs with (B)LSC(F)-based electrodes. The lower electrochemical performance of the micro-SOFCs obtained in this work is attributed mainly to the poor electrochemical activity of the spin-coated LSC cathodes. It has been shown in the previous chapter that the 250 nm thick LSC cathodes post-annealed at 650 °C for 1 h subsequent to spin coating have area specific polarization resistance of 15 Ω cm^2 at 550 °C under open-circuit conditions. The possibility of the formation of an insulating layer at the LSC/YSZ interface is neglected, since micro-SOFCs are subjected to relatively low temperatures during fabrication and fuel cell testing. The leveling off of the power density above 455 °C indicated by an extrapolation in Figure 6-11 is attributed to the fast degradation of the Pt anode [112], [192]. This is also in good agreement with the microstructural observations regarding the anode degradation.

As already discussed in previous chapter, the electrochemical activity of the spin-coated LSC cathodes can be improved by a number of approaches such as blending the LSC cathodes with GDC20 nanoparticles leading to nanocomposite thin film electrodes, post-annealing of the spin-coated LSC cathodes at higher temperatures than 650 °C, and increasing the electrode thickness. The initial experiments aiming the proof of concept for the fabrication of porous micro-SOFC electrodes by spin coating do not cover those approaches due to the following reasons: Firstly, the
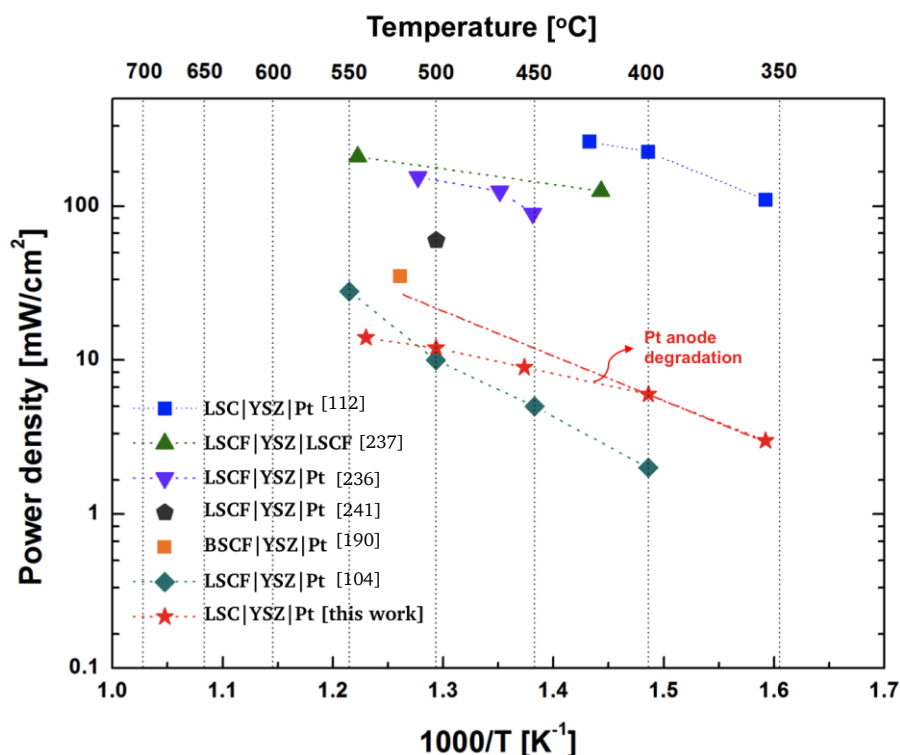
Figure 6-11: The peak power densities of micro-SOFCs with (B)LSC(F)-based electrodes.

LSC-GDC composite cathodes are not considered for the purpose of the performance comparison with the micro-SOFCs utilizing typically single phase (B)LSC(F)-based electrodes. Even though LSC-GDC cathodes have enhanced electrochemical performance in conventional SOFC design, which typically utilizes an additional current collector layer, percolating GDC nanoparticles within the LSC cathodes might reduce the in-plane electronic conductivity of the cathode layers and eventually current collection ability, as no additional current collector layer is utilized in fuel cell testing experiments. Secondly, the maximum post annealing temperature is limited to 600 °C in accordance with the thermomechanical stability study of freestanding YSZ membranes by Evans *et. al.* [223]. The annealing duration is also kept as short as possible (maximum 1 hour) to prevent any interfacial reactions towards zirconate formation. Finally, the electrode thickness of 250 nm is not exceeded due to the uncertainty about the thermomechanical limits of the micro-SOFC membranes.

6.2. LSC Cathodes in Anode-supported SOFC Design

Within this part of the thesis, the spin-coated and screen-printed LSC cathodes are implemented in the state-of-the-art anode-supported SOFC design to demonstrate the applicability.

The half-cells consisting of NiO-GDC20 (60:40 wt.%) anode supports and thin GDC10 electrolyte layers are fabricated identically for all samples. The anode-supported SOFC design with spin coated LSC cathodes is shown schematically in Figure 6-12a and denoted as SC-SOFC (spin-coated SOFC) hereafter. In the SC-SOFC samples, the screen-printed LSM current collector layers are utilized to improve the current collection from the thin film LSC cathode layers. On the other hand, a current collector layer is not applied to the samples with screen-printed LSC cathodes (Figure 6-12b), as the thickness of the cathode layers are sufficiently high for the proper current collection. The anode-supported SOFCs with screen-printed LSC cathodes are abbreviated as SP-SOFCs.

Figure 6-12c shows the photographs of a pre-sintered anode support (I), a GDC10|NiO-GDC20 half-cell (II), and a full SOFC (LSC|GDC10|Ni-GDC20) with a screen-printed LSC cathode (III). Both screen printing and spin coating deposition techniques lead to a proper and uniform surface coverage of the substrates with desired electrolyte and cathode layers. The deposition and post sintering steps do not lead to any visible cracks or delamination within the samples. After the co-sintering step of anode support/electrolyte bilayers, no obvious bending is observed from the edges of the sample. The cell area is limited by the size of anode supports, even though it is possible to fabricate SOFC components in larger scales by spin coating and screen printing deposition techniques. Readers may refer to the Sections 3.2 and 3.4 for detailed information on the fabrication of individual SOFC components and anode-supported SOFCs.

The cross-sectional SEM images of the SC-SOFC are given in Figure 6-13. The low magnification image given in Figure 6-13a shows that after sintering at 1400 °C for 3 h, the screen-printed GDC10 electrolyte layer is dense without any open pores between the Ni-GDC20 cermet anode support (bottom layer) and the LSC/LSM bi-layered cathode layer (top layer), which indicates that the GDC10 electrolyte layers are gas-tight. The electrolyte layer is uniform in thickness and adheres well to the adjoining cell components. The average thickness of the GDC10 electrolyte is found to be approximately 11 μm. Both electrodes have a porous microstructure, which is favored for an effective gas circulation. High magnification images in Figure 6-13b and c show that both cathode and anode layers adhere well to the GDC10 electrolyte and show an excellent continuity along the electrode/electrolyte interfaces. The cathode layer of the SC-SOFC sample consists of a thin spin-coated nanoparticulate LSC layer with an approximate thickness of 1.5 μm and a screen-printed LSM current collector layer with an approximate thickness of 17 μm. The cathode bilayer is homogenous, continuous, and well formed. The Ni-GDC20 anode support has the thickness of approximately 1 mm (not shown in SEM images in Figure 6-13) and a porous microstructure, which provides not only easy transport of the fuel gas but also higher surface area for the fuel oxidation. To confirm homogeneity of the Ni and GDC20 phases within the anode support, the elemental distribution is characterized at micrometer scale by EDS displaying the integrated intensity of elemental signals as a function of beam position in the SEM. The SEM image in Figure 6-14a and the corresponding elemental distributions of Ni, Ce, and Gd (Figure 6-14b–d) show that the Ni and GDC20 phases are homogeneous and well percolated in the anode supports. The comparison between the microstructures of LSC cathode layer and anode support indicate that Ni-GDC20 anode support consists of much coarser particles, which is due to the high
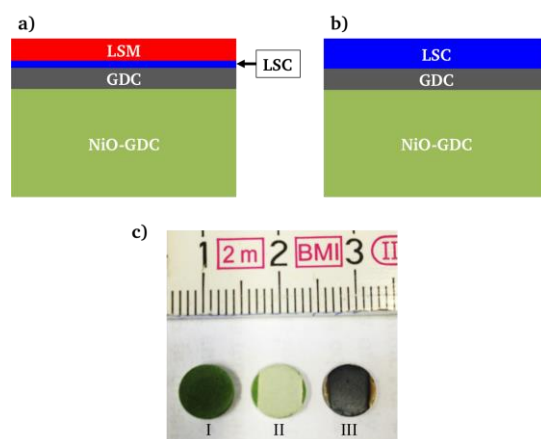
Figure 6-12: Schematic representations of the (a) spin-coated (SC-SOFC) and (b) screen-printed (SP-SOFC) anode-supported SOFC designs used for the fuel cell testing. c) The photograph showing (I) a pre-sintered NiO-GDC20 anode support, (II) a NiO-GDC20|GDC10 half cell prior to the sintering, and (III) a Ni-GDC20|GDC10|LSC SP-SOFC after post-deposition annealing at 900 °C.
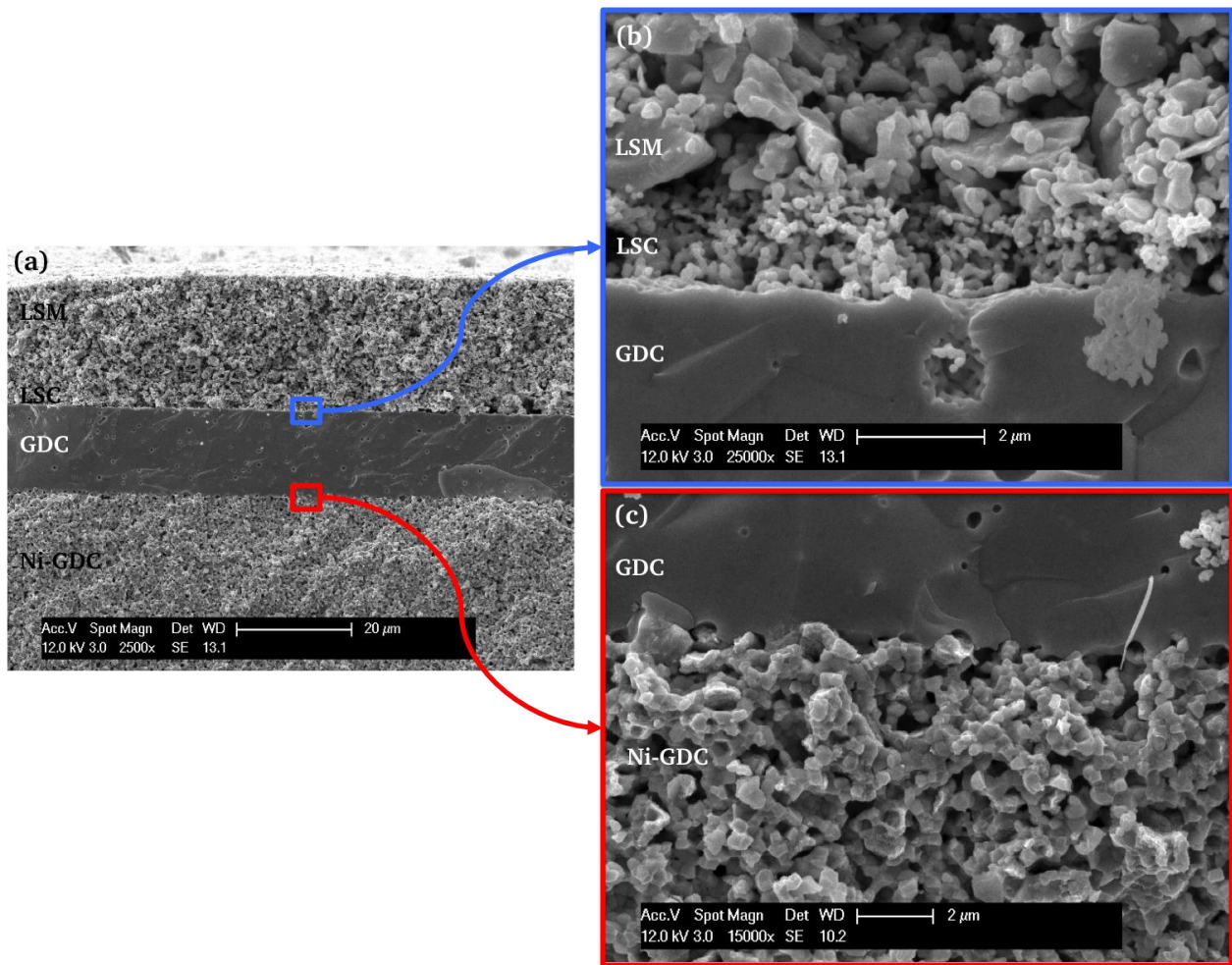
Figure 6-13: Cross-sectional SEM images of a fractured SC-SOFC before fuel cell testing. a) Low magnification cross-sectinal image showing the porous electrode and dense electrolyte layers. b, c) High magnification images of the electrode/electrolyte interfaces. The anode side of the sample is reduced prior to the SEM investigation to confirm the porosity of the anode support.

sintering temperature of the anode support/electrolyte bilayers. The SEM images before and after the fuel cell tests indicate that the porous microstructure of the anode supports is induced upon the volume change accompanied by the reduction of NiO to Ni by the fuel gas flow. The typical bimodal pore distribution reported in cermet anode supports [242]–[244] is not observed, as no pore-forming agents are used during the anode support fabrication. The decomposition of the pore formers usually leads to pores with larger sizes, whereas the fine pores typically originate from the reduction of NiO to Ni.

Figure 6-15 shows the current-voltage and power density characteristics of the SC-SOFC at different temperatures. The open circuit voltage values are 0.908, 0,96, and 1.093 V at 600, 550,
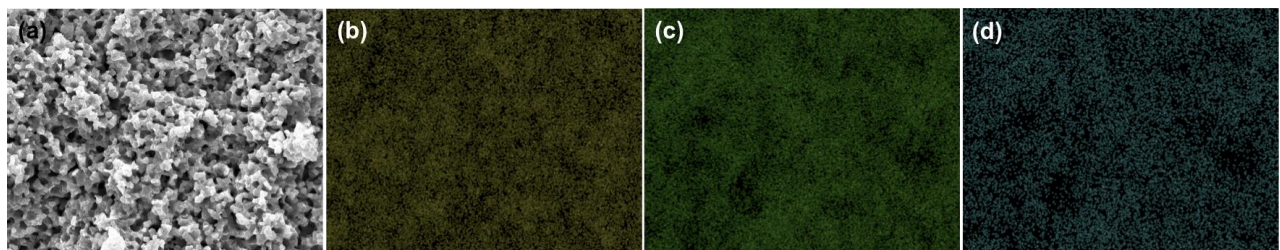
Figure 6-14: SEM image of the Ni-GDC20 anode support (a) and corresponding elemental EDX maps showing the distribution of (b) Ni, (c) Ce, and (d) Gd.
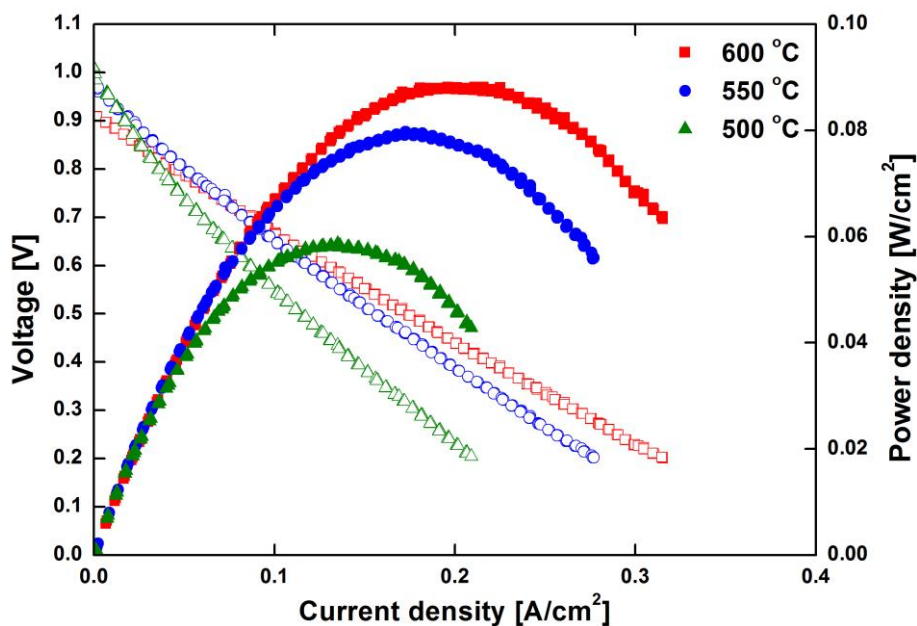
Figure 6-15: Cell voltage and power density curves obtained from the SC-SOFC at 600, 550, and 500 °C using air as oxidant and humidified 5 vol.% H_2 in Ar as fuel.

and 500 °C, respectively, which are acceptable for GDC-based SOFCs [245] and in a good agreement with the OCV values of the GDC based SOFCs reported in the literature [185], [186], [188]. The lower OCVs than the theoretical ones are attributed to the internal short circuit of the GDC electrolyte layer induced by the exposure to the reducing atmospheres [188]. It can be seen that there is a non-linear relationship between the cell voltage and the current density, which can be explained by distinct sources of the cell polarization at different current densities. At lower current densities the overpotential can be attributed to the activation polarizations, while at higher current densities the Ohmic polarization is mainly responsible for the reduction of the cell voltage, as the cell voltage decreases linearly with increasing current density. The maximum power densities are 88, 79, and 58 mW/cm^2 at 600, 550, and 500 °C, respectively.

To determine the possible reasons for the poor electrochemical performance of the cells with spin-coated LSC thin film cathodes, EIS measurements are conducted. Figure 6-16 shows the impedance spectrum of a single SC-SOFC measured under open circuit conditions at 600 °C using air as oxidant and humidified 5 vol.% H_2 in Ar as fuel. The positive imaginary component at high frequency part of the complex impedance plot is attributed to the inductance of the electrical cables of the measurement system [246]. The impedance spectrum consists of partially overlapping semicircles and can be divided into three regions: a high-frequency region with $f > 1$ kHz, a mid-frequency region with 1 Hz $< f < 1$ kHz, and a low-frequency region with $f < 10$ mHz. Based on the literature [247], the high- and mid- frequency semicircles are associated with the electrode related charge transfer and the surface exchange processes, while the low-frequency semicircles are typically attributed to the gas diffusion limitations within the electrode layers. The area specific Ohmic resistance (ASR$_{Ohmic}$) of the cell is determined from the high frequency intercept of the impedance spectrum with the real axis of the Nyquist plot, while the area normalized electrode polarization resistance (ASR$_{pol}$) is obtained from the difference between the high and low frequency intercepts of the impedance spectrum with the real axis of the Nyquist plot. Since the low frequency data does not reach to the real axis, the intercept point at low frequency part of the spectra is estimated by extrapolation. The extremely high ASR$_{Ohmic}$ of 3.7 Ω cm^2 and ASR$_{pol}$ of approximately 60 Ω cm^2 can be explained by several potential complications. Since the OCV values are in a good agreement with literature data, the low performance of the cell
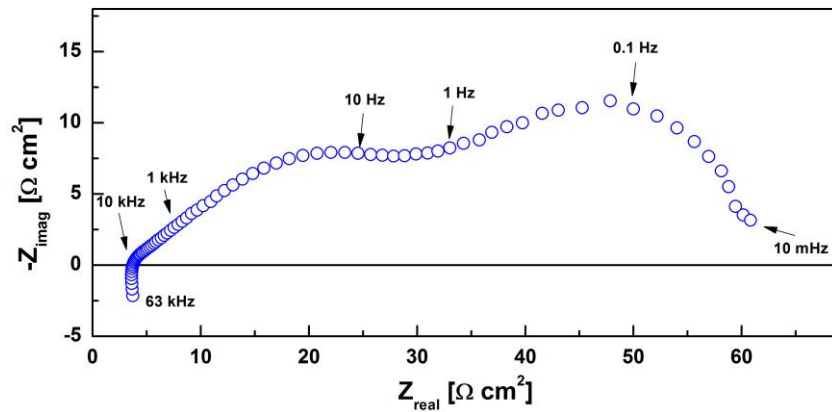
Figure 6-16: Impedance spectrum of the SC-SOFC at 600 °C recorded using air as oxidant and humidified 5 vol.% H_2 as fuel under open circuit conditions.

is not attributed to the failure of the electrolyte layer. The possibility of the formation of any insulating layers at the cathode/electrolyte interface is also neglected, as the cathode layers are not subjected to high temperatures during the fabrication and the fuel cell testing. Instead, the SEM analyses after the fuel cell testing confirm the delamination between the spin-coated LSC cathode layers and the GDC10 electrolyte. The cracks at the interfaces are shown in Figure 6-17a–c. The complete failure of the cathode layer is also observed in other parts of the same sample (Figure 6-17d). The failure of the cathode layer is most probably due to the thermal expansion
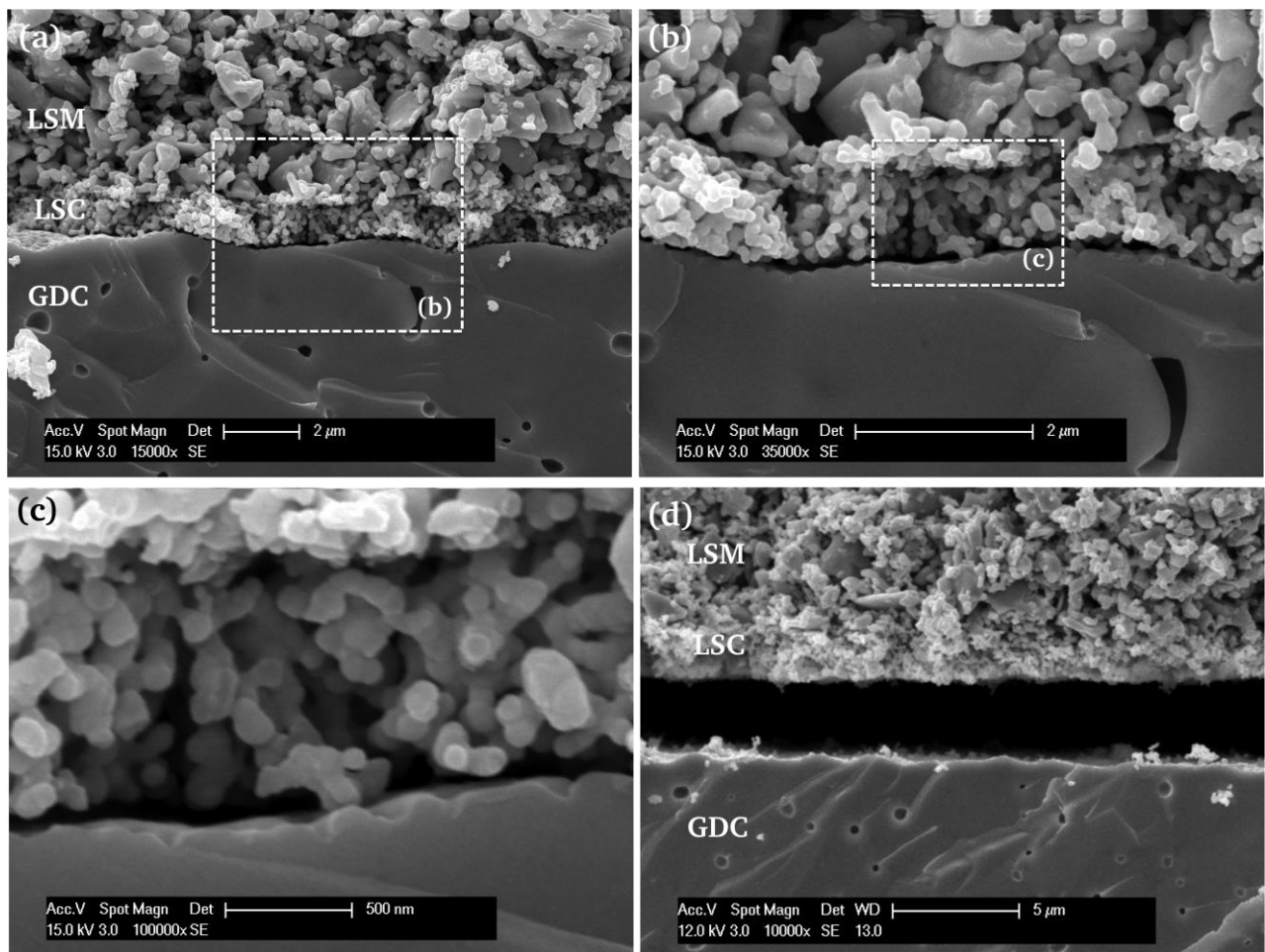
Figure 6-17: Cross-sectional SEM images of SC-SOFC after the fuel cell testing. a, b, c) SEM images showing surface cracks at different magnifications. d) SEM image shows the delamination at the cathode/electrolyte interface.

coefficient mismatch between the GDC10 electrolyte ($TEC_{GDC}=12\times10^{-6}$ 1/K [90]) and the cathode components of LSC (18–26×10^{-6} 1/K [81], [84], [88], [89]) and LSM ($TEC_{LSM}=12.4\times10^{-6}$ 1/K [248]). The delamination of the cathode layer causes the decrease of reaction sites and eventually leads to larger ASR values.

The symmetrical cells consisting of GDC10 electrolyte, LSC thin cathodes, and LSM current collector layers were utilized in the previous chapter to characterize the electrochemical performance of the spin-coated thin LSC cathode layers. However, no sign of delamination was observed in those samples. The distinct behavior of the same interfaces might be attributed to the different experimental conditions. The symmetrical samples with LSM/LSC/GDC interfaces were only characterized under open circuit conditions, whereas the LSM/LSC/GDC interfaces in anode-supported SOFC configuration undergo cathodic overpotentials.

To overcome the possible thermomechanical stresses leading to the delamination of the LSC cathode/LSM current collector bi-layer from the GDC10 electrolyte, only a screen-printed LSC layer is utilized as cathode (Figure 6-12b). The cross-sectional SEM micrographs of the SP-SOFC are given in Figure 6-18. The microstructural features of the GDC10 electrolyte and Ni-GDC20 anode support are indistinguishable from ones of SC-SOFC samples, as they are fabricated identically for all samples. The screen-printed LSC electrode layer with an approximate thickness of 10 μm has a porous microstructure, which is favored for an effective gas circulation. High magnification images in Figure 6-18b–d show that the screen-printed LSC cathode adheres well to
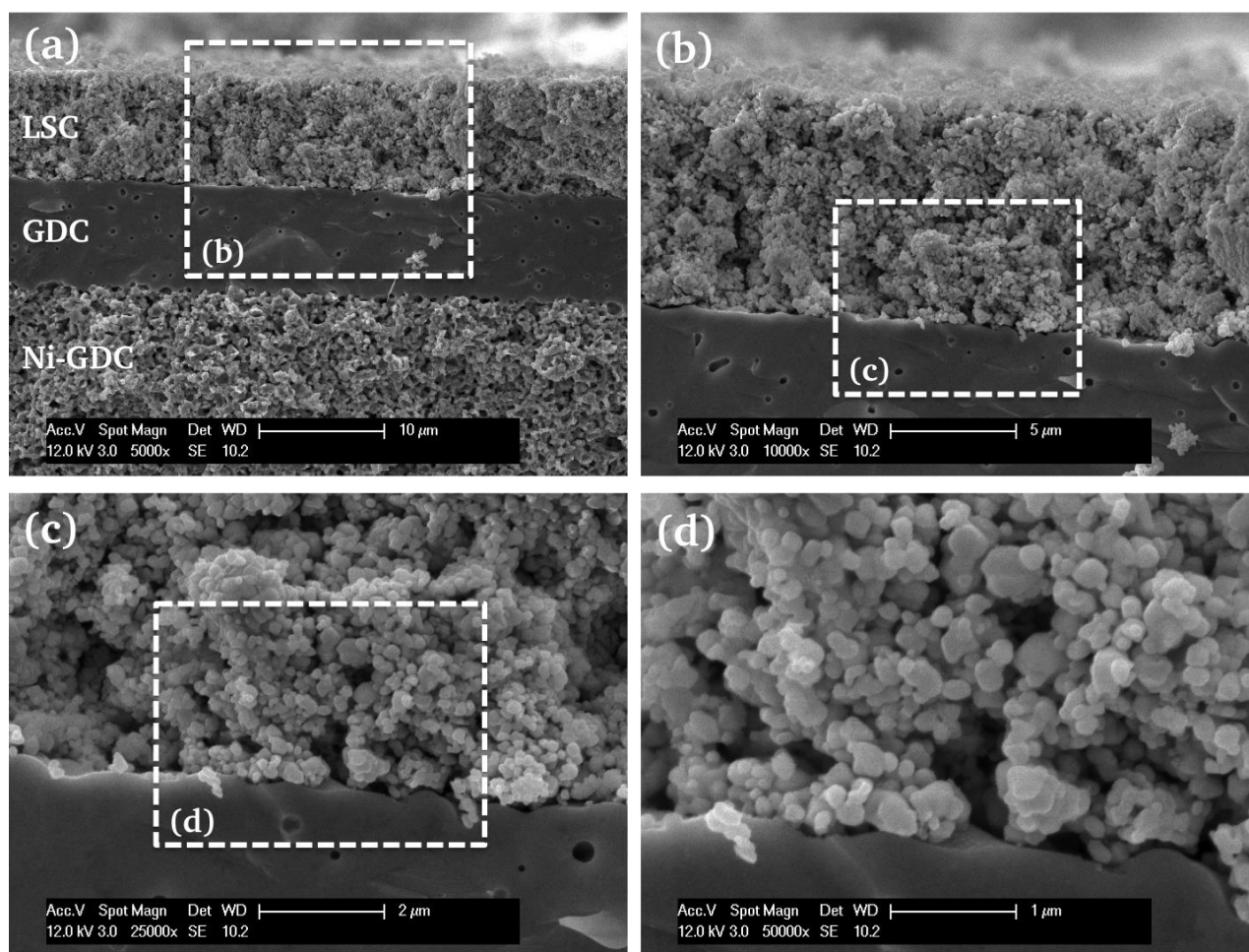
Figure 6-18: Cross-sectional SEM images of a fractured SP-SOFC before fuel cell testing. a) Low magnification cross-sectinal image showing the porous electrode and dense electrolyte layers. b, c, d) High magnification images of the electrode/electrolyte interfaces. The anode side of the sample is reduced prior to the SEM investigation to confirm the porosity of the anode support.

the GDC10 electrolyte and shows an excellent continuity along the cathode/electrolyte interface.

Figure 6-19 shows the current-voltage and power density characteristics of the SP-SOFC at different temperatures. The open circuit voltage (OCV) values are 0.938, 0.921, and 0.952 V at 600, 550, and 500 °C, respectively. Similar to the SC-SOFCs, there is a non-linear relationship between the cell voltage and current density, which can be explained by distinct sources of the cell polarization at different current densities. The maximum power densities are 318, 153, and 52 mW/cm^2 at 600, 550, and 500 °C, respectively. The peak power density at 600 °C is improved from 88 to 318 mW/cm^2 by changing the cathode design from bi-layered LSC-LSM to one-layered LSC cathode, which can be attributed to the better thermomechanical stability of the screen-printed LSC cathode layers, as no evidence of delamination is found in SEM investigations conducted after the fuel cell tests.

In Table 6-1, the maximum power density value obtained in this work is compared to those reported in the literature with similar cell designs and comparable electrode material systems. Recently, Lee *et. al.* [245] have reported the Ni-GDC10|GDC10(4.9 μm)|BSCF-GDC10 cell with a core/shell cathode microstructure exhibiting exceptional power densities above 2 W/cm^2 at 600 °C. Gwon *et. al.* [172] have also obtained impressive power density (1.58 W/cm^2 at 600 °C) from the GDC-based anode-supported SOFCs with LSC-GDC composite cathode synthesized by a Pechini method. The relatively lower power density value (318 mW/cm^2 at 600 °C) reported in this work might stem from several reasons. The most conspicuous cause for the low power density is the low concentration of H$_2$ in the fuel used in fuel cell testing, which might contribute to the electrode polarization of the anode supports by increasing the mass transport losses. The low reactant concentration can be problematical issue at the anode side of the SOFC due to the large thickness of the anode support layers (0.8–1 mm). Furthermore, high Ohmic and activation polarization losses might also lead to the reduction of the power density of cells. To determine the origins of cell polarizations individually, EIS measurements are conducted.
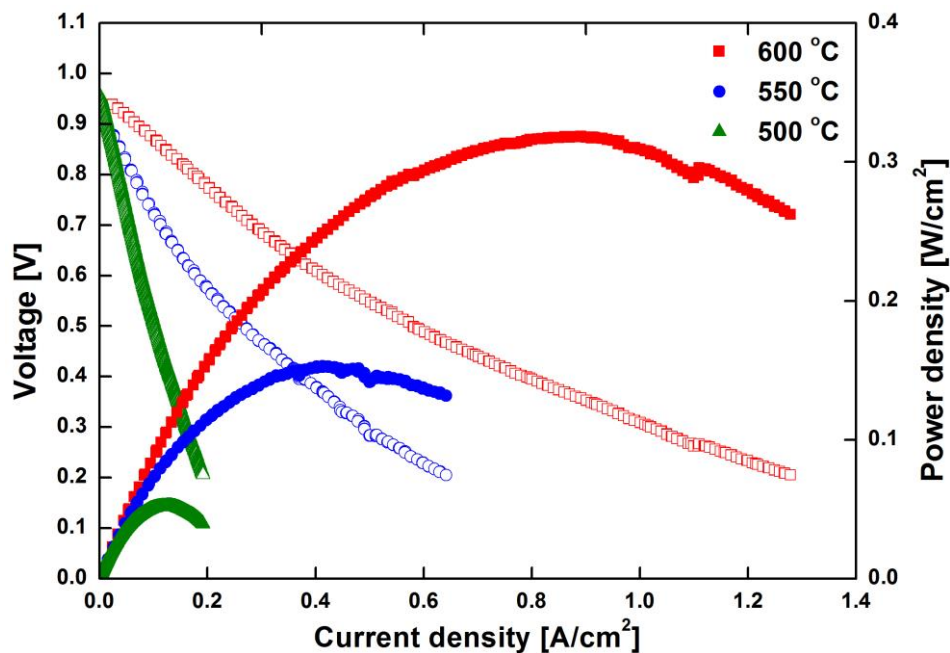
Figure 6-19: Cell voltage and power density curves obtained from the SP-SOFC.

Table 6-1: Peak power density values of GDC-based anode-supported SOFCs obtained at 600 °C with comparable electrode materials. All SOFCs ustilize air as oxidant.

Anode|Electrolyte|Cathode	Electrolyte thickness (μm)	Power density (mW/cm^2)	Fuel	Ref
Ni-GDC|GDC|BSCF-GDC	4.9	2110	Pure H$_2$	[245]
Ni-SDC|GDC|BSCF-SDC	20	1010	3 vol.% humidified H$_2$	[37]
Ni-GDC|GDC|LSCF-GDC	30	1021	3 vol.% humidified H$_2$	[185]
Ni-GDC|GDC|LSC-GDC	14.8	1580	3 vol.% humidified H$_2$	[172]
Ni-GDC|GDC|LSC	10	318	Humidified H$_2$:Ar 1:19	This work

Figure 6-20 shows the impedance spectrum obtained from the SP-SOFC sample at 600 °C under open circuit conditions using 21 vol.% air in N$_2$ as oxidant and humidified 5 vol. % H$_2$ in Ar as fuel. Similar to the SC-SOFC, the impedance spectrum consists of partially overlapping semicircles and can be divided into three regions: a high-frequency region with $f>1$ kHz, a mid-frequency region with 1 Hz$<f<1$ kHz, and a low-frequency region with $f<10$ mHz. Due to the overlapping of the time constants of the distinct processes, the total impedance response of the cell cannot be reliably fitted using an equivalent circuit. Therefore, the Ohmic loss of the cell is obtained from the high frequency intercept, while the electrode polarization resistance is extracted from the difference between the high and low frequency intersections/projections on real axis of the Nyquist plots. Under specified measurement conditions, the ASR$_{Ohmic}$ and ASR$_{pol}$ values are found to be as 0.17 and 1.92 Ω cm^2, respectively. In comparison to the reported Ohmic resistance values of the anode-supported SOFCs of Ni-GDC10\|GDC10(30 μm)\|LSCF-GDC10 (ASR$_{Ohmic}$=0.06 Ω cm^2 at 600 °C [185]) and Ni-GDC10\|GDC10(10 μm)\|BSCF (ASR$_{Ohmic}$=0.07 Ω cm^2 at 600 °C [249]) cells having comparable electrolyte thicknesses, the higher Ohmic resistance obtained for the cells in this work might be attributed to higher Ohmic resistance of electrode layers and/or poor current collection from the cells.

Even though the Ohmic loss of the SP-SOFC is slightly higher than those reported in the literature, the performance of the cell is limited by non-Ohmic losses, as the ASR$_{pol}$ is one order of magnitude larger than the ASR$_{Ohmic}$. In order to observe the effect of the H$_2$ concentration on the fuel cell performance, the impedance spectroscopy measurements are conducted using the same

Figure 6-20: Impedance spectrum of the SP-SOFC at 600 °C recorded using air as oxidant and humidified 5 vol.% H$_2$ as fuel under open circuit conditions.
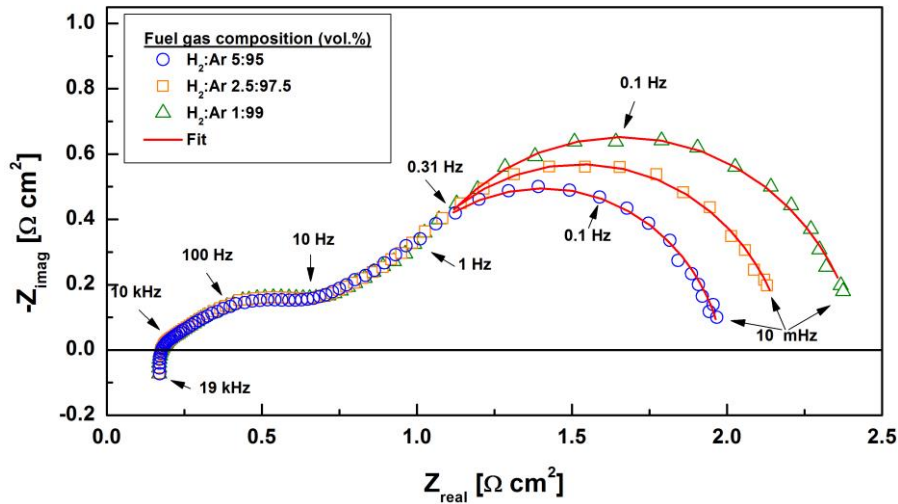
Figure 6-21: Impedance spectra of the SP-SOFC at 600 °C under open circuit conditions.

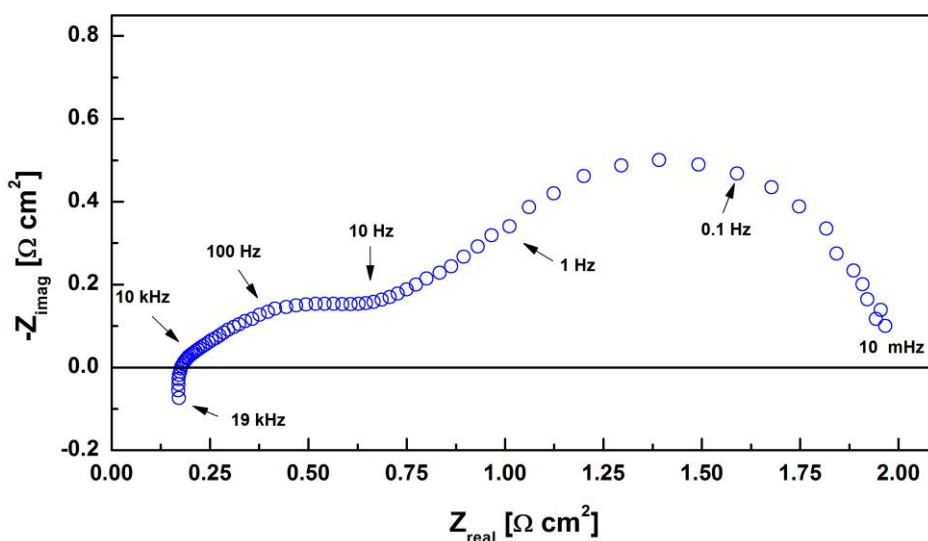sample by systematically changing the concentration of H_2 in the fuel gas, while the oxygen concentration remains constant at the cathode side of the cell. Figure 6-21 shows the evolution of the impedance spectra upon the dilution of the fuel gas. As the fuel is diluted, the ASR_{pol} of the cell increases. Furthermore, it is observed that only the low frequency processes are influenced by the fuel composition, while the processes at higher frequency parts of the spectra are unaffected. Therefore, the low frequency part of the impedance spectra are fitted using an equivalent circuit consisting of a resistance (R_L) and a constant phase element (CPE_L) connected in parallel. The fits are shown with solid red lines in the Nyquist plot in Figure 6-21 and the fitting parameters are listed in Table 6-2 along with the estimated Ohmic (ASR_{Ohmic}) and total polarization (ASR_{pol}) losses.

Table 6-2: The parameters used for the equivalent circuit model fitting of a part (0.3–0.01 Hz) of the impedance spectra recorded at 600 °C obtained from the SP-SOFC by changing the concentration of H_2 in the fuel gas. The true capacitance (C^*) and the relaxation frequency (f^*) values calculated using the CPE parameters are also given for each process. Estimated Ohmic (ASR_{Ohmic}) and total polarization (ASR_{pol}) losses are also listed for the purpose of the comparison.

H_2 concentration in fuel gas (vol. %)	ASR_{Ohmic} (Ω cm^2)	ASR_{pol} (Ω cm^2)	R_L (Ω cm^2)	CPE_L		C_L^* (F/cm^2)	f_L^* (Hz)
				Q_L	n_L		
1	0.17	2.38	1.58	1	0.89	1.05	0.09
2.5	0.17	2.17	1.37	0.86	0.88	0.87	0.14
5	0.17	1.92	1.13	0.85	0.88	0.84	0.14

Depending of the magnitude of the calculated capacitance values, the low frequency semicircles might be attributed to the mass transfer processes rather than the charge transfer and the surface exchange including the adsorption/diffusion/dissociation processes [33], [247]. Apparently, the low frequency semicircle is dependent of the partial pressure of H_2 and decreases as the concentration of H_2 in the fuel gas increases. Furthermore, the polarization loss of the SP-SOFC is dominated by the processes observed at low frequency part of the impedance spectra. This indicates that higher power densities can be obtained simply by utilizing fuels with higher H_2 concentration than 5 vol.%.

6.3. Summary & Conclusion

The proof of concept for the fabrication of porous micro-SOFC electrodes by spin coating of suspensions onto freestanding membranes is demonstrated for the first time. The amount of the

compressive stress present in the 3YSZ membranes has an effect on mechanical and thermomechanical stability of the micro-SOFCs during the fabrication and the operation. Thin LSC cathodes are fabricated by spin coating on weakly buckled (compressive stress) 3YSZ freestanding membranes successfully with a survival rate higher than 95%. The thermal expansion coefficient mismatch between the LSC and 3YSZ is compensated by the intrinsic compressive stress of the 3YSZ membranes. A micro-SOFC membrane consisting of an LSC cathode (250 nm), a weakly buckled 3YSZ electrolyte (300 nm), and a Pt anode (80 nm) exhibit an open-circuit voltage of 1.05 V and a maximum power density of 12 mW/cm^2 at 500 °C. The low electrochemical performance of the micro-SOFC membranes is attributed to the high electrode polarization originating most probably from the LSC cathode. Due to the thermomechanical ambiguity, the LSC|3YSZ bi-layers cannot be annealed at temperatures higher than 550 °C subsequent to spin coating, even though relatively higher temperatures and longer durations are needed to obtain LSC cathodes with improved electrochemical properties. Furthermore, the fuel cell testing is limited by the Pt anode degradation, which is observed by the presence of the leveling off the power densities above 450 °C.

The state-of-the-art electrode materials LSC and NiO-GDC20 obtained by salt-assisted spray pyrolysis are utilized for the fabrication of electrodes for the anode-supported SOFCs. The disc-like NiO-GDC20 anode support/GDC10 electrolyte bi-layers are obtained by uniaxial pressing of spray-pyrolyzed NiO-GDC20 nanopowders and subsequent GDC10 electrolyte deposition by screen printing. The SOFCs with the spin-coated thin LSC cathodes show poor electrochemical performance, which is mainly attributed to the thermomechanical failure of the cathode layers during the fuel cell testing. On the other hand, the SOFCs with the screen-printed LSC cathodes exhibit promising electrochemical performance (318 mW/cm^2 at 600 °C). The performance improvement in the maximum power density of the SOFCs is attributed to the improved thermomechanical stability of the cell components. Electrochemical impedance spectroscopy experiments indicate that the lower electrochemical performance of the anode-supported SOFCs compared to those reported in the literature might stem from the use of diluted fuel, high activation losses associated with the electrodes, and poor current collection.

7. Conclusions and Outlook

7.1. Conclusions

The main findings of the research covered in this thesis are summarized as follows:

I. The salt-assisted spray pyrolysis method allows for the synthesis of phase pure nanostructured electrode materials of $La_{0.6}Sr_{0.4}CoO_{3-\delta}$ and $NiO-Ce_{0.8}Gd_{0.2}O_{2-\delta}$. The morphology of the powders can be tailored in terms of particle size from the micro scale down to the 50 nm by adjusting the synthesis parameters, *i.e.*, pyrolysis temperature and NaCl concentration of the precursor solution.

II. The modification of the ultrasonic spray pyrolysis method by the utilization of NaCl does not only result in nanoparticles with smaller particle sizes and narrower size distributions but also leads to a substantial increase in specific surface area by 50%, which is particularly crucial since high surface area of nanoparticulate electrodes would significantly increase the length of triple phase boundaries and the number of active reaction sites of composite and mixed ionic-electronic conductive electrodes, respectively.

III. The spectroscopic analyses confirm the chemical composition and the purity of the electrode materials both at micro (SEM) and nanoscale (STEM). It is verified that utilization of NaCl does not lead to any contamination of the products, as neither Na nor Cl signal is detected in the EDX spectroscopy analyses. In addition, the STEM–EDX elemental mapping experiments indicate that a homogeneous elemental distribution at nanoscale is obtained.

IV. The nanostructured LSC cathodes and Ni-GDC20 anodes with thicknesses in the range of 200–800 nm are successfully fabricated on the electrolyte substrates by spin coating of the stabilized dispersions of the synthesized nanoparticles. The resulting thin film electrodes exhibit porous microstructure. Additionally, they are continuous, crack-free, and homogeneous.

V. The electrochemical impedance spectroscopy measurements conducted on symmetrical cells show that a post-deposition annealing step at 650 °C for 1 hour leads to the polarization resistance values of 3.71 and 30.3 Ω cm^2 at 600 °C for the 500 nm thick LSC and Ni-GDC20 electrodes, respectively. These initial low performances of the electrodes are attributed to the potentially high contact resistance within the electrodes and at the electrode/electrolyte interfaces. As an alternative to the conventional sintering approach at elevated temperatures to obtain improved inter- and intra-layer contacts, the efforts to improve the electrochemical performance of the LSC cathodes

focus on the fabrication of LSC-GDC20 nanocomposite cathodes. Using this approach, the polarization resistance values of the 500 nm thick LSC cathodes are successfully reduced from 3.71 down to 0.24 Ω cm^2 by only percolating highly ionic conductive commercially available GDC20 nanoparticles within the cathode microstructure. This performance improvement by a factor of more than one order of magnitude is promising, since no high-temperature annealing step is employed. Therefore, the proposed cathode fabrication method can be integrated to the fabrication of the micro-SOFC devices as an alternative to the costly and time-consuming physical vapor deposition methods.

VI.   Further investigations reveal that the post-deposition annealing steps have also an impact on the electrochemical performance of the LSC cathodes. The 500 nm thick LSC cathodes annealed at 900 °C for 2 hours lead to the minimum polarization resistance value of 0.096 Ω cm^2, which puts the spin-coated thin film LSC cathodes obtained in this work among the best (B)LSC(F)-based cathodes with submicron thicknesses reported in the literature. Similar to the LSC cathodes, the post-deposition annealing step at 900 °C for 2 hours lead to the minimum polarization resistance value of 8.2 Ω cm^2 for the 500 nm thick Ni-GDC20 anodes, which is also comparable to the reported polarization resistance values of the anodes with similar thicknesses, microstructural features, and composition. The versatility of the proposed method and the high electrochemical performance of the resulting electrodes make this electrode fabrication technique an important candidate for the nanoscaled electrode technology for low temperature SOFCs operating at 600 °C and below.

VII.   The proof of concept for the fabrication of porous micro-SOFC electrodes by spin coating of dispersions on the freestanding membranes is demonstrated for the first time. The amount of the compressive stress present in the 3YSZ membranes has an effect on the mechanical and thermomechanical stability of the micro-SOFCs during the fabrication and the operation. Thin LSC cathodes are fabricated by spin coating on the weakly buckled (compressive stress) 3YSZ freestanding membranes successfully with a survival rate higher than 95%. A micro-SOFC membrane consisting of an LSC cathode (250 nm), a weakly buckled 3YSZ electrolyte (300 nm), and a Pt anode (80 nm) exhibit an open-circuit voltage of 1.05 V and a maximum power density of 12 mW/cm^2 at 500 °C.

VIII.   The LSC and NiO-GDC20 electrode materials obtained from salt-assisted spray pyrolysis are utilized for the fabrication of electrodes for the anode-supported SOFCs. The disc-like NiO-GDC20 anode support/GDC10 electrolyte bi-layers are obtained by uniaxial pressing of spray-pyrolyzed NiO-GDC20 nanopowders and subsequent GDC10 electrolyte deposition by screen printing. The SOFCs with the spin-coated thin LSC cathodes show poor electrochemical performance, which might be attributed to the thermomechanical failure of the cathode layers during the fuel cell testing due to the thermal expansion coefficient mismatch between the thin LSC cathode functional layer and the thick LSM current collector layer. On the other hand, the SOFCs with the screen-printed LSC cathodes exhibit promising electrochemical performance (318 mW/cm^2 at 600 °C). The performance improvement in the maximum power density of the SOFCs is attributed to the improved thermomechanical stability of the cell components. Electrochemical impedance spectroscopy experiments indicate that the lower electrochemical performance of the anode-supported SOFCs compared to those reported in the literature might stem from the use of diluted fuel, high activation losses associated with the electrodes, and poor current collection.

7.2. Outlook

I. The electrochemical performances of the electrodes are strongly dependent on the number of the active reaction sites that they provide. The modification of the synthesis method to obtain nanoparticles with smaller grain sizes than 50 nm would be one of the most promising future work to improve the electrochemical performance of the reported nanostructured electrodes in this work.

II. For the future work concerning the thin film electrodes for the micro-SOFC devices, the optimization of the thermomechanical stability of the LSC|3YSZ bilayer at higher annealing temperatures than 550 °C is necessary to obtain micro-SOFC membranes with higher power outputs. The maximum LSC thickness that can be deposited without leading to a thermomechanical failure of the micro-SOFC membrane would also be interesting to know, as an increase in the cathode thickness will provide more reaction sites for oxygen reduction. Moreover, the utilization of the LSC-GDC20 nanocomposite cathodes can be considered to obtain higher power densities. Furthermore, engineering of a current collector layer might improve the electrochemical performance of the micro-SOFCs. Finally, microstructurally stable anodes with high electrochemical activities towards fuel oxidation have to replace currently employed Pt anodes.

III. It is important to note that the electrode layers of the anode-supported SOFCs fabricated in this work are not optimized to obtain highest power density values. First of all, the development of a current collector layer with high electronic conductivity and better thermomechanical compatibility with the other cell components is necessary. Secondly, the optimum cathode thickness leading to the highest electrochemical performance must be investigated in the anode-supported SOFC design. Furthermore, the microstructure of the Ni-GDC20 anode supports can be engineered to reduce the high mass transfer losses observed in the impedance spectroscopy experiments. The bi-layered anode support design can be followed, in which the highly porous layer supports the cell mechanically and allows a proper gas circulation, while the anode functional layer with an ultrafine microstructure creates high number of active reaction sites for the fuel oxidation.

List of Abbreviations

AACVD	Aerosol-assisted Chemical Vapor Deposition
AC	Alternating Current
AFC	Alkaline Fuel Cell
ALD	Atomic Layer Deposition
ASR	Area Specific Resistance
BET	Brunauer–Emmett–Teller method
BSCF	*general*: $Ba_{1-x}Sr_xCo_{1-y}Fe_yO_{3-\delta}$
CPE	Constant Phase Element
CVD	Chemical Vapor Deposition
DC	Direct Current
EDX	Energy-Dispersive X-ray Spectroscopy
EIS	Electrochemical Impedance Spectroscopy
FIB	Focused Ion Beam
GDC	*general:* $Ce_{1-x}Gd_xO_{2-\delta}$
GDC10	$Ce_{0.9}Gd_{0.1}O_{2-\delta}$
GDC20	$Ce_{0.8}Gd_{0.2}O_{2-\delta}$
LSC	*general*: $La_{1-x}Sr_xCoO_{3-\delta}$
	this work: the specific composition $La_{0.6}Sr_{0.4}CoO_{3-\delta}$
LSCF	*general*: $La_{1-x}Sr_xCo_{1-y}Fe_yO_{3-\delta}$
LSGM	*general*: $La_{1-x}Sr_xGa_{1-y}Mg_yO_{3-\delta}$
LSM	*general*: $La_{1-x}Sr_xMnO_{3-\delta}$
MCFC	Molten Carbonate Fuel Cell
MEMS	Micro-Electro-Mechanical Systems
MIEC	Mixed Ionic-Electronic Conduction/Conductor
Micro-SOFC	Micro-Solid Oxide Fuel Cell
MOCVD	Metal-Organic Chemical Vapor Deposition
Ni-GDC	*general*: cermet of nickel and gadolinia-doped ceria
	this work: the specific composition $NiO-Ce_{0.8}Gd_{0.2}O_{2-\delta}$ (60:40 wt.%)
Ni-YSZ	*general*: cermet of nickel and yttria-stabilized zirconia
OCV	Open Circuit Voltage
ORR	Oxygen Reduction Reaction
PAFC	Phosphoric Acid Fuel Cell
PEMFC	Polymer Electrolyte Membrane Fuel Cell
PLD	Pulsed Layer Deposition
RDS	Rate-Determining Step
RIE	Reactive Ion Etching
SASP	Salt-Assisted Spray Pyrolysis
SDC	*general:* $Ce_{1-x}Sm_xO_{2-\delta}$
SEM	Scanning Electron Microscopy
SOFC	Solid Oxide Fuel Cell
STEM	Scanning Transmission Electron Microscopy
TEC	Thermal Expansion Coefficient
TEM	Transmission Electron Microscopy
TPB	Triple Phase Boundary
USP	Ultrasonic Spray Pyrolysis
YDC	*general:* $Ce_{1-x}Y_xO_{2-\delta}$

| YSZ | Yttria-Stabilized Zirconia |
| XRD | X-ray Diffraction |

List of Symbols

a	Lattice parameter
a_i	Activities of species in electrochemical reactions
α	Symmetry factor in Butler-Volmer-type equations (charge transfer coefficient)
α_{int}	Interaxial angle
ASR_{ohmic}	Area-specific resistance caused by Ohmic losses
ASR_{pol}	Area-specific resistance caused by electrode polarization
C	Capacitance
C_R^*	Bulk reactant concentration
D^{eff}	Effective reactant diffisuvity
$\Delta\hat{s}$	Molar entropy change
$\Delta\hat{G}°$	Standard molar free energy change
E	Actual voltage output of an SOFC
E_a	Activation energy
E^0	Standard-state reversible voltage
E_{Nernst}	Nernst voltage
E_T	Reversible voltage of a cell at temperature, T
η	Mean oxidation state of Co in LSC
F	Faraday's constant
f	Frequency
I	Current
j	Current density
j_0	Exchange current density
j_L	Limiting current density
k	Tafel slope
n	Degree of the deviation form the ideal capacitance behavior
P_i	Partial pressure of the species
P^0	Standard pressure
η_{act}	Activation polarization
η_{ohmic}	Ohmic polarization
η_{conc}	Concentration polarization
R	Universal gas constant
R	Resistance
R_{elec}	Electrical resistance
R_{ionic}	Ionic resistance
r_i	Ionic radius of species
s	Tafel intercept
σ_{el}	Electronic conductivity
σ_{ion}	Ionic conductivity
δ	Oxygen nonstoichiometry
T	Absolute temperature
T_0	Standard temperature

t	Time
t_G	Goldschmidt tolerance factor
τ	Electrode diffusion layer thickness
τ_{RC}, τ_{RQ}	Time constants
ϕ	Phase difference between voltage and current
TEC_i	Thermal expansion coefficient of materials
V	Voltage
v_i	Stoichiometric coefficient of the species in electrochemical reactions
ω	Angular frequency
ω_R	Relaxation frequency
x, y	Dopant concentration
Z	Total electrochemical impedance
$|Z|$	Absolute impedance
Z_{imag}	Imaginary part of the impedance
Z_{real}	Real part of the impedance
Z_{RC}	Impedance of an RC element
Z_{RQ}	Impedance of a constant phase element

Cirriculum Vitae

Name: Cahit Benel
Date and Place of Birth: 21.07.1985, Istanbul, Turkey
Nationality: Turkish

Education

06.2011-present
Doctoral studies in Material Science
Joint Research Laboratory for Nanomaterials, Technische Universität Darmstadt/Karlsruhe Institute of Technology, Darmstadt, Germany
Title of Ph.D. thesis: "Nanostructured Electrodes for Low Temperature Solid Oxide Fuel Cells" supervised by Prof. Dr. Horst Hahn

10.2008-01.2011
M.Sc. in Material Science
Advanced Materials (Specialization in Nanomaterials), Ulm University, Ulm, Germany
Title of master thesis: "Optical Spectroscopy of Rare Earth doped Nanoparticles on Metallic Nanostructures" supervised by Prof. Dr. Ulrich Herr

09.2003–06.2008
B.Sc. in Material Science and Engineering
Sabancı University, Istanbul, Turkey

Professional Record

06.2011-present
Research Associate at the Joint Research Laboratory for Nanomaterials, Technische Universität Darmstadt/Karlsruhe Institute of Technology, Darmstadt, Germany

01.2011-05.2011
Research Assistant at the Institute of Micro and Nanomaterials, Ulm University, Ulm, Germany

Honors & Awards

12.2014
Nomination for *Best Poster Award* for the poster "Synthesis and Characterization of Nanoparticulate LSC Cathodes for Thin Film Solid Oxide Fuel Cells", MRS 2014 Fall Meeting (Boston, MA, USA) in the symposium of "Advances in Material Science, Processing and Engineering for Fuel Cells and Electrolyzers"

05.2012
Best poster award for the poster "Nanostructured Thin Film LSC synthesized via salt-assisted spray pyrolysis for micro-SOFC application", E-MRS 2012 Spring Meeting (Strasbourg, France) in the symposium of "Solid State Ionics: Mass and Charge Transport across and along Interfaces of Functional Materials"

List of Publications

R. Djenadic, M. Botros, C. Benel, O. Clemens, S. Indris, A. Choudhary, T. Bergfeldt, H. Hahn; Nebulized spray pyrolysis of Al-doped $Li_7La_3Zr_2O_{12}$ solid electrolyte for battery applications; Solid State Ionics 263, 49–56 (2014).

C. Benel, A. J. Darbandi, R. Djenadic, A. Evans, R. Tölke, M. Prestat, H. Hahn; Synthesis and characterization of nanoparticulate $La_{0.6}Sr_{0.4}CoO_{3-\delta}$ cathodes for thin-film solid oxide fuel cells; Journal of Power Sources 229, 258–264 (2013).

A. Evans, C. Benel, A. J. Darbandi, H. Hahn, J. Martynczuk, L. J. Gauckler, M. Prestat; Integration of Spin-Coated Nanoparticulate-Based $La_{0.6}Sr_{0.4}CoO_{3-\delta}$ Cathodes into Micro-Solid Oxide Fuel Cell Membranes; FUEL CELLS 13, 441–444 (2013).

References

[1]   N. Q. Minh, "Ceramic Fuel Cells," *J. Am. Ceram. Soc.*, vol. 76, pp. 563–588, 1993.

[2]   S. Singhal, "Advances in solid oxide fuel cell technology," *Solid State Ionics*, vol. 135, no. 1–4, pp. 305–313, 2000.

[3]   C. Song, "Fuel processing for low-temperature and high-temperature fuel cells: Challenges, and opportunities for sustainable development in the 21st century," *Catal. Today*, vol. 77, no. 1–2, pp. 17–49, 2002.

[4]   R. M. Ormerod, "Solid oxide fuel cells," *Chem. Soc. Rev.*, vol. 32, pp. 17–28, 2003.

[5]   S. M. Haile, "Fuel cell materials and components," *Acta Mater.*, vol. 51, no. 19, pp. 5981–6000, 2003.

[6]   R. O'Hayre, S.-W. Cha, W. G. Collella, and F. B. Prinz, *Fuel Cell Fundamentals*, 2nd ed. Wiley, 2009.

[7]   S. C. Singhal and K. Kendall, *High Temperature Solid Oxide Fuel Cells: Fundamentals, Design and Applications*. Elsevier, 2003.

[8]   E. D. Wachsman and K. T. Lee, "Lowering the Temperature of Solid Oxide Fuel Cells," *Science*, vol. 334, no. 6058, pp. 935–939, 2011.

[9]   H. S. Noh, K. J. Yoon, B. K. Kim, H. J. Je, H. W. Lee, J. H. Lee, and J. W. Son, "The potential and challenges of thin-film electrolyte and nanostructured electrode for yttria-stabilized zirconia-base anode-supported solid oxide fuel cells," *J. Power Sources*, vol. 247, pp. 105–111, 2014.

[10]   A. Evans, A. Bieberle-Hütter, J. L. M. Rupp, and L. J. Gauckler, "Review on microfabricated micro-solid oxide fuel cell membranes," *J. Power Sources*, vol. 194, pp. 119–129, 2009.

[11]   H. Huang, M. Nakamura, P. Su, R. Fasching, Y. Saito, and F. B. Prinz, "High-Performance Ultrathin Solid Oxide Fuel Cells for Low-Temperature Operation," *J. Electrochem. Soc.*, vol. 154, no. 1, p. B20, 2007.

[12]   B. K. Lai, K. Kerman, and S. Ramanathan, "On the role of ultra-thin oxide cathode synthesis on the functionality of micro-solid oxide fuel cells: Structure, stress engineering and in situ observation of fuel cell membranes during operation," *J. Power Sources*, vol. 195, no. 16, pp. 5185–5196, 2010.

[13]   I. Garbayo, A. Tarancón, J. Santiso, F. Peiró, E. Alarcón-LLadó, A. Cavallaro, I. Gràcia, C. Cané, and N. Sabaté, "Electrical characterization of thermomechanically stable YSZ membranes for micro solid oxide fuel cells applications," *Solid State Ionics*, vol. 181, no. 5–7, pp. 322–331, 2010.

[14]   C. W. Kwon, J. W. Son, J. H. Lee, H. M. Kim, H. W. Lee, and K. B. Kim, "High-performance micro-solid oxide fuel cells fabricated on nanoporous anodic aluminum oxide templates," *Adv. Funct. Mater.*, vol. 21, pp. 1154–1159, 2011.

[15]   P. C. Su, C. C. Chao, J. H. Shim, R. Fasching, and F. B. Prinz, "Solid oxide fuel cell with corrugated thin film electrolyte," *Nano Lett.*, vol. 8, no. 8, pp. 2289–2292, 2008.

[16]   S. Rey-Mermet, Y. Yan, C. Sandu, G. Deng, and P. Muralt, "Nanoporous YSZ film in electrolyte membrane of Micro-Solid Oxide Fuel Cell," *Thin Solid Films*, vol. 518, no. 16, pp. 4743–4746, 2010.

[17]   J. An, Y. B. Kim, J. Park, T. M. Gür, and F. B. Prinz, "Three-dimensional nanostructured bilayer solid oxide fuel cell with 1.3 W/cm^2 at 450 °C," *Nano Lett.*, vol. 13, pp. 4551–4555, 2013.

[18]   C. K. Dyer, "Fuel cells for portable applications," *J. Power Sources*, vol. 106, no. 1–2, pp. 31–34, 2002.

[19]   A. Bieberle-Hütter, D. Beckel, A. Infortuna, U. P. Muecke, J. L. M. Rupp, L. J. Gauckler, S. Rey-Mermet, P. Muralt, N. R. Bieri, N. Hotz, M. J. Stutz, D. Poulikakos, P. Heeb, P. Müller, A. Bernard, R. Gmür, and T. Hocker, "A micro-solid oxide fuel cell system as battery replacement," *J. Power Sources*, vol. 177, pp. 123–130, 2008.

[20]   G. Jose La O, H. Jin In, E. Crumlin, G. Barbastathis, and Y. Shao-Horn, "Recent advances in microdevices for electrochemical energy conversion and storage," *Int. J. energy Res.*, vol. 31,

no. August 2007, pp. 548–575, 2007.

[21] A. J. Jacobson, "Materials for solid oxide fuel cells," *Chem. Mater.*, vol. 22, pp. 660–674, 2010.

[22] D. L. Maricle, T. E. Swarr, and S. Karavolis, "Enhanced Ceria - A Low Temperature SOFC Electrolyte," *Solid State Ionics*, vol. 52, pp. 173–182, 1992.

[23] J. P. P. Huijsmans, F. P. F. van Berkel, and G. M. Christie, "Intermediate temperature SOFC – a promise for the 21st century," *J. Power Sources*, vol. 71, no. 1–2, pp. 107–110, 1998.

[24] J. W. Fergus, "Electrolytes for solid oxide fuel cells," *J. Power Sources*, vol. 162, no. 1, pp. 30–40, 2006.

[25] T. Hibino, A. Hashimoto, T. Inoue, J. Tokuno, S. Yoshida, and M. Sano, "A Low-Operating-Temperature Solid Oxide Fuel Cell in Hydrocarbon-Air Mixtures," *Science*, vol. 288, pp. 2031–2033, 2000.

[26] V. V. Kharton, F. M. B. Marques, and A. Atkinson, "Transport properties of solid oxide electrolyte ceramics: A brief review," *Solid State Ionics*, vol. 174, no. 1–4, pp. 135–149, 2004.

[27] W. Suksamai and I. S. Metcalfe, "Measurement of proton and oxide ion fluxes in a working Y-doped $BaCeO_3$ SOFC," *Solid State Ionics*, vol. 178, no. 7–10, pp. 627–634, 2007.

[28] K. D. Kreuer, "PROTON-CONDUCTING OXIDES," *Annu. Rev. Mater. Res.*, vol. 33, no. 1, pp. 333–359, 2003.

[29] C. Zuo, S. Zha, M. Liu, M. Hatano, and M. Uchiyama, "$Ba(Zr_{0.1}Ce_{0.7}Y_{0.2})O_{3-\delta}$ as an electrolyte for low-temperature solid-oxide fuel cells," *Adv. Mater.*, vol. 18, no. 24, pp. 3318–3320, 2006.

[30] J. M. Serra and W. A. Meulenberg, "Thin-film proton $BaZr_{0.85}Y_{0.15}O_3$ conducting electrolytes: toward an intermediate-temperature solid oxide fuel cell alternative," *J. Am. Ceram. Soc.*, vol. 90, no. 7, pp. 2082–2089, 2007.

[31] N. Ito, M. Iijima, K. Kimura, and S. Iguchi, "New intermediate temperature fuel cell with ultra-thin proton conductor electrolyte," *J. Power Sources*, vol. 152, no. 1–2, pp. 200–203, 2005.

[32] E. Fabbri, L. Bi, D. Pergolesi, and E. Traversa, "Towards the next generation of solid oxide fuel cells operating below 600 °C with chemically stable proton-conducting electrolytes," *Adv. Mater.*, vol. 24, no. 2, pp. 195–208, 2012.

[33] N. Mahato, A. Banerjee, A. Gupta, S. Omar, and K. Balani, "Progress in Material Selection for Solid Oxide Fuel Cell Technology: A Review," *Prog. Mater. Sci.*, vol. 72, pp. 141–337, 2015.

[34] E. Ivers-Tiffée, A. Weber, and D. Herbstritt, "Materials and technologies for SOFC-components," *J. Eur. Ceram. Soc.*, vol. 21, no. 10–11, pp. 1805–1811, 2001.

[35] S. P. Jiang, "Development of lanthanum strontium manganite perovskite cathode materials of solid oxide fuel cells: A review," *J. Mater. Sci.*, vol. 43, no. 21, pp. 6799–6833, 2008.

[36] S. B. Adler, "Factors Governing Oxygen Reduction in Solid Oxide Fuel Cell Cathodes," *Chem. Rev.*, vol. 104, pp. 4791–4843, 2004.

[37] Z. Shao and S. M. Haile, "A high-performance cathode for the next generation of solid-oxide fuel cells.," *Nature*, vol. 431, no. 7005, pp. 170–173, 2004.

[38] W. Wang and M. Mogensen, "High-performance lanthanum-ferrite-based cathode for SOFC," *Solid State Ionics*, vol. 176, no. 5–6, pp. 457–462, 2005.

[39] J. Januschewsky, M. Ahrens, A. Opitz, F. Kubel, and J. Fleig, "Optimized $La_{0.6}Sr_{0.4}CoO_{3-\delta}$ thin-film electrodes with extremely fast oxygen-reduction kinetics," *Adv. Funct. Mater.*, vol. 19, no. 19, pp. 3151–3156, 2009.

[40] D. Oh, D. Gostovic, and E. D. Wachsman, "Mechanism of $La_{0.6}Sr_{0.4}Co_{0.2}Fe_{0.8}O_3$ cathode degradation," *J. Mater. Res.*, vol. 27, no. 15, pp. 1992–1999, 2012.

[41] L. Qiu, T. Ichikawa, a. Hirano, N. Imanishi, and Y. Takeda, "$Ln_{1-x}Sr_xCo_{1-y}Fe_yO_{3-\delta}$ (Ln=Pr, Nd, Gd; x=0.2, 0.3) for the electrodes of solid oxide fuel cells," *Solid State Ionics*, vol. 158, no. 1–2, pp. 55–65, 2003.

[42] A. Mai, V. A. C. Haanappel, S. Uhlenbruck, and F. Tietz, "Ferrite-based perovskites as

cathode materials for anode- supported solid oxide fuel cells Part I . Variation of composition," *Solid State Ionics*, vol. 176, no. 37, pp. 1–14, 2008.

[43] A. McEvoy, "Anodes," in *High Temeprature Solid Oxide Fuel Cells - Fundamentals, Design and Applications*, S. C. Singhal and K. Kendall, Eds. Elsevier, 2003.

[44] H. Spacil, "ELECTRICAL DEVICE INCLUDING NICKEL-CONTAINING STABILIZED ZIRCONIA ELECTRODE," 1970.

[45] J. B. Goodenough and Y.-H. Huang, "Alternative anode materials for solid oxide fuel cells," *J. Power Sources*, vol. 173, pp. 1–10, 2007.

[46] J. B. Wang, J. C. Jang, and T. J. Huang, "Study of Ni-samaria-doped ceria anode for direct oxidation of methane in solid oxide fuel cells," *J. Power Sources*, vol. 122, no. 2, pp. 122–131, 2003.

[47] R. Maric, S. Ohara, T. Fukui, H. Yoshida, M. Nishimura, T. Inagaki, and K. Miura, "Solid Oxide Fuel Cells with Doped Lanthanum Gallate Electrolyte and $LaSrCoO_3$ Cathode, and Ni-Samaria-Doped Ceria Cermet Anode," *J. Electrochem. Soc.*, vol. 146, no. 6, pp. 2006–2010, 1999.

[48] W. Z. Zhu and S. C. Deevi, "A review on the status of anode materials for solid oxide fuel cells," *Mater. Sci. Eng. A*, vol. 362, no. 1–2, pp. 228–239, 2003.

[49] M. Gong, X. Liu, J. Trembly, and C. Johnson, "Sulfur-tolerant anode materials for solid oxide fuel cell application," *J. Power Sources*, vol. 168, pp. 289–298, 2007.

[50] O. a. Marina, N. L. Canfield, and J. W. Stevenson, "Thermal, electrical, and electrocatalytical properties of lanthanum-doped strontium titanate," *Solid State Ionics*, vol. 149, no. 1–2, pp. 21–28, 2002.

[51] Y.-H. Huang, R. I. Dass, Z.-L. Xing, and J. B. Goodenough, "Double Perovskites as Anode," *Science*, vol. 312, no. April, pp. 254–258, 2006.

[52] B. H. Smith and M. D. Gross, "A Highly Conductive Oxide Anode for Solid Oxide Fuel Cells," *Electrochem. Solid-State Lett.*, vol. 14, no. 1, p. B1, 2011.

[53] S. Tao and J. T. S. Irvine, "A redox-stable efficient anode for solid-oxide fuel cells.," *Nat. Mater.*, vol. 2, no. 5, pp. 320–323, 2003.

[54] R. J. Gorte and J. M. Vohs, "Nanostructured anodes for solid oxide fuel cells," *Curr. Opin. Colloid Interface Sci.*, vol. 14, no. 4, pp. 236–244, 2009.

[55] H. R. Ellamla, I. Staffell, P. Bujlo, B. G. Pollet, and S. Pasupathi, "Current status of fuel cell based combined heat and power systems for residential sector," *J. Power Sources*, vol. 293, pp. 312–328, 2015.

[56] E. Ivers-Tiffee and A. V. Virkar, "Electrode Polarizations," in *High Temeprature Solid Oxide Fuel Cells - Fundamentals, Design and Applications*, S. C. Singhal and K. Kendall, Eds. 2003.

[57] S. H. Chan, K. A. Khor, and Z. T. Xia, "A complete polarization model of a solid oxide fuel cell and its sensitivity to the change of cell component thickness," *J. Power Sources*, vol. 93, no. 1–2, pp. 130–140, 2001.

[58] A. Chroneos, B. Yildiz, A. Tarancón, D. Parfitt, and J. a. Kilner, "Oxygen diffusion in solid oxide fuel cell cathode and electrolyte materials: mechanistic insights from atomistic simulations," *Energy Environ. Sci.*, vol. 4, no. 8, p. 2774, 2011.

[59] N. Jiang and E. D. Wachsman, "Structural Stability and Conductivity of Phase-Stabilized Cubic Bismuth Oxides," *J. Am. Ceram. Soc.*, vol. 82, no. 11, pp. 3057–3064, 1999.

[60] T. Ishihara, N. M. Sammes, and O. Yamamoto, "Electrolytes," in *High Temeprature Solid Oxide Fuel Cells - Fundamentals, Design and Applications*, S. C. Singhal and K. Kendall, Eds. Elsevier, 2003.

[61] V. M. Goldschmidt, "Die Gesetze der Krystallochemie," *Naturwissenschaften*, vol. 14, no. 21, pp. 477–485, 1926.

[62] T. Ishihara, "Structure and Properties of Perovskite Oxides," in *Perovskite Oxide for Solid Oxide Fuel Cells*, T. Ishihara, Ed. Springer, 2009.

[63] K. Huang, R. Tichy, and J. B. Goodenough, "Superior Perovskite Oxide-Ion Conductor; Strontium- and Magnesium-Doped $LaGaO_3$: III, Performance Tests of Single Ceramic Fuel Cells," *J. Am. Ceram. Soc.*, vol. 81, no. 10, pp. 2581–2585, 1998.

[64] K. Q. Huang and J. B. Goodenough, "A solid oxide fuel cell based on Sr- and Mg-doped LaGaO$_3$ electrolyte: the role of a rare-earth oxide buffer," *J. Alloys Compd.*, vol. 303, pp. 454–464, 2000.

[65] F. Tietz, "Thermal expansion of SOFC materials," *Ionics (Kiel).*, vol. 5, no. 1–2, pp. 129–139, 1999.

[66] D. W. Dees, T. D. Claar, and D. C. Fee, "Conductivity of Porous Ni/ZrO$_2$-Y$_2$0$_3$ Cermets," *J. Electrochem. Soc.*, vol. 134, no. 9, pp. 2141–2146, 1987.

[67] P. Costamagna, "Micro-modelling of solid oxide fuel cell electrodes," *Electrochim. Acta*, vol. 43, no. 97, pp. 375–394, 1998.

[68] T. Suzuki, Z. Hasan, Y. Funahashi, T. Yamaguchi, Y. Fujishiro, and M. Awano, "Impact of anode microstructure on solid oxide fuel cells," *Science*, vol. 325, pp. 852–855, 2009.

[69] W. G. Bessler, M. Vogler, H. Störmer, D. Gerthsen, A. Utz, A. Weber, and E. Ivers-Tiffée, "Model anodes and anode models for understanding the mechanism of hydrogen oxidation in solid oxide fuel cells," *Phys. Chem. Chem. Phys.*, vol. 12, no. 42, p. 13888, 2010.

[70] A. Bieberle, L. P. Meier, and L. J. Gauckler, "The Electrochemistry of Ni Pattern Anodes Used as Solid Oxide Fuel Cell Model Electrodes," *J. Electrochem. Soc.*, vol. 148, no. 6, p. A646, 2001.

[71] J. Mizusaki, H. Tagawa, T. Saito, T. Yamamura, K. Kamitani, K. Hirano, S. Ehara, T. Takagi, T. Hikita, and M. Ippommatsu, "Kinetic studies of the reaction at the nickel pattern electrode on YSZ in H$_2$-H$_2$O atmospheres," *Solid State Ionics*, vol. 70–71, pp. 52–58, 1994.

[72] S. W. Tao and J. T. S. Irvine, "Fuel Electrodes for Solid Oxide Fuel Cells," in *Metal Oxides*, J. L. G. Fierro, Ed. Taylor&Francis, 2006.

[73] O. A. Marina, C. Bagger, S. Primdahl, and Mogensen, "A solid oxide fuel cell with a gadolinia-doped ceria anode: preparation and performance," *Solid State Ionics*, vol. 123, pp. 199–208, 1999.

[74] S. McIntosh and R. J. Gorte, "Direct hydrocarbon solid oxide fuel cells," *Chem. Rev.*, vol. 104, no. 10, pp. 4845–4865, 2004.

[75] S. Litster and G. McLean, "PEM fuel cell electrodes," *J. Power Sources*, vol. 130, no. 1–2, pp. 61–76, 2004.

[76] F. W. Poulsen, "Defect chemistry modelling of oxygen-stoichiometry , vacancy concentrations , and conductivity of (La$_{1-x}$Sr$_x$)yMnO$_3$," *Solid State Ionics*, vol. 129, pp. 145–162, 2000.

[77] A. Mitterdorfer and L. J. Gauckler, "La$_2$Zr$_2$O$_7$ formation and oxygen reduction kinetics of the La$_{0.85}$Sr$_{0.15}$Mn$_y$O$_3$, O$_2$(g)|YSZ system," *Solid State Ionics*, vol. 111, pp. 185–218, 1998.

[78] A. Endo, M. Ihara, H. Komiyama, and K. Yamada, "Cathodic reaction mechanism for dense Sr-doped lanthanum manganite electrodes," *Solid State Ionics*, vol. 2738, no. 86–88, pp. 1191–1195, 1996.

[79] J. Hayd, L. Dieterle, U. Guntow, D. Gerthsen, and E. Ivers-Tiffée, "Nanoscaled La$_{0.6}$Sr$_{0.4}$CoO$_{3-\delta}$ as intermediate temperature solid oxide fuel cell cathode: Microstructure and electrochemical performance," *J. Power Sources*, vol. 196, no. 17, pp. 7263–7270, 2011.

[80] C. Sun, R. Hui, and J. Roller, "Cathode materials for solid oxide fuel cells: A review," *J. Solid State Electrochem.*, vol. 14, no. 7, pp. 1125–1144, 2010.

[81] M. Søgaard, P. Vang Hendriksen, and M. Mogensen, "Oxygen nonstoichiometry and transport properties of strontium substituted lanthanum ferrite," *J. Solid State Chem.*, vol. 180, no. 4, pp. 1489–1503, 2007.

[82] J. Mizusaki, Y. Mima, S. Yamauchi, and K. Fueki, "Nonstoichiometry of the Perovskite-Type Oxides La$_{1-x}$Sr$_x$CoO$_{3-d}$," *J. Solid State Chem.*, vol. 80, pp. 102–111, 1989.

[83] A. N. Petrov, O. F. Kononchuk, A. V. Andreev, V. A. Cherepanov, and P. Kofstad, "Crystal structure, electrical and magnetic properties of La$_{1-x}$Sr$_x$CoO$_{3-y}$," *Solid State Ionics*, vol. 80, no. 95, pp. 189–199, 1995.

[84] A. Petric, P. Huang, and F. Tietz, "Evaluation of La-Sr-Co-Fe-O perovskites for solid oxide fuel cells and gas separation membranes," *Solid State Ionics*, vol. 135, no. 1–4, pp. 719–725, 2000.

[85] T. Inoue, J. Kamimae, M. Ueda, K. Eguchi, and H. Arai, "Ionic and Electronic Conductivities of $LaCoO_3$- and $LaMnO_3$-based Perovskite-type Oxides measured by the A.C. Impedance Method with Electron-blocking Electrodes," *J. Mater. Chem.*, vol. 3, no. 7, p. 751, 1993.

[86] S. B. Adler, "Chemical Expansivity of Electrochemical Ceramics," *J. Am. Ceram. Soc.*, vol. 84, no. 9, pp. 2117–2119, 2001.

[87] X. Y. Chen, J. S. Yu, and S. B. Adler, "Thermal and Chemical Expansion of Sr-Doped Lanthanum Cobalt Oxide ($La_{1-x}Sr_xCoO_{3-\delta}$)," *Chem. Mater.*, vol. 17, no. 17, p. 4537, 2005.

[88] L. W. Tai, M. M. Nasrallah, H. U. Anderson, D. M. Sparlin, and S. R. Sehlin, "Structure and Electrical-Properties of $La_{1-x}Sr_xCo_{1-y}Fe_yO_3$. Part 1. The System $La_{0.8}Sr_{0.2}Co_{1-y}Fe_yO_3$," *Solid State Ionics*, vol. 76, no. 3–4, pp. 259–271, 1995.

[89] Y. Ohno, S. Nagata, and H. Sato, "Properties of oxides for high temperature solid electrolyte fuel cell," *Solid State Ionics*, vol. 9&10, pp. 1001–1007, 1983.

[90] K. Park, S. Yu, J. Bae, H. Kim, and Y. Ko, "Fast performance degradation of SOFC caused by cathode delamination in long-term testing," *Int. J. Hydrogen Energy*, vol. 35, no. 16, pp. 8670–8677, 2010.

[91] C. Peters, "Grain-Size Effects in Nanoscaled Electrolyte and Cathode Thin Films for Solid Oxide Fuel Cells (SOFC)," 2008.

[92] M. Sase, D. Ueno, K. Yashiro, A. Kaimai, T. Kawada, and J. Mizusaki, "Interfacial reaction and electrochemical properties of dense $(La,Sr)CoO_{3-\delta}$ cathode on YSZ (1 0 0)," *J. Phys. Chem. Solids*, vol. 66, no. 2–4, pp. 343–348, 2005.

[93] H. Yokokawa, N. Sakai, T. Kawada, and M. Dokiya, "Thermodynamic Analysis on Interface between perovskite Electrode and YSZ Electrolyte," *Solid State Ionics*, vol. 40/41, pp. 398–401, 1990.

[94] M. Kubicek, A. Limbeck, T. Frömling, H. Hutter, and J. Fleig, "Relationship between Cation Segregation and the Electrochemical Oxygen Reduction Kinetics of $La_{0.6}Sr_{0.4}CoO_{3-\delta}$ Thin Film Electrodes," *J. Electrochem. Soc.*, vol. 158, no. 6, p. B727, 2011.

[95] E. J. Crumlin, E. Mutoro, Z. Liu, M. E. Grass, M. D. Biegalski, Y.-L. Lee, D. Morgan, H. M. Christen, H. Bluhm, and Y. Shao-Horn, "Surface strontium enrichment on highly active perovskites for oxygen electrocatalysis in solid oxide fuel cells," *Energy Environ. Sci.*, vol. 5, no. 3, p. 6081, 2012.

[96] Z. Cai, M. Kubicek, J. Fleig, and B. Yildiz, "Chemical Heterogeneities on $La_{0.6}Sr_{0.4}CoO_{3-\delta}$ Thin Films - Correlations to Cathode Surface Activity and Stability," *Chem. Mater.*, vol. 24, pp. 1116–1127, 2012.

[97] G. M. Rupp, A. Limbeck, M. Kubicek, A. Penn, M. Stöger-Pollach, G. Friedbacher, and J. Fleig, "Correlating surface cation composition and thin film microstructure with the electrochemical performance of lanthanum strontium cobaltite (LSC) electrodes," *J. Mater. Chem. A*, vol. 2, no. 19, p. 7099, 2014.

[98] F. S. Baumann, "Oxygen reduction kinetics on mixed conducting SOFC model cathodes," 2006.

[99] K. Kendall, N. Q. Minh, and S. C. Singhal, "Cell and Stack Designs," in *High Temperature Solid Oxide Fuel Cells - Fundamentals, Design and Applications*, S. C. Singhal and K. Kendall, Eds. Elsevier, 2003.

[100] M. C. Tucker, "Progress in metal-supported solid oxide fuel cells: A review," *J. Power Sources*, vol. 195, no. 15, pp. 4570–4582, 2010.

[101] R. Hui, "Materials and Processing for Metal-Supported Solid Oxide Fuel Cells," in *Materials for High-Temperature Fuel Cells*, S. P. Jiang and Y. Yan, Eds. Wiley-VCH, 2013, pp. 309–340.

[102] R. J. F. van Gerwen, "Systems and Applications," in *High Temperature Solid Oxide Fuel Cells: Fundamentals, Design and Applications*, S. C. Singhal and K. Kendall, Eds. Elsevier, 2003.

[103] J. H. Shim, C. C. Chao, H. Huango, and F. B. Prinz, "Atomic layer deposition of yttria-stabilized zirconia for solid oxide fuel cells," *Chem. Mater.*, vol. 19, no. 15, pp. 3850–3854, 2007.

[104] U. P. Muecke, D. Beckel, A. Bernard, A. Bieberle-Hütter, S. Graf, A. Infortuna, P. Müller, J. L. M. Rupp, J. Schneider, and L. J. Gauckler, "Micro solid oxide fuel cells on glass ceramic

substrates," *Adv. Funct. Mater.*, vol. 18, pp. 3158–3168, 2008.

[105] J. H. Joo and G. M. Choi, "Simple fabrication of micro-solid oxide fuel cell supported on metal substrate," *J. Power Sources*, vol. 182, pp. 589–593, 2008.

[106] A. Evans, A. Bieberle-Hütter, H. Galinski, J. L. M. Rupp, T. Ryll, B. Scherrer, R. Tölke, and L. J. Gauckler, "Micro-solid oxide fuel cells: Status, challenges, and chances," *Monatshefte fur Chemie*, vol. 140, pp. 975–983, 2009.

[107] C. W. Kwon, J. Il Lee, K. B. Kim, H. W. Lee, J. H. Lee, and J. W. Son, "The thermomechanical stability of micro-solid oxide fuel cells fabricated on anodized aluminum oxide membranes," *J. Power Sources*, vol. 210, pp. 178–183, 2012.

[108] A. Evans, C. Benel, a. J. Darbandi, H. Hahn, J. Martynczuk, L. J. Gauckler, and M. Prestat, "Integration of Spin-Coated Nanoparticulate-Based $La_{0.6}Sr_{0.4}CoO_{3-\delta}$ Cathodes into Micro-Solid Oxide Fuel Cell Membranes," *Fuel Cells*, vol. 13, no. 3, pp. 441–444, 2013.

[109] R. Tölke, A. Bieberle-Hütter, A. Evans, J. L. M. Rupp, and L. J. Gauckler, "Processing of Foturan glass ceramic substrates for micro-solid oxide fuel cells," *J. Eur. Ceram. Soc.*, vol. 32, pp. 3229–3238, 2012.

[110] Y. Okada and Y. Tokumaru, "Precise determination of lattice parameter and thermal expansion coefficient of silicon between 300 and 1500 K," *J. Appl. Phys.*, vol. 56, no. 2, pp. 314–320, 1984.

[111] R. Tölke, L. J. Gauckler, U. Kunz, A. Krauss, and M. Prestat, "Investigation of the mechanical stability of micro-solid oxide fuel cell membranes using scanning laser vibrometry," *Fuel Cells*, vol. 13, no. 5, pp. 695–702, 2013.

[112] A. Evans, J. Martynczuk, D. Stender, C. W. Schneider, T. Lippert, and M. Prestat, "Low-Temperature Micro-Solid Oxide Fuel Cells with Partially Amorphous $La_{0.6}Sr_{0.4}CoO_{3-\delta}$ Cathodes," *Adv. Energy Mater.*, vol. 5, p. 1400747, 2015.

[113] I. Garbayo, G. Dezanneau, C. Bogicevic, J. Santiso, I. Gràcia, N. Sabaté, and A. Tarancón, "Pinhole-free YSZ self-supported membranes for micro solid oxide fuel cell applications," *Solid State Ionics*, vol. 216, pp. 64–68, 2012.

[114] S. Gamble, "Fabrication-microstructure-performance relationships of reversible solid oxide fuel cell electrodes-review," *Mater. Sci. Technol.*, vol. 27, no. 10, pp. 1485–1497, 2011.

[115] P. Singh and N. Q. Minh, "Solid Oxide Fuel Cells: Technology Status," *Int. J. Appl. Ceram. Technol.*, vol. 1, pp. 5–15, 2004.

[116] A. Sanson, E. Roncari, S. Boldrini, P. Mangifesta, and L. Doubova, "Eco-Friendly Screen-Printing Inks of Gadolinia Doped Ceria," *J. Fuel Cell Sci. Technol.*, vol. 7, no. October, p. 51013, 2010.

[117] K. T. Lee, H. S. Yoon, and E. D. Wachsman, "The evolution of low temperature solid oxide fuel cells," *J. Mater. Res.*, vol. 27, no. 16, pp. 2063–2078, 2012.

[118] D. Beckel, "Thin Film Cathodes for Micro Solid Oxide Fuel Cells," Doctoral Thesis, ETH Zurich, 2007.

[119] D. Beckel, A. Bieberle-Hütter, A. Harvey, A. Infortuna, U. P. Muecke, M. Prestat, J. L. M. Rupp, and L. J. Gauckler, "Thin films for micro solid oxide fuel cells," *J. Power Sources*, vol. 173, pp. 325–345, 2007.

[120] A. A. Solovyev, N. S. Sochugov, S. V. Rabotkin, A. V. Shipilova, I. V. Ionov, A. N. Kovalchuk, and A. O. Borduleva, "Application of PVD methods to solid oxide fuel cells," *Appl. Surf. Sci.*, vol. 310, pp. 272–277, 2014.

[121] T. Suzuki, T. Suzuki, T. Yamaguchi, H. Sumi, K. Hamamoto, Y. Fujishiro, and W. Shin, "Fabrication and characterization of YSZ thin films for SOFC application," *J. Ceram. Soc. Japan*, vol. 4, no. 123, pp. 250–252, 2015.

[122] L. Wang, E. Thiele, and S. Barnett, "Sputter deposition of yttria-stabilized zirconia and silver cermet electrodes for SOFC applications," *Solid State Ionics*, vol. 52, no. 1–3, pp. 261–267, 1992.

[123] E. Gourba, P. Briois, A. Ringued, M. Cassir, and A. Billard, "Electrical properties of gadolinia-doped ceria thin films deposited by sputtering in view of SOFC application," *J. Solid State Electrochem.*, vol. 8, no. 9, pp. 633–637, 2004.

[124] S. W. Kim, Y. Lee, and G. M. Choi, "Electrical conductivity of Gd-doped ceria film at low temperatures (300-500 °C)," *Solid State Ionics*, vol. 262, pp. 411–415, 2014.

[125] W. Wu, X. Wang, Z. Liu, Z. Zhao, D. Ou, B. Tu, and M. Cheng, "Influence of deposition temperature of GDC interlayer deposited by RF magnetron sputtering on anode-supported SOFC," *Fuel Cells*, vol. 14, no. 2, pp. 171–176, 2014.

[126] F. J. Garcia-Garcia, F. Yubero, A. R. González-Elipe, S. P. Balomenou, D. Tsiplakides, I. Petrakopoulou, and R. M. Lambert, "Porous, robust highly conducting Ni-YSZ thin film anodes prepared by magnetron sputtering at oblique angles for application as anodes and buffer layers in solid oxide fuel cells," *Int. J. Hydrogen Energy*, vol. 40, no. 23, pp. 7382–7387, 2015.

[127] G. Jose La O, J. Hertz, H. Tuller, and Y. Shao-Horn, "Microstructural features of RF-sputtered SOFC anode and electrolyte materials," *J. Electroceramics*, vol. 13, pp. 691–695, 2004.

[128] A. Bieberle-Hütter and H. L. Tuller, "Fabrication and structural characterization of interdigitated thin film La1-xSrxCoO3 (LSCO) electrodes," *J. Electroceramics*, vol. 16, pp. 151–157, 2006.

[129] J. W. Lee, Z. Liu, L. Yang, H. Abernathy, S. H. Choi, H. E. Kim, and M. Liu, "Preparation of dense and uniform $La_{0.6}Sr_{0.4}Co_{0.2}Fe_{0.8}O_{3-d}$ (LSCF) films for fundamental studies of SOFC cathodes," *J. Power Sources*, vol. 190, no. 2, pp. 307–310, 2009.

[130] K. Rodrigo, J. Knudsen, N. Pryds, J. Schou, and S. Linderoth, "Characterization of yttria-stabilized zirconia thin films grown by pulsed laser deposition (PLD) on various substrates," *Appl. Surf. Sci.*, vol. 254, no. 4, pp. 1338–1342, 2007.

[131] J. H. Joo and G. M. Choi, "Electrical conductivity of YSZ film grown by pulsed laser deposition," *Solid State Ionics*, vol. 177, no. 11–12, pp. 1053–1057, 2006.

[132] R. Knibbe, J. Hjelm, M. Menon, N. Pryds, M. Søgaard, H. J. Wang, and K. Neufeld, "Cathode-electrolyte interfaces with CGO barrier layers in SOFC," *J. Am. Ceram. Soc.*, vol. 93, no. 9, pp. 2877–2883, 2010.

[133] J. H. Joo and G. M. Choi, "Open-circuit voltage of ceria-based thin film SOFC supported on nano-porous alumina," *Solid State Ionics*, vol. 178, no. 29–30, pp. 1602–1607, 2007.

[134] T. Ishihara, H. Eto, and J. Yan, "Intermediate temperature solid oxide fuel cells using $LaGaO_3$ based oxide film deposited by PLD method," *Int. J. Hydrogen Energy*, vol. 36, no. 2, pp. 1862–1867, 2011.

[135] J. Hwang, H. Lee, J.-H. Lee, K. J. Yoon, H. Kim, J. Hong, and J.-W. Son, "Specific considerations for obtaining appropriate $La_{1-x}Sr_xGa_{1-y}Mg_yO_{3-\delta}$ thin films using pulsed-laser deposition and its influence on the performance of solid-oxide fuel cells," *J. Power Sources*, vol. 274, pp. 41–47, 2015.

[136] F. S. Baumann, J. Fleig, H. U. Habermeier, and J. Maier, "$Ba_{0.5}Sr_{0.5}Co_{0.8}Fe_{0.2}O_{3-\delta}$ thin thin film microelectrodes investigated by impedance spectroscopy," *Solid State Ionics*, vol. 177, no. 35–36, pp. 3187–3191, 2006.

[137] B. A. Boukamp, N. Hildenbrand, P. Nammensma, and D. H. A. Blank, "The impedance of thin dense oxide cathodes," *Solid State Ionics*, vol. 192, no. 1, pp. 404–408, 2011.

[138] E. Koep, C. Jin, M. Haluska, R. Das, R. Narayan, K. Sandhage, R. Snyder, and M. Liu, "Microstructure and electrochemical properties of cathode materials for SOFCs prepared via pulsed laser deposition," *J. Power Sources*, vol. 161, no. 1, pp. 250–255, 2006.

[139] U. P. Muecke, K. Akiba, A. Infortuna, T. Salkus, N. V. Stus, and L. J. Gauckler, "Electrochemical performance of nanocrystalline nickel/gadolinia-doped ceria thin film anodes for solid oxide fuel cells," *Solid State Ionics*, vol. 178, pp. 1762–1768, 2008.

[140] P. Plonczak, A. Bieberle-Hütter, M. Søgaard, T. Ryll, J. Martynczuk, P. V. Hendriksen, and L. J. Gauckler, "Tailoring of $La_xSr_{1-x}Co_yFe_{1-y}O_{3-\delta}$ Nanostructure by Pulsed Laser Deposition," *Adv. Funct. Mater.*, vol. 21, no. 14, pp. 2764–2775, 2011.

[141] G. Meng, H. Song, C. Xia, X. Liu, and D. Peng, "Novel CVD Techniques for Micro- and IT-SOFC Fabrication," *Fuel Cells*, vol. 4, no. 12, pp. 48–55, 2004.

[142] G. Meng, "Application of novel aerosol-assisted chemical vapor deposition techniques for

SOFC thin films," *Solid State Ionics*, vol. 175, no. 1–4, pp. 29–34, 2004.

[143] M. Cassir, A. Ringuedé, and L. Niinistö, "Input of atomic layer deposition for solid oxide fuel cell applications," *J. Mater. Chem.*, vol. 20, no. 41, p. 8987, 2010.

[144] H. Z. Song, H. B. Wang, S. W. Zha, D. K. Peng, and G. Y. Meng, "Aerosol-assisted MOCVD growth of Gd_2O_3-doped CeO_2 thin SOFC electrolyte film on anode substrate," *Solid State Ionics*, vol. 156, no. 3–4, pp. 249–254, 2003.

[145] J. Will, A. Mitterdorfer, C. Kleinlogel, D. Perednis, and L. J. Gauckler, "Fabrication of thin electrolytes for second-generation solid oxide fuel cells," *Solid State Ionics*, vol. 131, no. 1, pp. 79–96, 2000.

[146] G. Garcia, J. Caro, J. Santiso, J. A. Pardo, A. Figueras, and A. Abrutis, "Pulsed injection MOCVD of YSZ thin films onto dense and porous substrates," *Chem. Vap. Depos.*, vol. 9, no. 5, pp. 279–284, 2003.

[147] J. L. M. Rupp, "Nanocrystalline Ceria-based Electrolyte Thin Films for Micro-Solid Oxide Fuel Cells," Doctoral Thesis, ETH Zurich, 2006.

[148] P. Charpentier, P. Fragnaud, D. M. Schleich, and E. Gehain, "Preparation of thin film SOFCs working at reduced temperature," *Solid State Ionics*, vol. 135, no. 1–4, pp. 373–380, 2000.

[149] J. L. M. Rupp and L. J. Gauckler, "Microstructures and electrical conductivity of nanocrystalline ceria-based thin films," *Solid State Ionics*, vol. 177, pp. 2513–2518, 2006.

[150] D. Beckel, U. P. Muecke, T. Gyger, G. Florey, A. Infortuna, and L. J. Gauckler, "Electrochemical performance of LSCF based thin film cathodes prepared by spray pyrolysis," *Solid State Ionics*, vol. 178, pp. 407–415, 2007.

[151] A. J. Darbandi, T. Enz, and H. Hahn, "Synthesis and characterization of nanoparticulate films for intermediate temperature solid oxide fuel cells," *Solid State Ionics*, vol. 180, no. 4–5, pp. 424–430, 2009.

[152] L. Da Conceição, L. Dessemond, E. Djurado, and M. M. V. M. Souza, "Thin films of $La_{0.7}Sr_{0.3}MnO_{3-\delta}$ dip-coated on Fe-Cr alloys for SOFC metallic interconnect," *Int. J. Hydrogen Energy*, vol. 38, no. 35, pp. 15335–15347, 2013.

[153] A. J. Darbandi and H. Hahn, "Nanoparticulate cathode thin films with high electrochemical activity for low temperature SOFC applications," *Solid State Ionics*, vol. 180, no. 26–27, pp. 1379–1387, 2009.

[154] L. Baqué and A. Serquis, "Microstructural characterization of $La_{0.4}Sr_{0.6}Co_{0.8}Fe_{0.2}O_{3-\delta}$ films deposited by dip coating," *Appl. Surf. Sci.*, vol. 254, no. 1 SPEC. ISS., pp. 213–218, 2007.

[155] M. Chen, B. H. Kim, Q. Xu, B. G. Ahn, and D. P. Huang, "Effect of Ni content on the microstructure and electrochemical properties of Ni-SDC anodes for IT-SOFC," *Solid State Ionics*, vol. 181, no. 23–24, pp. 1119–1124, 2010.

[156] X. Xu, C. Xia, S. Huang, and D. Peng, "YSZ thin films deposited by spin-coating for IT-SOFCs," *Ceram. Int.*, vol. 31, no. 8, pp. 1061–1064, 2005.

[157] Q. Zhu and B. Fan, "Low temperature sintering of 8YSZ electrolyte film for intermediate temperature solid oxide fuel cells," *Solid State Ionics*, vol. 176, no. 9–10, pp. 889–894, 2005.

[158] J. Hierso, P. Boy, K. Vallé, J. Vulliet, F. Blein, C. Laberty-Robert, and C. Sanchez, "Nanostructured ceria based thin films (≤ 1 μm) As cathode/electrolyte interfaces," *J. Solid State Chem.*, vol. 197, pp. 113–119, 2013.

[159] Y. D. Zhen, a. I. Y. Tok, S. P. Jiang, and F. Y. C. Boey, "Fabrication and performance of gadolinia-doped ceria-based intermediate-temperature solid oxide fuel cells," *J. Power Sources*, vol. 178, no. 1, pp. 69–74, 2008.

[160] P.-Y. Chu and R. C. Buchanan, "Characteristics of oxide thin films from carboxylate precursors," *J. Mater. Res.*, vol. 6, no. 8, pp. 1736–1743, 1991.

[161] C. Endler-Schuck, A. Weber, E. Ivers-Tiffée, U. Guntow, J. Ernst, and J. Ruska, "Nanoscale Gd-Doped CeO_2 Buffer Layer for a High Performance Solid Oxide Fuel Cell," *J. Fuel Cell Sci. Technol.*, vol. 8, no. 4, p. 41001, 2011.

[162] K. Hayashi, M. Hosokawa, T. Yoshida, Y. Ohya, Y. Takahashi, O. Yamamoto, and H. Minoura, "$La_{1-x}Sr_xMnO_3$-YSZ composite film electrodes prepared by metal-organic decomposition for solid oxide fuel cells," *Mater. Sci. Eng. B*, vol. 49, no. 3, pp. 239–242,

1997.

[163] E. Barsoukov and J. R. Macdonald, *Impedance Spectroscopy: Theory, Experiment, and Applications*. John Wiley & Sons, 2005.

[164] A. J. Bard and L. R. Faulkner, *ELECTROCHEMICAL METHODS: Fundamentals and applications*. John Wiley & Sons, 2001.

[165] N. I. Karageorgakis, A. Heel, A. Bieberle-Hütter, J. L. M. Rupp, T. Graule, and L. J. Gauckler, "Flame spray deposition of $La_{0.6}Sr_{0.4}CoO_{3-\delta}$ thin films: Microstructural characterization, electrochemical performance and degradation," *J. Power Sources*, vol. 195, no. 24, pp. 8152–8161, 2010.

[166] A. Heel, P. Holtappels, and T. Graule, "On the synthesis and performance of flame-made nanoscale $La_{0.6}Sr_{0.4}CoO_{3-\delta}$ and its influence on the application as an intermediate temperature solid oxide fuel cell cathode," *J. Power Sources*, vol. 195, no. 19, pp. 6709–6718, 2010.

[167] Y. Tao, J. Shao, J. Wang, and W. G. Wang, "Synthesis and properties of $La_{0.6}Sr_{0.4}CoO_{3-\delta}$ thin nanopowder," *J. Power Sources*, vol. 185, pp. 609–614, 2008.

[168] J.-H. Park, W.-S. Hong, K. J. Yoon, J.-H. Lee, H.-W. Lee, and J.-W. Son, "Physical and Electrochemical Characteristics of Pulsed Laser Deposited $La_{0.6}Sr_{0.4}CoO_{3-\delta}$-$Ce_{0.9}Gd_{0.1}O_{2-\delta}$ Nanocomposites as a Function of the Mixing Ratio," *J. Electrochem. Soc.*, vol. 161, no. 1, pp. F16–F22, 2014.

[169] S. Wang, J. Yoon, G. Kim, D. Huang, H. Wang, and A. J. Jacobson, "Electrochemical Properties of Nanocrystalline $La_{0.5}Sr_{0.5}CoO_{3-x}$ Thin Films," *Chem. Mater.*, vol. 22, no. 3, pp. 776–782, 2010.

[170] C. Peters, A. Weber, and E. Ivers-Tiffée, "Nanoscaled $(La_{0.5}Sr_{0.5})CoO_{3-d}$ Thin Film Cathodes for SOFC Application at 500 °C<T<700 °C," *J. Electrochem. Soc.*, vol. 155, no. 7, p. B730, 2008.

[171] Y. Tao, J. Shao, W. G. Wang, and J. Wang, "Optimisation and Evaluation of $La_{0.6}Sr_{0.4}CoO_{3-\delta}$ Cathode for Intermediate Temperature Solid Oxide Fuel Cells," *Fuel Cells*, vol. 9, no. 5, pp. 679–683, 2009.

[172] O. Gwon, S. Yoo, J. Shin, and G. Kim, "Optimization of $La_{1-x}Sr_xCoO_{3-\delta}$ perovskite cathodes for intermediate temperature solid oxide fuel cells through the analysis of crystal structure and electrical properties," *Int. J. Hydrogen Energy*, vol. 39, no. 35, pp. 3–8, 2014.

[173] L. Baqué, A. Caneiro, M. S. Moreno, and A. Serquis, "High performance nanostructured IT-SOFC cathodes prepared by novel chemical method," *Electrochem. commun.*, vol. 10, no. 12, pp. 1905–1908, 2008.

[174] D. A. Macedo, F. M. L. Figueiredo, C. A. Paskocimas, A. E. Martinelli, R. M. Nascimento, and F. M. B. Marques, "Ni–CGO cermet anodes from nanocomposite powders: Microstructural and electrochemical assessment," *Ceram. Int.*, vol. 40, no. 8, pp. 13105–13113, 2014.

[175] M. R. Somalu, V. Yufit, D. Cumming, E. Lorente, and N. P. Brandon, "Fabrication and characterization of Ni/ScSZ cermet anodes for IT-SOFCs," *Int. J. Hydrogen Energy*, vol. 36, no. 9, pp. 5557–5566, 2011.

[176] L. Liu, G.-Y. Kim, A. C. Hillier, and A. Chandra, "Microstructural and electrochemical impedance study of nickel–$Ce_{0.9}Gd_{0.1}O_{1.95}$ anodes for solid oxide fuel cells fabricated by ultrasonic spray pyrolysis," *J. Power Sources*, vol. 196, no. 6, pp. 3026–3032, 2011.

[177] M. K. Rath, M.-J. Lee, and K.-T. Lee, "Preparation of nano-structured Ni–$Ce_{0.8}Gd_{0.2}O_{1.9}$ anode materials for solid oxide fuel cells via the water-in-oil (W/O) micro-emulsion route," *Ceram. Int.*, vol. 40, no. 1, pp. 1909–1917, 2014.

[178] K. Yamamoto, T. Hashishin, M. Matsuda, N. Qiu, Z. Tan, and S. Ohara, "High-performance Ni nanocomposite anode fabricated from Gd-doped ceria nanocubes for low-temperature solid-oxide fuel cells," *Nano Energy*, vol. 6, pp. 103–108, 2014.

[179] L. Almar, B. Colldeforns, L. Yedra, S. Estradé, F. Peiró, A. Morata, T. Andreu, and A. Tarancón, "High-temperature long-term stable ordered mesoporous Ni–CGO as an anode for solid oxide fuel cells," *J. Mater. Chem. A*, vol. 1, no. 14, p. 4531, 2013.

[180] M. B. Jörger, "CuO-CGO Anodes for Solid Oxide Fuel Cells," Doctoral Thesis, ETH Zurich,

2004.

[181] S. Wang, M. Ando, T. Ishihara, and Y. Takita, "High performance Ni-$Sm_{0.15}Ce_{0.85}O_{2-\delta}$ cermet anodes for intermediate temperature solid oxide fuel cells using $LaGaO_3$ based oxide electrolytes," *Solid State Ionics*, vol. 174, pp. 49–55, 2004.

[182] F. Han, R. Mücke, T. Van Gestel, A. Leonide, N. H. Menzler, H. P. Buchkremer, and D. Stöver, "Novel high-performance solid oxide fuel cells with bulk ionic conductance dominated thin-film electrolytes," *J. Power Sources*, vol. 218, pp. 157–162, 2012.

[183] D. Koltz, J. Hayd, J. Szasz, N. H. Menzler, and E. Ivers-Tiffee, "Nano-scaled Mixed Conductors for High Performance SOFC at <600 °C," *ECS Trans.*, vol. 61, no. 1, pp. 23–29, 2014.

[184] P. Moller, R. Kanarbik, I. Kivi, G. Nurk, and E. Lust, "Influence of Microstructure on the Electrochemical Behavior of LSC Cathodes for Intermediate Temperature SOFC," *J. Electrochem. Soc.*, vol. 160, no. 11, pp. F1245–F1253, 2013.

[185] Y. Chen, Y. Zhang, J. Baker, P. Majumdar, Z. Yang, M. Han, and F. Chen, "Hierarchically oriented macroporous anode-supported solid oxide fuel cell with thin ceria electrolyte film," *ACS Appl. Mater. Interfaces*, vol. 6, pp. 5130–5136, 2014.

[186] J. G. Lee, C. M. Lee, M. G. Park, S. J. Jung, and Y. G. Shul, "Performance evaluation of anode-supported $Gd_{0.1}Ce_{0.9}O_{1.95}$ cell with electrospun $La_{0.6}Sr_{0.4}Co_{0.2}Fe_{0.8}O_{3-\delta}$-$Gd_{0.1}Ce_{0.9}O_{1.95}$ cathode," *Electrochim. Acta*, vol. 108, pp. 356–360, 2013.

[187] Y. Leng, S. H. Chan, and Q. Liu, "Development of LSCF-GDC composite cathodes for low-temperature solid oxide fuel cells with thin film GDC electrolyte," *Int. J. Hydrogen Energy*, vol. 33, no. 14, pp. 3808–3817, 2008.

[188] C. Ding, H. Lin, K. Sato, K. Amezawa, T. Kawada, J. Mizusaki, and T. Hashida, "Effect of thickness of $Gd_{0.1}Ce_{0.9}O_{1.95}$ electrolyte films on electrical performance of anode-supported solid oxide fuel cells," *J. Power Sources*, vol. 195, no. 17, pp. 5487–5492, 2010.

[189] S. Kang, P. C. Su, Y. I. Park, Y. Saito, and F. B. Prinz, "Thin-Film Solid Oxide Fuel Cells on Porous Nickel Substrates with Multistage Nanohole Array," *J. Electrochem. Soc.*, vol. 153, no. 3, p. A554, 2006.

[190] K. Kerman, B. K. Lai, and S. Ramanathan, "Thin film nanocrystalline $Ba_{0.5}Sr_{0.5}Co_{0.8}Fe_{0.2}O_3$: Synthesis, conductivity, and micro-solid oxide fuel cells," *J. Power Sources*, vol. 196, no. 15, pp. 6214–6218, 2011.

[191] A. Evans, A. Bieberle-Hütter, L. J. Bonderer, S. Stuckenholz, and L. J. Gauckler, "Micro-solid oxide fuel cells using free-standing 3mol.% yttria-stabilised-tetragonal-zirconia-polycrystal electrolyte foils," *J. Power Sources*, vol. 196, no. 23, pp. 10069–10073, 2011.

[192] K. Kerman, B. K. Lai, and S. Ramanathan, "$Pt/Y_{0.16}Zr_{0.84}O_{1.92}/Pt$ thin film solid oxide fuel cells: Electrode microstructure and stability considerations," *J. Power Sources*, vol. 196, no. 5, pp. 2608–2614, 2011.

[193] Y. Takagi, S. Adam, and S. Ramanathan, "Nanostructured ruthenium-Gadolinia-doped ceria composite anodes for thin film solid oxide fuel cells," *J. Power Sources*, vol. 217, pp. 543–553, 2012.

[194] S. Brunauer, P. H. Emmett, and E. Teller, "Adsorption of Gases in Multimolecular Layers," *J. Am. Chem. Soc.*, vol. 60, no. 1, pp. 309–319, 1938.

[195] A. J. Darbandi, "Nanoparticulate Cathode Films for Low Temperature Solid Oxide Fuel Cells," Doctoral Thesis, TU Darmstadt, 2012.

[196] O. Milosevic, L. Mancic, M. E. Rabanal, L. S. Gomez, and K. Marinkovic, "Aerosol route in processing of nanostructured functional materials," *KONA Powder Part. J.*, vol. 27, no. 27, pp. 84–106, 2009.

[197] J. G. Li, T. Ikegami, J. H. Lee, and T. Mori, "Characterization and sintering of nanocrystalline CeO_2 powders synthesized by a mimic alkoxide method," *Acta Mater.*, vol. 49, pp. 419–426, 2001.

[198] A. Martino, S. Yamanaka, and J. Kawola, "Encapsulation of gold nanoclusters in silica materials via an inverse micelle/sol-gel synthesis," *Chem. Mater.*, vol. 4756, no. 24, pp. 423–429, 1997.

[199] S. E. Pratsinis, "Flame aerosol synthesis of ceramic powders," *Prog. Energy Combust. Sci.*, vol. 24, no. 97, pp. 197–219, 1998.

[200] S. Seifried, M. Winterer, and H. Hahn, "Nanocrystalline Titania Films and Particles by Chemical Vapor Synthesis," *Chem. Vap. Depos.*, vol. 6, no. 5, pp. 239–244, 2000.

[201] G. L. Messing, S.-C. Zhang, and G. V. Jayanthi, "Ceramic Powder Synthesis," *J. Am. Ceram. Soc.*, vol. 76, pp. 2707–2726, 1993.

[202] I. W. Lenggoro, T. Hata, F. Iskandar, M. M. Lunden, and K. Okuyama, "An experimental and modeling investigation of particle production by spray pyrolysis using a laminar flow aerosol reactor," *J. Mater. Res.*, vol. 15, no. 3, pp. 733–743, 2000.

[203] B. Xia, I. Lenggoro, and K. Okuyama, "Synthesis of CeO_2 nanoparticles by salt-assisted ultrasonic aerosol decomposition," *J. Mater. Chem.*, vol. 11, pp. 2925–2927, 2001.

[204] B. Bin Xia, W. Lenggoro, and K. Okuyama, "Novel Route to Nanoparticle Synthesis," *Adv. Mater.*, vol. 13, no. 20, pp. 1579–1582, 2001.

[205] E. Konysheva, R. Blackley, and J. T. S. Irvine, "Conductivity behavior of composites in the $La_{0.6}Sr_{0.4}CoO_3$-CeO_2 system: Function of connectivity and interfacial interactions," *Chem. Mater.*, vol. 22, no. 12, pp. 4700–4711, 2010.

[206] S. Dikmen, P. Shuk, M. Greenblatt, and H. Gocmez, "Hydrothermal synthesis and properties of $Ce_{1-x}Gd_xO_{2-\delta}$ solid solutions," *Solid State Sci.*, vol. 4, pp. 585–590, 2002.

[207] B. Cela, D. A. De MacEdo, G. L. De Souza, A. E. Martinelli, R. M. Do Nascimento, and C. A. Paskocimas, "NiO-CGO in situ nanocomposite attainment: One step synthesis," *J. Power Sources*, vol. 196, no. 5, pp. 2539–2544, 2011.

[208] G. S. Lewis, a. Atkinson, B. C. H. Steele, and J. Drennan, "Effect of Co addition on the lattice parameter, electrical conductivity and sintering of gadolinia-doped ceria," *Solid State Ionics*, vol. 152–153, pp. 567–573, 2002.

[209] C. Benel, A. J. Darbandi, R. Djenadic, A. Evans, R. Tölke, M. Prestat, and H. Hahn, "Synthesis and characterization of nanoparticulate $La_{0.6}Sr_{0.4}CoO_{3-\delta}$ cathodes for thin-film solid oxide fuel cells," *J. Power Sources*, vol. 229, pp. 258–264, 2013.

[210] B. Scherrer, A. Evans, A. J. Santis-Alvarez, B. Jiang, J. Martynczuk, H. Galinski, M. Nabavi, M. Prestat, R. Tölke, A. Bieberle-Hütter, D. Poulikakos, P. Muralt, P. Niedermann, A. Dommann, T. Maeder, P. Heeb, V. Straessle, C. Muller, and L. J. Gauckler, "A thermally self-sustained micro-power plant with integrated micro-solid oxide fuel cells, micro-reformer and functional micro-fluidic carrier," *J. Power Sources*, vol. 258, pp. 434–440, 2014.

[211] C. Meier, T. Hocker, A. Bieberle-Hütter, and L. J. Gauckler, "Analyzing a micro-solid oxide fuel cell system by global energy balances," *Int. J. Hydrogen Energy*, vol. 37, pp. 10318–10327, 2012.

[212] H. Galinski, T. Ryll, P. Elser, J. L. M. Rupp, A. Bieberle-Hütter, and L. J. Gauckler, "Agglomeration of Pt thin films on dielectric substrates," *Phys. Rev. B*, vol. 82, no. 23, p. 235415, 2010.

[213] H. Jung, K. Bae, D. Y. Jang, Y. H. Lee, S.-W. Cha, and J. H. Shim, "Evaluation of porous platinum, nickel, and lanthanum strontium cobaltite as electrode materials for low-temperature solid oxide fuel cells," *Int. J. Hydrogen Energy*, vol. 39, no. 31, pp. 17828–17835, 2014.

[214] A. C. Johnson, B. K. Lai, H. Xiong, and S. Ramanathan, "An experimental investigation into micro-fabricated solid oxide fuel cells with ultra-thin $La_{0.6}Sr_{0.4}Co_{0.8}Fe_{0.2}O_3$ cathodes and yttria-doped zirconia electrolyte films," *J. Power Sources*, vol. 186, no. 2, pp. 252–260, 2009.

[215] O. A. Williams, J. Hees, C. Dieker, W. Jäger, L. Kirste, and C. E. Nebel, "Size-dependent reactivity of diamond nanoparticles.," *ACS Nano*, vol. 4, no. 8, pp. 4824–30, 2010.

[216] Y.-J. Shin, C.-C. Su, and Y.-H. Shen, "Dispersion of aqueous nano-sized alumina suspensions using cationic polyelectrolyte," *Mater. Res. Bull.*, vol. 41, no. 10, pp. 1964–1971, 2006.

[217] H. S. Noh, H. Lee, B. K. Kim, H. W. Lee, J. H. Lee, and J. W. Son, "Microstructural factors of electrodes affecting the performance of anode-supported thin film yttria-stabilized zirconia electrolyte solid oxide fuel cells," *J. Power Sources*, vol. 196, no. 17, pp. 7169–7174, 2011.

[218] A. Evans, "Fabrication and electrochemical characterization of micro-solid oxide fuel cell

membranes," Doctoral Thesis, ETH Zurich, 2012.

[219] M. J. Jørgensen and M. Mogensen, "Impedance of Solid Oxide Fuel Cell LSM/YSZ Composite Cathodes," *J. Electrochem. Soc.*, vol. 148, no. 5, p. A433, 2001.

[220] Z. Bi, M. Cheng, Y. Dong, H. Wu, Y. She, and B. Yi, "Electrochemical evaluation of $La_{0.6}Sr_{0.4}CoO_3$–$La_{0.45}Ce_{0.55}O_2$ composite cathodes for anode-supported $La_{0.45}Ce_{0.55}O_2$–$La_{0.9}Sr_{0.1}Ga_{0.8}Mg_{0.2}O_{2.85}$ bilayer electrolyte solid oxide fuel cells," *Solid State Ionics*, vol. 176, no. 7–8, pp. 655–661, 2005.

[221] H. J. Ko, J. Myung, J.-H. Lee, S.-H. Hyun, and J. S. Chung, "Synthesis and evaluation of $(La_{0.6}Sr_{0.4})(Co_{0.2}Fe_{0.8})O_3$ (LSCF)–$Y_{0.08}Zr_{0.92}O_{1.96}$ (YSZ)–$Gd_{0.1}Ce_{0.9}O_{2-\delta}$ (GDC) dual composite SOFC cathodes for high performance and durability," *Int. J. Hydrogen Energy*, vol. 37, no. 22, pp. 17209–17216, 2012.

[222] Y. M. Park, J. H. Kim, and H. Kim, "High-Performance composite cathodes for solid oxide fuel cells," *Int. J. Hydrogen Energy*, vol. 36, no. 15, pp. 9169–9179, 2011.

[223] A. Evans, M. Prestat, R. Tölke, M. V. F. Schlupp, L. J. Gauckler, Y. Safa, T. Hocker, J. Courbat, D. Briand, N. F. De Rooij, and D. Courty, "Residual stress and buckling patterns of free-standing yttria-stabilized- zirconia membranes fabricated by pulsed laser deposition," *Fuel Cells*, vol. 12, no. 4, pp. 614–623, 2012.

[224] E. Mutoro, E. J. Crumlin, M. D. Biegalski, H. M. Christen, and Y. Shao-Horn, "Enhanced oxygen reduction activity on surface-decorated perovskite thin films for solid oxide fuel cells," *Energy Environ. Sci.*, vol. 4, no. 9, p. 3689, 2011.

[225] S. P. Yoon, S. W. Nam, J. Han, T. H. Lim, S. A. Hong, and S. H. Hyun, "Effect of electrode microstructure on gas-phase diffusion in solid oxide fuel cells," *Solid State Ionics*, vol. 166, no. 1–2, pp. 1–11, 2004.

[226] S. B. Adler, X. Y. Chen, and J. R. Wilson, "Mechanisms and rate laws for oxygen exchange on mixed-conducting oxide surfaces," *J. Catal.*, vol. 245, no. 1, pp. 91–109, 2007.

[227] A. Jun, J. Kim, J. Shin, and G. C. Kim, "Optimization of Sr content in layered $SmBa_{1-x}SrCo_2O_{5+d}$ perovskite cathode for intermediate-temperature solid oxide fuel cells," *Int. J. Hydrogen Energy*, vol. 37, no. 23, pp. 18381–18388, 2012.

[228] D. Mori, H. Oka, Y. Suzuki, N. Sonoyama, A. Yamada, R. Kanno, Y. Sumiya, N. Imanishi, and Y. Takeda, "Synthesis, structure, and electrochemical properties of epitaxial perovskite $La_{0.8}Sr_{0.2}CoO_3$ film on YSZ substrate," *Solid State Ionics*, vol. 177, no. 5–6, pp. 535–540, 2006.

[229] U. P. Muecke, S. Graf, U. Rhyner, and L. J. Gauckler, "Microstructure and electrical conductivity of nanocrystalline nickel- and nickel oxide/gadolinia-doped ceria thin films," *Acta Mater.*, vol. 56, pp. 677–687, 2008.

[230] F. S. Torknik, M. Keyanpour-Rad, A. Maghsoudipour, and G. M. Choi, "Effect of microstructure refinement on performance of $Ni/Ce_{0.8}Gd_{0.2}O_{1.9}$ anodes for low temperature solid oxide fuel cell," *Ceram. Int.*, vol. 40, no. 1, pp. 1341–1350, 2014.

[231] S. P. Jiang and S. H. Chan, "A review of anode materials development in solid oxide fuel cells," *J. Mater. Sci.*, vol. 39, no. 14, pp. 4405–4439, 2004.

[232] Q. X. Fu, F. Tietz, and D. Stöver, "$La_{0.4}Sr_{0.6}Ti_{1-x}Mn_xO_{3-\delta}$ Perovskites as Anode Materials for Solid Oxide Fuel Cells," *J. Electrochem. Soc.*, vol. 153, p. D74, 2006.

[233] M. V. Sandoval, A. Matta, T. Matencio, R. Z. Domingues, G. a. Ludwig, M. De Angelis Korb, C. De Fraga Malfatti, P. Gauthier-Maradei, and G. H. Gauthier, "Barium-modified NiO-YSZ/NiO-GDC cermet as new anode material for solid oxide fuel cells (SOFC)," *Solid State Ionics*, vol. 261, pp. 36–44, 2014.

[234] A. Bieberle, "The electrochemistry of solid oxide fuel cell anodes: experiments, modeling, and simulations," Doctoral Thesis, ETH Zurich, 2000.

[235] M. K. Rath, B. H. Choi, M. J. Ji, and K. T. Lee, "Eggshell-membrane-templated synthesis of hierarchically-ordered $NiO-Ce_{0.8}Gd_{0.2}O_{1.9}$ composite powders and their electrochemical performances as SOFC anodes," *Ceram. Int.*, vol. 40, no. 2, pp. 3295–3304, 2014.

[236] M. Tsuchiya, B.-K. Lai, and S. Ramanathan, "Scalable nanostructured membranes for solid-oxide fuel cells." *Nat. Nanotechnol.*, vol. 6, no. 5, pp. 282–286, 2011.

[237] B.-K. Lai, K. Kerman, and S. Ramanathan, "Nanostructured $La_{0.6}Sr_{0.4}Co_{0.8}Fe_{0.2}O_3/Y_{0.08}Zr_{0.92}O_{1.96}/La_{0.6}Sr_{0.4}Co_{0.8}Fe_{0.2}O_3$ (LSCF/YSZ/LSCF) symmetric thin film solid oxide fuel cells," *J. Power Sources*, vol. 196, no. 4, pp. 1826–1832, 2011.

[238] I. Garbayo, V. Esposito, S. Sanna, A. Morata, D. Pla, L. Fonseca, N. Sabaté, and A. Tarancón, "Porous $La_{0.6}Sr_{0.4}CoO_{3-\delta}$ thin film cathodes for large area micro solid oxide fuel cell power generators," *J. Power Sources*, vol. 248, pp. 1042–1049, 2014.

[239] C.-H. Chen, N. Wakiya, K. Shinozaki, and N. Mizutani, "Effects of thermal coefficient and lattice constant mismatches on mosaic dispersion of heteroepitaxial YSZ/Si(001) thin films," *J. Phys. D. Appl. Phys.*, vol. 35, no. 2, p. 151, 2001.

[240] Y. Safa, T. Hocker, M. Prestat, and A. Evans, "Post-buckling design of thin-film electrolytes in micro-solid oxide fuel cells," *J. Power Sources*, vol. 250, pp. 332–342, 2014.

[241] B. K. Lai, A. C. Johnson, H. Xiong, and S. Ramanathan, "Ultra-thin nanocrystalline lanthanum strontium cobalt ferrite ($La_{0.6}Sr_{0.4}Co_{0.8}Fe_{0.2}O_{3-\delta}$) films synthesis by RF-sputtering and temperature-dependent conductivity studies," *J. Power Sources*, vol. 186, pp. 115–122, 2009.

[242] C. Fu, X. Ge, S. H. Chan, and Q. Liu, "Fabrication and characterization of anode-supported low-temperature SOFC based on Gd-doped ceria electrolyte," *Fuel Cells*, vol. 12, no. 3, pp. 450–456, 2012.

[243] Y. G. Choi, J. Y. Park, H. Song, H. R. Kim, J. W. Son, J. H. Lee, H. J. Je, B. K. Kim, H. W. Lee, and K. J. Yoon, "Microstructure-polarization relations in nickel/gadolinia-doped ceria anode for intermediate-temperature solid oxide fuel cells," *Ceram. Int.*, vol. 39, no. 4, pp. 4713–4718, 2013.

[244] M. Chen, B. H. Kim, Q. Xu, B. G. Ahn, and D. P. Huang, "Fabrication and performance of anode-supported solid oxide fuel cells via slurry spin coating," *J. Memb. Sci.*, vol. 360, no. 1–2, pp. 461–468, 2010.

[245] J. G. Lee, J. H. Park, and Y. G. Shul, "Tailoring gadolinium-doped ceria-based solid oxide fuel cells to achieve 2 W cm^{-2} at 550 °C," *Nat. Commun.*, vol. 5, no. May, 2014.

[246] S. Cruz-Manzo, R. Chen, and P. Rama, "Inductive Effect on the Fuel Cell Cathode Impedance Spectrum at High Frequencies," *J. Fuel Cell Sci. Technol*, vol. 9, no. 5, pp. 51002–51010, 2012.

[247] C. Endler-Schuck, A. Leonide, A. Weber, S. Uhlenbruck, F. Tietz, and E. Ivers-Tiffée, "Performance analysis of mixed ionic-electronic conducting cathodes in anode supported cells," *J. Power Sources*, vol. 196, no. 17, pp. 7257–7262, 2011.

[248] E. V. Tsipis and V. V. Kharton, "Electrode materials and reaction mechanisms in solid oxide fuel cells: A brief review: I Electrochemical behavior vs. materials science aspects," *J. Solid State Electrochem.*, vol. 12, pp. 1367–1391, 2008.

[249] Q. L. Liu, K. A. Khor, and S. H. Chan, "High-performance low-temperature solid oxide fuel cell with novel BSCF cathode," *J. Power Sources*, vol. 161, pp. 123–128, 2006.